AIX-MARSEILLE UNIVERSITÉ

ECOLE DOCTORALE 352

OFFICE NATIONAL D'ÉTUDES ET DE RECHERCHES AÉROSPATIALES

SPACE TELESCOPE SCIENCE INSTITUTE

LABORATOIRE D'ASTROPHYSIQUE DE MARSEILLE/UMR 7326

Thèse présentée pour obtenir le grade universitaire de docteur

Discipline: Physique et sciences de la matière
Spécialité: Optique, Photonique et Traitement d'Image

Lucie LEBOULLEUX

Contrôle de front d'onde optimal pour l'imagerie à haut contraste
Application au cophasage de miroirs segmentés

Optimal wavefront control for high-contrast imaging
Application to cophasing of segmented mirrors

Soutenue le 17/10/2018 devant le jury composé de:

Sylvie ROQUES	IRAP - CNRS/Université Toulouse III - Paul Sabatier	Rapporteur
Marshall PERRIN	Space Telescope Science Institute	Rapporteur
Marc FERRARI	Laboratoire d'Astrophysique de Marseille	Examinateur
Frantz MARTINACHE	UMR Lagrange	Examinateur
Pierre BAUDOZ	Observatoire de Meudon - LESIA	Examinateur
Thierry FUSCO	ONERA - Laboratoire d'Astrophysique de Marseille	Directeur de thèse
Rémi SOUMMER	Space Telescope Science Institute	Invité/Encadrant
Jean-François SAUVAGE	ONERA - Laboratoire d'Astrophysique de Marseille	Invité/Encadrant
Laurent PUEYO	Space Telescope Science Institute	Invité/Encadrant

Numéro national de thèse/suffixe local: 2018AIXM0561/077ED352

Remerciements

Cette thèse n'aurait pas été sans le soutien, les conseils, et l'intérêt porté par de nombreuses personnes, que je tiens à remercier du fond du cœur.

Tout d'abord, je souhaite exprimer toute ma gratitude aux membres du jury pour avoir montré intérêt et investissement tant en amont que le jour de ma soutenance : Marc Ferrari, Frantz Martinache, Marshall Perrin qui est venu de beaucoup trop loin, Pierre Baudoz et Sylvie Roques, qui ont aussi eu à affronter des complications de dernière minute. Sylvie Roques et Marshall Perrin, en particulier, ont courageusement lu chaque page de ce manuscrit. Aussi dans mon jury, mais surtout présents chaque jour de ces trois années : Thierry Fusco et Jean-François Sauvage d'une part et Rémi Soummer et Laurent Pueyo d'autre part m'ont permis de travailler dans de bonnes conditions, de grandir et d'apprendre à me faire confiance. Je leur suis particulièrement reconnaissante pour la confiance qu'ils ont eue en moi, que ce soit pour l'avancée de mon travail comme pour le choix du nom de mon algorithme, malgré la distance et les difficultés liées à mon double voire triple rattachement.

Il est difficile de mentionner mes directeurs de thèse et encadrants sans parler des structures qui, à travers eux, m'ont accueillie et soutenue. Le Space Telescope Science Institute, que j'ai d'abord découvert en stage de master 1, m'a à nouveau chaleureusement ouvert ses locaux et son extraordinaire labo en thèse. En particulier, l'équipe du Makidon Lab m'a permis d'évoluer dans une bulle aussi chaleureuse qu'efficace ! J'aimerais aussi remercier Anand pour nos discussions, ses corrections et encouragements. Je suis aussi reconnaissante au french aerospace lab ONERA qui a accepté de m'accueillir et de financer la seconde partie de ma thèse malgré les difficultés organisationnelles, et en particulier Olivier et Laurent pour nos échanges toujours constructifs et nos aventures sur MITHIC. Enfin, je tiens à remercier le Laboratoire d'Astrophysique de Marseille et en particulier Emmanuel Hugot pour m'avoir généreusement offert un bureau sous le soleil et près de la mer, joint à de multiples conseils et services. J'aurais difficilement pu rêver mieux que ces laboratoires pour mener

cette thèse à bout !

Au travers de mes voyages transatlantiques, j'ai eu la chance de rencontrer des personnes incroyables, passionnées et passionnantes. A Baltimore, Peter m'a soutenue sans réserve au cours de ces années, ainsi que mes chers Brendan et Nikita, et les admirables Camilla, Elena et Vicente, parmi un groupe tout aussi adorable mais malheureusement trop nombreux pour être entièrement listé. A mi-chemin entre Baltimore et la France, j'aimerais remercier la persévérante et courageuse Elodie, Elena, amie, coloc et maintenant docteure, et enfin Mamadou, probablement la personne la plus gentille que j'aie pu rencontrer. Sans vraiment savoir où le placer sur la petite Terre qui occupe mon esprit en ce moment, je suis très reconnaissante à Johan pour les coups de boost au moral (et au physique ! Mon premier et dernier semi-marathon restera un grand moment), les conseils et recommandations, les chichas à 2h du matin, les dégustations de thés et de whisky et les cours de lindy hop.

Parler de lindy hop m'amène naturellement à Marseille : merci aux swingueurs d'avoir tenté de distiller un peu de rythme et d'élégance dans les pattes des joyeux lurons que nous sommes. Et merci, merci aux joyeux lurons : Thibault pour le montage, Arthur pour sa disponibilité et ses conseils, Charlotte, formidable camarade de bureau et plus généralement formidable personne, Simona, toujours intrépide et si compréhensive, Michmich, ami polisson et polisseur et incroyable professeur, Oliv' pour les nœuds d'esprit, de mots et de fils de pêche, Anaïs, si généreuse et courageuse, toujours partante pour un thé avec quelques heures de discussion en accompagnement, Val' pour l'accueil et la gentillesse, Sabri qui mériterait d'être la vedette de plus d'un clip, mon cher Taï, si loin et si proche. Merci à la nouvelle génération de thésards : Mel, déjà, allégorie de l'enthousiasme, de l'engagement et de la motivation. Merci à Kelly et Vincent, vous êtes incroyables, et vous avez tant à montrer, tant à m'apprendre ! Enfin, merci à mes incroyables colocs pour ce cocon généreux, déjanté et décalé que vous avez su tisser : Laure, Cécile, Marie, Albin et Thomas. Vous avez tous et toutes contribué à faire de ces séjours à Marseille des moments exceptionnels et m'avez aidée à chaque instant.

J'aimerais remercier Alexia, une des personnes les plus folles que je connais, qui a vécu une aventure très parallèle à la mienne et m'a initiée à l'astro. Je pense aussi très fort à toi, Marine, souviens-toi de nos divagations sur les bancs stéphanois et merci encore de m'avoir suivie dans mes délires astro à Supop ! Je tiens aussi à remercier Romain, bientôt docteur lui aussi, pour ces charmantes discussions au détour des ruelles parisiennes. Delphine, bien sûr, tu es devenue dès les premières semaines un pilier sur lequel j'ai pu compter. Nous irons bientôt danser ensembles et pourrons reprendre nos entraînements pour Top Chef ! Merci à Philine, ma plus ancienne amie, nul besoin de poser des mots sur ce que je te dois.

Enfin, merci aux trois iridescents : Nico pour son soutien et son pouvoir de me faire tout relativiser, Marc pour sa gentillesse et ses conseils avisés jusqu'à quelques heures avant ma soutenance, et enfin Sylvain, qui aurait pu apparaître à chaque ligne de ces remerciements et sans qui cette thèse et moi serions autrement.

Je dédie les dernières lignes de ces remerciements à ma famille. A celles et ceux qui sont là, à celles et ceux qui ne sont plus. A Manou, l'aventurière. A Papé, à qui j'envoie un baiser. A Papy, si gentil. Aux tatas, aux tontons, aux cousines et aux cousins, qui m'ont tous et toutes encouragée et que j'encourage au centuple. Enfin, à Papa, Maman, et Juju, pour ça et tout le reste : un manuscrit de mille pages resterait insuffisant pour décrire ce que cette thèse et moi vous devons.

Merci d'avoir voyagé avec moi. Merci d'avoir chanté. Merci d'avoir ri. Merci d'avoir discouru. Merci d'avoir dansé. Merci d'être là.

Abstract

Since the discovery of the first exoplanet in 1992, more than 4000 exoplanets have been detected, each of them having impacted the knowledge on planetary systems formation and evolution and the understanding of the origin of life.

Direct imaging is a method of detection and characterization that consists in measuring directly the photons coming from the planet. It proposes several advantages, including the possibility of reconstructing the spectrum of the planet and therefore the chemical composition of its atmosphere, a witness for the possible presence of life markers on the planet.

The main limitation of this technique comes from the fact that the star is much brighter than its companion: an Earth-like planet is around 10^{10} times dimmer than its host star. Furthermore exo-Earths are extremely close to the host star, typically within an angular separation of around 0.1". Such planets are then inaccessible to current instruments, including the most powerful ones such as SPHERE at the VLT and GPI at the Gemini South telescope.

To push the limits of current direct imaging to the so-called high-contrast imaging, dedicated to the search for Earth-like planets, several tools have to be combined:

- The angular separation improving with the size of the telescope, primary mirrors tend to be larger. For manufacturing and transportation reasons, we tend to use segmented mirrors, ie. mirrors made of smaller mirrors, often hexagonal. However they generate issues such as phasing errors or segment vibrations.

- To block the starlight, we use a specific instrument called the coronagraph which increases the visibility of the companion. It aims at removing the starlight for a system without optical aberrations. The smallest residual wavefront aberration directly turns into residual light in the image, which deteriorates the detection. The measurement and control of the aberrations (WFS and WFC), in particular the ones due to the segmented structure of the telescope, are crucial.

During my PhD, I focused on the application of these tools to segmented mirrors.

First, I developed a model of the contrast of a coronagraphic system in presence of a segmented pupil. Such a model, simple and fast, enables to analyze the performance and to set up constraints on the optical aberrations of this kind of system during the design phase of the instrument. This Pair-based Analytical model for Segmented Telescopes Imaging from Space (PASTIS) takes into account the specificities of high-contrast instruments: configuration of the primary mirror segments, optical aberrations typically due to the segmentation, vibrations, coronagraph. It runs also much faster than any classical model of light propagation while providing a similar estimation of the instrument performance. I applied this model to the case of the LUVOIR telescope (36 hexagonal segments), in order to analyze the main modes limiting the contrast and therefore optimizing the repartition of the constraints on the optical aberrations.

In parallel, I worked on the analysis of the coronagraphic wavefront in presence of a segmented telescope on the experimental testbed called HiCAT. I ran a first demonstration of the wavefront sensor COFFEE enabling to reconstruct phasing errors in presence of a coronagraph with a high precision.

Eventually, I ran a comparative analysis of existing methods of wavefront control and experimentally validated one of them (Non Linear Dark Hole) in a simplified case on the MITHIC testbed at LAM. This algorithm is particularly promising in the case of segmented telescopes since it showed very encouraging results in simulation.

Short abstract

One of the prime goals in astronomy is observing another Earth. However this is equivalent to taking a picture of a firefly located at 1m from the Créac'h lightning house (the brightest of Europe)... from Moscow!

To do so, several tools exist, such as the coronagraph (an instrument composed in particular of a mask limiting the starlight), sensors and correctors of the optical defaults.

In order to collect photons coming from the planet and improve the telescope capacity to distinguish objects very close to each other, we use huge mirrors, most probably segmented, ie. composed of small hexagonal mirrors. The tools mentioned before have to be tested and probably adapted to this segmentation that deteriorates the telescope performance.

During my PhD, I developed a method enabling to estimate the impact of the segmentation on a telescope performance, before its manufacturing. I also tested in laboratories sensors and correctors of optical aberrations.

Résumé

Depuis la découverte de la première exoplanète en 1992, plus de 4000 exoplanètes ont été détectées, chacune ayant impacté nos connaissances sur la formation et l'évolution des systèmes planétaires et sur l'origine de la vie.

L'imagerie directe est une méthode de détection et de caractérisation qui consiste à mesurer directement les photons provenant de la planète. Elle présente plusieurs avantages dont la possibilité de reconstruire le spectre de la planète et donc la composition chimique de son atmosphère, témoin de la présence éventuelle de marqueurs de vie.

La principale difficulté de cette technique vient du fait que l'étoile est bien plus lumineuse que son compagnon : une planète tellurique est de l'ordre de 10^{10} fois moins lumineuse que son hôte. De plus, les exo-Terres sont très proches de leur étoile, typiquement à une séparation angulaire d'environ 0.1". De telles planètes sont donc inaccessibles aux instruments actuels, y compris les plus performants tels SPHERE sur le VLT et GPI sur le Gemini South telescope.

Afin de repousser les limites de l'imagerie directe pour atteindre l'imagerie dite à haut contraste, dédiée à la recherche d'exo-Terres, plusieurs outils doivent être combinés :

- La résolution s'améliorant avec la taille du télescope, les miroirs primaires tendent à s'élargir. Pour des raisons de conception et de transport, on opte de plus en plus pour des miroirs dits segmentés, ie. composés de miroirs plus petits, souvent hexagonaux. Cependant, ils génèrent des problèmes tels que les erreurs de phasage ou les vibrations des segments.

- Pour bloquer la lumière stellaire, on utilise un instrument spécifique appelé coronographe ce qui augmente la visibilité du compagnon. Il est à même d'éteindre la lumière stellaire pour un système sans aberrations optiques. Le moindre résidu de front d'onde va directement se transformer en résidu lumineux dans l'image, amenant une mauvaise détection. La mesure et le contrôle des aberrations (WFS et WFC), en particulier celles liées à la structure segmentée du télescope, est donc primordiale.

Ma thèse s'inscrit dans la problématique de l'application de ces outils au cas des télescopes segmentés.

Tout d'abord, j'ai développé un modèle du contraste d'un système coronographique en présence d'une pupille segmentée. Un tel modèle, simplifié et rapide, permet d'analyser les performances mais aussi de mieux contraindre les aberrations optiques d'un système de ce type lors de la phase de design de l'instrument. Ce Pair-based Analytical model for Segmented Telescopes Imaging from Space (PASTIS) prend en compte les spécificités des instruments de haut contraste : configuration des segments du miroir primaire, aberrations optiques typiques dues à la segmentation, vibrations, coronographe. Il tourne aussi beaucoup plus rapidement qu'un modèle de propagation classique tout en fournissant une estimation équivalente des performances du télescope. Je l'ai utilisé dans le cadre du télescope LUVOIR (36 segments hexagonaux), afin d'analyser les modes principaux limitant le contraste et ainsi mieux répartir les contraintes sur les aberrations optiques.

Par la suite, j'ai travaillé sur l'analyse de front d'onde coronographique en présence d'un télescope segmenté sur le banc expérimental HiCAT. J'ai mené une première démonstration de mesure de front d'onde COFFEE permettant de reconstruire les erreurs de phasage, en présence d'un coronographe, avec une grande précision.

Enfin, j'ai mené une analyse comparative des multiples méthodes de contrôle de front d'onde existantes dans le monde et valider l'une d'elles (Dark Hole Non Linéaire) expérimentalement dans un cadre simplifié sur le banc MITHIC du LAM. Cet algorithme est particulièrement prometteur dans

le cadre des télescopes segmentés puisqu'il a montré des résultats très encourageants en simulation.

Résumé court

Un des objectifs majeurs en astronomie est d'observer une autre Terre. Mais c'est équivalent à voir une luciole volant à 1 m du phare breton du Créac'h (le plus puissant d'Europe)... depuis Moscou !

Plusieurs outils existent afin de faciliter cette tâche, comme le coronographe (un instrument composé limitant la lumière de l'étoile) et des analyseurs et correcteurs de défauts optiques.

Afin de capter les photons de la planète et d'améliorer la capacité des télescopes à discerner des objets très proches l'un de l'autre, on utilise des miroirs immenses et segmentés, ie. composés de petits miroirs hexagonaux. Les outils mentionnés plus haut doivent être testés et adaptés à cette segmentation qui détériore les performances du télescope.

Durant ma thèse, j'ai donc développé une méthode permettant d'estimer l'impact de la segmentation sur les performances d'un télescope en amont de sa construction. J'ai aussi testé en laboratoire des techniques d'analyse et de correction des défauts optiques.

Résumé long

1. Introduction à l'imagerie à haut contraste

Depuis la découverte de 51 Pegasi en 1995, presque 4000 exoplanètes ont été découvertes. Le prochain défi à relever consiste alors à détecter une planète habitable ressemblant Ãă la nôtre en terme de taille, masse, température de surface, composition chimique de son atmosphère... La réunification de tels paramètres, en particulier la connaissance du spectre de l'atmosphère, n'est possible que grâce à l'imagerie directe.

Jusqu'à maintenant, les instruments les plus performants en imagerie directe d'exoplanètes (SPHERE au Very Large Telescope ou VLT et GPI au Gemini South Observatory) n'ont permis de détecter que des compagnons relativement loin de leur étoile hôte. Imager des compagnons type Terre, donc à des séparations angulaires faibles, requiert des instruments permettant d'atteindre des performances jamais égalées.

En parallèle de ce premier objectif technologique, cet objectif nécessite d'isoler les photons provenant de la planète de ceux provenant de l'étoile. Cette tâche est très complexe puisque le rapport des flux lumineux de la planète et de l'étoile, aussi appelé contraste, est de l'ordre de 10^{-10}. Dans ce but, des outils technologiques spécifiques sont développés : des télescopes géants afin d'atteindre une rÃľsolution suffisante, des coronographes et des correcteurs de surface d'onde. Pour les télescopes terrestres, on parle des Extremely Large Telescopes (ELTs), de plusieurs dizaines de mètres de diamètre. Pour les télescopes spatiaux, il s'agira certainement de télescopes d'une quinzaine de mètres de diamètre, par exemple le projet Large UV-Optical-InfraRed survey (LUVOIR). Ces miroirs primaires géants ne peuvent être monolithiques, leur construction et transport étant alors impossible. On se tourne alors vers les pupilles dites segmentées, formées d'un pavage de petits miroirs hexagonaux.

Cependant, cette segmentation du miroir primaire génère de multiples problèmes. En particulier, elle crée des artefacts diffractifs dans le plan du détecteur, qui nécessitent une adaptation du coronographe et des outils d'analyse et de contrôle de surface d'onde. De plus, les segments doivent être phasés et stabilisés, puisque toute erreur de surface d'onde détériore drastiquement le contraste. Pour le James Webb Space Telescope (JWST), par exemple, cela signifie l'alignement conjoint de 18 segments, pour LUVOIR de 36 segments, et pour l'ELT de 798 segments !

Pour répondre à ces problématiques, plusieurs solutions existent : tout d'abord un budget d'erreur précis et complet permet de définir des contraintes sur les aberrations optiques dès l'étape de conception et jusqu'à celle de phasage des segments afin de maintenir la performance cible ; de plus, la reconstruction des aberrations

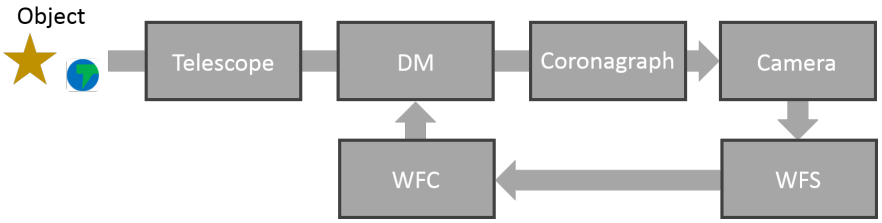

Figure 0.0.1: Chaîne du photon dans un système d'imagerie à haut contraste.

présentes dans le système optique combinée à un contrôleur de champ électrique permet de nettoyer le plan focal (ou du moins une zone réduite du plan focal, appelée le dark hole) des résidus lumineux dûs aux aberrations, les speckles.

Au cours de ma thèse et de ce résumé, j'ai cherché à explorer ces différentes solutions. Après un chapitre de présentation détaillée des outils d'imagerie à haut contraste mentionnés plus haut, je me suis intéressée à la sensibilité des instruments coronographiques en présence d'aberrations locales sur les segments. Dans la partie 4, je propose une validation expérimentale de l'analyseur de surface d'onde COFFEE pour la reconstruction d'erreur de phasage. Dans la partie 5, je m'attache à une technique de contrôle de front d'onde, appelée le Dark Hole Non Linéaire (DHNL), permettant de creuser le contraste dans le dark hole. Enfin, dans la partie 6, je présente les principales conclusions de cette thèse.

2. Outils pour l'imagerie à haut contraste

Atteindre la performance ultime permettant d'imager des exoplanètes requiert une combinaison de différents outils. Le schéma 0.0.1 présente la configuration traditionnelle d'un tel instrument : le télescope permet de récolter les photons de l'objet scientifique, planètes et étoile, tandis que le coronographe bloque la lumière stellaire. La caméra scientifique permet ensuite de faire une image du système résiduel. En parallèle du système d'imagerie, un analyseur permet de reconstruire les aberrations du système optique, information traitée par le contrôleur de surface d'onde qui déduit la commande à envoyer à un miroir déformable (DM), visant à modifier le front d'onde afin de creuser le contraste dans le dark hole.

2.1. Coronographie

Afin d'atténuer le flux stellaire sans impacter celui de la planète, on utilise un instrument optique appelé un coronographe. Un schéma expliquant ses composants est visible sur la figure 0.0.2 : le masque plan focal (FPM), conjugué à l'image de l'étoile, occulte les rayons lumineux émis par l'étoile. Le Lyot stop (LS), en plan pupille, bloque les effets diffractifs dus à la forme du FPM. Enfin, l'apodiseur A, en plan pupille, sert à optimiser la répartition du faisceau lumineux émis par l'étoile

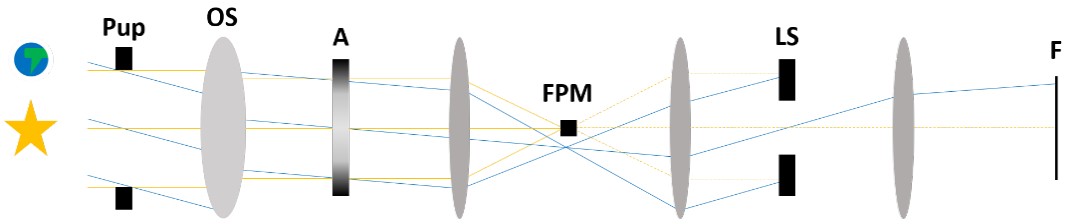

Figure 0.0.2: Schéma d'un coronographe. L'apodiseur A et le Lyot stop LS sont en plans pupille, le FPM et le détecteur F sont en plans focaux. Les rayons émis par l'étoile sont jaunes, ceux émis par la planète sont bleus.

afin qu'il soit au maximum bloqué par le FPM. Ce dernier masque n'est pas présent dans tous les types de coronographes.

L'apodiseur et le FPM peuvent être des masques de phase comme d'amplitude, permettant à une large variété de coronographes d'avoir été développée. On en trouve aujourd'hui sur de nombreux instruments, tels SPHERE, GPI ou encore NIRCam sur le JWST. Les performances de certains coronographes de Lyot apodisés (apodiseur, FPM et Lyot stop en amplitude) et des coronographes type vortex (FPM de phase) sont suffisantes, en simulation, pour imager directement des exo-Terres.

2.2. Analyse de surface d'onde

L'analyse de surface d'onde consiste en la reconstruction des aberrations de phase voire d'amplitude qui détériorent la performance du système optique. Cette étape est nécessaire en amont du contrôle du miroir déformable.

L'analyse de surface d'onde est particulièrement complexe, puisque le détecteur ne fournit que l'intensité du champ électrique, et non son amplitude. C'est pour cette raison que ce processus requiert des entrées multiples : soit prises à des moments différents (séparation temporelle), soit prises à des endroits différents du banc (séparation spatiale).

Les méthodes à séparation spatiale des images consistent en l'utilisation d'un analyseur de surface d'onde sur un bras optique supplémentaire, donc après séparation physique du faisceau. L'avantage principal de ces méthodes est qu'elles n'altèrent pas la prise de données avec la caméra scientifique sur le bras principal. Cependant, l'utilisation d'un bras optique séparé du bras scientifique génère des aberrations non communes, qui constituent une erreur parfois non négligeable dans l'estimation des aberrations détériorant l'image scientifique. C'est pour cette raison que les méthodes à séparation temporelle utilisent directement la caméra scientifique comme analyseur. Au moins deux images successives sont prises, en insérant une aberration connue dans le chemin optique.

Au cours de la thèse, je me suis intéressée à une méthode appartenant à cette seconde catégorie, qui présente aussi l'avantage d'être compatible avec l'utilisation

Prerequisite\Method	Speckle Nulling	Speckle Field Nulling	Electric Field Conjugation	Stroke Minimization	Non Linear Dark Hole
Preliminary WFS		X	X	X	X
Coronagraph model		X			X
DM calibration	X	X			X
Pupil to focal plane calibration	X		X	X	

Figure 0.0.3: Tableau comparatif des différentes méthodes de contrôle de front d'onde.

d'un coronographe : COFFEE (COronagraphic Focal plane wave-Front Estimation for Exoplanet detection). Cette méthode convient particulièrement à notre problématique, puisqu'on souhaite une modification minimale du système optique tout en évitant les aberrations différentielles.

2.3. Contrôle de surface d'onde

Le contrôle de surface d'onde vise à corriger les aberrations du système optique. Il requiert donc une estimation préliminaire de ces aberrations. Le contrôle est rendu possible grâce à l'utilisation d'un voire de plusieurs miroirs déformables, dont au moins un est placé en plan pupille.

Si l'objectif premier de cette étape de contrôle est de compenser les aberrations présentes dans le système optique, la correction peut être optimisée afin d'aller plus loin en répartissant autrement les aberrations, afin par exemple de limiter les effets de diffraction dans l'image finale dus à l'araignée ou à la segmentation, voire de limiter au maximum l'intensité lumineuse de l'étoile dans une zone réduite, au détriment du reste du plan focal. Dans ce dernier cas, la zone de haut contraste est aussi appelée dark hole et est en général inclue dans le dark hole généré par le coronographe seul.

Afin de déterminer la commande à envoyer au miroir déformable, différents algorithmes de contrôle existent. Nous avons conduit une analyse comparative de plusieurs de ces techniques (voir Fig. 0.0.3), en identifiant les différents prérequis nécessaires à leur mise en application.

L'une de ces techniques, en particulier, sied à notre type d'applications : le dark hole non linéaire (DHNL). En effet, il s'agit de l'unique méthode qui ne fait aucune approximation sur la phase et reste donc valide sur un large intervalle d'aberrations. Pour cette raison, nous avons choisi d'étudier le DHNL sur des pupilles segmentées, les résultats sont proposés en partie V.

3. Modélisation d'un télescope d'imagerie à haut-contraste

La performance ultime d'un instrument coronographique ne peut pas être atteinte à moins d'un contrôle parfait des aberrations, qui peuvent avoir des causes

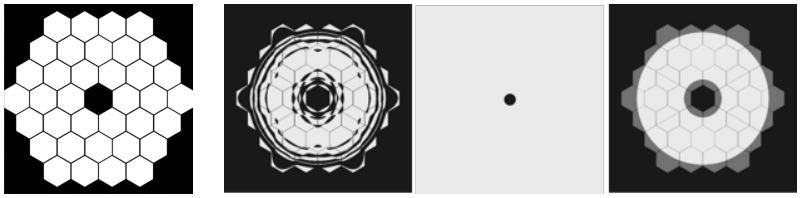

(a) (b)

Figure 0.0.4: Pupille et apodiseur de l'APLC utilisés pour notre cas d'application : (a) la pupille, composée de 36 segments hexagonaux et d'une obstruction centrale hexagonale, (b) le coronographe (apodiseur, FPM et Lyot stop), compatible avec la pupille à 36 segments.

multiples : instabilités mécaniques, aberrations quasi-statiques internes, désalignements voire vibrations des segments...

Dans ce chapitre, nous étudions l'impact des aberrations locales sur les segments sur le contraste d'une image coronographique. Nous avons développé PASTIS (Pair-based Analytical model for Segmented Telescopes Imaging from Space), qui permet de calculer directement le contraste moyen dans le dark hole en fonction des aberrations locales sur les segments, en s'affranchissant des calculs traditionnels de propagation (aussi appelés end-to-end ou E2E), basés sur des transformées de Fourier.

Considérons une pupille segmentée formée de segments de formes et tailles identiques, comme celle de la Fig. 0.0.4 (a). La formule PASTIS stipule :

$$C = C_0 + AMA^t \tag{1}$$

Où C est le contraste moyen dans le dark hole (symÃľtrique), C_0 est le "deep contrast", ie. le contraste en l'absence d'aberrations, A est le vecteur contenant les coefficients de Zernike des aberrations présentes sur tous les segments et M est la matrice d'influence du système : c'est donc une matrice constante, qui ne dépend que de l'architecture de la segmentation, du système coronographique considéré, et des polynômes de Zernike étudiés. A l'inverse, A est l'unique variable de cette équation.

Pour le cas d'application de PASTIS, nous avons choisi d'utiliser la pupille type LUVOIR, combiné à un coronographe APLC composé de l'apodiseur, d'un FPM et d'un Lyot stop (voir Fig. 0.0.4 (b)). En calculant le contraste grâce à la formule PASTIS pour de multiples erreurs de phasage des segments, nous obtenons la courbe de la Fig. 0.0.5, sur laquelle nous avons aussi indiqué les contrastes obtenus avec les mêmes erreurs de phasage mais grâce à une simulation end-to-end. En conclusion, l'erreur entre ces deux méthodes de calcul est d'environ 5%, et le contraste grâce à PASTIS est de l'ordre de 10^7 fois plus rapide à calculer que la simulation end-to-end.

PASTIS apparaît donc ici comme un outil efficace de remplacement des simula-

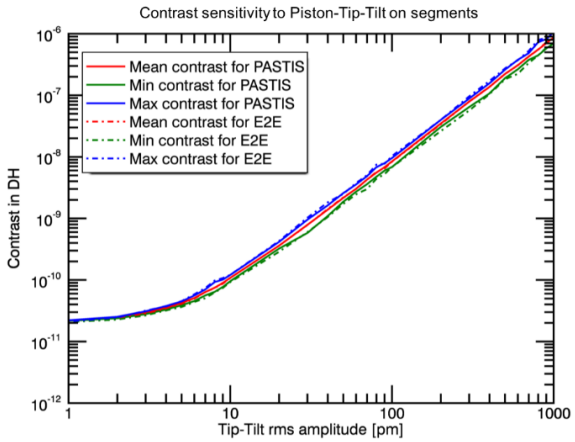

Figure 0.0.5: Contraste en fonction de l'erreur rms de phasage des segments (piston, tip, tilt), calculé à la fois par la méthode E2E et par PASTIS.

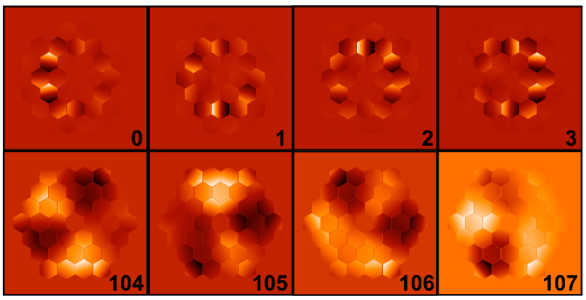

Figure 0.0.6: Quelques modes propres pour des aberrations de phasage (piston, tip, tilt) sur les segments.

tions end-to-end. Mais ce n'est pas là son unique utilité : grâce à l'expression directe du contraste en fonction des aberrations, il est possible d'inverser la formule : la décomposition en valeurs singulières de la matrice M fournit les modes propres du miroir ainsi que leurs valeurs propres associées. Ces modes propres (Fig. 0.0.6) contribuent indépendamment les uns des autres à la détérioration du contraste et forment une base intéressante dans laquelle projeter notre étude de contraintes. Dans cette base, et en faisant l'hypothèse que tous les modes contribuent également au contraste cible, on obtient :

$$\sigma_p = \sqrt{\frac{C_p}{\lambda_p}}. \tag{2}$$

Où σ_p correspond à la contrainte imposée sur le p-ème mode, C_p la fraction de contraste due à la contrainte sur le p-ème mode et λ_p est la p-ème valeur propre.

Cet outil permet donc non seulement d'accélérer les calculs de performance en

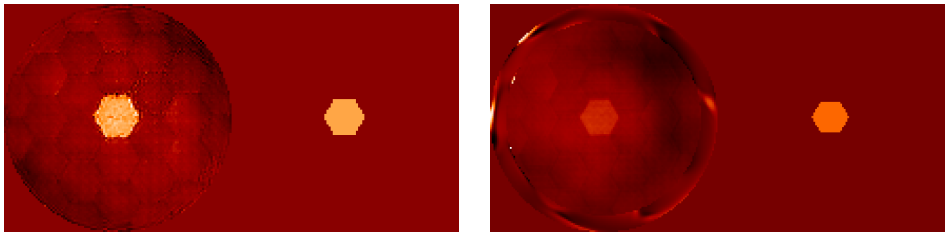

(a) (b)

Figure 0.0.7: Exemples de reconstruction d'une erreur de piston sur les segments, (a) sans coronographe et (b) avec coronographe. Dans chaque cas, à gauche : la phase brute, à droite : la phase théorique.

présence d'aberrations sur les segments, mais aussi d'avoir une méthode directe de tolérancement qui prend en compte les disparités inter-segments (position, couverture par l'apodisation...) et permet d'éviter les multiples itérations de la méthode traditionnelle. PASTIS peut aussi être appliqué sur d'autres coronographes et d'autres télescopes segmentés, tels le JWST, l'ELT, le Keck...

4. Validation expérimentale d'un analyseur de front d'onde en plan focal

L'instrument coronographique est généralement combiné à un système d'analyse et contrôle du front d'onde. Dans cette partie, nous nous intéressons à la reconstruction du front d'onde, et en particulier aux erreurs de phasage du miroir primaire segmenté. Pour cela, nous avons appliqué l'analyseur COFFEE sur le banc de haut-contraste HiCAT (High-Contrast Imager for Complex Aperture Telescopes), qui est équipé d'un miroir segmenté à 37 segments hexagonaux et d'un coronographe de Lyot (FPM et Lyot stop) dont le FPM peut être automatiquement enlevé si nécessaire. Il s'agit donc d'une première application expérimentale d'un analyseur dans une configuration aussi complexe.

L'avantage principal de COFFEE pour ce type d'application est sa capacité à utiliser l'image scientifique en entrée de l'analyse, même en présence d'un coronographe.

Pour notre expérimentation, nous appliquons différentes phases sur le miroir segmenté et prenons des images avec la caméra en plan focal, avec le DM à plat puis avec un focus de 150nm, avec et sans coronographe. Nous reconstruisons séparément les erreurs de phase sans puis avec coronographe grâce à COFFEE, afin de les comparer à l'erreur appliquée sur le miroir segmenté.

Sans coronographe, les aberrations de phasage sont bien reconstruites (voir Fig. 0.0.7 (a)) : on note respectivement une erreur de 1.97 nm RMS, 1.68 nm RMS et 3.58 nm RMS sur l'estimation du piston, tip, et tilt moyens sur les segments.

En présence du coronographe, en revanche, les estimations sont sous-évaluées, et des aberrations de bas ordres, non présentes dans le système optique et différant

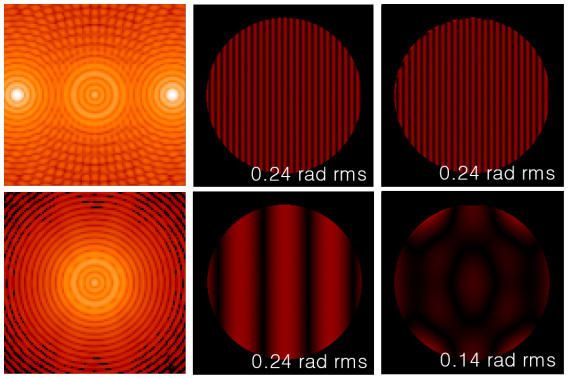

Figure 0.0.8: Simulation de la transmission de différentes fréquences spatiales au travers du système coronographique et reconstruction par COFFEE : (haut) 15 cy/pup, (bas) 2 cy/pup, (gauche) PSFs simulées, (milieu) phases théoriques de test, (droite) phases reconstruites par COFFEE.

d'une reconstruction à l'autre, sont reconstruites (voir Fig. 0.0.7 (b)).

Ce phénomène trouve son explication dans la nature même du coronographe : le FPM constitue un filtre passe-haut, dont la fréquence de coupure correspond au rayon. Ainsi, l'analyseur est aveugle aux aberrations de bas-ordre, coupées par le FPM. Cette hypothèse a été validée en simulation, en étudiant la transmission par un tel coronographe et la reconstruction par COFFEE de différentes fréquences spatiales. La Fig. 0.0.8 illustre les conclusions de cette étude théorique : les fréquences spatiales coupées par le FPM ne peuvent pas être convenablement reconstruites par COFFEE, alors que les fréquences spatiales non coupées sont retrouvées en sortie de l'analyseur.

Or, la densité spectrale de puissance (DSP) d'un segment comporte des composantes basses fréquences. Ces basses fréquences ne peuvent pas être convenablement reconstruites par COFFEE, ce qui explique les résultats obtenus sur banc.

Dans cette partie, on a pu pointer une limitation de l'analyseur COFFEE en configuration coronographique : le FPM agit comme un filtre passe-haut et l'analyseur ne peut pas reconstruire convenablement les basses fréquences qu'il coupe. Cette étude a donc permis de poser des contraintes sur l'utilisation de COFFEE lors de futures applications.

5. De l'analyse au contrôle de surface d'onde

Après le coronographe et l'analyseur de surface d'onde, le dernier composant d'un instrument d'imagerie à haut contraste est le contrôle de front d'onde. De nombreuses méthodes, déjà mentionnées plus tôt, ont été développées. Dans notre cas, nous nous intéressons à la technique de DHNL, dont l'avantage principal est de converger en moins d'itérations que les méthodes linéaires usuelles. Cette caractéristique est intéressante en imagerie à haut contraste, qui est particulièrement

complexe à stabiliser sur de longs temps d'exposition.

Dans cette section, nous cherchons à appliquer le DHNL dans le cas des télescopes à pupille segmentée. Plusieurs études ont été menées, afin de répondre aux questions suivantes :

- Quelle est l'évolution de la performance du DHNL lorsqu'on passe d'un télescope monolithique à segmenté ?

- L'utilisation d'un miroir segmenté pour appliquer la correction peut-elle permettre d'améliorer les performances du DHNL ?

- Quel est l'impact de la position et de la taille du dark hole ciblé sur la performance finale du DHNL ?

- Cet algorithme est-il robuste aux erreurs de phasage du miroir primaire ?

Pour ces études, nous avons utilisé la pupille JWST (18 segments) combinée à un coronographe Roddier Roddier. De plus, le DM de correction a 41 actuateurs sur son diamètre. Dans cette configuration, nous avons pu conclure que :

- le DHNL est transposable sur une pupille segmentée : le contraste est alors amélioré d'un facteur 120, contre 136 dans le cas de la pupille monolithique,

- l'utilisation d'un miroir segmenté en complément du miroir déformable continu n'améliore pas la performance de la correction. Presque toute la phase de correction est d'ailleurs envoyée sur le miroir continu,

- la performance de cet algorithme dépend de la position plus que de sa taille : plus le dark hole est loin de l'image de l'étoile, meilleure est la performance. Le contraste s'améliore d'un facteur 161 lorsque le dark hole passe de $[4\lambda/D, 10\lambda/D]$ à $[15\lambda/D, 17.6\lambda/D]$,

- enfin, le DHNL semble robuste aux aberrations de phasage : de 0 à 1000 nm RMS d'aberrations type piston sur les segments, il permet d'obtenir des contrastes équivalents dans le dark hole. Ce point est particulièrement intéressant puisque le caractère non linéaire de cet algorithme le rend performant à la fois sur les petites et fortes aberrations.

L'algorithme de DHNL a été appliqué pour la première fois expérimentalement, sur le banc MITHIC (Marseille Imaging Testbed for HIgh Contrast). La configuration était plus simple que lors des études théoriques : pupille circulaire, miroir monolithique, pas de coronographe.

Nous avons pu creuser un dark hole en forme de demi-donut, entre 2 et $5\lambda/D$, améliorant légèrement le contraste dans cette zone ($C = 2.12 \times 10^{-4} \pm 1.77 \times 10{-}4$) (voir Fig. 0.0.9).

Cette première validation expérimentale a été suivie d'une seconde application, sur le banc THD2 et en présence d'un coronographe, par O. Herscovici-Schiller. La

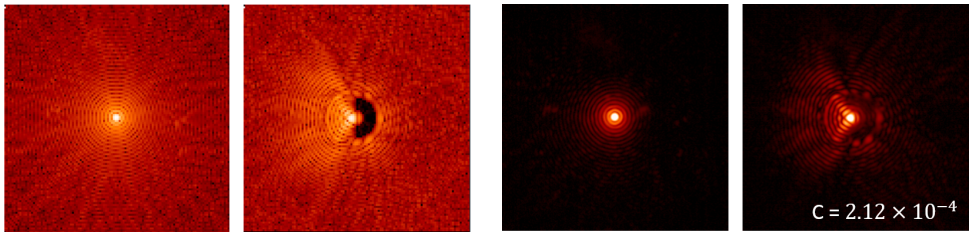

(a) (b)

Figure 0.0.9: PSFs (a) en simulation et (b) sur banc. Dans chaque cas, (gauche) avant et (droite) après correction.

prochaine étape sera donc d'appliquer le DHNL en présence d'un coronographe sur une pupille segmentée, ce que nos études théoriques considèrent comme faisable.

6. Conclusions et perspectives

Ces trois années de thèse m'ont permis d'explorer les différents outils nécessaires à l'imagerie à haut contraste et de les appliquer au cas des télescopes spatiaux segmentés : coronographie, analyse et contrôle de surface d'onde.

J'ai pu développer un modèle analytique, PASTIS, simplifiant grandement les tolérancements des télescopes segmentés combinés à des instruments coronographiques. PASTIS offre encore de nombreuses possibilités d'applications (contraintes moindres comme le JWST, télescopes sol comme le Keck ou l'ELTâĂę... et de développement, notamment sur les aspects longue pause ou encore optimisation de l'architecture de la pupille (densité des segments, apodisation par segment).

Ensuite, je me suis intéressée à l'analyseur COFFEE, et l'ai appliqué expérimentalement sur le banc de haut contraste HiCAT. COFFEE a permis de reconstruire des aberrations de phasages d'un miroir segmenté en l'absence de coronographe, et de poser des contraintes particulières en présence du coronographe. COFFEE pourrait à l'avenir être testé sur des pupilles à plus haute densité de segments, ou en présence de FPM plus petits.

Enfin, j'ai pu adapter et tester l'algorithme de contrôle DHNL au cas des pupilles segmentées : il a fourni des résultats très prometteurs. Je l'ai aussi validé pour la première fois sur banc, expérience qui a déjà été renouvelée sur le THD2 en présence d'un coronographe et devra être ré-itérée en présence d'une pupille segmentée.

Acronyms

Acronym	Name
ACAD-OSM	Active Compensation of Aperture Discontinuities-Optimized SM
ACS	Advanced Camera for Surveys
AIC	Achromatic Interfero Coronagraph
ALTAIR	ALTtitude conjugate Adaptive optics for the InfraRed
AMI	Aperture Masking Interferometry
AO	Adaptive Optics
APLC	Apodized Pupil Lyot Coronagraph
APP	Apodized Phase Plate
CGI	CoronaGraph Instrument
CHARA	Center for High Angular Resolution Astronomy
CHARIS	Coronagraphic High Angular Resolution Imaging Spectrograph
CHEOPS	CHaracterising ExOPlanets Satellite
CNES	Centre National d'Études Spatiales
COFFEE	COronagraphic Focal plane wave-Front Estimation for Exoplanet detection
CoRoT	Convection, Rotation, & Transits
CRIRES	CRyogenic high-resolution InfraRed Echelle Spectrograph
CSA	Canadian Space Agency
DH	Dark Hole
DM	Deformable Mirror
DZPM	Dual Zone Phase Mask
ECLIPS	Extreme Coronagraph for Living Planetary Systems
EFC	Electric Field Conjugation
ELASTIC	Estimation of Large Amplitude Subaperture Tip-tilt by Image Correlation
ELT	Extremely Large Telescope
EPICS	ELT Planetary Imaging Camera and Spectrograph
ESA	European Space Agency
ESO	European Southern Observatory
ExEP	Exoplanet Exploration Program
E2E	End-to-End
FFREE	Fresnel-FRee Experiment for EPICS
FPM	Focal Plane Mask

FWHM	Full Width at Half Maximum
GAIA	Global Astrometric Interferometer for Astrophysics
GMT	Giant Magellan telescope
GPI	Gemini Planet Imager
GSFC	Goddard Space Flight Center
HabEx	Habitable Exoplanet mission
HARMONI	High Angular Resolution - Monolithic - Optical and Near-infrared - Integral field spectrograph
HARPS	High Accuracy Radial velocity Planet Searcher
HCIL	High-Contrast Imaging Laboratory
HCIT	High-Contrast Imaging Testbed
HDC	High Dispersion Coronagraphy
HiCAT	High-contrast imager for Complex Aperture Telescopes
HiCIAO	High-Contrast Coronographic Imager for Adaptive Optics
HIPPARCOS	HIgh Precision PARallax COllecting Satellite
HiRISE	High-Resolution Imaging and Spectroscopy of Exoplanets
HST	Hubble Space Telescope
IFS	Integral Field Spectrometer
IR	InfraRed
IRAC	InfraRed Array Camera
IRDIS	InfraRed Dual-band Imager and Spectrograph
IRF	Impulse Response Function
IRS	InfraRed Spectrograph
IWA	Inner Working Angle
JATIS	Journal of Astronomical Telescopes, Instruments, and Systems
JOST	JWST Optical Simulation Testbed
JWST	James Webb Space Telescope
KPIC	Keck Planet Imager and Characterizer
LAM	Laboratoire d'Astrophysique de Marseille
LBT	Large Binocular Telescope
LUVOIR	Large UV/Optical/InfraRed surveyor
MAOT	Multiple-Aperture Optical Telescope
METIS	Mid-Infrared E-ELT Imager and Spectrograph
MICADO	Multi-AO Imaging Camera for Deep Observations
MIPS	Multiband Imaging Photometer
MIRI	Mid-InfraRed Instrument
MITHIC	Marseille Imaging Testbed for HIgh Contrast
MMT	Multiple Mirror Telescope

MOA	Microlensing Observations in Astrophysics
MTF	Modulation Transfer Function
NaCo	NAOS Near-Infrared Imager and Spectrograph (CONICA)
NAOS	Nasmyth Adaptive Optics System
NASA	National Aeronautics and Space Administration
NCPA	Non Common Path Aberrations
NICMOS	Near Infrared Camera and Multi-Object Spectrometer
NIRCam	Near InfraRed Camera
NIRISS	Near InfraRed Imager and Slitless Spectrograph
NIRSPec	Near-InfraRed Spectrometer
NLDH	Non-Linear Dark Hole controller
NRM	Non-Redundant Mask
OAP	Off-Axis Parabola
OGLE	Optical Gravitational Lensing Experiment
OHP	Observatoire de Haute-Provence
ONERA	Office National d' Études et de Recherches Aérospatiales (or French Aerospace Lab)
OPERA	Optimized PhasE Retrieval Algorithm
OST	Origins Space Telescope
OTE	Optical Telescope Element
OTF	Optical Transfer Function
OWA	Outer Working Angle
PALAO	PALomar Adaptive Optics
PALC	Prolate Apodized Lyot Coronagraph
PASTIS	Pair-based Analytical model for Segmented Telescopes Imaging from Space
PCS	Planetary Camera and Spectrograph
PIAA	Phase-Induced Amplitude Apodization
PLATO	PLAnetary Transits and Oscillations of stars
PSD	Power Spectral Distribution
PSF	Point Spread Function
PTF	Phase Transfer Function
PV	Peak-to-Valley
PWFS	Pyramid WaveFront Sensor
RIA	Research Instrument Analyst
RMS	Root Mean Square
R&R	Roddier & Roddier
SCC	Self-Coherent Camera

SCDA	Segmented Coronagraph Design & Analysis
SCExAO	Subaru Coronagraphic Extreme Adaptive Optics
SCI	SPICA Coronagraphic Instrument
SFN	Speckle Field Nulling
SIRTF	Space Infrared Telescope Facility (or Spitzer)
SLED	Superluminescent Light Emitting Diode
SLM	Spatial Light Modulator
SM	Stroke Minimization
SN	Speckle Nulling
SNR	Signal-to-Noise Ratio
SOHO	SOlar and Heliospheric Observatory
SOPHIE	Spectrographe pour l'Observation des Phénomènes des Intérieurs stellaires et des Exoplanètes
SPC	Shaped Pupil Coronagraph
SPEED	Segmented Pupil Experiment for Exoplanet Detection
SPHERE	Spectro Polarimetric High contrast Exoplanet REsearch
SPICA	SPace Infrared telescope for Cosmology and Astrophysics
SR	Strehl Ratio
STScI	Space Telescope Science Institute
SVD	Singular Value Decomposition
TESS	Transiting Exoplanet Survey Satellite
THD	Très Haute Dynamique testbed
TMT	Thirty Meter Telescope
VAMPIRES	Visible Aperture-Masking Polarimetric Interferometer for Resolving Exoplanetary Signatures
VLT	Very Large Telescope
VLTI	VLT Interferometer
VMLM-B	Variable Metric with Limited Memory and Bounds
VNC	Visible Nulling Coronagraph
WFC	WaveFront Control
WFI	Wide-Field Instrument
WFIRST	Wide Field Infrared Survey Telescope
WFS	WaveFront Sensing
ZELDA	Zernike sensor for Extremely Low-level Differential Aberrations
ZIMPOL	Zurich IMaging POLarimeter
4QPM	Four-Quadrant Phase Mask coronagraph
8OPM	Eight-Octant Phase Mask coronagraph

Contents

There's a greater love
In the little things

— Janelle Monaé

1 Introduction

1995 saw the very first discovery of an exoplanet around a main sequence star, 51 Pegasi. Since then, near 4000 exoplanets have been confirmed and detecting life or at least a planet able to sustain life in another planetary system became one of the next challenges to achieve. It is expected for such a planet to reunite similar conditions than the Earth in terms of size, mass, temperature, chemical composition of its atmosphere, distance to its host star... However, among all techniques of detection of exoplanets, only direct imaging enables to access the spectrum of the planet light informing about the possible presence of life markers.

So far, the main instruments dedicated to direct imaging of exoplanets such as SPHERE (Very Large Telescope or VLT) and GPI (Gemini South observatory) enabled to detect only companions far from their host star, since they cannot resolve objects with angular separations smaller than 5 AU in the near infrared light spectrum. More evolved instruments made of unprecedented performance tools are then necessary to access smaller angular separations (around $0.1"$) corresponding to habitable zones of stars and therefore to Earth-like planet detection.

In addition to this first technological goal, imaging an Earth-like planet means being able to isolate the planet photons from the star photons, a very complex task since the light flux ratio between star and planet, also called contrast, is of the order of 10^{10}. In other words, for each photon emitted by the planet, 10 billions photons come from the star.

The access to high contrasts at small angular separations implies the development of technological feats, such as giant telescopes, coronagraphy, and wavefront correction.

The planetary signal is flood with the starlight dazzling the detector. Therefore, in order to decrease the stellar flux without affecting the planet light, an optical device called

the coronagraph has been developed. Numerous designs exist today, several of them being even implemented on instruments (SPHERE at the VLT, GPI at the Gemini South observatory, SCExAO at the Subaru telescope, NICMOS on the Hubble Space Telescope, NIRCam on the cupcoming James Webb Space Telescope...). However their performance remains unsufficient for Earth-like planet imaging, except in most recent simulation developments (apodized pupil Lyot coronagraph, vortex coronagraph...).

However, the performance of the coronagraph is degraded by optical aberrations such as atmospheric turbulence, mechanical unstabilities, quasi-static aberrations, or internal optical defects and misalignments. All these sources of wavefront errors generate speckles in the detector plane, which increases the photon noise of the image while decreasing the achieved contrast. To address this issue, several solutions can be put forward: first, a precise error budget can set up requirements during the design, manufacturing, and alignment phases to maintain the level of aberrations below a threshold allowing to achieve the target performance; secondly, for ground-based telescopes, an adaptive optics correction can compensate for most of the turbulence effects, leaving only residual quasi-static aberrations in the system, due for instance to optical and mechanical defects, misalignment, and thermal drifts; and eventually, a sensing of the aberrations, combined with an electric field controller, can clean up the focal plane (or at least a reduced zone of the focal plane called the dark hole) from speckles. This very last point can be done either with the wavefront sensor on an additional channel to avoid wavefront perturbations due to the coronagraph, or ideally with the science detector to avoid non common path aberrations. It is also a particularly complex step since the detector has only access to the intensity of the electric field.

The search for exoplanets and in particular for Earth-like planets requires the next generation of telescopes to combine these tools under their most performant capabilities. Some are already under development on the instruments KPIC (Keck telescope) and HiRISE, an upgrade of the instrument SPHERE (VLT), and on the Wide Field Infrared Survey Telescope (WFIRST), albeit at more modest target contrasts. For higher contrasts compatible with Earth-like planet imaging, it will be necessary to wait for the Large Ultra-Violet Optical Infrared (LUVOIR) telescope, the Habitable Exoplanet Imaging Mission (HabEx), and the second generation instruments of the Extremely Large Telescope such as the Planetary Camera and Spectrograph (PCS).

If some of these telescopes show monolithic primary mirrors (VLT and WFIRST), most of them have segmented pupils: the Keck telescope, LUVOIR, the Extremely Large Telescope (ELT), and maybe HabEx. Indeed, to improve the angular separation achievable by the telescopes, their primary mirrors have to be larger. Then, to facilitate the mirror manufacturing, polishing, and transportation, mainly when it comes to make it fit into a launch vehicle, segmented mirrors are privileged. However, the segmentation creates diffraction artifacts in the detector plane which require an adaptation of the coronagraphic, sensing, and control tools, in addition to specific alignment and stability issues: the James Webb Space Telescope (JWST) is for instance composed of 18 segments, LUVOIR would count at least 36 segments, while at the ELT, 798 segments will have to be phased!

My thesis positions itself in this specific problematic: how do these different tools dedicated to high-contrast imaging behave in presence of a segmented pupil and segmentation-related issues? I present hereafter the contents of this thesis, aiming at answering this question. We can notice that the last three chapters focus on the three main components of an high-contrast instruments: the coronagraph and more precisely its robustness to segment-level aberrations (chapter 4), the wavefront sensor (chapter 5), and the wavefront controller (chapter 6).

The chapter 2 of this thesis consists in an overview of the field of exoplanet detection, from a brief history to a description of the different detection techniques and instruments.

The chapter 3 aims at focusing on high-contrast imaging and in particular the different tools that serve it: coronagraphy, wavefront sensing, and wavefront control. This chapter will also help at defining the notions and setting the basis of the formalism of image formation and wavefront propagation through optical systems that are used in this entire thesis.

In the chapter 4, we focus on performance stability in presence of segmentation-related wavefront errors. Indeed, as mentioned before, the segmentation of the primary mirror generates specific issues such as phasing errors, segment-level instabilities, resonance effects... To quantify the constraints applied on the segments, in terms of manufacturing, alignment, edge sensors, stability, and support architecture while reaching and maintaining the target contrast, an error budget must be conducted. During my PhD, I developed the Pair-based Analytical model for Segmented Telescopes Imaging from Space (PASTIS), a tool providing the contrast in the dark hole of the detector in presence of aberrations on the segments and usable in replacement of time- and energy-consuming end-to-end simulations. This tool is generic and can be applied to different coronagraphs and telescopes, ie. segmentation configurations, for performance from the ELT to LUVOIR.

In the chapter 5, I propose a first experimental validation of the wavefront sensor COFFEE to the reconstruction of cophasing errors. The main advantage of COFFEE is its ability to use the science image as an input of the reconstruction, even in presence of a coronagraph. The non-coronagraphic reconstruction provided very exciting results with a well estimation of the phasing errors of the segmented mirror. The post-processing of the coronagraphic data put into light a limitation of this sensor: because of the size of the focal plane coronagraphic mask that acts like a high-pass filter, the sensor remains blind to low-order wavefront errors. This study enabled to set up constraints for future COFFEE applications.

Such a knowledge on the wavefront errors is powerful: it not only allows to compensate for them to flatten the wavefront, but it also leaves the opportunity to dig into the diffraction artifacts in the dark hole to reach contrasts that no perfectly flat wavefronts could get. This second point is made possible by non linear control techniques such as the one introduced in the chapter 6, that also has the advantage of fitting coronagraphic optical trains. In addition to a preliminary experimental validation of this controller for a monolithic pupil, I ran a set of studies to test the robustness and quantify its performance in the presence of segmentation.

Eventually, the chapter 7 presents the main conclusions of these three years of studies on the high-contrast toolkit and its adaptation on segmented telescopes and proposes some perspectives and developments for the near and further future.

There's so many different worlds
So many different suns
And we have just one world

— Dire Straits

2 Context

This informative chapter aims at providing an overview of the scientific field of this PhD. We start (section 2.1) with a brief history on research of exoplanets, then (section 2.2) we describe the different detection techniques currently used, including the technique I focus on, ie. direct imaging. In section 2.3.2, we project to the future with the coming missions that will perform exoplanet imaging, and eventually (section 2.4) we describe the position of this thesis in this context.

2.1 Hunting other worlds

The existence of other worlds remained for long a religious and philosophical question more than a scientific one. From the Ancient history the geocentric model was defended, stating that the Earth is motionless at the center of the Universe, and that all spatial objects are contained in a sphere and revolving around it. For the Catholic Church, this theory confirmed the unicity of the Creation and was also strongly defended by different philosophers such as Aristotle (384-322 BC), Hipparchus ($\sim$ 190-120 BC), and Ptolemy ($\sim$ 90-168).

We have to wait until the XIIIth century to reconsider this statement. The Muslim astronomers Nasir ad-Din at-Tusi (1201-1274) and Ibn al-Shâtir (1304-1375) developed a modern model of planetary system, refuting some hypotheses of geocentrism. Nicolaus Copernicus (1473-1543) later used their model to develop the theory of the heliocentrism, proposing that the Earth actually orbits around the Sun supposedly at the center of the Universe.

But according to the philosopher Giordano Bruno (1548-1600), Copernicus' model is not enough developed: the Earth indeed revolves around the Sun, but the Sun cannot be at

(a) (b)

Figure 2.1.1: Posters designed for NASA to celebrate the discoveries (a) of the first exoplanet around a star, 51 Pegasi b and (b) of the first Earth-like planet, Trappist-1 e. Courtesy of JPL/NASA and NASA.

the center of the Universe since the Universe is infinite, occupied with many other stars and worlds like ours. The Universe acquires depth and other planets with life are considered, which had already been mentioned by Epicurus (341-270 BC) and Lucretius (Ist century BC). However, this idea was not proven by scientific facts yet and was still considered as scandalous by the Inquisition and the scientific and religious community.

Ten years after Bruno's murder by the Italian Inquisition, Galileo Galilei (1564-1642) perfected the refracting telescope and scientifically confirmed these new theories on heliocentrism and satellite motions of planets around the Sun, and of natural satellites around planets (the Moon and Jupiter's moons).

However, the first detection of an exoplanet arrived only in 1992, when Wolszczan and Frail (1992) discovered three planets revolving around the pulsar PSR 1257 + 12, using the 305-m Arecibo radiotelescope. It was followed in Mayor and Queloz (1995) by the first detection of a planet around a main sequence star, 51 Pegasi (see Fig. 2.1.1 (a)), by applying the radial velocity technique on the spectrograph ELODIE of the Haute-Provence Observatory (OHP) (see section 2.2.1.1).

Since then, nearly 4000 exoplanets have been discovered, using various techniques (see

section 2.2) and enabling to develop the knowledge on exoplanets' and planetary systems' formation and evolution. In 2015 and 2017, the discovery of the planetary system Trappist-1, composed of seven planets revolving around an ultra-cool red dwarf star, three of them considered in the habitable zone [de Wit et al. (2016) and Luger et al. (2017)]. In particular, the exoplanet Trappist-1 e remains today the closest to Earth ever detected in terms of stellar flux (see Fig. 2.1.1 (b)).

2.2 Techniques of detection of exoplanets

Detecting an exoplanet remains a challenging task, since the observed object is necessarily fainter than and close to a bright star. Several techniques of detection have been developed. They can be divided in two main categories: indirect imaging, where the measured signal does not directly come from the exoplanet but rather from the star, and direct imaging, when the photons of the planet are directly imaged on the detector independently from its star. This section proposes a short review on these different techniques of detection and imaging. The numbers of exoplanets detected with each technique come from the website http://exoplanet.eu/, that provides an updated list of all known exoplanets. This website also enables to obtain the diagram of Fig. 2.2.1, that indicates for each known planet its mass, orbital period, and the technique used to detect it. The values were taken on September 1st 2018.

2.2.1 Indirect imaging

To detect exoplanets, the first techniques used were indirect methods. Today they still remain the most commonly used techniques and were developed before direct imaging could achieve a good enough performance to detect exoplanets, since they only require a large and stable telescope.

The list of techniques introduced here is not comprehensive, and others that will only be mentioned in this thesis exist, such as the transit-timing variation method, or the technique based on the variations of pulsar pulsation rate.

2.2.1.1 Radial velocities

If a planet revolves around a star, the two objects form a two-body system orbiting around its barycenter. In particular, the distance between the star and the observer on Earth varies periodically. This phenomenon generates a Doppler effect, ie. the absorption lines of the stellar spectrum show a periodic shift in wavelength. Therefore, detecting this spectral shift provides the radial velocity of the star, ie. the speed of its motion along the observation axis (see Fig. 2.2.2 (b)). This enables to confirm the existence of a planet, but also gives information about its orbit around the star (period, ellipse' parameters) and its minimal mass.

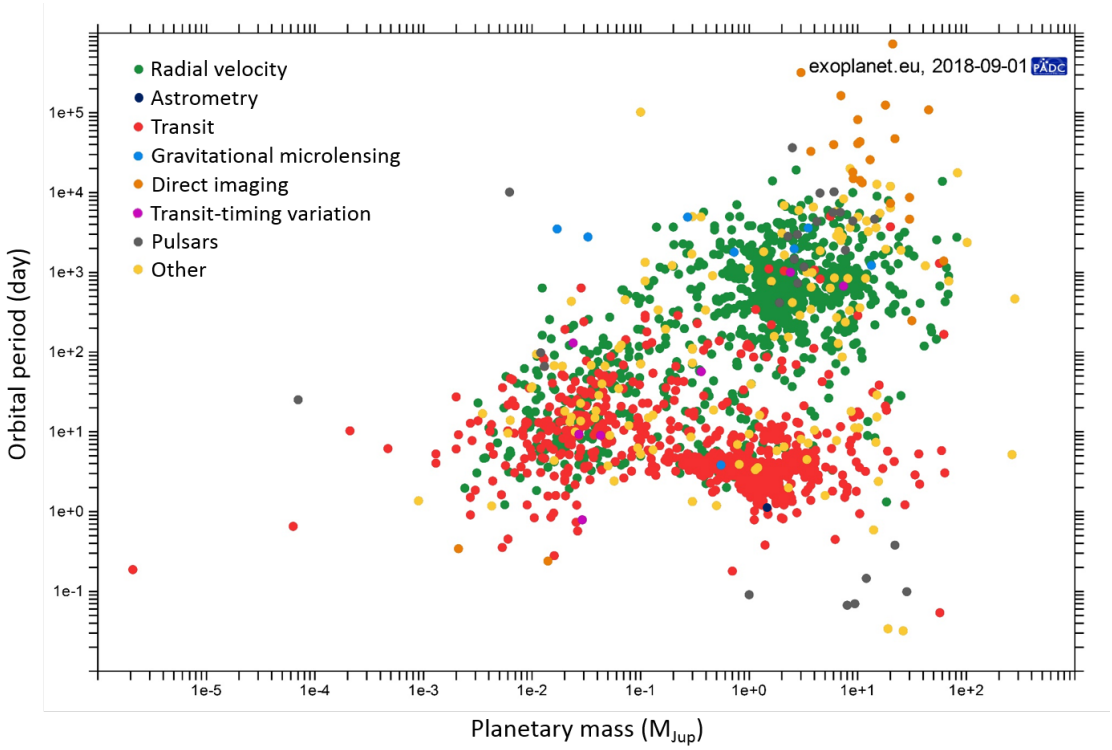

Figure 2.2.1: Mass-orbital period diagram of known exoplanets, for different detection techniques.

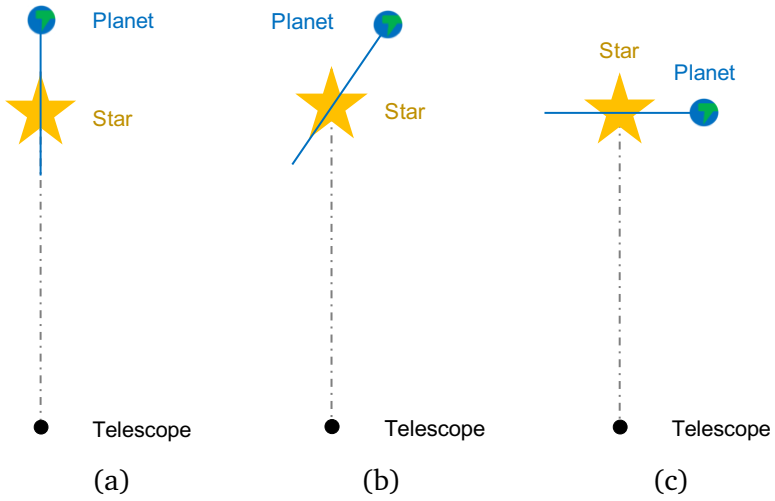

Figure 2.2.2: Illustration of the impact of the angle between the planet's elliptical motion and the observation axis. (a) The angle is null, and the radial velocity enables to compute precisely the planet's mass. (b) The angle is not null, the radial velocity provides an underestimation of the planet's mass. (c) The observation axis is normal to the plane of the planet's motion so the planet does not impact the radial velocity of the star and therefore cannot be detected with this method.

The reason why it only provides the minimal mass of the planet is that only the velocity of the star along the observation axis is known. Fig. 2.2.2 proposes three different configurations. In each of the three schemes, the grey dotted line represents the observation axis, and the blue line the amplitude of the planet motion. In Fig. 2.2.2 (a), the planet evolves in a plane containing the observation axis and so the computed radial velocity of the star corresponds to the actual velocity of the star. Therefore the mass can be precisely computed. Otherwise (Fig. 2.2.2 (b)) the computed velocity of the star is biased by the inclination angle between the planet ellipse and the observation axis and underestimated, which also provides an underestimation of the planet mass. Fig. 2.2.2 (c) corresponds to the most extreme case, where the planet does not impact at all the radial velocity of the star and therefore cannot be detected.

A first uncertainty appears here: the mass of the planet cannot be estimated with certainty with this method only. Another issue is that some star's gas can periodically expand or shrink which can generate false positives. The younger stars, having a lot of surface movement, are also adding a strong noise to the Doppler effect and reduce this method capacities. In general, the study of the planet needs to be completed with another method.

This technique particularly fits to the detection of large planets (see Fig. 2.2.1), since they have a higher impact on the position of the star.

This method enabled the discovery of the exoplanet 51 Pegasi b with the spectrograph ELODIE at the OHP [Mayor and Queloz (1995), Baranne et al. (1996)]. It also provided the large majority of the exoplanets detection since 1995 and until the first observations of Kepler (see section 2.2.1.3). It still enabled so far to detect around 20% of the confirmed

exoplanets (763 exoplanets), remaining extremely used on many telescopes: the spectrograph SOPHIE (Spectrographe pour l'Observation des Phénomènes des Intérieurs stellaires et des Exoplanètes) replaced ELODIE at the OHP [Perruchot et al. (2011)], the instruments HARPS (High Accuracy Radial velocity Planet Searcher) at La Silla observatory [Mayor et al. (2003)] and HARPS-N at the Telescopio Nazionale Galileo provide extremely precise estimation of the star velocity (down to 1 m/s), and the Lick observatory and Keck telescope for instance also enable exoplanet detection with radial velocity of stars [Radovan et al. (2010), Butler et al. (2017)].

2.2.1.2 Astrometry

Like the previous method, the astrometry technique is based on the impact of a companion on the position of the parent star since once again both orbit around their barycenter. But on the contrary of the other method, we do not observe the radial motion of the star, but the projection of its motion on the observable plane, ie. the plane orthogonal to the observation axis (and radial axis). With precise measurements of the position and motion of the star among time, in general using other nearby stars as immobile references, we can deduce the presence of a secondary object, but also information about its ellipse and mass.

The main issue of this method is that, like in the previous technique, we don't have a direct estimation of the motion of the star in three dimensions, but of the projection of its motion on the observable plane. This can generate biases when computing the parameters of the orbit and the mass of the planet. This is why this method is used in general as a complement to another method such as radial velocities. Recombining data from these methods eliminates the ambiguities on these parameters.

Even if the method is quite robust to variations of flux of the host star, on the opposite of the previous technique, it requires a very precise knowledge of the star's position. Therefore it is extremely sensitive to atmospheric turbulence and is generally applied from space telescopes. The Gaia (Global Astrometric Interferometer for Astrophysics) satellite of the European Space Agency (ESA), launched in 2013, was specifically designed for astrometric measurements [Gaia Collaboration et al. (2016, 2018)] and replaced the satellite Hipparcos (HIgh Precision PARallax COllecting Satellite) that initiated astrometric measurements from 1989 to 1993.

Because of the difficulties to precisely measure the position of the star among time, the larger the motion is, the more easily it can be measured. Therefore this technique is particularly adapted to the case of massive companions far from the star, or to the case of young stars. So far, it enabled the detection of four exoplanets.

2.2.1.3 Transit

Similar to a solar eclipse, a transit happens when a planet, its host star, and the observer are aligned. By doing so, the planet blocks a fraction of the light coming from the star and decreases its apparent brightness.

The period of the transit then informs us about the period of the planet's orbit. Combining this information with the third Kepler's law provides the semi-major axis of the orbit, which for instance inform us if the planet belongs or not to the habitable zone of the stellar system. Furthermore, quite obviously the bigger the planet, the more light is blocked: if the star's characteristics are known, we can deduce the diameter of the planet. Eventually, in the case of a planet with an atmosphere, comparing the spectra of the star when the planet does not block it and when it is transiting gives us the chemical composition and the temperature of the planet atmosphere, which is particularly interesting when it comes to possible life marker research.

This method requires the unification of many constraints. First, it has to happen periodically to confirm the presence of a planet. Secondly, as said earlier, the transiting planet has to pass exactly between the star and the observer, ie. there is a constraint on the inclination of the planet's orbit to be close to 90°. This provides a first limitation of this technique: when looking for a planet transiting in front of a specific star, the probability that the constraint is respected is very low and many planets cannot be detected. This is why telescopes dedicated to transit detection cover a huge portion of the sky to observe as many stars as possible. This technique is also quite sensitive to the variation of apparent flux of the star itself, and to turbulence effect, which is why it is generally applied from space, even if even from space, this technique is still limited by the intrinsic flux variation of the star. As an example, a solar spot on the Sun's surface would look exactly like an exoplanet transit.

Several missions are partly dedicated to the study of planetary transits. The CoRoT (Convection, Rotation, & Transits) space telescope of ESA and CNES (Centre National d'Études Spatiales) was operating between 2006 and 2014 and enabled in particular the discovery of the exoplanet Corot-7b, the smallest planet ever discovered at that time, with a radius of 1.7 times the Earth radius [Baglin (2003), Léger et al. (2009)]. The Kepler satellite of NASA (National Aeronautics and Space Administration) was launched in 2009 and since then it discovered more than half of the known planets [Borucki (2017)]. The Transiting Exoplanet Survey Satellite (TESS) was chosen through the program Explorer (NASA) and launched in April 2018 [Ricker et al. (2015)]. Two future missions will also enable detection of transiting planets: the CHaracterising ExOPlanets Satellite (CHEOPS, 2019) of ESA and Switzerland [Fortier et al. (2014)] and the PLAnetary Transits and Oscillations of stars (PLATO) satellite around 2026. So far, 74% of the confirmed exoplanets were detected with this technique (2838 exoplanets), mainly since the Kepler's first light. This technique particularly suits to the detection of quite large planets close to their host star (see Fig. 2.2.1), since they then get a higher chance to pass in front of the star and block more starlight.

2.2.1.4 Gravitational microlensing

The last indirect imaging technique presented here is microlensing, that enables to detect faint objects in general and is directly applicable to exoplanets. It is based on the principle of gravitational lensing: when passing between a background bright object (source) and the observer, a massive object (lens) deviates the light rays emitted by the source and reaching

the observer like a magnifying star. Therefore, by studying the increase of flux from the source, it is possible to deduce the presence and information about the lens object.

Similarly, a planet-star system behaves like multiple lenses on the photons coming from a background star and can be detected with a photometric survey over time. This technique enabled to set in particular the hypothesis that in general each star has at least one planet. It also permitted to study other objects, such as moons or free-floating planets.

The Microlensing Observations in Astrophysics (MOA) [Bond et al. (2002)] and the Optical Gravitational Lensing Experiment (OGLE) [Udalski et al. (1992)] are two collaborations dedicated to the study of microlensing effects and discovered 78 exoplanets (2% of the confirmed exoplanets). The future mission WFIRST (Wide Field Infrared Survey Telescope) will also partly perform microlensing and should participate to the discovery of many planets.

2.2.2 Direct imaging

2.2.2.1 Principle

In opposition to the techniques previously introduced, direct imaging focuses on the planet signal only. It consists in measuring the photons flux coming directly from the planet to get an image of it. Several advantages can be attributed to this technique, including:

- there is no uncertainty on the mass of the planet,

- the planet is in general visible on the whole orbit,

- studying photons coming directly from the planet enables to reconstruct its spectrum.

This last point is specifically interesting since it enables to obtain the chemical composition of its atmosphere. This information is useful for two reasons: first the spectral signature of an exoplanet is very different from a star and such spectrum allows to identify a planet at once, with no need to observe at different epochs. Secondly the chemical composition of the atmosphere is an excellent witness for the possible presence of life markers on the planet.

The star is much brighter than the planet: for instance, in the far IR, ie. the wavelength range where the detected photons are actually emitted by the planet itself, a hot Jupiter is around 10^3 times less bright than its host star, while a telluric planet is around 10^6 times less bright than its host star. These detection constraints are even more drastic in visible/near-IR light, ie. the wavelength range where the detected photons are actually stellar light reflected by the planet: a hot Jupiter is around 10^6 times less bright than its host star, while a telluric planet is around 10^{10} times less bright than its host star.

Because of this brightness difference between planet and star and the fact that the natural diffraction of light in a telescope focal plane spreads any light over the whole focal plane, the starlight covers by far the planet's light (see Fig. 2.2.3). Direct imaging is then easier to do when the planet is bright and therefore large and far from its host star. In order to increase the range of detectable planets, two main parameters need to be improved:

we want to image planets with smaller angular separation and several order of magnitude fainter than their star.

As a comparison with the techniques previously described, 2.4% of the confirmed planets have been detected using direct imaging (92 exoplanets). Because of technological limits, the planets detected with direct imaging so far were extremely large (several times the mass of Jupiter) and far from their host star (see Fig. 2.2.1). This technique will be more detailed in the next section, since this PhD focuses on it.

2.2.2.2 Past and current instruments and results

2.2.2.2.1 Ground-based instruments

The ground-based instruments can be divided in two main categories: the instruments exclusively dedicated to observations, such as SPHERE (Spectro Polarimetric High contrast Exoplanet REsearch) and GPI (Gemini Planet Imager), and the instruments enabling research and development testing, such as SCExAO (Subaru Coronagraphic Extreme Adaptive Optics) and P1640.

In 2004, 2M1207 b became the first exoplanet ever detected with direct imaging [Chauvin et al. (2004)]. It was observed in the infrared without coronagraph but with the adaptive optics instrument NaCo (short for Nasmyth Adaptive Optics System (NAOS) Near-Infrared Imager and Spectrograph (CONICA)), from the Very Large Telescope (VLT) [Rousset et al. (2003) and Lenzen et al. (2003)].

The VLT then gained SPHERE, a second-generation instrument dedicated to the detection of exoplanets [Beuzit et al. (2008), Fusco et al. (2006), Sauvage et al. (2016), and Fusco et al. (2016)]. It is composed of a 1400-actuator deformable mirror to compensate for the atmospheric turbulence, and three instruments: ZIMPOL (Zurich IMaging POLarimeter) is a camera working in visible and near infrared light capable of measuring light polarisation, IRDIS (InfraRed Dual-band Imager and Spectrograph) is a camera working in near-infrared, and eventually the IFS (Integral Field Spectrograph) provides spectra of the observed planets in the near-IR. Each of these subsystems provides the option of using a coronagraph. SPHERE discovered and analyzed its first exoplanet in 2017 by combining observations from IRDIS and the IFS [Chauvin et al. (2017)].

GPI [Graham et al. (2007) and Macintosh et al. (2006)] was built at the Gemini South telescope to detect and image young giant planets, but also to study protoplanetary disks, transition disks, and debris disks. It provides in spectroscopy and polarimetry of the observed objects in near-infrared (0.9 to 2.4 μm), for a contrast of around 10^{-6} for angular separations between 0.2 and 1 arcsec. This instrument is composed of an extreme AO system using two DMs, a calibration unit, a coronagraph (apodized pupil Lyot coronagraph), and an IFS. One of the main result on GPI was the discovery of the Jupiter-like exoplanet 51 Eridani b, who was also the first exoplanet discovered with GPI [Macintosh et al. (2015)].

The SCExAO instrument [Jovanovic et al. (2015)] is located at the Subaru telescope

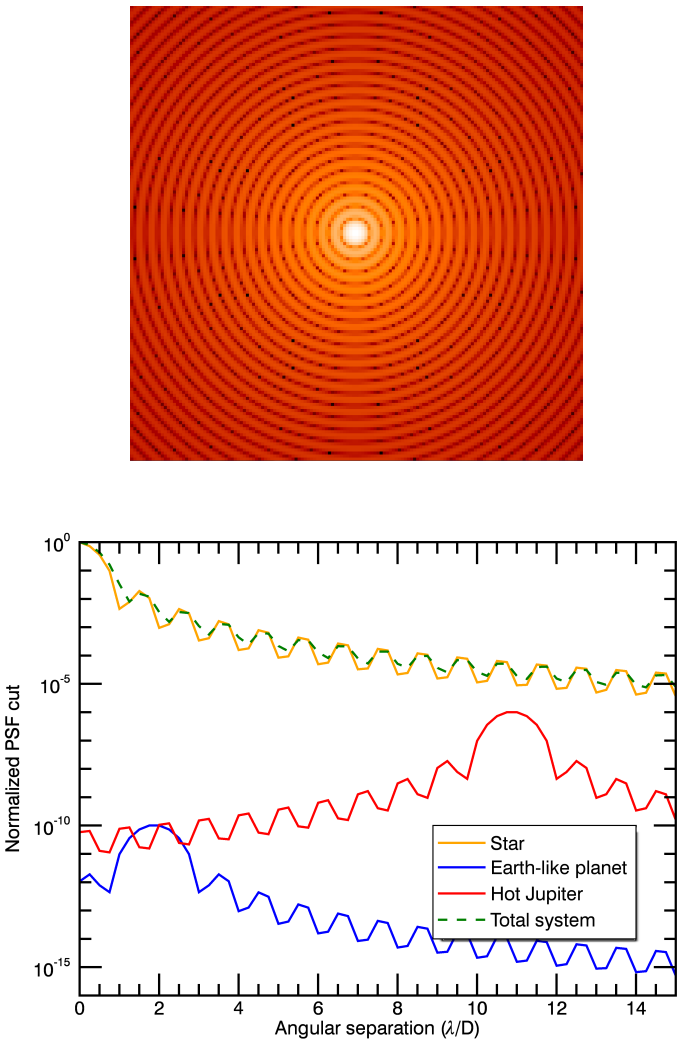

Figure 2.2.3: (top) Image of a planetary system composed of a star, a Earth-like planet located at $2\lambda/D$ and a hot Jupiter-like planet located at $11\lambda/D$. The image is normalized by the peak intensity of the star, and the exo-Earth is 10^{10} times dimmer than the star, while the exo-Jupiter is 10^{6} times dimmer than the star. (bottom) Radial cuts of the image with (orange) the star only, (blue) the exo-Earth only, (red) the exo-Jupiter, and (green) the total planetary system.

in Hawaii. It provides two types of studies: on-sky applications for high-contrast imaging of exoplanets and disks around nearby stars [Currie et al. (2017)] and also a testbed to develop and test high-contrast imaging tools [Currie et al. (2018) and Lozi et al. (2018)]. It works between 600 and 2500 nm and is coupled with an adaptive optics system (AO188) to perform fine Adaptive Optics (AO) correction. Then the light goes through a coronagraph to other instruments, such as the Coronagraphic High Angular Resolution Imaging Spectrograph (CHARIS) [Groff et al. (2017)] and Visible Aperture-Masking Polarimetric Interferometer for Resolving Exoplanetary Signatures (VAMPIRES) [Norris et al. (2015)]. The High-Contrast Coronographic Imager for Adaptive Optics (HiCIAO) used to also be a module at Subaru telescope dedicated to the search of exoplanets but was decommissioned in 2016 [Tamura et al. (2006)].

The project P1640 was also designed to image and get the spectra of as many planets and brown dwarfs orbiting around nearby stars as possible. It is mounted at the Palomar 200-inch telescope since 2008 and is composed of an AO system (PALM-3000, already part of the Palomar AO system), an apodized pupil Lyot coronagraph, a Mach-Zender interferometer, and an IFS operating between 995 and 1775 nm [Hinkley et al. (2011)]. Two exoplanet candidates have been discovered so far.

2.2.2.2.2 Space-based instruments and telescopes

The Hubble Space Telescope (HST), operational since 1990, is composed of a 2.4 meter primary mirror allowing to get images with an angular resolution of 0.1 arcsec (PI: Matt Mountain). On the dozen of instruments that it carried in total, several enabled the study of circumstellar disks and planets. In particular, the Advanced Camera for Surveys (ACS) provided images of giant planets.

Spitzer or the Space Infrared Telescope Facility (SIRTF) was a NASA telescope operating between 2003 and 2009 before entering into its warm mission [Werner (2005)]. It is composed of a camera (Infrared Array Camera (IRAC)), a spectrograph (Infrared Spectrograph (IRS)), and a photometer (Multiband Imaging Photometer (MIPS)). This telescope enables for instance the study of protoplanetary disks and thus planet formation. It was also the first telescope to directly detect the light coming from an exoplanet and could enable the study of planets' atmospheres.

2.3 High-contrast imaging of Earth-like planets

2.3.1 Principle of high-contrast imaging

As seen in section 2.2.2.1, direct imaging enables to get specific information about the target exoplanet, for instance the temperature, pressure, and chemical composition of its atmosphere.

However, imaging habitable worlds remains extremely challenging: by comparison with our planet, it is expected that the light reflected by an exo-Earth, ie. an exoplanet with a similar size, mass, temperature, pressure, and stellar flux than the Earth, is at least 10^{10} times dimmer than the light emitted by its host star (in the visible and near-infrared). The actual limit of contrast for an exoplanet detection can be reached with instruments such as SPHERE and GPI with a contrast of 10^{-6}, ie. the planets are 10^{6} times dimmer than their star.

To this first limitation, another one has to be added: exo-Earth are extremely close to the host star. We typically look for objects within an angular separation of around 0.1" (0.5" for Jupiter-like planets), which is not achievable with current instruments. Typically, Earth-like planets correspond to very small planetary masses and short orbital periods on the diagram of Fig. 2.2.1.

The angular separation being of the order of λ/D where λ is the observing wavelength and D is the telescope diameter (see also section 3.1.1.3), it is improved when the telescope is larger and not affected by atmospheric turbulence or combined with an extreme AO system. It could have also been chosen to reduce the observation wavelength, but the contrast of the planet depends on the wavelength and a trade-off has to be made between facilitating performance in contrast and in resolution. In general, instruments observe in visible and/or near infrared light.

In parallel to an increase of the telescope diameter, to disentangle the star and the planet, complex imaging systems composed of several functionalities have been developed. Fig. 2.3.1 describes a typical optical imaging system. The photons coming from both the star and the planet are collected by the telescope. For ground-based telescopes, the wavefront has been disturbed by the atmosphere and is corrected by an AO system. It is combined with a wavefront controller with a high-density deformable mirror that corrects for static and quasi static aberrations (see sections 3.1.2 and 3.4). This control loop also requires a very high-performance wavefront sensor, most probably in a focal plane than in a pupil plane (see section 3.3). The light then goes through a so-called coronagraph, that aims at physically removing the starlight (see section 3.2). After the image being taken by the camera, it is processed and analyzed to provide information about the planet (separation from the star, diameter, spectrum...).

Because of the complexity of this goal, imaging Earth-like planets has not been achieved yet and is still not doable with today's instruments and telescopes, described in section 2.2.2.2. However, some future instruments will be dedicated to this kind of applications and hopefully will fulfill this challenge (see section 2.3.2).

2.3.2 Future missions

The instruments currently set up on telescopes and dedicated to exoplanet imaging did not find all expected planets. In addition, none of the observing instruments has been designed to directly image exo-Earths. Coming telescopes and instruments are dedicated to overcome these lacks.

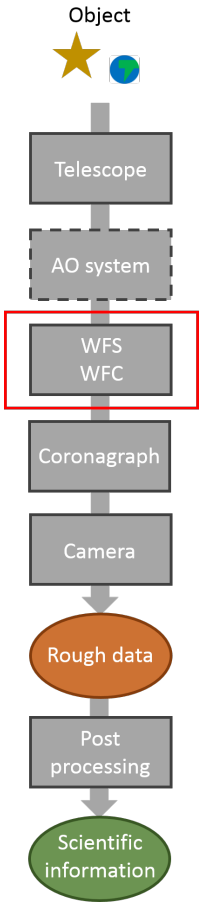

Figure 2.3.1: Generic photon chain through a high-contrast imaging system. The photons from the science objects are collected by the telescope. An AO system corrects for the wavefront aberrations, mainly due to the turbulence (ground-based applications). Then a wavefront control system enables to increase the wavefront quality, by correcting for static and quasi-static aberrations. A coronagraph removes the starlight so the planet is revealed on the detector. Eventually, the data from the camera is processed and analyzed to obtain the interest information.

2.3.2.1 Ground-based missions

We have seen that the size of the telescope is the fundamental limitation to the observations. Therefore, the next generation of ground-based telescopes include giant segmented telescopes. Even if their first light instruments will not be dedicated to very high-contrast imaging, they aim at detecting exoplanets and the second generation of instruments should include Earth-like planets imaging.

For instance, the Extremely Large Telescope (ELT) is developed by the European Southern Observatory (ESO) and is currently under construction in Chile. It will correspond to the largest telescope, with a primary mirror of 39.3 m composed of 798 hexagonal segments. Imaging Earth-like planets belongs to its main science goals and several instruments are designed for this purpose: the Mid-Infrared E-ELT Imager and Spectrograph (METIS) [Brandl et al. (2014, 2016)] combining coronagraphy, spectroscopy (3 to 9 μm), and an IFS unit (2.9 to 5.3 μm), the Multi-AO Imaging Camera for Deep Observations (MICADO) allowing direct imaging and spectroscopy of exoplanets also with a coronagraph [Davies et al. (2016)], and the High Angular Resolution - Monolithic - Optical and Near-infrared - Integral field spectrograph (HARMONI), an IFS providing high-contrast imaging, combined with different AO systems and covering a small field of view (1 to 10 arcsec) for a spectral range from 0.5 to 2.4 μm [Dohlen et al. (2018)]. Furthermore, a specific ELT instrument of the second generation, the Planetary Camera and Spectrograph (PCS), will be dedicated to the direct imaging of Neptune and super Earth-like planets [Carlotti et al. (2014)].

Similarly, the Thirty Meter Telescope (TMT) and the Giant Magellan Telescope (GMT) [Fanson et al. (2018) and Codona (2004)] belong to the next generation of giant ground-based telescopes that will be partly dedicated to the search for exoplanets. Like the Keck telescope and the ELT, the TMT and the GMT have segmented pupils, even if the GMT primary mirror is not made of hexagonal segments but circular ones.

In parallel to these coming giant telescopes, a few tools have been developed to increase accessibility of already existing telescopes to planets, with typical diameters of 8 to 10 m.

The Keck Planet Imager and Characterizer (KPIC) is a High Dispersion Coronagraphy (HDC) tool currently being set up at the Keck telescope [Mawet et al. (2016)]. This instrument fits with the Keck AO system and is composed of a near-infrared pyramid wavefront sensor, a 1k actuator deformable mirror (in addition to the 349 actuator deformable mirror already existing at Keck), a coronagraph, and a single mode fiber placed at the position of the planet. With this fiber, the light from the planet is relayed through a spectrograph to obtain the spectrum of the planet atmosphere.

The project HiRISE (High-Resolution Imaging and Spectroscopy of Exoplanets) [Vigan et al. (2018)] aims at setting up a high spectral resolution upgrade instrument on the instruments SPHERE and CRIRES+ (successor of CRIRES, the CRyogenic high-resolution InfraRed Echelle Spectrograph) of the VLT, with the installation of a fiber injection unit.

2.3.2.2 Space missions

The James Webb Space Telescope (JWST) is a NASA space telescope operating in the infrared whose launch is planned for 2021 [Stevenson et al. (2016)]. In its primary objectives, we find the study of exoplanets using direct imaging and spectroscopy. Its primary mirror is composed of 18 hexagonal segments which make it the first segmented telescope being launched in space. Various coronagraphs will also be available. Please see section 4.3.1 for more details about the JWST.

WFIRST is another NASA project, that should be launched around 2025-2030 [Spergel et al. (2013)]. It belongs to the Exoplanet Exploration Program (ExEP), the direct imaging of giant exoplanets being part of its main science goals. It contains two instruments: the Wide-Field Instrument (WFI) is a near-infrared camera (0.7 to 2 μm) and the Coronagraph Instrument (CGI) is combined with an IFS and is dedicated to starlight removal for wavelength between 0.4 and 1 μm. This second instrument aims at reaching a 10^{-9} contrast around 0.1 arcsec from the observed stars [Mandell et al. (2017)].

Exo-C is a lower-cost alternative to WFIRST, specifically dedicated to the imaging of planets orbiting nearby stars [Stapelfeldt et al. (2015)]. It would also be composed of a coronagraph (hybrid Lyot coronagraph), a wavefront control system, an imaging camera, and an IFS.

The NASA successor of the JWST and WFIRST will be selected through the decadal survey concept study. Two of the four projects proposed to the decadal survey are dedicated to the direct imaging of exoplanets, with specifications including the observation of earth-like planets [Wang et al. (2017)]:

- the Large UV/Optical/Infrared (LUVOIR) surveyor would have a primary mirror of 8 (design B) to 15 m (design A). The Extreme Coronagraph for Living Planetary Systems (ECLIPS) will be specifically dedicated to research for Earth-like planets. In addition to the coronagraph and maybe a starshade, it would also be composed of at least one deformable mirror and would have the possibility to operate in multiple wavelengths (0.1 to 5 μm) [Arney et al. (2017)].

- the Habitable Exoplanet (HabEx) imaging mission is specifically dedicated to terrestrial worlds. Like LUVOIR, its observation wavelength range would also be quite large (0.4 to 1 μm, maybe extended in the near-infrared (IR)), and it would count either a coronagraph or a starshade in its components. The pupil format being not defined yet, it is still unsure if the final design will be monolithic or segmented [Martin et al. (2017)]].

As an information, the two other propositions to the decadal survey are the Origins Space Telescope (OST) and the Lynx X-ray Surveyor.

Another study worth mentioning is the Segmented Coronagraph Design & Analysis (SCDA) survey [Zimmerman et al. (2016)]. It is at the origin of a toolkit providing coronagraph designs for segmented apertures. This study is particularly used as part of the

LUVOIR design process, which is quite new: for the first time, the coronagraph design is thought ahead of the telescope's architecture itself.

2.3.2.3 Conclusion on the different direct imaging instruments

In Fig. 2.3.2, we propose on a unique temporal scale the different telescopes and instruments dedicated to direct imaging of exoplanets presented in the previous sections. The red dotted line corresponds to 2018, the current year, and the red star to the first direct image of an exoplanet. The green lines correspond to ground-based missions while the blue ones to space missions. Furthermore, the pattern of the pupil can be recognized as the style of the lines: uniform for monolithic pupils, concatenation of hexagons for pupils made of hexagonal segments, and concatenation of disks for the GMT, ie. the one pupil formed of circular segments. I also indicated on the right the diameter in meters of the entrance pupil. It also has to be noted that the HST has counted various instruments imaging exoplanets or circumstellar disks, so the line covers the entire mission instead of the set up of each single instrument.

In this graph, we notice a clear trend towards segmented telescopes, both for ground-based and space missions. Segmented apertures have the advantages of being able both to reach larger diameters so better angular separation, but also to fold space telescopes to make them fit into launch vehicles.

2.4 Position of this thesis in this problematic

As explained in the previous sections, the ambitious science goal of imaging Earth-like planets requires large telescopes and very high-performance optical systems with tools such as AO, coronagraphy, WaveFront Sensing (WFS), WaveFront Control (WFC), and efficient post-processing algorithms (see Fig. 2.3.1). In this thesis, we focus on a specific portion of the photon chain presented here: from the wavefront controller to the camera, ie. without including the AO correction system and the data post-processing.

The final performance of a high-contrast imaging system is mainly driven by the quasi-static aberrations remaining uncorrected, as well as the diffraction residuals. The core of this thesis is the fine comprehension of the aberrations residuals generated by a segmented telescope, their propagation in a high contrast instrument, and their impact on the final performance in a very high-contrast regime.

From HST/NICMOS in 1997, most of the instruments have a coronagraph, and from VLT/NaCo, most of them have a wavefront correction system (AO or wavefront controller). A complete understanding of the performance of a high-contrast system in presence of segmentation obviously appears necessary in the context of extremely high-contrast performance. In particular, the perturbations coming from the segmented pupil have to be

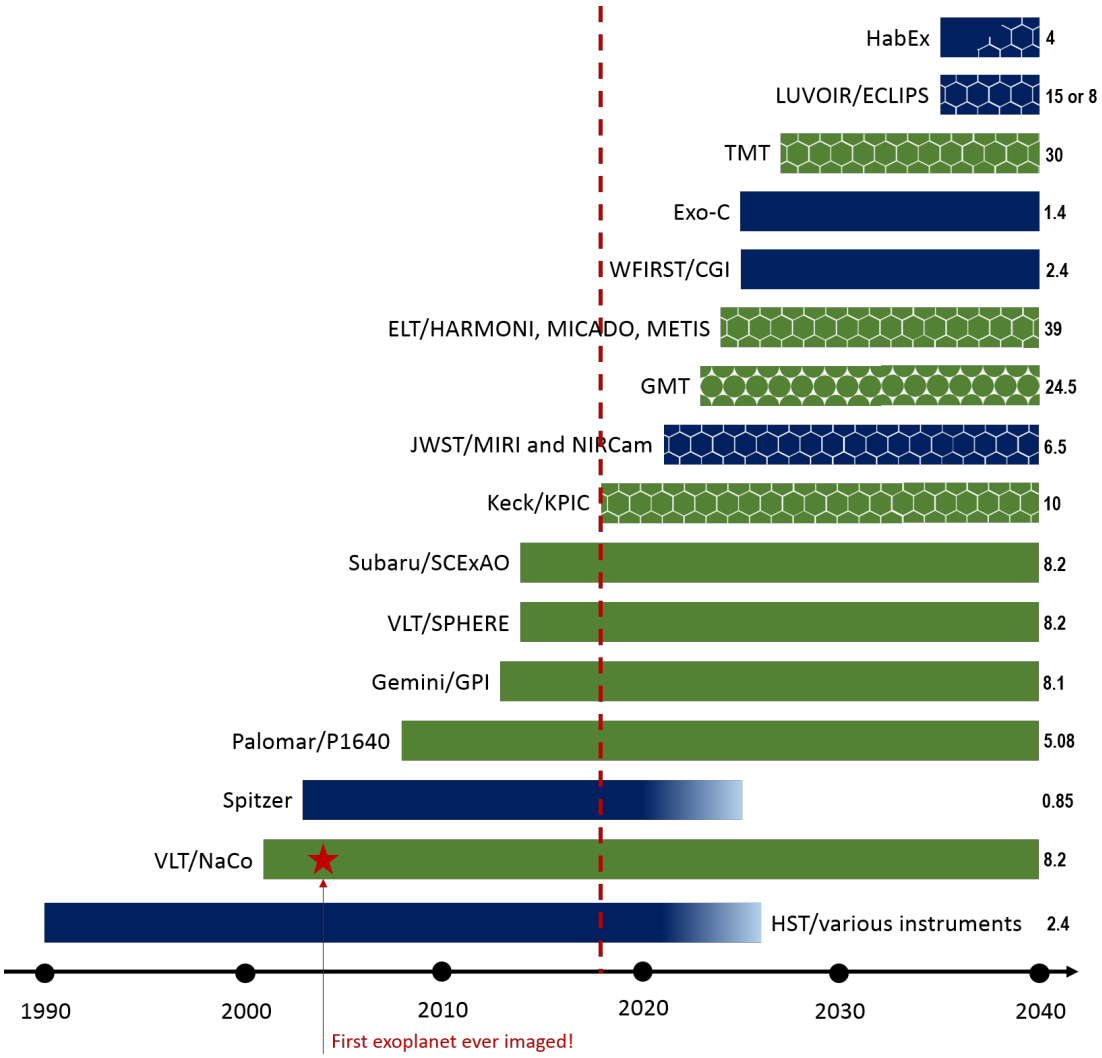

Figure 2.3.2: Half a century of direct imaging of exoplanets. Red line: today (2018). Blue: space missions. Green: ground-based missions. No pattern: monolithic primary mirror. Hexagonal pattern: pupil made of hexagonal segments. Disk pattern: pupil made of circular segments. Numbers on the right: diameters of the primary mirrors.

taken into special consideration: difficulties of segment phasing, vibrations, tighter requirements...

To build the next very high-contrast instruments, a fine comprehension of the coronagraphic system and of its performance in presence of pupil segmentation is necessary, in order to set requirements for segment manufacturing, polishing, and alignment (error budget). In the first part of my PhD, I developed a model of performance prediction for space high-contrast instruments. This model takes into account the particularities of a segmented space telescope: specific segmentation, coronagraph, segment-level aberrations such as phasing errors... Such a model enables to provide an analysis of performance and sensitivity and to understand and master the performance. This whole aspect is developed in section 4.

In parallel, tools that have been developed for AO (active turbulence correction) such as Deformable Mirrors (DMs) and wavefront sensors are now used on a regular basis to push forward the system performance (see VLT/SPHERE and Gemini/GPI). One more step can be done to use them in the case of wavefront errors specific to segmented pupils, such as segment phasing, and more generally for compensation of pupil discontinuities (ACAD-OSM standing for Active Compensation of Aperture Discontinuities-Optimized Stroke Minimization, NLDH standing for Non-Linear dark Hole controller). During my PhD, I demonstrated on an experimental bench that the tools able to measure the wavefront and to correct the diffraction residuals are able to reach the performance in a segmented aperture. These two aspects are addressed in sections 5 and 6. This step is pointed out in red in Fig. 2.3.1, since it consists in a key point of my PhD.

The lights are on, but everyone's gone

— Gossip

3 Tools and techniques

This section aims at explaining the principles of the tools and give a formalism to image formation, with introduction of the notations that will be used in this manuscript. The goal is mainly to describe the propagation of an electromagnetic wave through an optical system. Since we only record an averaged intensity on the detector, the temporal fast variation of the EM field is left out. We consider only the wavefront notion, being the temporal advances and delay of the electromagnetic field, as it participates strongly to the final light distribution in the focal plane.

First, we describe the image formation, from a perfect optical system to different phenomena that can deteriorate it: internal aberrations, turbulence, pupil segmentation. Then we introduce different techniques aiming at increasing the contrast of the image, sometimes by counterbalancing these effects: adaptive optics, coronagraphy, wavefront sensing, and wavefront control.

3.1 Theory of image formation

This section consists of a theoretical approach on direct imaging of an object through a telescope and a description by the impact of different phenomena: aberrations and pupil segmentation.

3.1.1 Direct imaging through a telescope

In this first section, we focus on an ideal and simplified case: the photons from the science object are collected with a telescope and focused on a detector to form an image (see

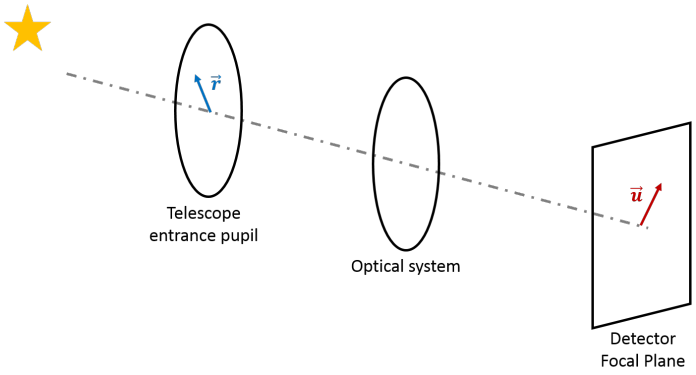

Figure 3.1.1: Schematic view of an optical system. The object is far enough to be considered at infinity. The photons are collected by the telescope entrance pupil and focus on the detector, located on a focal plane. For later in this document, all position vectors will be called $\mathbf{r}$ in pupil planes and $\mathbf{u}$ in focal planes.

Fig. 3.1.1).

3.1.1.1 Direct image formation

We consider a space or ground-based telescope imaging a star. The star is located far enough to be considered at infinity, which means that the wavefront coming from the star arriving at the telescope is considered as flat. The electric field coming from the star is called E in the entrance pupil plane of the telescope, ie. the primary mirror. It can be expressed as:

$$E(\mathbf{r}) = P(\mathbf{r})E_0(\mathbf{r}) \tag{3.1}$$

where $\mathbf{r}$ is the position vector in the pupil plane (see also Fig. 3.1.1), P is the pupil function, and $E_0(\mathbf{r})$ is the electric field generated by the object in the pupil plane. The pupil function corresponds to a binary mask:

$$P(\mathbf{r}) = \begin{cases} 1 \text{ in the pupil} \\ 0 \text{ out of the pupil} \end{cases} \tag{3.2}$$

This expression might account for the presence of spiders, or segmented shape apertures (see also section 3.1.3).

The intensity in the focal plane image is:

$$I(\mathbf{u}) = h * o \tag{3.3}$$

where $h = \left\|\widehat{P}(\mathbf{u})\right\|^2$ is the Impulse Response Function (IRF) of the system, depending only on the telescope. $o = \left\|\widehat{E_0}(\mathbf{u})\right\|^2$ corresponds to the luminous distribution of the object, ie. what its image would look like if the pupil had an infinite diameter. This parameter

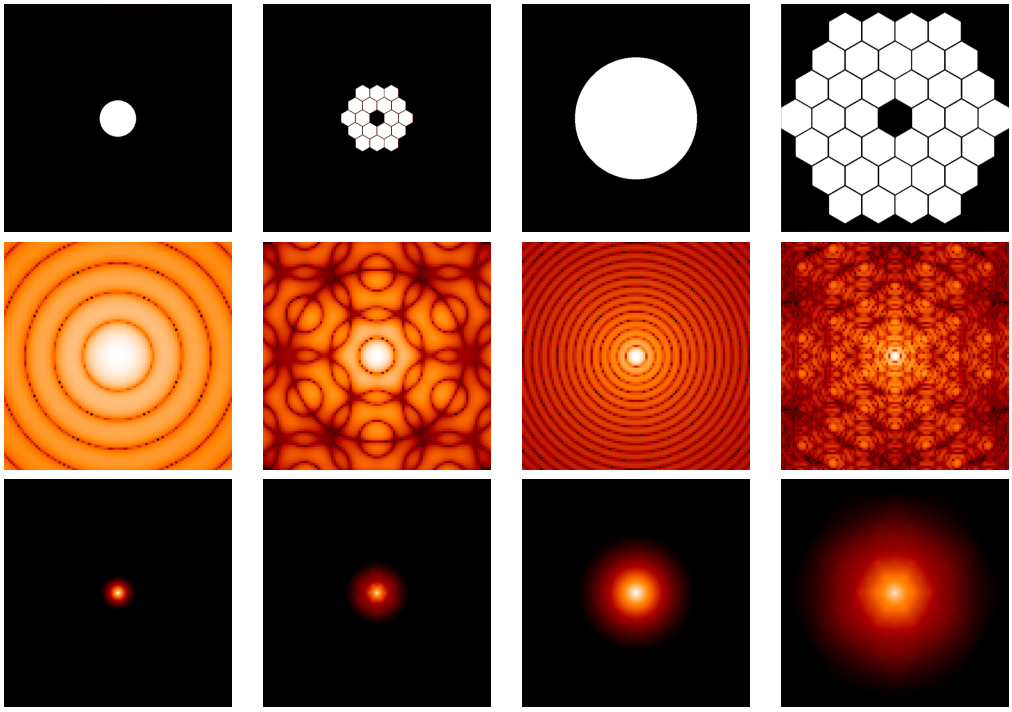

(a) (b) (c) (d)

Figure 3.1.2: Illustration of pupils (first line), corresponding normalized PSF (second line), and MTF (third line) for (a) the HST configuration (diameter of 2.4 m), (b) the JWST configuration (diameter of 6.5 m), (c) one of the VLT units (diameter of 8 m), and (d) one of the configurations considered for the LUVOIR geometry (here diameter of 15 m).

depends only on the object. For instance, if several objects are observed, the image simply becomes:

$$I(\mathbf{u}) = \left\| \widehat{P}(\mathbf{u}) \right\|^2 * \sum_{k=1}^{n_{obj}} o_k(\mathbf{u}) \tag{3.4}$$

where n_{obj} is the number of objects to observe, and $(o_k(\mathbf{u}))_{k\in[1,n_{obj}]}$ their luminous distributions.

A few examples are shown in Fig. 3.1.2: the HST (diameter of 2.4 m), the JWST (diameter of 6.5 m), one of the VLT units (diameter of 8 m), and a LUVOIR-like configuration (here diameter of 15 m). On the first line, the pupil of each telescope is shown and on the second line the corresponding perfect normalized Point Spread Functions (PSFs).

3.1.1.2 Description of the optical system

We already set that the optical system can be described thanks to its IRF $h(\mathbf{u})$. The Fourier transform of this IRF is called the Optical Transfer Function (OTF), it also corresponds to

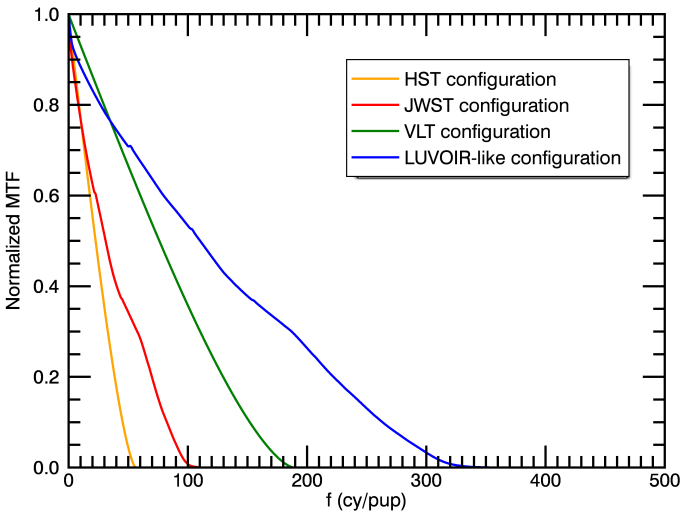

Figure 3.1.3: Normalized MTFs of the four configurations of Fig. 3.1.2.

the autocorrelation of the pupil:

$$\begin{aligned} OTF(\nu) &= \widehat{h}(\nu) \\ &= P \otimes P(\nu) \end{aligned} \tag{3.5}$$

The Modulation Transfer Function (MTF) and the Phase Transfer Function (PTF) respectively correspond to the modulus and the phase of the OTF. The MTF in particular shows that an optical system typically behaves like a low-pass filter with a cutoff frequency ν_c depending on the wavelength and the diameter of the telescope pupil. It provides also a good understanding of an optical system.

$$OTF(\nu) = MTF(\nu)e^{iPTF(\nu)} \tag{3.6}$$

Fig. 3.1.2 indicates the MTF corresponding to the different telescope (HST, JWST, VLT, and LUVOIR-like configurations). Their radial averages are also plotted in Fig. 3.1.3, they provide the theoretical limits of the telescopes. The larger the telescope is, the higher the cutoff frequency is, and the better the resolution of the telescope is.

3.1.1.3 Case of a circular monolithic telescope

We consider here an instrument with a monolithic, circular pupil. We observe a point-like object located far enough to be considered at infinity. The imaging system is aberration-free.

The IRF in this situation is the well-known Airy disk, expressed with a Bessel function

Telescope	Pupil diameter (m)	Angular resolution (")
HST	2.4	0.058
JWST	6.5	0.021
VLT	8	0.017
ELT	40	0.0035

Table 3.1.1: Illustration with a few examples of the correlation between pupil diameter and angular resolution.

of order one:

$$\left\|\widehat{P}(\mathbf{u})\right\|^2 = I_0 \left(2\frac{J_1(u)}{u}\right)^2 \tag{3.7}$$

where u is the modulus of $\mathbf{u}$. This Airy pattern has a typical Full Width at Half Maximum (FWHM) of λ/D, where D is the diameter of the telescope. This value also corresponds to the limit of resolution of the instrument: the system cannot resolve details closer than λ/D. Therefore, it is also related to the cutoff frequency of the MTF, in m^{-1}:

$$\nu_c = \frac{1}{f'}\frac{D}{\lambda} \tag{3.8}$$

where f' is the focal length of the optical system.

We can also conclude that for a diffraction-limited system the larger the diameter D of the pupil is, the finer the details the system can resolve are. For instance, for a wavelength of 550 nm, the pupil diameters and angular resolutions of the HST, JWST, VLT, and the ELT are indicated in the table 3.1.1. Even if the angular resolutions shown here are theoretical (in particular, ground-based telescopes are affected by turbulence), a strong correlation can be observed between pupil diameter and angular separation of these telescopes.

Fig. 3.1.4 constitutes an illustration of the resolving power of a telescope. Below a certain angular separation threshold ($1\lambda/D$), the telescope cannot resolve two separate objects.

3.1.2 Aberrations

As quickly seen in section 3.1.1.2, the effect of optical aberrations is to spread the light from its diffraction shape. They deteriorate the quality of the image, and decrease the resolving ability of the telescope.

3.1.2.1 Origin of aberrations

The real wavefront is different from the ideal one, which is flat: a local absorption of the electromagnetic field amplitude generates a so-called amplitude aberration, while a local delay or advance of the electromagnetic wavefront generates a phase aberration.

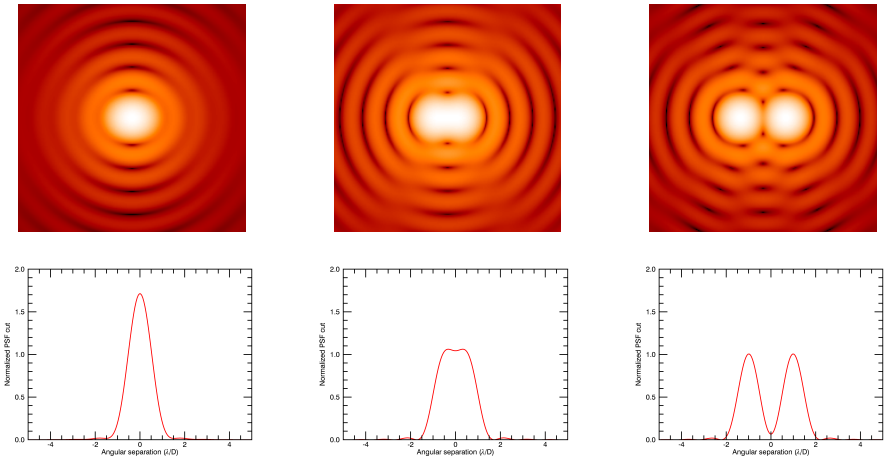

(a) (b) (c)

Figure 3.1.4: Observation of a binary object composed of two sources with an angular separation of (a) $0.5\lambda/D$, (b) $1\lambda/D$, and (c) $2\lambda/D$, $1\lambda/D$ being the limit to distinguish two objects.

The amplitude aberrations can typically be due to a local decrease or cancellation of the reflection coefficient (for catoptric systems) or transmission coefficient (for dioptric systems). This can be generated by small masking, dust on the optical components' surfaces, or local imperfections of surface treatment or finishing. In our case, we will note the amplitude aberrations $e^{\alpha(\mathbf{r})}$.

The phase aberrations typically depend on the position of the object, the position of the pupil, the geometry of the system, and the quality of the opto-mechanical design ans set up. Typically, in a telescope, it can be due to misalignments and manufacturing (polishing) errors.

The phase aberrations are noted $\phi(\mathbf{r})$, defined as:

$$\phi(\mathbf{r}) = \frac{2\pi\delta(\mathbf{r})}{\lambda} \tag{3.9}$$

where $\delta(\mathbf{r})$ is the optical path difference in nanometers between the real wavefront and the ideal flat wavefront. If, in certain cases, it can be chromatic, we will consider it achromatic in the following scetions.

3.1.2.2 Zernike polynomials' basis

Any phase aberration can be projected on a common basis. Different bases exists nowadays, however the most common one is the Zernike polynomials' basis. It is an orthonormal basis, specific to phase aberrations defined on circular pupils. A real surface phase ϕ (such as the real wavefront or the mirror surface) is expressed as a linear combination of the different

n	m	Expression	Name	Notation
0	0	1	piston	Z_0^0
1	-1	$2\rho\cos(\varphi)$	tip	Z_1^{-1}
	1	$2\rho\sin(\varphi)$	tilt	Z_1^1
2	0	$\sqrt{3}(2\rho^2-1)$	defocus	Z_2^0
	-2	$\sqrt{6}\rho^2\cos(2\varphi)$	45°-astigmatism	Z_2^{-2}
	2	$\sqrt{6}\rho^2\sin(2\varphi)$	0°-astigmatism	Z_2^2
3	-1	$\sqrt{8}(3\rho^3-2\rho)\cos(\varphi)$	coma Y	Z_3^{-1}
	1	$\sqrt{8}(3\rho^3-2\rho)\sin(\varphi)$	coma X	Z_3^1
4	0	$\sqrt{5}(6\rho^4-6\rho^2+1)$	spherical aberration	Z_4^0

Table 3.1.2: Some Zernike polynomials. In these expressions, $\rho = \frac{2\|\mathbf{r}\|}{D}$ and $\varphi = \arg(\mathbf{r})$.

Zernike polynomials:

$$\phi(\mathbf{r}) = \sum_{n=0}^{+\infty} \sum_{m=-n,\text{step}=2}^{n} a_n^m Z_n^m(\mathbf{r}) \tag{3.10}$$

where (a_n^m) are the Zernike coefficients and (Z_n^m) the Zernike polynomials [Born and Wolf (1999)]. These polynomials are defined on table 3.1.2 and illustrated in Fig. 3.1.5. We can notice in particular that the higher n is, the higher the spatial frequency of the Zernike is.

3.1.2.3 Expression of the aberrations and impact on the image

The electric field can be expressed as a function of the amplitude and phase aberrations:

$$E_0(\mathbf{r}) = E_0^0 P(\mathbf{r}) e^{\alpha(\mathbf{r})+i\phi(\mathbf{r})} \tag{3.11}$$

where E_0^0 is the amplitude of the electric field.

For small aberrations ($\|\alpha(\mathbf{r}) + i\phi(\mathbf{r})\| \ll 2\pi$), we can use a Taylor expansion:

$$E_0(\mathbf{r}) = E_0^0(P(\mathbf{r}) + \alpha(\mathbf{r}) + i\phi(\mathbf{r})) \tag{3.12}$$

We also consider here that the supports of the amplitude and phase aberrations are the pupil, which means that $\alpha = P\alpha$ and $\phi = P\phi$.

Therefore we obtain:

$$o = E_0^{0^2}\left(\left\|\widehat{P}(\mathbf{u}) + \widehat{\alpha}(\mathbf{u}) + i\widehat{\phi}(\mathbf{u})\right\|^2\right) \tag{3.13}$$

Eq. 3.3 then becomes:

$$I(\mathbf{u}) = E_0^{0^2} h * \left(\left\|\widehat{P}(\mathbf{u})\right\|^2 + 2\Re\{\widehat{P}(\mathbf{u})(\widehat{\alpha}^*(\mathbf{u}) + i\widehat{\phi}^*(\mathbf{u}))\} + \left\|\widehat{\alpha}(\mathbf{u}) + i\widehat{\phi}(\mathbf{u})\right\|^2\right) \tag{3.14}$$

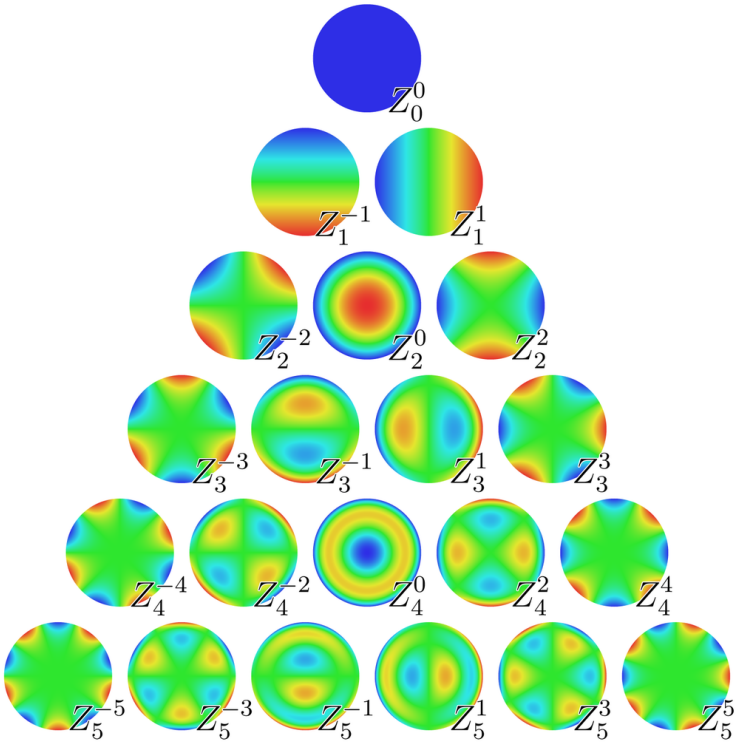

Figure 3.1.5: First Zernike polynomials. Credit to https://en.wikipedia.org/wiki/Zernike_polynomials.

$E_0^{0^2} h * \left\|\widehat{P}(\mathbf{u})\right\|^2$ corresponds here to the aberration-free image, while $h * \left\|\widehat{\alpha}(\mathbf{u}) + i\widehat{\phi}(\mathbf{u})\right\|^2$ is the main responsible for a field of speckles, all having the same diameter λ/D than the central image.

Without aberration, we would have $E_0 = E_0^0 P = o$ and the image would be $I = E_0^{0^2} \left\|\widehat{P}(\mathbf{u})\right\|^2 * h$. Therefore, Eq. 3.14 can also be seen as:

$$I(\mathbf{u}) = o * h'(\mathbf{u}) \tag{3.15}$$

where $h' = \left\|\widehat{P}\right\|^2 + 2\Re\{\widehat{P}(\widehat{\alpha}^* + i\widehat{\phi}^*)\} + \left\|\widehat{\alpha} + i\widehat{\phi}\right\|^2$. Aberrations impact the IRF of the optical system and decrease the quality of the image (ie. the resolution and/or the contrast).

A good criterion to quantify the quality and resolution of an optical system is the Strehl Ratio (SR). It is a number between 0 and 1 which corresponds to the intensity on axis of the PSF divided by the intensity on axis of the IRF. In a perfect optical system, with no aberration, the PSF is equal to the IRF and the SR is equal to 1. However, in a realistic system, aberrations decrease the maximum value of the PSF and increase the amplitude of the secondary peaks. Therefore, the SR decreases. In general, the SR is between 0 and 1.

$$SR = \frac{PSF(\mathbf{0})}{IRF(\mathbf{0})} \tag{3.16}$$

In the case of phase aberrations only:

$$SR \approx \left\|\langle e^{\frac{i2\pi\delta}{\lambda}} \rangle_{P_E}\right\|^2 \tag{3.17}$$

where $\langle f \rangle_{P_E}$ is the mean value of the function f over the exit pupil P_E and $\delta = \lambda\frac{\phi}{2\pi}$ is the difference between the real wavefront and the ideal wavefront (flat). For small aberrations, the SR can be approximated with:

$$SR \approx e^{-(\frac{2\pi\sigma}{\lambda})^2} \tag{3.18}$$

where σ is the standard deviation of the wavefront, in nanometers. Fig. 3.1.6 illustrates the effect of the SR on the shape of the image: the first PSF has a SR of 100% (perfect PSF), the second one a SR of 90%, and the third one a SR of 45%. In high-contrast imaging, any deterioration of contrast or resolution affect the observations, so the comprehension and control of the aberrations are critical.

André Maréchal established a criterion to evaluate the quality of an optical system. According to the so-called Maréchal criterion, the rms optical path difference σ has to remain below $\lambda/14$, which provides a SR over 82%.

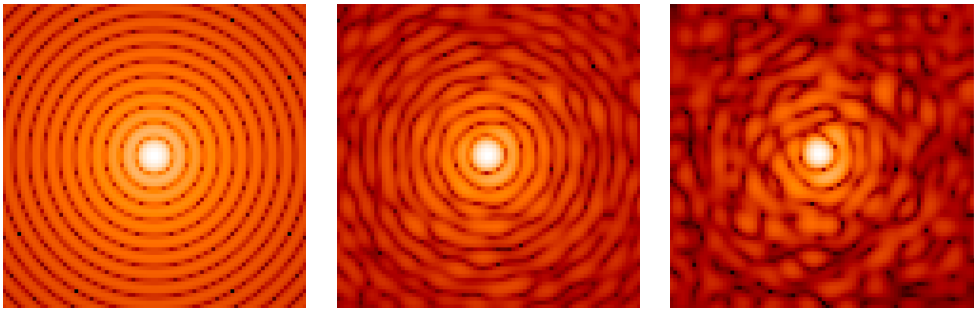

(a) (b) (c)

Figure 3.1.6: Examples of PSFs with different SRs: (a) $SR = 100\%$, (b) $SR = 90\%$, and (c) $SR = 45\%$.

3.1.3 Impact of pupil segmentation on the image

3.1.3.1 Benefits of segmentation

Ground- and space-based astronomy saw the emergence of segmented aperture telescopes, also called Multiple-Aperture Optical Telescopes (MAOTs). These telescopes are made of several subapertures whose combination enables to reach the diffraction limit of a monolithic telescope covering all the segments.

Some configurations are dedicated to interferometric observations, such as the Center for High Angular Resolution Astronomy (CHARA array) at the Mount Wilson Observatory (USA) composed of six telescopes [ten Brummelaar et al. (2016)] or the VLT Interferometer (VLTI) at Cerro Paranal in the Atacama Desert (Chile). Compared to the next case, in which the objective is to fill the pupil with segments and avoid gaps, this type of segmented apertures requires the sub-pupils to be ideally placed to avoid baseline redundancies which generates many gaps in the pupil plane. In this case, there is one secondary mirror per aperture and the system involves delay lines between the different sub-pupils.

In this thesis we focus on the large segmented telescopes, with non diluted pupils made of segmented mirrors identical in geometric shape (not necessarily in curvature). In opposite to the previous case, the goal is to obtain a direct image of the observation field. Some examples of telescopes are visible in Fig. 3.1.7: the Keck telescope is made of 36 hexagonal segments, the ELT is made of 798 hexagonal segments, the JWST is made of 18 hexagonal segments, and the last example, a possible architecture of the LUVOIR surveyor, is made of 36 hexagonal segments. Some telescopes have non-hexagonal segments, such as the GMT composed of seven circular segments. However, because of photons' loss, the gaps between its segments make this telescope not optimal for high-contrast observations and hexagonal segments remain the most conventional segment design. As a parenthesis, the problem of finding the optimal segment shape to fill a surface with no overlap or gap between the segments is a well-known mathematical problem called tessellation.

Why are segmented pupils becoming more and more common? In section 3.1.1.3 we saw that the resolution of the telescope improves when the diameter of the pupil D in-

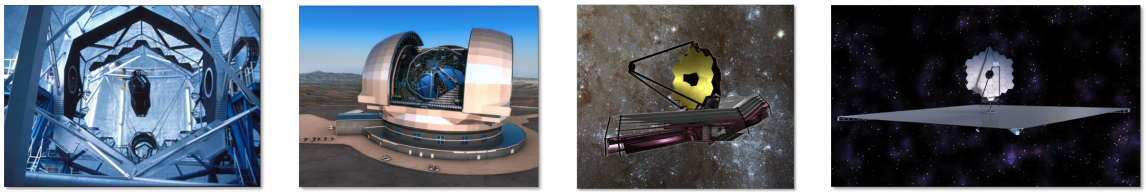

(a) (b) (c) (d)

Figure 3.1.7: Examples of segmented telescopes or missions: (a) one of the twin Keck telescopes composed of 36 hexagonal segments, (b) the future Extremely Large Telescope (ELT) made of 798 hexagonal segments, (c) the James Webb Space Telescope (JWST) with 18 hexagonal segments, and (d) a possible configuration of the Large UV-Optical-InfraRed (LUVOIR) survey, here made of 36 hexagonal segments.

creases. Therefore telescopes tend to be larger. However building primary mirrors of diameters of more than a few meters brings manufacturing and transportation issues, which segmentation enables to avoid. For space telescopes, an additional issue can be solved with segmentation: the telescope needs to fit in a rocket and segmentation enables to fold the primary mirror.

For ground-based astronomy, segmented telescopes can now reach diameters of several dozens of meters. For example, the ELT and the TMT will respectively have a primary mirror of 39.3 meters' and 30 meters' diameter. In space astronomy, the JWST's primary mirror is 6.5 meters, while LUVOIR's could reach 15 meters.

3.1.3.2 Impact of the segmentation on the optical system performance

In this section, we study the impact of a segmented pupil without aberration on the optical system performance, mainly in terms of resolution. This is doable by studying directly the impact of the segmentation on the OTF.

The entrance pupil of our optical system is called P. It is made of n_{seg} identical segments of shape mask S. $\mathbf{r}$ is the position vector in the pupil plane, and $\mathbf{r_k}$ the coordinates of the center of the k-th segment. The pupil is then:

$$\begin{aligned} P(\mathbf{r}) &= \sum_{k=1}^{n_{seg}} S(\mathbf{r} - \mathbf{r_k}) \\ &= \sum_{k=1}^{n_{seg}} S * \delta_{\mathbf{r_k}}, \end{aligned} \tag{3.19}$$

where $\delta_{\mathbf{r_k}}$ is the Dirac delta function centered at the position $\mathbf{r_k}$. The optical transfer func-

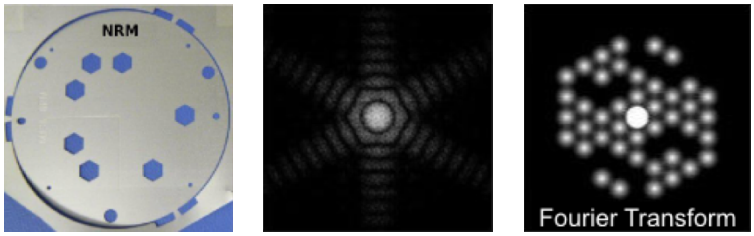

(a) (b) (c)

Figure 3.1.8: (a) The NRM of the instrument NIRISS of the JWST, (b) simulation of an image obtained with this NRM for an on-axis point-like source, and (c) Fourier transform of this image. This figure is adapted from JWST user documentation.

tion corresponds to the autocorrelation of the pupil, therefore:

$$\begin{aligned} OTF(\nu) &= \sum_{k=1}^{n_{seg}} S * \delta_{\mathbf{r_k}} \otimes \sum_{k'=1}^{n_{seg}} S * \delta_{\mathbf{r_{k'}}} \\ &= (S \otimes S) * \sum_{k=1}^{n_{seg}} \sum_{k'=1}^{n_{seg}} \delta_{\mathbf{r_k} - \mathbf{r_{k'}}} \end{aligned} \tag{3.20}$$

This OTF has a central peak (case where $k' = k$ in the double sum) and symmetrical satellite peaks. Each symmetrical pair of satellite peaks corresponds to a baseline. In interferometry, we avoid redundancy in the segmentation, which means each pair of satellite peak is related to a unique pair of segments, while in the non-interferometry case, several pairs of segments can be responsible for the same peaks.

Furthermore, we can recognize in Eq. 3.20 an autocorrelation of the segment. Indeed, each peak will have the same shape (just not the same amplitude): the autocorrelation of the segment, which indicates that the segment creates its own OTF, just decentered to the spatial frequency $\frac{1}{f'}\frac{\mathbf{r_k}-\mathbf{r_{k'}}}{\lambda}$. The sum of the segments' OTFs corresponds to the full pupil's OTF. The further in the pupil the segments, the larger the cutoff frequency of the whole pupil and the resolution of the telescope improves. It is also important that as many baselines as possible are present in the pupil, so the pupil's OTF has no "hole" or spatial frequencies the telescope cannot resolve. The impact of of segmentation on the optical system performance was particularly well studied in Baron et al. (2008).

The instrument NIRISS (Near Infrared Imager and Slitless Spectrograph) of the JWST will propose an Aperture Masking Interferometry (AMI) observing mode. It uses a Non-Redundant Mask (NRM) made of seven holes. Fig. 3.1.8 shows the NRM, an example of detector image (simulation) and the corresponding power-spectrum of this image, in which we can see the pattern of the MTF [Maszkiewicz (2017)].

3.1.3.3 Drawbacks of segmentation

In a segmented mirror or an interferometric assembly, the subpupils are not mechanically tied together and therefore can generate phase aberrations due to phasing errors. In particular, positioning errors and segment vibrations can impact strongly the resulting image. A good control on these errors is crucial to obtain the desired quality.

A segmented primary mirror can for example have edge sensors at each segment to measure their relative alignment and further control piston, tip, and tilt positions. Efficient pupil and focal planes' wavefront sensors have also been developed and are still under development to increase the accuracy of the wavefront estimation, and can be used for segments' phasing (see section 3.3). Some wavefront sensors are even specifically dedicated to segmented mirrors, such as the Estimation of Large Amplitude Subaperture Tip-tilt by Image Correlation (ELASTIC) method [Vievard et al. (2016, 2017)].

The impact of phasing errors on image formation and system performance will be largely discussed in chapter 4.

3.2 Coronagraphy

Imaging faint objects close to a star requires the use of a coronagraph. The goal of this component is to physically cancel as much starlight possible while preserving the faint flux from the surrounding from the star.

The objects to observe can be and originally were the corona of the Sun, and require the use of so-called solar coronagraphs [Lyot (1932)]. The most famous example of satellite using a solar coronagraph is the Solar and Heliospheric Observatory (SOHO), a joint mission of NASA and ESA dedicated to the observation of the solar corona and nearby comets.

However, in this thesis, we focus on stellar coronagraphs, aiming at imaging circumstellar disks or exoplanets around stars. We will quickly describe the general principle of a coronagraph, then its theoretical impact on the image formation, the important parameters in coronagraph's design, and finally the different types of coronagraphs.

It is important to point out here that an alternative to coronagraphy has been developed: the starshade consists in wide occulting mask located ahead of the telescope and that blocks the starlight while allowing the planet light to pass and reach the telescope. This tool is for instance considered for the LUVOIR and HabEx missions and could replace their coronagraphs.

3.2.1 Principle

Coronagraphy has been largely discussed in literature, such as in Wang and Vaughan (1988), Malbet (1996), and Sivaramakrishnan et al. (2001).

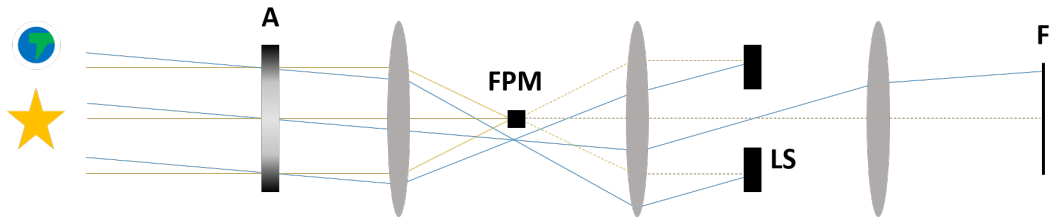

Figure 3.2.1: Generic scheme of a coronagraph. The Apodizer A and the Lyot stop LS are in pupil planes, while the FPM and the detector F are in focal planes. The rays emitted by the star are in yellow and the ones from the planet are in blue.

Except for the interferometric coronagraphs (see section 3.2.4), all coronagraphs have up to three components: an apodizer, a Focal Plane Mask (FPM), and a Lyot stop. A scheme of a typical coronagraph is presented Fig. 3.2.1.

The objects are considered at infinity. Their wavefronts go through a first component, the apodizer (A) located in a pupil plane. This apodizer aims at shaping the star wavefront so its image on the next focal plane fits the optical mask with mitigation of the diffraction effect. After the apodizer the incoherent beams from the star and from the planet converge into the focal plane, which contains this small on-axis mask (FPM in the figure) blocking most of the photons from the star. However, this mask generates diffraction effects, that are mostly blocked by the Lyot stop (LS in the figure), set in the next pupil plane. The off-axis object to observe, disk or planet, is not blocked by the FPM. The Lyot stop just affects its wavefront by limiting its diameter. Finally, the residual photons from the star and the wavefront from the object to observe reach the detector, located in the final focal plane (named F in the figure).

All three components are not mandatory in coronagraphy as we will see in section 3.2.4. However, the apodizer-FPM-Lyot stop triplet is at the basis of the coronagraphic image formalism presented in section 3.2.2.

3.2.2 Coronagraphic image formalism

All these coronagraphs aim at decreasing the intensity of the star image while preserving as much as possible the image of the off-axis object. The effect of the optical system for the on-axis object is different than the one for the off-axis object. In this section, we study the impact of the coronagraph on on- and off-axis objects. We will separate two cases: the ideal or perfect coronagraph and a realistic coronagraph.

3.2.2.1 Perfect coronagraph

The expression of the intensity has been introduced in Eq. 3.3. However, in the hypothesis of a perfect coronagraph, the amplitude of the on-axis electric field generated by the star is removed [Malbet et al. (1995), Quirrenbach (2005), Cavarroc et al. (2006), and Sauvage

et al. (2010)]. This is equivalent to considering a new electric field E':

$$E'(\mathbf{r}) = E(\mathbf{r}) - E_0^0 P(\mathbf{r}) \tag{3.21}$$

In absence of aberrations $E = E_0^0 P$ so E' is null and the intensity in the detector plane is null. Therefore, the goal of a perfect coronagraph is to totally cancel the image of the star in absence of aberrations in the whole focal plane. Through this equation, the coronograph can also be seen as following : this device generates a flat wave in opposition to the incoming wave, leading to destructive interferences in the following of the optical system.

In presence of aberrations and with linearization approximation, Eq. 3.12 becomes:

$$E'(\mathbf{r}) = E_0^0(\alpha(\mathbf{r}) + i\phi(\mathbf{r})) \tag{3.22}$$

Then Eq. 3.3 provides:

$$I(\mathbf{u}) = {E_0^0}^2 h * \left\| (\widehat{\alpha} + i\widehat{\phi})(\mathbf{u}) \right\|^2 \tag{3.23}$$

We can observe that the PSF of a perfect coronagraph corresponds to the spectrum of the aberrations convoluted with the direct PSF without coronagraph. Without aberrations, the intensity of the focal plane would be null, and speckles (and so the deterioration of contrast) are direct consequences from these aberrations.

3.2.2.2 Real coronagraph

In a realistic coronagraph, the image of the pupil cannot be removed, ie. $E_0^0 P(\mathbf{r})$ cannot be suppressed from $E(\mathbf{r})$ in Eq. 3.21.

We consider here a general case of a coronagraph made of an apodizer, a focal plane mask, and a Lyot stop. These components can be amplitude or phase mask, and their respective mask functions M_A, M_{FPM}, and M_{LS} can be complex. If the considered coronagraph does not have one of these components, then the corresponding mask function is considered fully transmissive, so equal to 1 in the entire plane.

$E(\mathbf{r})$ being the electric field issued by the on-axis component of the object in the pupil plane as defined in Eq. 3.1, the electric field E_A in the first pupil plane, right behind the apodizer is:

$$E_A(\mathbf{r}) = M_A(\mathbf{r}) E(\mathbf{r}) \tag{3.24}$$

The electric field E_{FPM} in the focal plane right after the FPM is:

$$E_{FPM}(\mathbf{u}) = M_{FPM}(\mathbf{u}) \widehat{M_A E}(\mathbf{u}) \tag{3.25}$$

If the object is on axis, the mask M_{FPM} will impact its transmission. For an off-axis object, the mask has little to no effect and the light is fully transmitted.

The electric field E_{LS} in the next pupil plane right after the Lyot stop is:

$$E_{LS}(\mathbf{r}) = M_{LS}\overset{\vee}{M_{FPM}}\overset{\wedge}{M_A E}(\mathbf{r}), \tag{3.26}$$

where $\overset{\vee}{f}$ is the inverse Fourier transform of the function f. Eventually, the electric field E_f in the final plane (detector plane) is the Fourier transform of E_{LS}. All these steps corresponding to a multiplication by a mask, to a Fourier transform or to an inverse Fourier transform, they are all linear and therefore the global coronagraph function, providing E_f as a function of E is linear. Later in this document, this linear coronagraph function will be expressed as $\mathcal{C}$:

$$\begin{aligned} E_f(\mathbf{u}) &= \mathcal{C}(E(\mathbf{r})) \\ &= M_{LS}\overset{\vee}{M_{FPM}}\overset{\wedge}{M_A E}(\mathbf{u}) \end{aligned} \tag{3.27}$$

When a star and an incoherent off-axis object are observed, the intensity on the detector is:

$$I(\mathbf{r}) = I^{\star}(\mathbf{r}) + I^{\circ}(\mathbf{r}), \tag{3.28}$$

where $I^{\star}$ and I° are the intensities generated by respectively the star and the off-axis object, ie. $\left\|E_f^{\star}\right\|^2$ and $\left\|E_f^{\circ}\right\|^2$, where $E_f^{\star}$ and E_f° are the electric fields respectively of the star and of the off-axis object on the detector plane. The objective of the coronagraph is to minimize $I^{\star}$ in order to decrease the ratio $\max(I^{\star})/\max(I^{\circ})$ and detect the off-axis object.

This final equation is far from Eq. 3.4. This impact was modeled with the IRF, that was linear and therefore impacting similarly all objects. In the coronagraphic case, there is no IRF to represent the response of the system to an object, since on- and off-axis objects react differently to the optical system.

3.2.3 Important parameters in coronagraphy

Mazoyer et al. (2018b) proposes precise definitions of the different parameters used in coronagraphy, this section provides a few definitions.

A coronagraph is dedicated to a type of off-axis objects. The objects to observe provide constraints on the design in terms of maximal target contrast, range of angular separations, and bandwidth.

The contrast of an image can be a 2D array, a 1D vector or a single value. In this thesis, it is defined as follow:

$$\begin{cases} C(\mathbf{u}) = \frac{\max(I^{\star})}{I(\mathbf{u})} & \text{for a 2D-array contrast} \\ C(u) = \frac{\max(I^{\star})}{\langle I(ue^{i\theta})\rangle_{\theta}} & \text{for the radial mean contrast} \\ C = \frac{\max(I^{\star})}{\langle I(\mathbf{u})\rangle_{\mathbf{u}}} & \text{for the mean contrast over a certain region of the focal plane} \end{cases} \tag{3.29}$$

The contrast is affected by aberrations and segmentation. To detect an off-axis object, its normalized intensity $\max(I^\star)/\max(I^\circ)$ has to remain over the contrast. Therefore we define the maximal target contrast, ie. the ratio $\max(I^\star)/\max(I^\circ)$ for the faintest objects we want to observe. In a certain region of the final focal plane, called the Dark Hole (DH), the coronograph is designed to optimize the contrast, ie. the ratio between the residual star intensity at a certain position of the focal plane and the maximum of the star image without FPM in the optical train, so it remains lower than this maximal target contrast. In general, we look at the value of the contrast at each position of the DH, or its radial curves, or its average value in the DH. This notion is crucial when it comes to coronagraph's design.

The Inner Working Angle (IWA) corresponds to the smallest angular separation at which the contrast is achieved. It therefore defines the inner border of the DH. Similarly, an Outer Working Angle (OWA) can be defined.

The bandwidth corresponds to the wavelength range at which the coronagraph achieved the needed contrast. It should obviously be optimized to fit the type of source to observe.

Since the off-axis object can be very faint, each photon matters. Therefore, as many photons collected by the telescope as possible should pass the coronagraph. Because of the different masks, a portion of these photons is lost. To quantify this loss, the coronagraph designer can look at the throughput: at a certain angular separation, it corresponds to the ratio between the number of photons that reaches the core of the object PSF on the detector and the number of photons entering the telescope. It is also an important parameter in coronagraph's design.

Furthermore, in general a coronagraph's design is optimized for an entrance pupil electric field $E^\star$ without aberrations. However, conditions so perfect that no aberration deteriorate the contrast do not exist. It is then important to also study the sensitivity of the coronagraph to aberrations. Some recent designs are even optimized to be resistant to some aberrations, for example for low-order aberrations in N'Diaye et al. (2015).

3.2.4 Types of coronagraphs

All coronagraphs presented here except for interferometric coronagraphs are classified in Fig. 3.2.2.

3.2.4.1 Focal plane amplitude mask coronagraphs

The coronagraph principle was invented in 1931 by the astronomer Bernard Lyot [Lyot (1939)]. The main objective being to remove the starlight, the star is imaged in a focal plane where there is an opaque mask. Therefore, the light from the on-axis object (the star) is blocked, while off-axis objects or not blocked and can be reimaged on the detector, located in a second focal plane. However, a lot of starlight is diffracted by the FPM, and reimaged on the detector, decreasing the optimal efficiency of the coronagraph. Bernard Lyot added a second mask, the Lyot stop, in the pupil plane following the FPM, blocking

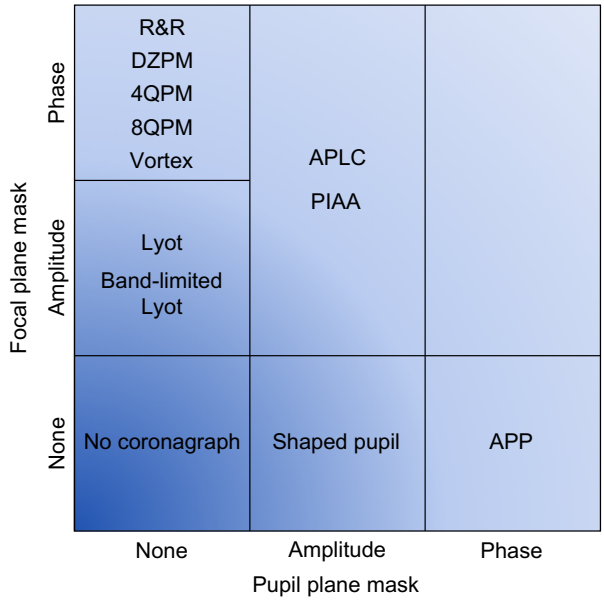

Figure 3.2.2: Classification of coronagraphs, except for the interferometric ones (see section 3.2.4.5).

the diffracted light. This FPM + Lyot stop doublet is at the origin of coronagraphy and is named, after its inventor, the Lyot coronagraph.

However, its shape is not optimal and allows too much light to pass the Lyot stop without being blocked. The band-limited Lyot coronagraph enables a better control of the diffracted light by optimizing the transmission of the FPM [Kuchner and Traub (2002)].

Lyot and band-limited Lyot coronagraphs have been installed on different ground-based telescopes, such as the Gemini telescope, the Keck telescope, the Subaru telescope, the Palomar telescope, and the VLT.

For space telescopes, the Near Infrared Camera and Multi-Object Spectrometer (NICMOS) of the HST has a Lyot coronagraph. The future NASA space telescope, the JWST will have two instruments able to perform coronagraphy: the Near Infrared Camera (NIRCam) has five Lyot-type coronagraphs (3 circular FPMs, 2 bars) [Krist et al. (2010) and Mao et al. (2011)], and the Mid-Infrared Instrument (MIRI) has one Lyot coronagraph in addition to three four-quadrant phase mask coronagraphs (4QPMs, see later) [Boccaletti et al. (2015)]. The components of the Lyot coronagraphs on NIRCam and MIRI are indicated in Fig. 3.2.3 and 3.2.4.

3.2.4.2 Focal plane phase mask coronagraphs

In a phase-mask coronagraph, the opaque disk of the FPM is replaced by a transparent FPM that shifts the phase of the on-axis light to generate destructive interferences. Different configurations of phase dephasing exist (see Fig. 3.2.5).

(a) (b) (c) (d) (e) (f)

Figure 3.2.3: Schemes and picture of the FPMs used on JWST. (a) MASK210R, used on NIRCam, (b) MASK335R, used on NIRCam, (c) MASK430R, used on NIRCam, (d) MASKSWB, used on NIRCam, (e) MASKLWB, used on NIRCam, (f) FPM used on MIRI. Adapted from Krist et al. (2010) and JWST User Documentation.

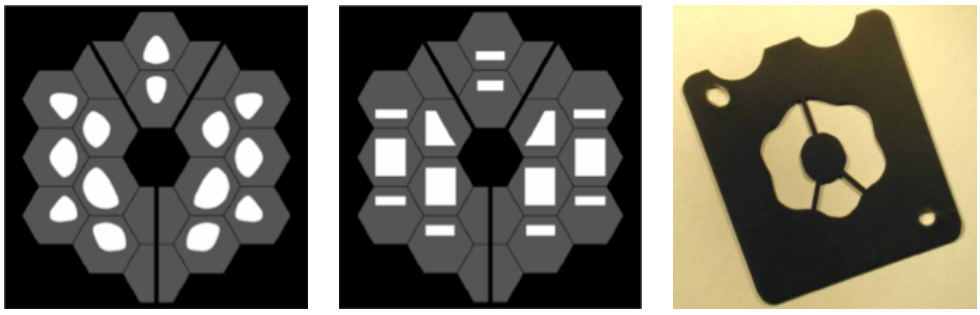

(a) (b) (c)

Figure 3.2.4: Schemes and picture of the Lyot stops used on JWST. (a) Lyot stop used on NIRCam with circular FPMs, (b) Lyot stop used on NIRCam with bar FPMs, (c) Lyot stop used on MIRI for the Lyot coronagraph. Adapted from Mao et al. (2011) and Boccaletti et al. (2015).

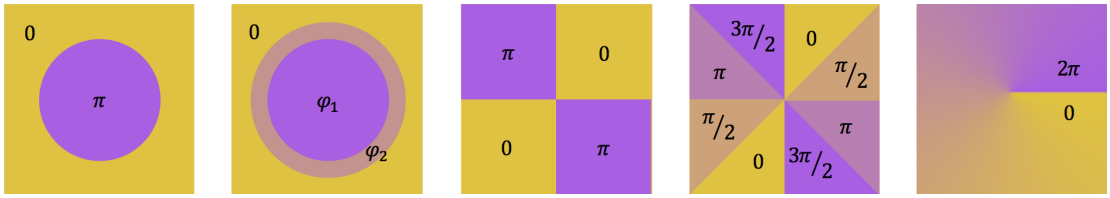

Figure 3.2.5: Scheme of some phase FPMs. (a) R&R phase mask, (b) DZPM, an extension of the R&R FPM optimized for broadband light, (c) 4QPM, (d) 8OPM, and (e) optical vortex mask.

The Roddier & Roddier (R&R) [Roddier and Roddier (1997)] phase mask has a π-phase shift at the center of the star PSF core, made of a thickness difference of the transmissive mask. Both the size of the central ϕ-phasing disk and the depth difference between the ϕ-phasing and 0-phasing areas depend on the wavelength, which makes this coronagraph very chromatic.

The Dual Zone Phase Mask (DZPM) [Soummer et al. (2003b)] is a more achromatic version of the R&R mask. A ring around the central phasing core introduces a different phase in the wavefront and enables the access to another parameter when optimizing the radii of the core and of the ring to null the on-axis image at broadband light.

Still to make the coronagraph less monochromatic, the 4QPM coronagraph [Rouan et al. (2000)] uses an FPM made of four quadrants: two of them do not shift the phase of the light, while the two others introduce a π-phase shift in the wavefront. The instrument MIRI of the JWST uses three 4QPM coronagraphs, and the VLT and the Large Binocular Telescope (LBT) can also perform coronagraphic imaging with a 4QPM coronagraph.

Other combinations of phase shifting areas can be found, such as in the eight-Octant Phase Mask (8OPM) coronagraph [Murakami et al. (2008)]. This coronagraph enables softer dephasings of the wavefront, since two neighbor areas introduce a phase delay of $\pi/2$ instead of π.

The most complex case of phase FPM is the optical vortex coronagraph [Mawet et al. (2010b)]. In this configuration, the FPM induces a phase shift that varies azimuthally around the center. It is used at the 200-inch Hale telescope at the Palomar observatory, at the VLT, and at the LBT [Mawet et al. (2010a)].

3.2.4.3 Pupil plane amplitude mask coronagraphs

All coronagraphs mentioned earlier are made of two components: the FPM in an intermediate focal plane and the Lyot stop in the next pupil plane. A third component can be added: the apodizer, located in the pupil plane before the focal plane. This component aims at reshaping the wavefront before it reaches the FPM, to increase its efficiency.

The Prolate Apodized Lyot Coronagraph (PALC) uses such amplitude apodizers based on prolate functions and provides a consequent improvement of the extinction of the on-axis

star, in monochromatic light. In Aime et al. (2002) and Soummer et al. (2003a), prolate apodizations are combined with R&R coronagraphs.

More recently new apodizations, far from the prolate functions, have been studied and provide extremely good results, turning the PALC into the more general Apodized Pupil Lyot Coronagraph (APLC). It was also adapted to the case of arbitrary apertures, in particular for segmented telescopes [Soummer (2005), Martinez et al. (2010), and Soummer et al. (2011)]. They have been validated on sky on GPI (Gemini South observatory) [Macintosh et al. (2014, 2015)] and SPHERE (VLT).

The main problem of such an apodization is that by cutting off a portion of the starlight, it also blocks part of the photons coming from the possible planet or disk. The ratio of light that is not blocked by the apodizer, ie. the throughput, is then a key criterion in apodizer design. The apodization, since it mainly blocks photons at the edges of the pupil, also impacts the apparent pupil, and therefore the IWA, keeping it at best around 3 or $4\lambda/D$.

To avoid these effects, techniques of pupil remapping were developed: the Phase-Induced Amplitude Apodization (PIAA) [Guyon (2003), Traub and Vanderbei (2003), and Galicher et al. (2005)] allows to perform a beam apodization with no or few light loss, to distribute the brightness less uniformly: ideally, the center of the pupil has to concentrate more light than the edges. It is obtained using two aspheric mirrors: the first one modified the distribution of the light, while the second one correct for the phase aberrations of the wavefront, to maintain it flat. A first version of the PIAA did not require any FPM, and the second mirror was correcting for the on-axis wavefront, however the off-axis object image was impacted by a lot of coma [Guyon et al. (2005) and Vanderbei and Traub (2005)]. The PIAA was then combined with an FPM to remove the starlight and the second aspheric mirror then corrected for the off-axis object wavefront [Guyon et al. (2006)]. The PIAA provides a throughput of almost 100% and the IWA can be smaller than $2\lambda/D$. It is also the coronagraph mainly used on SCExAO (Subaru telescope), designed to provide a 10^6 contrast at 1.5 λ/D and was more recently extended to the cases of arbitrary apertures [Guyon et al. (2014)].

Like the first versions of the PIAA coronagraph, the shaped pupil does not require an FPM + Lyot stop doublet [Kasdin et al. (2003) and Kasdin et al. (2005)]. A shaped pupil is similar to an amplitude transmission apodizer, like in the APLC. Some future space missions should have shaped pupils, such as the Shaped Pupil Coronagraph (SPC) on WFIRST [Cady et al. (2017)] and the SPace Infrared telescope for Cosmology and Astrophysics (SPICA) Coronagraphic Instrument (SCI), a joint proposition from the Japanese space agency JAXA and ESA for the M5 mission of ESA [Enya et al. (2011)].

3.2.4.4 Pupil plane phase mask coronagraphs

There exist less variations of phase apodization coronagraphs. The most famous one is the Apodized Phase Plate (APP), that clears out some diffraction rings and decreases the flux in the core of the star image, on one side of the detector. An APP was installed on the Multiple Mirror Telescope (MMT) [Codona et al. (2006) and Kenworthy et al. (2007)] and on the

instrument NAOS-CONICA (NACO, VLT) [Kenworthy et al. (2010b) and Kenworthy et al. (2010a)]. A less chromatic version, the Vector-APP was proposed in Snik et al. (2012). This coronograph is also proposed for the METIS ELT instrument [Wilby et al. (2017)].

3.2.4.5 Interferometric coronagraphs

Far from these configurations, some coronagraphs are only based on destructive interference of the star light, while all off-axis objects can be imaged. Like in the Michelson interferometer, the beam is separated in two arms. One arm is π-dephased before the two arms are combined again. Therefore, all on-axis object is nulled. Because of the absence of FPM, the off-axis object can even be imaged at $1\lambda/D$.

The most common one is called the Achromatic Interfero Coronagraph (AIC) and is described in Baudoz et al. (1998). In this system, the π-phasing is induced by a so-called cat-eye optical component on the focus. The Visible Nulling Coronagraph (VNC) [Lyon et al. (2010)] is based on a similar principle, but with a shear mechanism that allows to π-dephase the star only, while the off-axis object is not affected. Other nullers exist, but we will not describe them in this thesis.

3.3 Wavefront sensing

The wavefront sensor is an opto-electronical device able to measure the wavefront of an electro-magnetic wave. In the fields of AO and high-contrast imaging, where the wavefront aberrations directly translate into residual light in the focal plane, it is a crucial component of the system: the performance achieved depends on how efficiently the WFS measure wavefront quantities to reconstruct the wavefront.

Several techniques of wavefront sensing have been developed. They can be divided into two categories, depending if they use a temporal or spatial division of the wavefront as input.

3.3.1 Spatial separation of the wavefront

For sensors that require a spatial division of the wavefront to reconstruct the aberrations, the beam is divided into two optical paths. One of them goes to the sensor, while the other one goes to the science camera.

Using sensors from this category can present several drawbacks. Because of the division of the wavefront, two cameras are in general required: one for the science path, one as the sensor, which increase the price, volume, weight, and complexity of the system. Reconstructing the aberrations from a different wavefront than the one reaching the science camera also is also the source of a differential error, since the two optical paths do not have exactly the same aberrations. This differential error is usually called the Non Common Path

Aberrations (NCPA) and can be a strong limitation in high-contrast imaging, where the performance is so hard to achieve that the sensor is a strong critical element. Furthermore, in most cases the sensor is not compatible with the coronagraph, so the division of the wavefront is done upstream: the wavefront can then be well corrected up to the coronagraph, which increases the efficiency of the coronagraph, but the sensor remains blind to the aberrations after the coronagraph, which are not corrected. Also, in some cases, the light is spectrally divided, which means the beam of the two paths have different wavelengths. The reconstruction of the aberrations is then done at a different wavelength than the one observed with the science camera, which can generate chromatic errors between the reconstruction and the science image, specially when the system shows chromatic aberrations. In this case, we will then privilege achromatic sensors, efficient on large spectral bandwidth such as the Shack-Hartmann, to the detriment of sensors working only on narrow spectral bandwidth like the Zernike sensor for Extremely Low-level Differential Aberrations (ZELDA).

As a result, most of these sensors are typically adapted to ground-based instruments: the performance to achieve is in general less challenging than in high-contrast imaging systems and the whole system has other strong limitations to the performance.

In this section, we introduce a few wavefront sensors that require a spatial division of the wavefront. Some were well studied in Rousset (1999). Other techniques exist, such as the Zernike phase contrast wavefront sensor [Zernike (1934) and Bloemhof and Wallace (2003)] or the curvature sensor [Roddier (1988)], but we choose to not present them in this thesis, even if they remain very interesting.

3.3.1.1 Shack-Hartmann

The Shack-Hartmann wavefront sensor was developed by Shack and Platt (1971). It is composed of a matrix of micro-lenses that discretizes the entire pupil. Each of the micro-lenses images a short area of the pupil on the detector. For each of them, the difference in position between this PSF and the one well-aligned on the optical axis of the micro-lens provides the local slope of the wavefront. By combining all the discrete slopes, we can reconstruct the global aberrations on the pupil.

This sensor is probably the most common one, its main advantage being the easiness to set it up and its achromaticity, enabling to work at large bandwidths. It is for instance used on the adaptive-optics corrector ALTtitude conjugate Adaptive optics for the InfraRed (ALTAIR) at the Gemini North observatory, at the Magellan telescopes [Schechter et al. (2003)], at the VLT [Guisard et al. (2000)], or at the Palomar Adaptive Optics (PALAO) system on Palomar observatory [Troy et al. (2000)].

3.3.1.2 Zernike sensor for Extremely Low-level Differential Aberrations

The ZELDA sensor aims at reconstructing low aberrations [N'Diaye et al. (2013b)]. It requires a phase mask in the focal plane with a $\pi/2$ dephasing. The beam going through the

mask interferes with the light diffracted by the mask and provides an intensity proportional to the aberrations on the detector.

This sensor has been tested on the Marseille Imaging Testbed for HIgh Contrast (MITHIC) at the Laboratoire d´Astrophysique de Marseille (LAM) [N'Diaye et al. (2014)] and is currently routinely used on the instrument SPHERE of the VLT [N'Diaye et al. (2016)] for the calibration of quasi-static aberrations. It has also been proven efficient for reconstruction of phasing errors, in the context of the ELT [Janin-Potiron et al. (2017)].

3.3.1.3 Pyramid wavefront sensor

The pyramid wavefront sensors (PWFSs) were developed in Ragazzoni (1996) and Ragazzoni and Farinato (1999): at the focal plane, the light converges to the summit of an oscillating pyramidic optical component. The intensity of the pupil is projected to different areas of the detector, located in the next pupil plane. From these different pupil images, we can derive the aberrations. In general, PWFSs provide good improvements in terms of Signal-to-Noise Ratio (SNR) of the estimation compared to other pupil plane sensors such as the Shack-Hartmann.

The first PWFSs were made of 4 faces. In further developments, we can find 3-, 6-, and 8-face pyramids [Akondi et al. (2014)], and more extreme cases such as the infinite-faces' pyramid or cone wavefront sensors [Vohnsen et al. (2011)]. Fauvarque et al. (2015, 2017) also proposed an even more extreme variation of the PWFS with the flattened pyramid.

PWFSs have been implemented and validated on sky at the LBT [Esposito et al. (2012)], the Magellan telescope [Close et al. (2012)], and the Subaru telescope [Jovanovic et al. (2014)].

3.3.1.4 Mach-Zehnder Pupil Plane Interferometer

The Mach-Zehnder Pupil Plane Interferometer has been developed by Angel (1994).

The beam coming from the star is splitted into two identical beams, named A and B, with a beam splitter. Beam A is filtered using a small aperture mask at a focal plane, only very low aberrations remain. This beam is used as the reference "flat" wavefront. Beam B is reflected by a piezo-driven mirror which shifts it from several fractions of wavelength. The two beams are recombined and create interference fringes on two detectors, that vary with the piston applied on the piezo mirror. From these images, it is possible to reconstruct the aberrations.

Because low-order aberrations remain in the reference beam, it cannot detect them. Finally, it is sensitive to non common aberrations between the two arms of the interferometer.

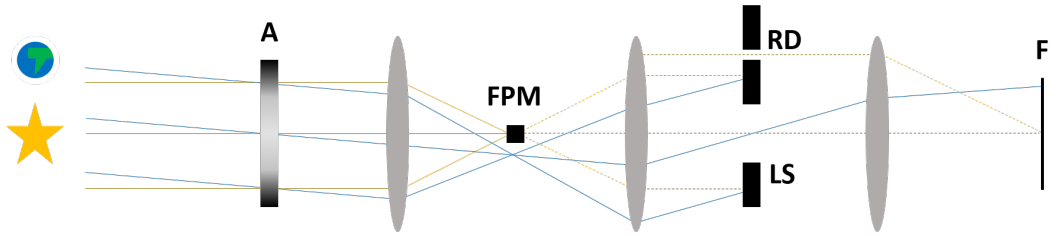

Figure 3.3.1: Scheme of the SCC. The Lyot mask is provided of a second hole, called the Reference Diaphragm (RD). The diffused starlights coming from both the Lyot stop hole and this reference diaphragm interfere in the image plane. The electric field estimation is based on an analysis of the final interference image.

3.3.1.5 The Self-Coherent Camera

The Self-Coherent Camera (SCC) is particular, since it requires a focal plane detector while the previous sensors require pupil plane detectors. It has been developed in Baudoz et al. (2006) and its use as a wavefront sensor has also been explained in Mazoyer et al. (2013).

Fig. 3.3.1 illustrates the set up of the SCC. The Lyot mask is modified so that a second hole is added. This second hole is called the reference diaphragm and is not accessible by the direct light of the planet. However, some of the star light is diffracted by the FPM outside of the pupil and therefore reaches the reference diaphragm.

In the final focal plane, this diffracted starlight interferes with the one that passes the Lyot stop. It generates interference fringes, perpendicular to the axis passing through the centers of both the Lyot stop and the reference diaphragm, with a spatial frequency proportional to $1/d$, where d is the distance between both centers.

For a circular pupil, the Fourier transform of the detector image is composed of a central disk due to the presence of the Lyot stop and two symmetrical disks generated by the presence of the reference diaphragm. Each of these satellites disks contains the information of the electric fields of the star from the Lyot stop and the reference diaphragm. If the diaphragm is smaller enough than the Lyot stop, then we can approximate that the reference diaphragm's star electric field is uniform on the diaphragm, and we can obtain the aberrations.

This technique has been successfully applied on the Très Haute Dynamique (THD) testbed at the Observatoire de Paris-Meudon [Baudoz et al. (2012) and Mazoyer et al. (2014)] and on the Segmented Pupil Experiment for Exoplanet Detection (SPEED) [Martinez et al. (2016)]. It has also been tested on the Palomar observatory [Galicher et al. (2018)], which led to a reduction by a factor of 10 of the speckle intensity,in the presence of a vortex coronagraph.

3.3.2 Temporal division of the wavefront

With sensors that require a temporal division of the wavefront, the science camera is used as detector for the reconstruction. In many cases, at least two images taken successively

are required, at least one of them with a known aberration being introduced on the optical path, which temporarily degrades the image on the detector, not usable for science. These sensors are mainly based on numerical computations rather than extra optical components.

The lack of extra camera and optical path brings a first advantage to this category: the volume and weight of the system is more limited than in the previous category. Furthermore, reconstructing wavefront errors on the same path than the science one removes uncertainty due to NCPA.

However, these methods are in general slower than the previous ones, since at two successive sets of images have to be taken (and processed!). An aberration is in general inserted in the optical path which degrades the science image: it is not possible to have at the same time both the image used for the sensing and the science image. The reconstruction is then never instantaneous or as fast as with spatial division of the wavefront sensors. Furthermore, they are mainly based on numerical computations and optimizations, which generates typical issues such as unstability or prerequisites or approximations on the system (influence matrices, model -often approximated- of the coronagraph, order of magnitude of the aberrations...).

These methods are mainly dedicated to high-contrast instruments, since they are not limited by NCPA. Furthermore, their gain of volume and weight and the simplification of the optical system compared to the spatial division of the wavefront sensors make them optimal for space telescopes. Eventually, the fact that they tend to be slower than the first category of sensors also tend to make them in particular adapted to space telescope, since temporal variations of the wavefront are less usual (no turbulence) and static and quasi static aberrations are the main limitation to the instrument performance. They can also be used on a secondary step for ground-based telescope, after a first AO-correction limiting fast variations of the wavefront.

In this section, we describe a few well-known sensors that require a temporal division of the wavefront, focusing in particular on a method called COronagraphic Focal plane wave-Front Estimation for Exoplanet detection (COFFEE), that I used during my PhD.

3.3.2.1 Pair-wise estimation

The pair-wise estimation method is in huge majority combined with the Electric Field Conjugation (EFC) control procedure (see section 3.4.2.3), therefore the sensing method is sometimes also called EFC.

It was developed by Bordé and Traub (2006) and Give'on et al. (2007, 2011) and improved with a Kalman filter in Groff and Kasdin (2013) and an iterative extended Kalman filter in Riggs et al. (2016b). In this section, we propose the formalism of the classical method.

Eq. 3.11 was defining the electric field in the pupil plane in presence of aberrations as:

$$E(\mathbf{r}) = E_0^0 P(\mathbf{r}) e^{\alpha(\mathbf{r})+i\phi(\mathbf{r})} \tag{3.30}$$

We call ϕ_{DM} the DM phase. It modifies the previous expression to:

$$E(\mathbf{r}) = E_0^0 P(\mathbf{r}) e^{\alpha(\mathbf{r})+i\phi(\mathbf{r})} e^{i\phi_{DM}(\mathbf{r})} \tag{3.31}$$

We consider that the system has a coronagraph. As seen is section 3.2.2.2, it can be modelized with a linear function $\mathcal{C}$ and the electric field in the image plane becomes:

$$E_f(\mathbf{u}) = \mathcal{C}\{E\}(\mathbf{u}) \tag{3.32}$$

The correction phases are considered as small:

$$\begin{aligned} E_f(\mathbf{u}) &= E_0^0 \mathcal{C}\{Pe^{\alpha+i\phi}(1+i\phi_{DM})\}(\mathbf{u}) \\ &= E_0^0 \mathcal{C}\{Pe^{\alpha+i\phi} + iP\phi_{DM}\}(\mathbf{u}) \\ &= E_0^0 \mathcal{C}\{Pe^{\alpha+i\phi}\}(\mathbf{u}) + E_0^0 \mathcal{C}\{iP\phi_{DM}\}(\mathbf{u}) \end{aligned} \tag{3.33}$$

where we successively approximate $e^{i\phi_{DM}}$ as $1 + i\phi_{DM}$ (Taylor extension to order 1) and $e^{\alpha+i\phi} i\phi_{DM}$ as $i\phi_{DM}$ (Taylor extension to order 1 of the product). We call E_f^A the electric field generated by the aberrations only, ie. $E_0^0 \mathcal{C}\{Pe^{\alpha+i\phi}\}$. The intensity on the detector is then:

$$\begin{aligned} I(\mathbf{u}) &= \left\| E_f^A(\mathbf{u}) + E_0^0 \mathcal{C}\{iP\phi_{DM}\}(\mathbf{u}) \right\|^2 \\ &= \left\| E_f^A(\mathbf{u}) \right\|^2 + E_0^{0\,2} \left\| \mathcal{C}\{iP\phi_{DM}\}(\mathbf{u}) \right\|^2 + 2E_0^0 \Re\{iE_f^{A*} \mathcal{C}\{P\phi_{DM}\}(\mathbf{u})\} \end{aligned} \tag{3.34}$$

We consider now two symmetrical DM phases: $+\phi_{DM}$ and $-\phi_{DM}$. The difference between the images I^+ and I^- obtained with the respective DM phases $+\phi_{DM}$ and $-\phi_{DM}$ is:

$$I^+(\mathbf{u}) - I^-(\mathbf{u}) = 4E_0^0 \Re\{iE_f^{A*} \mathcal{C}\{P\phi_{DM}\}(\mathbf{u})\} \tag{3.35}$$

For n phase doublets $(+\phi_{DM}^k, -\phi_{DM}^k)_{k\in[1,n]}$ generating n image doublets $(I_k^+, I_k^-)_{k\in[1,n]}$, we have:

$$\begin{bmatrix} I_1^+ - I_1^- \\ \dots \\ I_n^+ - I_n^- \end{bmatrix} = 4 \begin{bmatrix} E_0^0 \Re\{i\mathcal{C}\{P\phi_{DM}^1\}\} & E_0^0 \Im\{i\mathcal{C}\{P\phi_{DM}^1\}\} \\ \dots & \dots \\ E_0^0 \Re\{i\mathcal{C}\{P\phi_{DM}^n\}\} & E_0^0 \Im\{i\mathcal{C}\{P\phi_{DM}^n\}\} \end{bmatrix} \begin{bmatrix} \Re\{E_f^A\} \\ \Im\{E_f^A\} \end{bmatrix} \tag{3.36}$$

This equation can be inverted to obtain the complex electric field:

$$\begin{bmatrix} \Re\{E_f^A\} \\ \Im\{E_f^A\} \end{bmatrix} = \frac{1}{4} \begin{bmatrix} E_0^0 \Re\{i\mathcal{C}\{P\phi_{DM}^1\}\} & E_0^0 \Im\{i\mathcal{C}\{P\phi_{DM}^1\}\} \\ \dots & \dots \\ E_0^0 \Re\{i\mathcal{C}\{P\phi_{DM}^n\}\} & E_0^0 \Im\{i\mathcal{C}\{P\phi_{DM}^n\}\} \end{bmatrix}^{-1} \begin{bmatrix} I_1^+ - I_1^- \\ \dots \\ I_n^+ - I_n^- \end{bmatrix} \tag{3.37}$$

To make this matrix invertible, at least two pairs of DM phases are necessary, and the more pairs the more accurate the estimation is.

This method is quite easy to implement and use, and does not require any modification

of the optical system, compared to the SCC. However, it is based on the hypothesis that the aberrations and the correction are small, which is not always realistic. In general, this technique is implemented as an iterative procedure, to stay in the regime of small phases where this approximation can be done.

The pair-wise estimation has been experimentally validated, in particular at the High-Contrast Imaging Laboratory (HCIL) [Riggs et al. (2016b)], at the High-Contrast Imaging Testbed (HCIT) [Riggs et al. (2016a)], and on the Fresnel-FRee Experiment for EPICS (FFREE, and EPICS stands for ELT Planetary Imaging Camera and Spectrograph) [Vérinaud et al. (2011)].

3.3.2.2 Phase diversity

Phase diversity was developed by Gonsalves (1982) and is in general combined with a minimization technique. It requires the use of two images, I_f and I_d. I_f corresponds to the on focus image, ie. only impacted by the unknown aberrations ϕ we want to reconstruct. I_d is the diversity image, obtained after applying a known diversity phase ϕ_d in the pupil. I_d is also impacted by the aberrations ϕ. In these conditions, we have:

$$I_f = o * h^{\phi} + n_f \tag{3.38}$$

$$I_d = o * h^{\phi+\phi_d} + n_d \tag{3.39}$$

where n_f and n_d are the noises (detector and photon noises) of I_f and I_d respectively, and h^{ϕ} and $h^{\phi+\phi_d}$ the IRFs impacted by the aberrations ϕ and $\phi + \phi_d$ respectively.

In our case, we try to maximize the probability to observe the object o in presence of the aberrations ϕ, knowing the images I_f and I_d. This probability is noted $p(o, \phi | I_f, I_d)$ and from the Bayes' theorem it is also equal to:

$$p(o, \phi | I_f, I_d) = \frac{p(I_f, I_d | o, \phi) p(o, \phi)}{p(I_f, I_d)} \tag{3.40}$$

The estimates of o and ϕ with the minimization method are called $\tilde{o}$ and $\tilde{\phi}$ in this section.

$$\begin{aligned}(\tilde{o}, \tilde{\phi}) &= \underset{(o,\phi)}{\text{argmax}}\{p(o, \phi | I_f, I_d)\} \\ &= \underset{(o,\phi)}{\text{argmax}}\{\frac{p(I_f, I_d | o, \phi) p(o, \phi)}{p(I_f, I_d)}\} \\ &= \underset{(o,\phi)}{\text{argmax}}\{p(I_f, I_d | o, \phi) p(o, \phi)\}\end{aligned} \tag{3.41}$$

since $p(I_f, I_d)$ does not depend on o and ϕ. From this equation, we derive that maximizing $p(o, \phi | I_f, I_d)$ is equivalent to minimizing the criterion $-\ln\{p(I_f, I_d | o, \phi) p(o, \phi)\}$. We obtain:

$$\begin{aligned}(\tilde{o},\tilde{\phi}) &= \underset{(o,\phi)}{\text{argmin}}\{-\ln\{p(I_f,I_d|o,\phi)p(o,\phi)\}\} \\ &= \underset{(o,\phi)}{\text{argmin}}\{-\ln\{p(I_f,I_d|o,\phi)p(o)p(\phi)\}\}\end{aligned} \tag{3.42}$$

since o and ϕ are statistically independent variables. We note:

$$(\tilde{o},\tilde{\phi}) = \underset{(o,\phi)}{\text{argmin}}\{J_{MV}(o,\phi) + R_o + R_\phi\} \tag{3.43}$$

where J_{MV}, R_o, and R_ϕ are respectively called the likelihood term and the regularization terms. They are equal to:

$$\begin{aligned}J_{MV}(o,\phi) &= -\ln\{p(I_f,I_d|o,\phi)\} \\ R_o &= -\ln\{p(o)\} \\ R_\phi &= -\ln\{p(\phi)\}\end{aligned} \tag{3.44}$$

These parameters are also equal to:

$$\begin{aligned}J_{MV}(o,\phi) &= (I_f - o * h^\phi)^t C_{n_f}^{-1}(I_f - o * h^\phi) + (I_d - o * h^{\phi+\phi_d})^t C_{n_d}^{-1}(I_d - o * h^{\phi+\phi_d}) \\ R_o &= (o - \langle o\rangle)^t C_o^{-1}(o - \langle o\rangle) \\ R_\phi &= (\phi - \langle\phi\rangle)^t C_\phi^{-1}(\phi - \langle\phi\rangle)\end{aligned} \tag{3.45}$$

where $\langle f\rangle$ is the average of the variable f and C_x is the covariance matrix of the variable x. Minimizing the sum of these parameters can be seen as minimizing the differences between the real images and their estimates through the model, taking into account a regularization on the noises.

If the noises n_f and n_d are not correlated, then the covariance matrices are diagonal and:

$$J_{MV}(o,\phi) = \frac{1}{2}\left\|\frac{I_f - o * h^\phi}{\sigma_{n_f}}\right\|^2 + \frac{1}{2}\left\|\frac{I_d - o * h^{\phi+\phi_d}}{\sigma_{n_d}}\right\|^2 \tag{3.46}$$

where $\|f\|^2$ is the quadratic sum of the elements of f and σ_n is the standard deviation of the noise n.

Compared to the two previous cases, phase diversity requires direct imaging, ie. no FPM, to estimate the whole optical aberrations from the source down to the science camera. In a high contrast regime, we only want to measure and compensate for the aberrations down to the FPM. However, this method also proposes many advantages: 1) there is no approximation of small phases, 2) the statistics of the image noises are taken into account, 3) only two images are required to estimate the wavefront (compared to 4 in the pair-wise estimation), 4) the optical system is not modified (compared to the SCC), and 5) it also

enables to estimate the object's luminous distribution.

This method is in particular used to calibrate quasi-static aberrations on SPHERE (VLT) [Sauvage et al. (2012a)].

3.3.2.3 COFFEE

COFFEE technique is an extension of the phase diversity technique to coronagraphic images developed by Sauvage et al. (2012b) and Paul et al. (2013). The model of image formation used in COFFEE includes a coronagraph with all its components : apodizer, FPM, and Lyot stop, and different coronagraphs can be modelized: classical Lyot coronagraph, R&R, Vortex, 4QPM, and APLC.

Like in the previous case, two coronagraphic images, I_f and I_d, are needed. I_d is obtained after applying a known diversity phase ϕ_d in the entrance pupil plane. COFFEE enables to estimate two unknown phase aberrations: ϕ_{up} corresponds to the upstream phase aberrations, ie. before the coronagraph (typically in the apodizer plane) and ϕ_{do} to the downstream aberrations, ie. after the coronagraph (typically in the Lyot stop plane). Therefore we define a new coronagraph function $\mathcal{C}\{E_0^0 e^{i\phi_{up}}, e^{i\phi_{do}}\}$, similar to the one previously defined but with a multiplication by $e^{i\phi_{do}}$ in the Lyot stop plane. We also consider residual continuous backgrounds in the images,β_f and β_d, due to the coronagraph, such as:

$$I_f = \left\|\mathcal{C}\{E_0^0 e^{i\phi_{up}}, e^{i\phi_{do}}\}\right\|^2 + n_f + \beta_f \tag{3.47}$$

$$I_d = \left\|\mathcal{C}\{E_0^0 e^{i\phi_{up}+i\phi_d}, e^{i\phi_{do}}\}\right\|^2 + n_d + \beta_d \tag{3.48}$$

As before, we want to maximize $p(E_0^0, \beta_f, \beta_d, \phi_{up}, \phi_{do}|I_f, I_d)$, which is equivalent to minimizing the criterion $J_{MAP} = -\ln(p(E_0^0, \beta_f, \beta_d, \phi_{up}, \phi_{do}|I_f, I_d))$. Like in the previous case, this criterion is equivalent to:

$$\begin{aligned} J_{MAP}(E_0^0, \beta_f, \beta_d, \phi_{up}, \phi_{do}) = &\frac{1}{2}\left\|\frac{I_f - \left\|\mathcal{C}\{E_0^0 e^{i\phi_{up}}, e^{i\phi_{do}}\}\right\|^2 + \beta_f}{\sigma_{n_f}}\right\|^2 + \\ &\frac{1}{2}\left\|\frac{I_d - \left\|\mathcal{C}\{E_0^0 e^{i\phi_{up}+i\phi_d}, e^{i\phi_{do}}\}\right\|^2 + \beta_d}{\sigma_{n_d}}\right\|^2 + R_{\phi_{up}} + R_{\phi_{do}} \end{aligned} \tag{3.49}$$

where:

$$\begin{aligned} R_{\phi_{up}} &= (\phi_{up} - \langle\phi_{up}\rangle)^t C_{\phi_{up}}^{-1}(\phi_{up} - \langle\phi_{up}\rangle) \\ R_{\phi_{do}} &= (\phi_{do} - \langle\phi_{do}\rangle)^t C_{\phi_{do}}^{-1}(\phi_{do} - \langle\phi_{do}\rangle) \end{aligned} \tag{3.50}$$

Like in the previous case, this criterion has to be minimized. It usually calls a numerical minimization based on the Variable Metric with Limited Memory and Bounds (VMLM-B) method [Paul (2014)]. The minimization stops when the difference between two successive

values of the criterion is below a certain threshold, fixed by the user.

This method is particularly well suited for our goal : measuring the wavefront aberrations in a coronagraphic system, with no differential aberrations and as small modifications of the system as possible.

3.4 Wavefront control

Wavefront control aims at correcting for the phase aberrations of the optical system. It is then often coupled with an estimation technique, such as the ones previously described. It requires the use of one or several DMs, with at least one in the entrance pupil plane of the system.

The correction can also be optimized to not only compensate for the phase aberrations of the system, but also to mitigate the diffraction effects due to the spiders and segmentation on the final image [Mazoyer et al. (2016, 2018a,b)]. Finally, WFC can also deepen the contrast in a restricted area of the focal plane, at the disadvantage of the rest of the focal plane, which does not correspond to a true compensation of the aberrations. This restricted area corresponds to a DH specific to the WFC and is often included in the coronagraph DH.

In this section, we first describe the intrinsic effects of the deformable mirror on the focal plane, then we focus on some well-known techniques.

3.4.1 Effect of the deformable mirror on the correction

It is common to set a DM in the entrance pupil plane of the system. Because the correction is brought by a modification of the DM surface, it modifies the phase of the wavefront:

$$E_0(\mathbf{r}) = E_0^0 P(\mathbf{r}) e^{\alpha(\mathbf{r})+i\phi(\mathbf{r})+i\phi_{DM}(\mathbf{r})} \tag{3.51}$$

Using a DM to correct for phase aberrations and flatten the wavefront is called Phase Conjugation. This allows to cancel as much as possible the aberrations and therefore improve the contrast, but does not provide the highest possible performance as it does not cancel the diffraction residuals.

Bordé and Traub (2006) shows that one DM in a pupil plane can only correct for a non-symmetrical DH, ie. half of the interest area. To correct for a full symmetrical DH, another DM can be set out of the pupil plane and then also corrects for amplitude aberrations.

The correction is limited in spatial frequencies by the actuator density on the DM. This means that the DM can only correct the phase down to a certain frequency f_{min} (this frequency corresponding to a sine phase made of one oscillation covering the entire DM) and up to another frequency f_{max} (corresponding to the case where one actuator is up, the next one down, etc.). As an example, let's imagine a circular DM of 34 actuators in diameter. We also make the hypothesis that the pupil covers exactly all the DM. Then the DM can only correct for frequencies between $f_{min} = \lambda/D$ and $f_{max} = 34/2 \times \lambda/D = 17\lambda/D$. The

correction's DH has to belong to this range. We can conclude that the more dense in actuators the DM is, the larger the DH can be. However, it can be useful to use several DMs in different pupil planes, each of them correcting at a different range of frequencies and for both amplitude and phase aberrations. The THD2 testbench, for instance, contains three DMs: DM3 is a 32×32 actuators' DM in a pupil plane, but DM1 and DM2 are out of pupil: DM1 has a 34×34 actuators while DM2 has 12×12 actuators and focus more on low-order amplitude aberrations [Baudoz et al. (2018)].

Each actuator is not fully flat, so the full DM has a natural net-like surface, even at its flat position. This effect generates very specific speckles called satellite spots in the focal plane, at the frequencies of the net.

Finally, moving an actuator from its flat position deforms the surface around the actuator. We call the influence function of an actuator the 3D-shape of the surface generated by its deformation. The surface of the DM can be seen as a sum of these influence functions times the actuator strokes:

$$\phi_{DM}(\mathbf{r}) = \sum_{k=1}^{n_{act}} a_k f_k(\mathbf{r}) \tag{3.52}$$

The influence functions are often unified in a so-called influence matrix: it is a $n_{pix} \times n_{act}$ matrix indicating the deformation of the phase for each actuator, where n_{pix} is the number of pixels considered on the detector.

Another matrix is often used to describe the DM: the interaction matrix. It provides the relation between the voltages V applied on the DM actuators and the electric field on the detector plane. Therefore it is a $n_{act} \times n_{pix}$ matrix.

The DM used in WFC for high contrast requires a careful calibration procedure before applying any WFC techniques.

3.4.2 WFC techniques

In this section, we describe a few well-known wavefront control (WFC) algorithms. They were also described in Leboulleux et al. (2017), which some of the descriptions below are based on.

As we will see in this section, all these techniques do not require the same knowledge on the wavefront, on the optical testbed, or on the DM. They will be compared in the next section.

3.4.2.1 Speckle Nulling

The Speckle Nulling (SN) procedure was the first developed and is quite intuitive. It is also an estimation-free approach, which means no complementary wavefront sensing is needed.

This is an iterative method and each step aims at correcting for the brightest speckle in the dark hole. Indeed a speckle in the detector plane is equivalent to a sine function in the

pupil plane, its position and intensity being related to the frequency and amplitude of the phase. Therefore, a speckle can theoretically be removed by finding the right sine function that compensates for it. The command phase to apply on the DM is:

$$\phi_{DM}(\mathbf{r}) = A\sin(\phi_0 + 2\pi\mathbf{f_s}.\mathbf{r}) \tag{3.53}$$

where A is the amplitude of the sine, ϕ_0 is the origin phase and $\mathbf{f_s}$ is the spatial frequency of the phase. This frequency derives from the position $\mathbf{u_s}$ of the speckle. For instance, if we consider the brightest speckle being at $\mathbf{u_s} = (u_x\lambda/D, u_y\lambda/D)$, then $\mathbf{f_s} = (u_x/D, u_y/D)$.

Furthermore, the amplitude of the sine function A is proportional to the square root of the intensity of the speckle. However, a loop to test several amplitudes can be set to optimize the amplitude of the sine function.

The only parameter that cannot be obtained from the position and amplitude of the speckle is the phase ϕ_0. To get it, different sine commands with different phases are applied on the DM, and the amplitude of the target speckle is recorded. With an interpolation, it is possible to compute the optimal phase that minimizes the amplitude of the speckle.

Once the optimal phase ϕ_{DM} has been found, the voltages' vector V to send to the DM is:

$$V = F^{\dagger}\phi_{DM} \tag{3.54}$$

where F is the influence matrix, containing all the influence functions, and $F^{\dagger}$ is the generalized inverse matrix of F, obtained by Singular Value Decomposition (SVD).

Once the target speckle is extincted, a new iteration begins to remove the next brightest speckle and so on until the wanted contrast is obtained in the dark hole.

The main advantage of this algorithm is that it does not require any prerequisite on the system, such as a model of the coronagraph, and on the errors: no wavefront sensing is needed. This method also has many drawbacks. First, since at each iteration, one speckle only is corrected, thousands of iterations are needed to correct for the wavefront errors affecting the entire dark hole. Such a time-consuming correction is not compatible with space missions. Furthermore, adding thousands of sine commands does not take into account the physical limitations of the DM that has limited actuators' strokes.

This method has been several times used on testbeds and instruments including in broadband light, such as on the HCIT at JPL [Trauger et al. (2004) and Belikov et al. (2006)] or on the High-contrast imager for Complex Aperture Telescopes (HiCAT) at the Space Telescope Science Institute (STScI) [Soummer et al. (2018)].

3.4.2.2 Speckle Field Nulling

The main drawback of the SN algorithm being its speckle-by-speckle correction, the next methods are optimized to correct for the aberrations impacting the entire dark hole.

The Speckle Field Nulling (SFN) algorithm corresponds to a generalization to the SN technique. It is based on a minimization of the energy at once in the entire dark hole, ie. to

obtain:

$$\forall \mathbf{u} \in DH, E_f(\mathbf{u}) = 0 \tag{3.55}$$

As a reminder, Eq. 3.51 stipulates that:

$$E_0(\mathbf{r}) = E_0^0 P(\mathbf{r}) e^{\alpha(\mathbf{r})+i\phi(\mathbf{r})+i\phi_{DM}(\mathbf{r})} \tag{3.56}$$

We consider that the amplitude aberrations are negligible. If the correction is efficient, then $\phi + \phi_{DM}$ is small and the exponential function can be linearized:

$$E_0(\mathbf{r}) = E_0^0 P(\mathbf{r})(1 + i\phi(\mathbf{r}) + i\phi_{DM}(\mathbf{r})) \tag{3.57}$$

After the coronagraph:

$$E_f(\mathbf{u}) = E_0^0 \mathcal{C}\{P\}(\mathbf{u}) + iE_0^0 \mathcal{C}\{\phi\}(\mathbf{u}) + iE_0^0 \mathcal{C}\{\phi_{DM}\}(\mathbf{u}) \tag{3.58}$$

$\mathcal{C}\{P\}$ corresponds to the image of the star, $i\mathcal{C}\{\phi\}$ corresponds to the field of speckles, and $i\mathcal{C}\{\phi_{DM}\}$ is the correction brought by the DM as seen in the detector plane.

With a perfect coronagraph, the image of the star is cancelled:

$$E_f(\mathbf{u}) = iE_0^0 \mathcal{C}\{\phi\}(\mathbf{u}) + iE_0^0 \mathcal{C}\{\phi_{DM}\}(\mathbf{u}) \tag{3.59}$$

Using this last equation, the influence functions of the DM as defined in Eq. 3.52, and the objective set in Eq. 3.55, we obtain:

$$\sum_{k=1}^{n_{act}} a_k \mathcal{C}\{f_k\}(\mathbf{u}) = -\mathcal{C}\{\phi\}(\mathbf{u}) \tag{3.60}$$

This equation corresponds to a linear system in (a_k) and can be solved using an SVD or Fourier Expansion.

The main advantage of this method is that it provides a huge gain of time compared to the SN since the electric field in the entire dark hole is being corrected at once. However, several prerequisites are needed, such as an estimation of the wavefront errors, a good knowledge of the coronagraph to obtain the model $\mathcal{C}$, and a calibration of the DM to get the influence functions (f_k). Finally, it does not take into account the limited strokes of the DM, and amplitude aberrations are considered negligible.

3.4.2.3 Electric Field Conjugation

The EFC algorithm [Riggs et al. (2016b) and Give'on et al. (2011)] requires a preliminary estimation of the wavefront errors. It is generally associated with the pair-wise estimation sensor.

Like in the previous case, the goal is to obtain:

$$\forall \mathbf{u} \in DH, E_f(\mathbf{u}) = 0 \tag{3.61}$$

Once again, we use Eq. 3.51:

$$E_0(\mathbf{r}) = E_0^0 P(\mathbf{r}) e^{\alpha(\mathbf{r})+i\phi(\mathbf{r})+i\phi_{DM}(\mathbf{r})} \tag{3.62}$$

however, to linearize it, we consider this time that only the correction applied on the DM is small and can be extended:

$$E_0(\mathbf{r}) = E_0^0 P(\mathbf{r}) e^{\alpha(\mathbf{r})+i\phi(\mathbf{r})}(1 + i\phi_{DM}(\mathbf{r})) \tag{3.63}$$

In the DH, the electric field becomes:

$$E_f(\mathbf{u}) = iE_0^0 \mathcal{C}\{Pe^{A+i\phi}\}(\mathbf{u}) + iE_0^0 \mathcal{C}\{\phi_{DM}\}(\mathbf{u}) \tag{3.64}$$

As seen in section 3.4.1, the interaction matrix G provides the relation between the voltages V applied on the DM and their effect on the detector:

$$\mathcal{C}\{\phi_{DM}\} = GV \tag{3.65}$$

Combining these last two equations and the objective of canceling the electric field in the dark hole provides:

$$\mathcal{C}\{Pe^{A+i\phi}\} + iGV = 0 \tag{3.66}$$

This formula is equivalent to:

$$V = G^\dagger i\mathcal{C}\{Pe^{A+i\phi}\} \tag{3.67}$$

Finally, since V is necessary real:

$$V = \begin{bmatrix} \Re\{G^\dagger\} \\ \Im\{G^\dagger\} \end{bmatrix} \begin{bmatrix} \Re\{i\mathcal{C}\{Pe^{A+i\phi}\}\} \\ \Im\{i\mathcal{C}\{Pe^{A+i\phi}\}\} \end{bmatrix} \tag{3.68}$$

$\mathcal{C}\{Pe^{A+i\phi}\}$ is the electric field in the image plane obtained from the wavefront sensing preliminary step.

Additionally from the wavefront estimation, this algorithm also requires a good knowledge of the DM, with a precise estimation of the interaction matrix. Because of the linearization of the DM phase, it requires small correction and it is often used as an iterative method. The main advantage of this method remains that no model is needed for the coronagraph.

3.4.2.4 Stroke Minimization

In opposition from the three algorithms presented before, the Stroke Minimization (SM) method [Pueyo et al. (2009)] takes into account the physical constraints of the DM, ie. the limited strokes of the actuators. This algorithm combines two objectives: minimizing the quadratic sum of the actuator strokes $\sum_{k=1}^{n_{act}} a_k^2$ while achieving the target contrast:

$$\epsilon \leqslant C \tag{3.69}$$

where ϵ is the total energy in the dark hole, ie.:

$$\epsilon = \int\int_{DH} \|E_f(\mathbf{u})\|^2 \, \mathrm{d}\mathbf{u} \tag{3.70}$$

We define the criterion ϵ_M that combines these two requirements:

$$\epsilon_M = \frac{1}{2}\sum_{k=1}^{n_{act}} a_k^2 + \mu(\epsilon - C) \tag{3.71}$$

where μ is a weighting parameter that has to be optimized.

In practice, μ is set at a small value. ϵ_M is minimized by setting its derivative to 0 and we obtain a value for the actuator strokes $(a_k)_{k\in[1,n_{act}]}$. If the contrast constraint is respected, then the algorithm is finished. If not, the value of μ is increased, which is equivalent to increasing the importance of the contrast constraint in the criterion ϵ_M, and the algorithm is applied again, until the requirements are satisfied.

This algorithm can include multiple DMs which enables symmetric correction in the dark hole, by correcting for both amplitude and phase aberrations.

It has also lead to the development of the Active Correction of Aperture Discontinuities-Optimized Stroke Minimization (ACAD-OSM), an extension of the SM algorithm to the case of segmented telescopes with possible phasing errors [Mazoyer et al. (2018a,b)].

3.4.2.5 Non-linear Dark Hole

The previous methods, except for the SN one, were using an approximation valid only for small phases. In opposition to them, the so-called Non Linear Dark Hole (NLDH) algorithm [Paul (2014)] does not use a linearization of the phase. The objective is to minimize the energy ϵ in the dark hole, defined as:

$$\epsilon = \langle \|E_f(\mathbf{u})\|^2 \rangle_{DH} \tag{3.72}$$

where $\langle f \rangle_{DH}$ is the average in the dark hole of a function f.

where $E_f(\mathbf{u}) = \mathcal{C}\{E_0^0 e^{A+i\phi_{up}+i\phi_{DM}}, e^{i\phi_{do}}\}$, similarly to section 3.3.2.3. We notice that all aberrations are considered: the amplitude aberrations A, the upstream phase aberrations ϕ_{up} and the downstream phase aberrations ϕ_{do}. Since $\phi_{DM} = FV$, the electric field is:

$$E_f(\mathbf{u}) = \mathcal{C}\{E_0^0 e^{A+i\phi_{up}+iFV}, e^{i\phi_{do}}\} \tag{3.73}$$

The optimal voltages' vector V to send to the DM is defined as:

$$\begin{aligned} V &= \underset{V}{\mathrm{argmin}}\{\epsilon\} \\ &= \underset{V}{\mathrm{argmin}}\{\left\|\mathcal{C}\{E_0^0 e^{A+i\phi_{up}+iFV}, e^{i\phi_{do}}\}\right\|^2\} \end{aligned} \tag{3.74}$$

Criterion/Method	SN	SFN	EFC	SM	NLDH
Preliminary step for WFS		X	X	X	X
Coronagraph model		X			X
DM calibration	X	X			X
Pupil to focal plane calibration	X		X	X	

Table 3.4.1: Comparison of the WFC algorithm prerequisites.

Like in section 3.3.2.3, this minimization is done with the minimizer VMLM-B.

The main advantage of this method is that no linearization of the phase is done, and many sources of aberrations are taken into account: amplitude and phase, upstream and downstream. However, it requires a model of the coronagraph, which can generate approximation or errors.

3.4.3 Comparison of the different algorithms of WFC

Table 3.4.1 provides a comparison of the techniques introduced before, based on their main drawbacks and advantages. It is important to notice that even if some points can be seen as advantages, they can lead to secondary drawbacks. For example, the SN algorithm is the only one that does not require a preliminary step of WFS, but this leads to an extremely time consuming algorithm that requires thousands of iterations.

This chaos is killing me

— David Bowie

4

Modelization of a high-contrast segmented telescope

Different models have been developed to simplify the access to the performance of a segmented telescope. For instance, Baron et al. (2008) proposes an approach of segmented apertures based on the peaks of the MTF and Yaitskova et al. (2003) develops an analytical model for ELT-like applications for studies of the diffraction pattern and Strehl ratio. More models have been developed for high-contrast applications, but never for the specific case of segmented apertures. This case brings in particular many specific problems, since the segmentation generates issues such as phasing errors, missing segments, segment vibrations... A description of such segment-level aberrations is then needed as the basis of the development of an anlytical model.

This first chapter about my work during this PhD focuses on this gap in optical system modelization. The goal of this chapter is then to develop an analytical model to study high-contrast systems with segmented apertures, and to apply it on a concrete case of performance and stability analysis.

A segmented pupil can be seen as a multi-aperture interferometer. It seemed then natural to me to develop my model from a well-known model based on coherent light interference: the Young experiment. The model I proposed here, named the Pair-based Analytical model for Segmented Telescopes Imaging from Space (PASTIS), takes into account the specificities of the high-contrast imaging instruments: pupil shape and segmentation, typical optical aberrations due to the segmentation, vibrations, coronagraph... It also runs faster than any end-to-end simulation.

The chapter is organized as follows. First, I will describe the Young experiment as an introductory case to the model (see section 4.1). I will then describe the PASTIS model with

an article that has been published in the Journal of Astronomical Telescopes, Instruments, and Systems (JATIS) (see section 4.2). Further developments have been provided to the model since the publication of the article and will be introduced in the sections 4.2.2 and 4.2.3: the extension of PASTIS to less simple aberrations, composed of multiple Zernike polynomials, and a dynamic application, with segment-level vibrations. In parallel, the model is being applied on the JWST at STScI, this study will be explained in the section 4.3. Eventually, we describe in section 4.4 the aspects of this error budget study that would be interesting to develop in the future.

4.1 Introductory case: the Young interference experiment

My model being based on the formalism of multi-pupil interference, I remind here the Young experiment. Of course the experiment in itself is well known since decades now, but it allows me to introduce the formalism of PASTIS in a simple case of study.

The Young interference experiment, or double-slit experiment, was developed in the beginning of the nineteenth century by the British physician Thomas Young. This revolutionary experiment aimed in particular at demonstrating the wave theory of light, which was being neglected to the profit of the corpuscular theory. Nowdays it is still used to increase the resolution of telescopes by NRM or interferometric telescopes.

In this section, we briefly explain the mathematical formalism behind this experiment in both monochromatic and polychromatic lights. The phenomena and conclusions explained here can enlighten the results or developments of the following sections.

4.1.1 Case of a monochromatic light

The Young experiment is illustrated in Fig. 4.1.1. It is composed of an on-axis monochromatic source S that illuminates two identical holes S_1 and S_2 symmetrically positioned around the optical axis. Therefore the wavefront coming from S reaches S_1 and S_2 at the same time. Each aperture diffracts the light in a cone of angular radius λ/r, where r is the diameter of the hole. The volume in which the two cones are superimposed corresponds to the interference field, since S_1 and S_2 are both synchronized and coherent, being issued from the same source.

We consider a point M of this interference field, far enough from the two holes. It can for instance be located at infinity, ie. it belongs to a detector located in the focal plane of a converging lens. M is characterized by its angular position (θ, θ'), where θ belongs to the (y, z) plane, containing the optical axis and the two holes (see Fig. 4.1.1), while θ' belongs to the (x, z) plane, containing the optical axis and orthogonal to the two holes.

The electric fields from S_1 and S_2 reaching M are:

$$\begin{aligned} E_1(M) &= E_0 e^{i\phi_1} \\ E_2(M) &= E_0 e^{i\phi_2} \end{aligned} \tag{4.1}$$

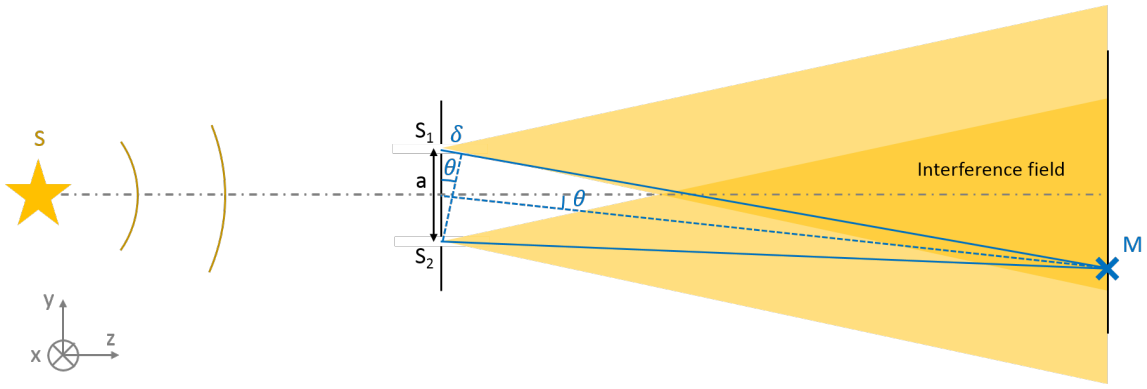

Figure 4.1.1: Description of the Young experiment.

where $\phi_2 = \phi_1 + 2\pi\delta/\lambda$. δ is the optical path difference, in our case (the optical index of the environment is 1) it corresponds to the extra distance the wavefront from S_2 needs to travel before being in phase with the wavefront at S_1. As illustrated in Fig. 4.1.1, we have:

$$\sin(\theta) = \frac{\delta}{a} \tag{4.2}$$

where a is the distance between the two holes. From a small angle θ, this can be approximated with:

$$\theta = \frac{\delta}{a} \tag{4.3}$$

We notice here that θ' does not affect δ: there is an independence along the θ' axis of the final pattern. Since S_1 ans S_2 are coherent, we have:

$$\begin{aligned} I(M) &= \|E_1(M) + E_2(M)\|^2 \\ &= \left\|E_1(M)(1 + e^{2\pi i\theta\frac{a}{\lambda}})\right\|^2 \\ &= E_0^2(1 + e^{2\pi i\theta\frac{a}{\lambda}})(1 + e^{-2\pi i\theta\frac{a}{\lambda}}) \\ &= 2E_0^2\left(1 + \cos(2\pi\theta\frac{a}{\lambda})\right) \end{aligned} \tag{4.4}$$

This corresponds to interference fringes orthogonal to the axis of the holes, with an angular spacing equal to λ/a.

4.1.2 Case of a polychromatic light

A polychromatic light source can be seen as an incoherent combination of monochromatic sources.

As seen in the previous case, each of these components produces interference fringes.

We express them as following:

$$I(M,\upsilon) = 2E_0^2\left(1+\cos(2\pi\theta\frac{a\upsilon}{c})\right) \tag{4.5}$$

where c is the speed of light and υ the light spectral frequency. These two parameters are related to the wavelength λ with the relation: $c = \lambda\upsilon$.

And since they are incoherent, the intensities of each spectral component are summed or integrated in the detector plane. In the appendix A, it is demonstrated that:

$$\begin{aligned} I(M) &= \frac{1}{\Delta\upsilon}\int_{\upsilon_0-\frac{\Delta\upsilon}{2}}^{\upsilon_0+\frac{\Delta\upsilon}{2}} I(M,\upsilon)\,\mathrm{d}\upsilon \\ &= 2E_0^2\left(1+\mathrm{sinc}\left(\pi\theta\Delta\upsilon\frac{a}{c}\right)\cos\left(2\pi\theta\upsilon_0\frac{a}{c}\right)\right) \end{aligned} \tag{4.6}$$

This equation looks a lot like the one of the monochromatic case, except for a low frequency envelope in sinc function that is multiplied to the higher frequency fringes (cosine function).

On the optical axis, ie. when $\theta = 0$, the intensity does not depend on the wavelength and all spectral frequencies of the range $[\upsilon_0 - \frac{\Delta\upsilon}{2}, \upsilon_0 + \frac{\Delta\upsilon}{2}]$ are present. This is the reason why, if the source corresponds to a white spectrum, this zone is called the white fringe. It also corresponds to the angular separation with the maximum of intensity. When θ increases, not all wavelengths are present since some correspond to constructive fringes while others to destructive fringes. We can even notice angular separations ($\theta_k = k\frac{c\pi}{a\Delta\upsilon}$ where k is a non-null integer) where the fringes from all wavelengths are destructive. This pattern is typical of non-monochromatic light in the Young experiment and is called a channelled spectrum.

4.2 High-contrast model for segmented telescopes

We develop in this section the model for high contrast in a segmented telescope. This model, based on an interferometric description as the one of Young's formalism, is first applied to the case of a phasing error of a segmented telescope, with the specific case of pure decorrelated static segment-level pistons, which means random local pistons are applied on the segments. This part is mainly based on the JATIS article that was published during this PhD [Leboulleux et al. (2018b)]. Then the model is developed in the case of any Zernike polynomial combination on the segments. We eventually study the case of a temporal evolution of vibrating segments.

4.2.1 Case of segment-level single Zernike polynomials

In the model introduced here just one kind of aberration described on the Zernike polynomials' basis is taken into account on the telescope pupil. We also provide tolerancing

for piston-like and astigmatism-like aberrations in the case of a 36-segment telescope, to obtain absolute and stability constraints on the phasing and polishing of the primary mirror for exo-Earth imaging applications.

The objective here is to study the case of segment phasing on the contrast. We have therefore developed the model for a single Zernike mode per segment.

The model PASTIS that we develop in the JATIS article describes the contrast of a segmented telescope. It allows us to derive a sensitivity analysis, which means to quantify how the contrast is degraded by segment-level errors, such as piston or astigmatism errors on the segments. By inverting this analysis, we can also estimate the maximum acceptable amplitude for the errors of each Zernike polynomial to reach a given contrast level.

Journal of Astronomical Telescopes, Instruments, and Systems

AstronomicalTelescopes.SPIEDigitalLibrary.org

Pair-based Analytical model for Segmented Telescopes Imaging from Space for sensitivity analysis

Lucie Leboulleux
Jean-François Sauvage
Laurent A. Pueyo
Thierry Fusco
Rémi Soummer
Johan Mazoyer
Anand Sivaramakrishnan
Mamadou N'Diaye
Olivier Fauvarque

SPIE.

Lucie Leboulleux, Jean-François Sauvage, Laurent A. Pueyo, Thierry Fusco, Rémi Soummer, Johan Mazoyer, Anand Sivaramakrishnan, Mamadou N'Diaye, Olivier Fauvarque, "Pair-based Analytical model for Segmented Telescopes Imaging from Space for sensitivity analysis," *J. Astron. Telesc. Instrum. Syst.* **4**(3), 035002 (2018), doi: 10.1117/1.JATIS.4.3.035002.

Journal of Astronomical Telescopes, Instruments, and Systems 4(3), 035002 (Jul–Sep 2018)

Pair-based Analytical model for Segmented Telescopes Imaging from Space for sensitivity analysis

Lucie Leboulleux,[a,b,c,*] Jean-François Sauvage,[b,c] Laurent A. Pueyo,[a] Thierry Fusco,[b,c] Rémi Soummer,[a] Johan Mazoyer,[d] Anand Sivaramakrishnan,[a,d] Mamadou N'Diaye,[e] and Olivier Fauvarque[b]
[a]Space Telescope Science Institute, Baltimore, Maryland, United States
[b]Aix Marseille Université, CNRS, Laboratoire d'Astrophysique de Marseille, UMR 7326, Marseille, France
[c]Office National d'Etudes et de Recherches Aérospatiales, Châtillon, France
[d]Johns Hopkins University, Department of Physics and Astronomy, Baltimore, Maryland, United States
[e]Université Côte d'Azur, Observatoire de la Côte d'Azur, CNRS, Laboratoire Lagrange, Bd de l'Observatoire, Nice, France

Abstract. The imaging and spectroscopy of habitable worlds will require large-aperture space-based telescopes, to increase the collecting area and the angular resolution. These large telescopes will necessarily use segmented primaries to fit in a rocket. However, these massively segmented mirrors make high-contrast performance very difficult to achieve and stabilize, compared with more common monolithic primaries. Despite space telescopes operating in a friendlier environment than ground-based telescopes, remaining vibrations and resonant modes on the segments can still deteriorate the performance. In this context, we present the Pair-based Analytical model for Segmented Telescopes Imaging from Space (PASTIS) that enables the establishment of a comprehensive error budget, both in terms of segment alignment and stability. Using this model, one may evaluate the influence of the segment cophasing and surface quality evolution on the final images and contrasts, and set up requirements for any given mission. One can also identify the dominant modes of a given geometry for a given coronagraphic instrument and design the feedback control systems accordingly. We first develop and validate this analytical model by comparing its outputs to the images and contrasts predicted by an end-to-end simulation. We show that the contrasts predicted using PASTIS are accurate enough compared with the end-to-end propagation results, at the exo-Earth detection level. Second, we develop a method for a fast and efficient error budget in terms of segment manufacturing and alignment that takes into account the disparities of the segment effects on the final performance. This technique is then applied on a specific aperture to provide static and quasistatic requirements on each segment for local piston and 45-deg astigmatism aberrations. Finally, we discuss potential application of this technique to future missions. [DOI: 10.1117/1.JATIS.4.3.035002]

Keywords: instrumentation; coronagraphy; exoplanets; high contrast; direct imaging; error budget; segmented telescopes; cophasing.

Paper 18003 received Feb. 1, 2018; accepted for publication Jun. 22, 2018; published online Aug. 17, 2018.

1 Introduction

Direct imaging and spectroscopy of Earth-like exoplanets will require future telescopes to be larger. Indeed, the science yield increases as a steep power of primary mirror diameter, especially so when using a coronagraph.[1] To fit these mirrors in launch vehicles, these large primary mirrors will have to be segmented. Coronagraphs adapted to these pupil geometries have already been designed and validated on ground-based telescopes such as the Keck telescopes. Even if coronagraphs on the Keck telescopes could be made to work at smaller inner working angle, they are dedicated to infrared observations and are limited by the atmosphere, and can therefore only reach a modest contrast.[2–4] Space segmented telescopes with similar contrast to Keck are imminent.[5,6] Until recently, segmented pupil coronagraph designs with sufficient performance to image Earth-like planets did not exist. However, the latest developments in coronagraph design promise contrasts on the order of 10^{-10}.[7–11] The most recent progress in coronagraphy on monolithic apertures with secondary mirrors and other necessary obstructions is being applied on the Wide Field Infrared Survey Telescope (WFIRST). This application will demonstrate wavefront sensing and control in the presence of thermal drifts;[12,13] however, WFIRST does not address stability issues associated with segmentation. For this reason, we need a good understanding of the impact of segment-level errors on coronagraphic point spread function (PSF) quality. On the upcoming segmented James Webb Space Telescope (JWST), relevant mission requirements only concern the encircled energy and Strehl ratio.[14,15] In this paper, we generalize the error budgeting on contrast requirements with a general tool that is applicable to any segmented pupil. Our work is also directly applicable to Extremely Large Telescopes (ELTs),[16–19] albeit at more modest contrasts. In particular, an analytical study has also been driven by Yaitskova et al.[20] for ELT-like configurations.

Several experiments in high-contrast imaging have produced very encouraging results. The best contrast achieved to date is a few 10^{-9}. This was obtained on the High-Contrast Imaging Testbed, with a circular aperture in extremely well-controlled

*Address all correspondence to: Lucie Leboulleux, E-mail: leboulleux@stsci.edu

2329-4124/2018/$25.00 © 2018 SPIE

conditions.[21] A contrast of a few 10^{-8} was also reached on the Très Haute Dynamique bench, at separations below 0.5 arc sec.[22,23] The latter would allow the detection of mature exo-Jupiters. However these experiments do not include segmentation, and moreover, are mostly static. More work is needed to extrapolate these results to our desired contrast. Similar experiments on segmented apertures are needed to build future telescopes for exoplanet imaging [such as the Large Ultraviolet Optical Infrared (LUVOIR) Telescope[24,25] or the Habitable Exoplanet Imaging Mission (HabEx)[26]].

To get stable imaging and maintain sufficient contrast over long times, error budgets must be an integral part of the optical systems being considered. As numerous factors can degrade the performance of the system, and since the objective is extremely challenging, a comprehensive error budget is essential to make wise decisions early enough during developments. Current methods for error budget are simulations of end-to-end propagation through the optical system, with variations of factors that are known to impact the contrast: segment phasing errors, segment surface quality, local or global vibrations, resonant modes on the segments, quasistatic aberrations due to thermal drift, and so on.[27,28] Because of the large number of factors that affect contrast, a multitude of cases need to be tested. Because of the computational burden involved, these studies can be dauntingly slow. Standard error budget methodology relies on multiple random realizations of disturbances, measuring science metrics based on simulated propagation of disturbances and establishing confidence intervals for acceptable operating points, given stated science requirements. In fact, even simple metrics such as encircled energy can be beyond the capabilities of numerical optical propagation.

This is the motivation behind our alternative fast method, which is based on the contrast criterion, and adaptable to any segmented pupil (such as JWST,[29,30] ELTs,[16–19] the HabEx mission,[26] or the LUVOIR Telescope[24,25]). This method is based on a so-called Pair-based Analytical model for Segmented Telescopes Imaging from Space (PASTIS), an analytical model to directly express the focal plane image and its contrast as a function of the Zernike coefficients of the segments' wavefront aberrations. A simple inversion of the model immediately provides the constraints in cophasing and stability that are necessary for obtaining the desired contrast. In this paper, we focus on the development of the analytical model, its validation, its formal inversion, and its application to tolerancing and stability constraints.

In Sec. 2, we introduce our analytical model, which is based on a segment-based model of the pupil with a perfect coronagraph, to enable sufficiently high-contrast performance. In particular, we develop a matrix-based version of the analytical model, which shortens the integrated contrast computation by a factor on the order of 10^7. In Sec. 3, we apply it to an example of a segmented pupil that we will use for the rest of the paper. We compare our model output with images created by an end-to-end simulation, where the segmented pupil is combined with an apodized pupil Lyot coronagraph (APLC) that enables a 10^{-10} contrast in a circular dark hole from $4\lambda/D$ to $9\lambda/D$ with a monochromatic light at $\lambda = 640$ nm. In the last section, we use this matrix-based analytical model to provide a method for a tolerancing and stability study on the segment alignment and manufacturing for all segmented pupils by sidestepping the iterative process of traditional error budgeting. Here, we apply our method to the cases of local pistons and 45-deg astigmatisms on the segments to provide results that agree very well with the much slower full optical propagation calculations.

2 Analytical Model of Image Formation and Contrast with a Segmented Pupil through a Coronagraph

In Sec. 2.1, we use the development of Bordé and Traub[31] to express the image in the final plane as a function of the aberrations in the pupil, behind a perfect coronagraph.

The model then developed in Secs. 2.2 and 2.3 is applicable to all segmented pupils composed from the repetition of a generic segment. A few examples are shown in Fig. 1.

2.1 *Image Formation with Phase Aberrations*

The electric field in the pupil plane is

$$E(\mathbf{r}) = P(\mathbf{r})e^{\alpha(\mathbf{r})+i\phi(\mathbf{r})}, \tag{1}$$

where P is the entrance pupil of our optical system, α are the amplitude aberrations, and ϕ are the phase aberrations in the pupil. Even if the amplitude errors are an important point in coronagraphy, they are not considered in this analytical model. The analytical formalism presented herein can, however, be readily generalized to include amplitude aberrations. Such considerations are left for further studies.

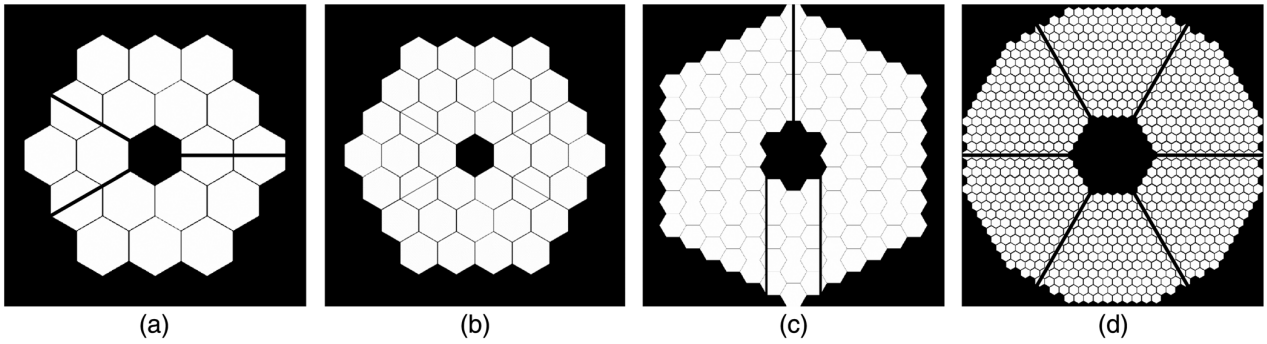

Fig. 1 (a) The JWST pupil (18 segments), (b) a pupil used for the SCDA study (36 segments), (c) one of the optional LUVOIR pupils (120 segments), and (d) the ELT pupil (798 segments). The pupil (b) will be used for applications later in this paper.

As the phase aberrations are small, Eq. (1) leads to

$$E(\mathbf{r}) = P(\mathbf{r}) + iP(\mathbf{r})\phi(\mathbf{r}). \tag{2}$$

As the phase aberration is defined on the pupil, this equation can be simplified using $P(\mathbf{r})\phi(\mathbf{r}) = \phi(\mathbf{r})$. Thus, the amplitude of the electric field in the detector plane becomes

$$E_f(\mathbf{u}) = \hat{P}(\mathbf{u}) + i\hat{\phi}(\mathbf{u}), \tag{3}$$

where $\mathbf{u}$ is the position vector in the detector plane (focal plane) and $\hat{f}$ is the Fourier transform of the function f.

Without coronagraph, the image intensity is

$$I(\mathbf{u}) = \|E_f(\mathbf{u})\|^2, \tag{4}$$

$$= \|\hat{P}(\mathbf{u})\|^2 + \|\hat{\phi}(\mathbf{u})\|^2 + 2\Re[\hat{P}^*(\mathbf{u})i\hat{\phi}(\mathbf{u})]. \tag{5}$$

This equation is made of a constant term, a term linear to the aberrations, and a quadratic term.

However, in the hypothesis of a perfect coronagraph, the amplitude of the on-axis electric field generated by the star is removed.[32–34] The intensity becomes

$$I(\mathbf{u}) = \|E_f(\mathbf{u}) - \hat{P}(\mathbf{u})\|^2, \tag{6}$$

$$= \|\hat{\phi}(\mathbf{u})\|^2. \tag{7}$$

2.2 *Case of a Segmented Pupil*

The pupil is now considered segmented in several identical segments.

2.2.1 *Pupil and phase models*

The entrance pupil P of our optical system consists of n_{seg} identical segments of shape mask S. We define the pupil as

$$P(\mathbf{r}) = \sum_{k=1}^{n_{\text{seg}}} S(\mathbf{r} - \mathbf{r_k}), \tag{8}$$

where $\mathbf{r}$ is the position vector in the pupil plane, and $\mathbf{r_k}$ is the position of the center of the k'th segment (Fig. 2).

We focus here on phasing, alignment, or polishing errors of the primary mirror. The phase aberration ϕ on the pupil P is expressed as the sum of global and local aberrations on the different segments (see Fig. 3). As the global aberrations can be seen as a sum of local aberrations,[35] we simply express the phase in the pupil as

$$\phi(\mathbf{r}) = \sum_{(k,l)=(1,1)}^{(n_{\text{seg}},n_{\text{zer}})} a_{k,l} Z_l(\mathbf{r} - \mathbf{r_k}), \tag{9}$$

where the coefficients $(a_{k,l})_{(k,l)\in[1,n_{\text{seg}}]\text{times}[1,n_{\text{zer}}]}$ are the local Zernike coefficients and $(Z_l)_{l\in[1,n_{\text{zer}}]}$ is the Zernike basis on a circular pupil that overfills the segment cropped by the shape of the generic segment. We could here have used the basis of polynomials specific to hexagonal apertures.[36,37] However since this basis' vectors are linear combinations of the common circular-aperture Zernike polynomials, both studies are quite equivalent, in particular for low-order polynomials and we decided to keep using the well-known Zernike polynomials basis.

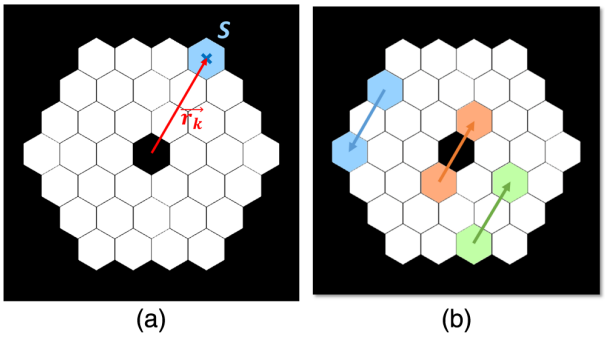

Fig. 2 (a) Definitions of the vectors $\mathbf{r_k}$ and of the shape of a segment S on a segmented pupil, here the SCDA primary mirror. In red, we can see one of the vectors $\mathbf{r_k}$, from the center of the pupil to the k'th segment, expressed in pixels. (b) Illustration of some redundant oriented pairs that correspond to one single nonredundant pair. Forty-two oriented pairs generate exactly the same interference fringes than the pair $\mathbf{r_{16}} - \mathbf{r_{28}}$ (blue), for example, the pairs $\mathbf{r_{25}} - \mathbf{r_{12}}$ (orange) and $\mathbf{r_{14}} - \mathbf{r_3}$ (green). As these 42 pairs have the same effect in the detector plane, they can all be replaced by one single pair, called the nonredundant pair.

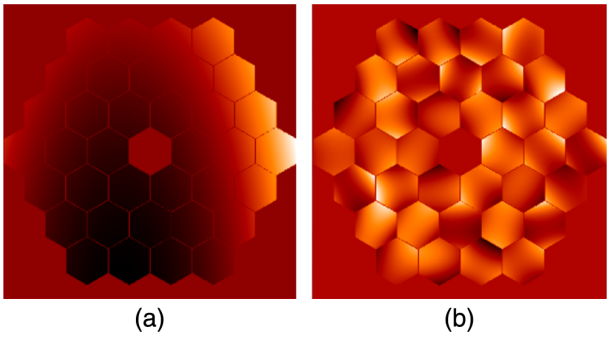

Fig. 3 (a) Global aberrations on a segmented mirror. (b) Local aberrations on the same segmented mirror.

Manufacturing, telescope alignment, and initial primary mirror cophasing remove most of the global and local aberrations, leaving only residual aberrations. Further studies could be done in the case of misalignment of the secondary mirror, which is known to impact significantly the performance of the system. However, in this article, the model is developed in the case of residual errors on the primary mirror only.

2.2.2 *Case of one single Zernike on the segments*

We first study the case where only one local Zernike polynomial Z_l is applied on the segments, even if the coefficient $a_{k,l}$ can vary with the segment k (see Fig. 8 for some examples of phases).

The intensity with a perfect coronagraph derives from Eqs. (7) and (9), this second one being used in the case of one single Zernike polynomial

$$I(\mathbf{u}) = \left\| \hat{Z}_l(\mathbf{u}) \sum_{k=1}^{n_{\text{seg}}} a_{k,l} e^{-i\mathbf{r_k}.\mathbf{u}} \right\|^2, \tag{10}$$

$$= \|\hat{Z}_l(\mathbf{u})\|^2 \sum_{i=1}^{n_{\text{seg}}} \sum_{j=1}^{n_{\text{seg}}} a_{i,l} a_{j,l} e^{i(\mathbf{r_j}-\mathbf{r_i}).\mathbf{u}}. \tag{11}$$

As the intensity is real, $\sum_{i=1}^{n_{\text{seg}}} \sum_{j=1}^{n_{\text{seg}}} a_{i,l} a_{j,l} e^{i(\mathbf{r_j}-\mathbf{r_i}).\mathbf{u}}$ is real, and therefore

$$I(\mathbf{u}) = \|\hat{Z}_l(\mathbf{u})\|^2 \left\{ \sum_{k=1}^{n_{\text{seg}}} a_{k,l}^2 + \sum_{i=1}^{n_{\text{seg}}} \sum_{j=1, j\neq i}^{n_{\text{seg}}} a_{i,l} a_{j,l} \cos[(\mathbf{r_j}-\mathbf{r_i}).\mathbf{u}] \right\}. \tag{12}$$

It appears here that studying the effect of random values of the same Zernike on all the segments is equivalent to studying the interference effects on each pair of segments and summing them.

$\{\mathbf{u} \to \cos[(\mathbf{r_j}-\mathbf{r_i}).\mathbf{u}]\}_{(i,j)\in[1,n_{\text{seg}}]^2}$ is a basis of cosine functions that describe the intensity distribution in the focal plane. Each vector of this basis is a cosine function, whose spatial periodicity and orientation depend on the pair of considered segments (i, j), very similarly to the Young fringes.[38] The amplitude in front of this function is simply the product of the amplitudes $a_{i,l}$ and $a_{j,l}$ of the respective Zernike coefficients on each segment. As a consequence, two pairs of segments having an identical configuration result in the same intensity pattern (see Fig. 2).

This equation shows also that the local Zernike polynomial Z_l acts on the final image plane as an envelope, which does not depend on the segment positions. Figure 4 shows the envelopes for the first Zernike polynomials.

We call n_{NRP} the number of nonredundant segment pairs and $(\mathbf{b_q})_{q\in[1,n_{\text{NRP}}]}$ the basis of nonredundant segment pairs. This basis corresponds to the family of all the vectors joining the centers of two different segments, where each vector appears once. Figure 2(b) shows the redundancy of some pairs of segments: the three vectors represented here are represented by a unique vector in the basis of nonredundant segment pairs. In the case of the segmented coronagraph design and analysis (SCDA) pupil, which contains 36 segments, there are 1260 possible oriented pairs of segments $\mathbf{r_j} - \mathbf{r_i}$ (obtained with the binomial coefficient $2 \times C_{36}^2$), but $n_{\text{NRP}} = 63$. In the case of JWST, there are 18 segments, 306 pairs of segments in total, but only 30 nonredundant pairs of segments. In the case of the ELT, there are 798 segments, 636,006 pairs of segments in total, and 1677 nonredundant pairs of segments. In all these examples, just a small fraction of the segment pairs, the nonredundant vectors, is responsible for the pattern in the focal plane.[39,40]

Thanks to this remark, we can rearrange the double sum of Eq. (12) as

$$I(\mathbf{u}) = \|\hat{Z}_l(\mathbf{u})\|^2 \left[\sum_{k=1}^{n_{\text{seg}}} a_{k,l}^2 + 2 \sum_{q=1}^{n_{\text{NRP}}} A_q \cos(\mathbf{b_q}.\mathbf{u}) \right], \tag{13}$$

with

$$\forall\, q \in [1, n_{\text{NRP}}], \qquad A_q = \sum_{(i,j)} a_{i,l} a_{j,l}, \tag{14}$$

where the couples (i, j) are all the couples that verify the equation $\mathbf{r_j} - \mathbf{r_i} = \pm\mathbf{b_q}$. This way the matrix multiplications associated with the focal plane sample arrays only has to be done n_{NRP}

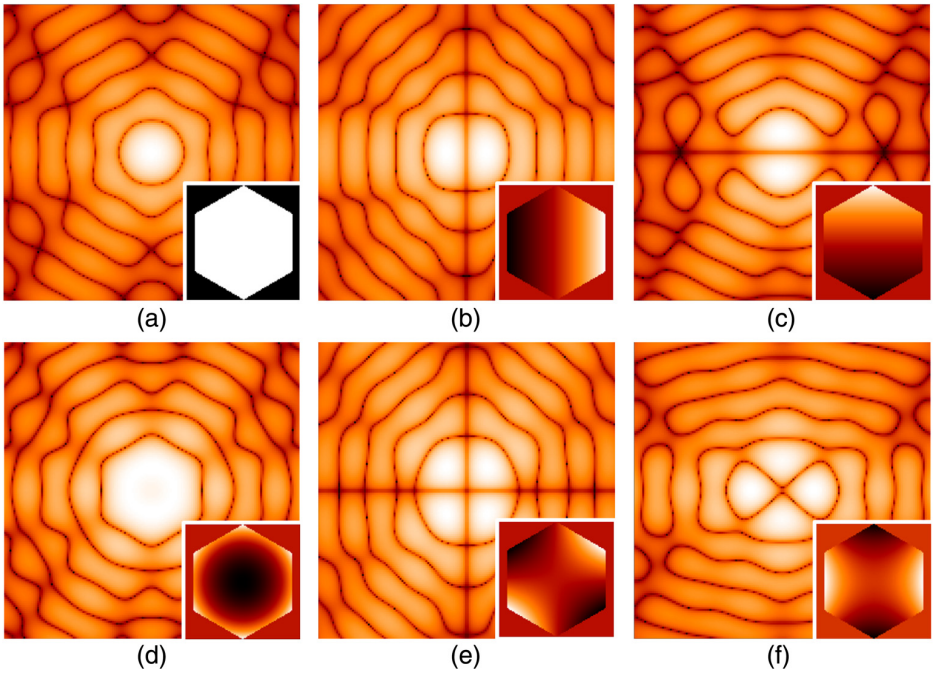

Fig. 4 Envelopes corresponding to the first few Zernike polynomials, in the logarithmic scale of the intensity, from 0 to $35\lambda/D$. (a) Piston, (b) tip, (c) tilt, (d) focus, (e) 45-deg astigmatism, and (f) 0-deg astigmatism.

times instead of n_{seg}^2 times. This equation saves computing time and resources and is strictly and mathematically equivalent to the Eq. (12): instead of summing independently all the cosines with their coefficients [Eq. (12)], we unify all the identical cosines and sum up their amplitudes [Eq. (13)].

We can conclude that it is possible to obtain a relation between the final image, a certain baseline, and the Zernike coefficients applied on each segment of the baseline.

2.2.3 *Case of an actual coronagraph*

Equation (13) establishes that the intensity in the image can be expressed as a function of the Zernike coefficients applied on the pupil. In this formula, all the individual segments have the same contribution to the final image pattern and its contrast. An actual coronagraphic system can include pupil apodizer, pupil phase, focal plane mask (phase or amplitude), and a Lyot stop. For the sake of our example in this paper, we only study pupil apodization, hard edge focal plane mask, and hard edge Lyot stop. These optical components, added to the spiders of the telescope, introduce a dependency on the segments: all the segments are not strictly equivalent. Therefore, the model needs to be refined.

In the case of direct imaging with a perfect coronagraph, we ignored the direct PSF $\hat{P}$ in the equation of the electric field in the final plane E_f. A real coronagraph has different impacts on the image. The coronagraph function modeled here as a linear function $\mathcal{C}$. In this general case, the intensity becomes

$$I(\mathbf{u}) = \|\mathcal{C}\{P\} + i\mathcal{C}\{\phi\}\|^2, \tag{15}$$

$$= \|\mathcal{C}\{P\}\|^2 + 2\Re\{\mathcal{C}\{P\}\mathcal{C}\{\phi\}^*\} + \|\mathcal{C}\{\phi\}\|^2. \tag{16}$$

Although it might seem different from Eq. (7), it can still be very close

- if ϕ is large enough, then $\|\mathcal{C}\{\phi\}\|^2$ dominates over the rest of the equation. As $\mathcal{C}\{\phi\} = \sum_{k=1}^{n_{\text{seg}}} \mathcal{C}\{a_{k,l} Z_l(\mathbf{r} - \mathbf{r_k})\}$, we approximate this coronagraph effect by putting weights $(c_{k,l})_{k\in[1,n_{\text{seg}}]}$ on the coefficients $(a_{k,l})_{k\in[1,n_{\text{seg}}]}$. These coefficients need to be computed. Therefore, the equation of the analytical model becomes

$$I(\mathbf{u}) = \|\hat{Z}_l(\mathbf{u})\|^2 \left\{ \sum_{k=1}^{n_{\text{seg}}} c_{k,l}^2 a_{k,l}^2 + \sum_{i=1}^{n_{\text{seg}}} \sum_{j=1, j\neq i}^{n_{\text{seg}}} c_{i,l} a_{i,l} c_{j,l} a_{j,l} \cos[(\mathbf{r_j} - \mathbf{r_i}).\mathbf{u}] \right\}. \tag{17}$$

In the nonredundant pair-configuration, we obtain

$$I(\mathbf{u}) = \|\hat{Z}_l(\mathbf{u})\|^2 \left[\sum_{k=1}^{n_{\text{seg}}} c_{k,l}^2 a_{k,l}^2 + 2 \sum_{q=1}^{n_{\text{NRP}}} A'_q \cos(\mathbf{b_q}.\mathbf{u}) \right], \tag{18}$$

where for $q \in [1, n_{\text{NRP}}]$, $A'_q = \sum_{(i,j)} c_{i,l} a_{i,l} c_{j,l} a_{j,l}$ and the couples (i, j) are all the couples that verify the equation $\mathbf{r_j} - \mathbf{r_i} = \pm \mathbf{b_q}$.

- In a general case, PASTIS aims at computing the contrast. Hereafter, $\langle f \rangle_{DH}$ corresponds to the mean value in the dark hole of the image f. If we consider the general equation of the intensity of Eq. (16), we notice that (1) $\langle \|\mathcal{C}\{P\}\|^2 \rangle_{DH}$ provides the deep contrast C_0 of the coronagraph and (2) $\langle 2\Re\{\mathcal{C}\{P\}\mathcal{C}\{\phi\}^*\} \rangle_{DH} = 0$ in a symmetrical dark hole (explanations in the Appendix). Therefore, the contrast in the dark hole C only takes into account the deep contrast C_0 and the average of the quadratic term $\langle \|\mathcal{C}\{\phi\}\|^2 \rangle_{DH}$. More explanations in this direction are provided in the next section.

In practice, we calibrate the coefficients for each Zernike by running the end-to-end simulation with the chosen coronagraph and the analytical model without calibration once for each segment

$$\forall\ k \in [1, n_{\text{seg}}], \qquad c_{k,l} = \sqrt{\frac{\langle I_C(k) \rangle_{DH}}{\langle I(k) \rangle_{DH}}}, \tag{19}$$

where $I_C(k)$ is the intensity image issued from the end-to-end simulation after applying a 1-nm aberration of the l'th Zernike polynomial on the k'th segment only, and $I(k)$ is the intensity image produced by the analytical model after applying exactly the same phase to the segments.

This calibration has to be performed only once and integrates the coronagraph effect in the focal plane into our model.

2.3 *Matrix-Based Model*

As explained in the previous section, the deep contrast $C_0 = \langle \|\mathcal{C}\{P\}\|^2 \rangle_{DH}$ can be taken into account. However, we prove in the Appendix that the average of the linear term $\langle 2\Re\{\mathcal{C}\{P\}\mathcal{C}\{\phi\}^*\} \rangle_{DH}$ is null in a symmetrical dark hole. Therefore, the mean contrast in the dark hole is

$$C = C_0 + \sum_{i=1}^{n_{\text{seg}}} \sum_{j=1}^{n_{\text{seg}}} c_{i,l} a_{i,l} c_{j,l} a_{j,l} \langle \|\hat{Z}_l(\mathbf{u})\|^2 \cos[(\mathbf{r_j} - \mathbf{r_i}).\mathbf{u}] \rangle_{DH}. \tag{20}$$

This equation can be expressed as a matrix product

$$C = C_0 + a_l M_l a_l^t, \tag{21}$$

where $a_l = (a_{1,l}, \ldots, a_{n_{\text{seg}},l})$ is the vector of the Zernike coefficients, a_l^t is the transpose vector of a_l, and $\forall\ (i, j) \in [1, n_{\text{seg}}]^2$, $M_l(i, j) = c_{i,l} c_{j,l} m_{i,j,l}$, where $m_{i,j,l} = \langle \|\hat{Z}_l(\mathbf{u})\|^2 \cos[(\mathbf{r_j} - \mathbf{r_i}).\mathbf{u}] \rangle_{DH}$.

This matrix-based version of the analytical model further reduces the computation time of the integrated contrast over a dark hole.

In the next section, the likelihood between the outputs issued from the PASTIS model and from the end-to-end simulation is quantified.

3 Results

In this section, we seek to validate the analytical model of the previous section, using a comparison with an end-to-end simulation. The chosen pupil and the coronagraph are described in Sec. 3.1 and the results of comparison in Secs. 3.2 and 3.3.

3.1 *End-to-End Simulations*

For this test, we choose the example pupil shown in Fig. 1(b), which is under study for future space telescopes in the SCDA program.[9] It is formed of 36 identical hexagonal segments and a hexagonal central obstruction.[41,42]

The end-to-end simulation explicitly computes the propagation of the electric field from plane to plane with a Fourier formalism, using the functions of Paul et al.[43] The coronagraph used in the end-to-end simulation is an APLC,[44–46] specially designed for this pupil. The APLC, whose components are shown in Fig. 5, is designed to enable an extremely high contrast of a few 10^{-11} in the dark hole, which corresponds to a circular area between $4\lambda/D$ and $9\lambda/D$ (see Fig. 6). The analytical model is valid only in the high-contrast area as $\hat{P}(\mathbf{u})$ is far from 0 out of this area and can then still not be neglected anymore. For this reason, we look at the intensity images and performance in this area only and compare them with the outputs of the model.

3.2 *Results and Comparison of the Matrix-Based Analytical Model*

In this section, we compare the mean contrasts in the dark hole computed from the images of the end-to-end simulation and from the matrix-based analytical model.

Figure 7 compares the output contrasts computed by the end-to-end simulation and from the matrix-based analytical model for piston aberrations from 1 pm to 10-nm-rms on the segments. For each rms value, we select 250 random phases and compute the mean, minimum, and maximum contrasts over the 250 output contrasts. As a comparison, highly similar curves obtained

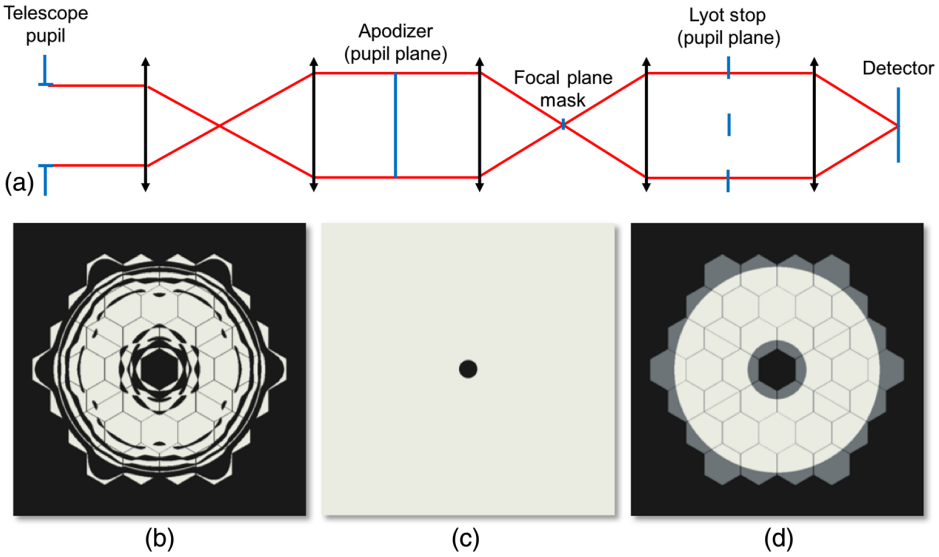

Fig. 5 (a) Optical configuration of the APLC as used in the end-to-end simulation. Bottom: Optical masks used in the end-to-end simulation. (b) The apodizer is located in the first pupil plane, (c) the focal plane mask on the following focal plane, its radius here being $4.5\lambda/D$, and the Lyot stop [circular aperture on the (d), here superposed with the entrance pupil] on the last pupil plane.

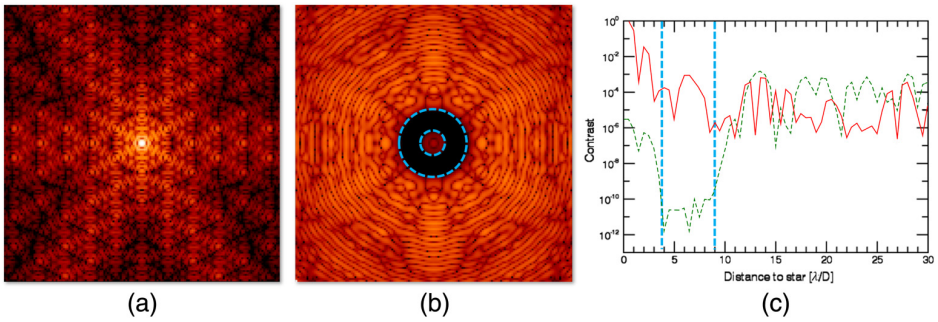

Fig. 6 (a) PSF in the presence of the SCDA pupil of Fig. 1, with an end-to-end numerical simulation without coronagraph and without aberration. (b) PSF in presence of the same SCDA pupil combined with the APLC, with no aberration. (c) Cut along the horizontal radius of the two previous PSFs (red: without APLC, green: with APLC). We can observe that the APLC brings a huge correction in the dark hole, delimited here by the blue dashed lines at $4\lambda/D$ and $9\lambda/D$. The average contrast in this region is a few 10^{-11}.

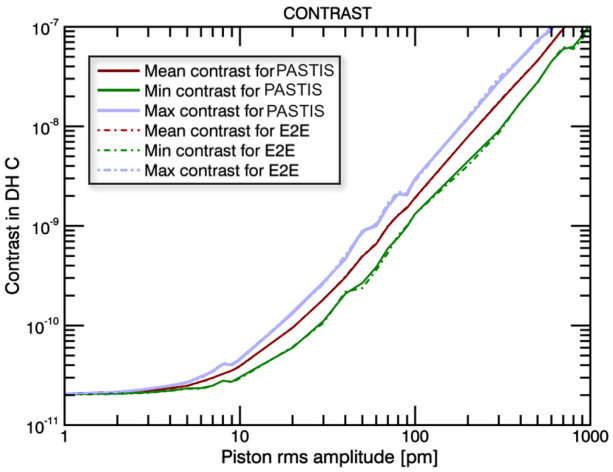

Fig. 7 Contrast as a function of the rms piston error phase on the pupil, computed from both the end-to-end simulation (E2E) and PASTIS. This plot illustrates two regimes: below 10-pm rms the contrast is limited by the coronagraph only and over a few 10-pm rms the contrast is limited by the aberrations and the quadratic term is majority in the analytical model.

thanks to end-to-end simulations only can be found in the studies of Stahl et al.,[47] later completed in Stahl et al.[48]

The curves of Fig. 7 issued from PASTIS are highly similar to the ones issued for the end-to-end simulation. To quantify the error between the end-to-end simulation and PASTIS, we obtain an error in the contrast of around 3% rms.

However, PASTIS shows its best interest in such heavy computations as its contrasts have been 10^7 times faster to compute than the contrasts issued from the end-to-end model. Indeed, PASTIS is a double multiplication between an n_{seg}-long vector, an $n_{\mathrm{seg}} \times n_{\mathrm{seg}}$-matrix, and another n_{seg}-long vector. Therefore, its computation complexity is on the order of n_{seg}^2. In contrast, one single end-to-end simulation requires three Fourier transforms, which dominate the computation time by being on the order of $n\ \log(n)$, where n is the size of the considered image. To plot figures with many iterations such as Fig. 7, which has 203,250 iterations, computation complexity has to be considered and PASTIS provides a significant gain of time and memory.

3.3 *Images Generated with PASTIS*

PASTIS has been validated in the previous section, providing a fast estimation of the contrast with a 3% error. In this section, we now look at the images obtained with the model before developing the matrix-based equation [Eq. (18)] to compare the morphology of the speckles in the images themselves.

To do so, we focus on the cases where only local low-order aberrations are applied on the segments: piston, tip, tilt, focus, and the two astigmatisms. Furthermore, for each Zernike polynomial, two different configurations are compared: a case where two segments only have local aberrations and a case where random low-order Zernike coefficients are applied on all the segments.

The PSFs resulting from the end-to-end simulation and the ones resulting from the analytical model are shown in Fig. 8. All panels are at the same scale, which illustrates once again that the analytical model provides a good prediction of the overall contrast level. We then use the correlations to quantify the agreement on the morphology of the speckles' intensity between the analytical model and the end-to-end simulations. The correlation here corresponds to the linear Pearson correlation coefficient, which, for two images I and J of N elements, is computed as

$$\mathrm{Cor}(I,J) = \frac{\sum_{k=1}^{N}(I(k)-\langle I\rangle)(J(k)-\langle J\rangle)}{\sqrt{\sum_{k=1}^{N}(I(k)-\langle I\rangle)^2 \sum_{k=1}^{N}(J(k)-\langle J\rangle)^2}}. \tag{22}$$

In the piston case, the images typically have correlations of around 70% and in the other cases, typically closer than 89%.

As a reminder, the envelopes of these different Zernike polynomials are shown in Fig. 4. In the piston case, it generates a circle at the limit of the dark hole. In the tip and tilt cases, they create a dark vertical or horizontal line crossing the center of the PSF. In the focus case, the envelope has a ring shape. Finally, in both astigmatisms, the envelopes create a cross in the dark hole. The effects of these different envelopes clearly appear in the images issued both from the end-to-end simulation and from the analytical model. As shown in Fig. 8, the envelopes also seem to be the main source of the difference between the PSFs issued from the analytical model and from the end-to-end simulation. This effect might be an artifact due to the apodization of the pupil: the envelopes were computed with a Zernike polynomial defined on a regular hexagonal segment, whereas the support shape depends on the apodization.

Another source of error is the scalar and the linear terms of Eq. (16), which are not taken into account in the model and therefore not displayed here.

This comparison between end-to-end simulation images and the outputs from the analytical model indicates that PASTIS allows to generate high-contrast images with a high-fidelity average contrast. Even if the morphologies of the images do not seem extremely accurate, mainly in the piston case (correlation around 70%, while over 90% for the other Zernike polynomials), the contrast values are close enough for error budgeting.

In practice, we keep using the matrix-based analytical model as it enables a fast estimate of the contrast in the dark hole, which is our chosen criterion for error budgeting, without the need of an actual image.

4 Sensitivity Analysis

A traditional error budget aims at quantifying the deterioration of the contrast with the rms error phase applied on the segments. For example, in the piston case, we can easily deduce from Fig. 7 the constraints in piston cophasing in term of rms error. For instance, to obtain a contrast of 10^{-10}, the piston phasing needs to be accurate to better than 20 pm rms.

PASTIS is a faster method to compute the deterioration of contrast due to segment-level aberrations. In particular, it can speed up large forward Monte Carlo to translate multiple realizations of deployment, phasing, or wavefront control. Similarly, it makes simulations of performance for long-time series of high-frequency vibrations possible. The most direct way to use PASTIS to find requirements for a given contrast is to apply it multiple times with multiple realizations of multiple errors, as shown in Fig. 7. However, we have then no clue of the repartition of these requirements on the segments, whereas

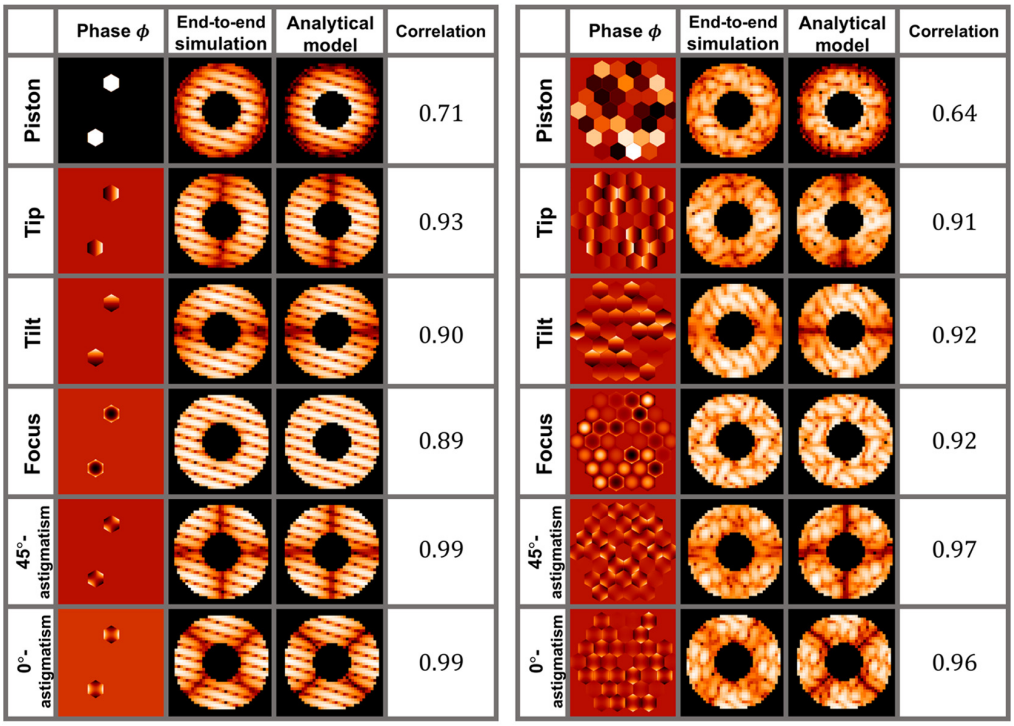

Fig. 8 Comparison of the PSFs (log scale) when (a) identical 1-nm aberrations are applied on a pair of segments and when (b) random aberration coefficients are applied on the segments for the first six Zernike polynomials (piston, tip, tilt, focus, and the astigmatisms). A binary mask is applied on the PSFs to display the dark hole only. The first column indicates the phase applied on the primary mirror. The PSFs of the second column are generated by a simulation of an end-to-end propagation through an APLC. The PSFs of the third column are generated by the analytical model. The last column gives the linear Pearson correlation coefficients between the end-to-end simulation and analytical model images. All the horizontal lines are at the same scale.

it is known that some segments have a bigger impact on the contrast than others: for example, the calibration coefficients $(c_{k,l})_{k\in[1,n_{\text{seg}}]}$ depend on the segment. PASTIS can actually identify these segments or group of segments. Using these modes, doing an error budget or designing wavefront sensing and control systems is a lot easier.

This is why we develop a sensitivity analysis method based on a modal projection of the phase, which takes into account this segment-dependent contribution to the contrast.

4.1 *Analytical Modal Inversion*

In Eq. (21) of Sec. 2.3, the contrast for the l'th Zernike depends on the matrix M_l. M_l being symmetric and positive-definite, there exist U_l, a matrix of eigen vectors, and D_l, a diagonal matrix of Eigen values, that satisfy

$$D_l = U_l M_l U_l^t. \tag{23}$$

We call $(\lambda_{p,l})_{p\in[0,n_{\text{seg}}-1]}$ the Eigen values of M_l and $(U_{p,l})_{p\in[0,n_{\text{seg}}-1]}$ their associated Eigen vectors. Therefore, we have

$$\forall\ p \in [0, n_{\text{seg}} - 1], \qquad \lambda_{p,l} = U_{p,l} M_l U_{p,l}^t. \tag{24}$$

As $(U_{p,l})_{p\in[0,n_{\text{seg}}-1]}$ forms a modal basis, the error phase segment coefficients A, which provides a final contrast C, can be expressed in an unique way as a function of these Eigen modes

$$A = \sum_{p=0}^{n_{\text{seg}}-1} \sigma_p U_{p,l}, \tag{25}$$

where σ_p is the contribution of the mode p.

The projection of the error phase Φ on each Eigen mode $U_{p,l}$ contributes as much as C_p to the final contrast.

$(U_{p,l})_{p\in[0,n_{\text{seg}}-1]}$ forming a basis of orthonormal vectors, the final contrast is indeed the sum of the contrasts generated by the different projections on the modes

$$C = \sum_{p=0}^{n_{\text{seg}}-1} C_p. \tag{26}$$

Therefore, we have

$$\forall\ p \in [0, n_{\text{seg}} - 1], \qquad C_p = (\sigma_p U_{p,l}) M_l (\sigma_p U_{p,l})^t, \tag{27}$$

$$= \sigma_p^2 \lambda_{p,l}. \tag{28}$$

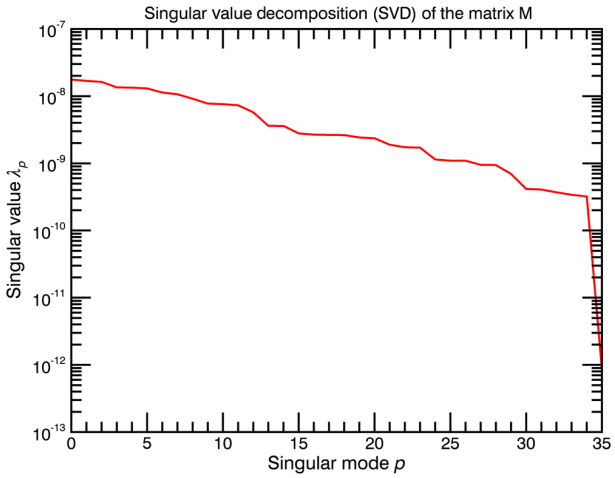

Fig. 9 Eigen values of the matrix M_1 in the segment-level piston case. The last eigen value, extremely lower than the others, corresponds to an eigen mode of a global piston on the primary mirror.

As a conclusion, to get a contribution to contrast smaller than C_p on the p'th mode, the projection of the phase on this mode has to be smaller than

$$\sigma_p = \sqrt{\frac{C_p}{\lambda_{p,l}}}. \tag{29}$$

4.2 *Strategy*

Hereafter, we define the contrast as a sum of a static contribution and a dynamic contribution

$$C = C^s \pm \Delta C. \tag{30}$$

We assume that the coronagraphic contrast is on the order of 10^{-10} in the dark hole, but we require system stability sufficient to support improving the contrast to 10^{-10}. Therefore, we make the assumptions that

$$\begin{cases} C^s = 10^{-10} \\ \Delta C = 10^{-10} \end{cases}. \tag{31}$$

Furthermore, the assumption is made that all the modes (except for the one with an extremely low eigen value) contribute equally and independently to the contrast and its stability. Therefore, we formulate the hypotheses

$$\begin{cases} C^s_p = \frac{C^s_p}{35} \\ \Delta C_p = \frac{\Delta C}{\sqrt{35}} \end{cases}. \tag{32}$$

Equation (29) provides both the mode contributions $(\sigma_p)_{p\in[0,n_{\text{seg}}-1]}$ that would generate such contrasts on each mode, and the mode contributions in terms of stability $(\Delta\sigma_p)_{p\in[0,n_{\text{seg}}-1]}$.

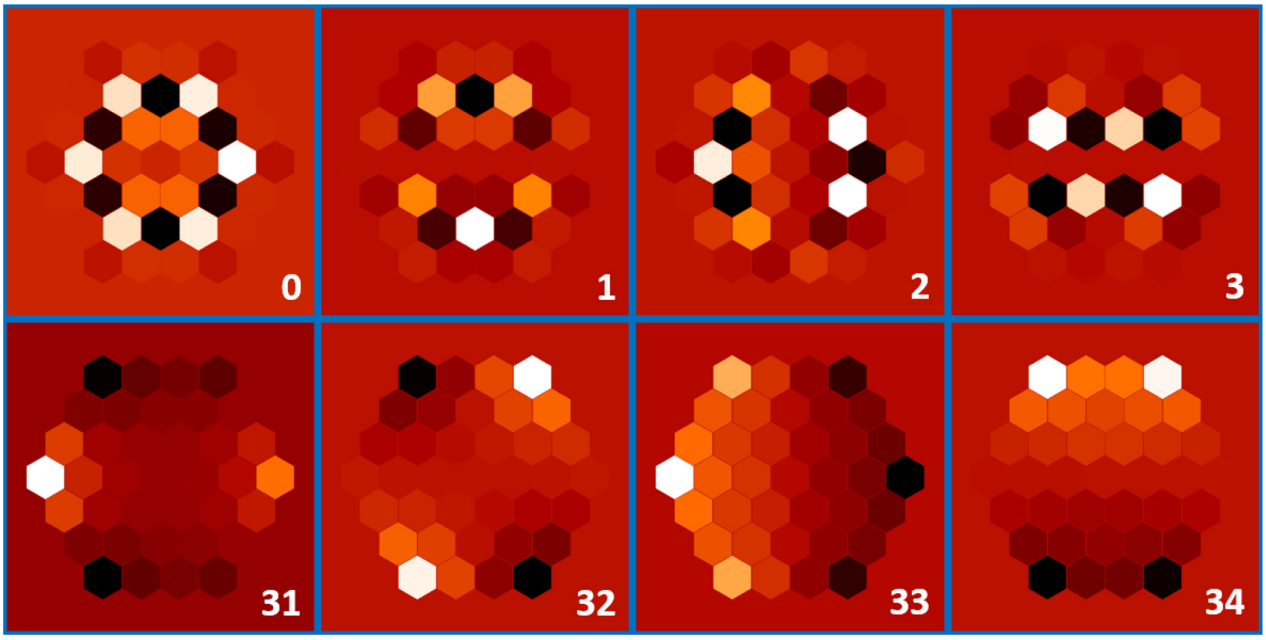

Fig. 10 Eigen modes in the local only piston case. The top line corresponds to the four modes with the highest eigen values, the bottom line to four of the modes with the lowest eigen values. In this second line, we can recognize discrete versions of some common low-order Zernike polynomials: the two astigmatisms and the tip and tilt. Furthermore, the last modes focus more on the corner segments that are typically the segments that impact the contrast the least as they are the most obscured by both the apodizer and the Lyot stop. Conversely, on the top line, we can also see that the segments with the most extreme piston coefficients correspond to the segments hidden by neither the apodizer nor the Lyot stop, and so are the segments that influence the contrast the most. This explains why they have the highest eigen values.

The latter sections impose the system stability requirements for piston and 45-deg astigmatism.

4.3 *Illustration in the Case of Local Pistons in the Pupil*

4.3.1 *Eigen modes*

In the piston case, $C = a_1 M_1 a_1^t$. A singular value decomposition (SVD) is applied to the matrix M_1, the eigen values are shown in Fig. 9. Figure 10 shows a few eigen modes computed from this SVD: on top, the four modes attached to the highest eigen values of M_1, and on the bottom, the four modes attached to low eigen values. The very last mode, which has an extremely low eigen value, is not indicated here and corresponds to a global piston on the primary mirror.

From this SVD, we can see that the last eigen modes correspond to discretized global low-order Zernike polynomials, the two astigmatisms (modes 31 and 32) and the tip and tilt (modes 33 and 34). We find that the lowest sensitivity modes of our simplified model are the discretized low-order Zernike modes tip and tilt, which the APLC has been designed to be robust to. This consolidates the realism of our analytical model PASTIS. Furthermore, the very last mode, not indicated in Fig. 10, is a global piston on the entire pupil, which has here an extremely low eigen value and is known not to affect the contrast in a realistic coronagraph. The highest eigen values correspond to the modes that affect the contrast the most, a combination of segments of the second ring, which are known to be the least apodized and the least hidden by the Lyot stop. In particular, we can conclude that these modes are specific to the chosen coronagraph.

4.3.2 *Constraints on phasing*

The hypotheses and strategy to compute the static constraints on the modes are indicated in Sec. 4.2.

After applying Eq. (29), we obtain the results indicated in Fig. 11: on the left, the mode contributions $(\sigma_p)_{p\in[0,n_{seg}-1]}$ that generate such contrasts are indicated and on the right, the cumulative contrasts generated by these constraints are shown. Each mode contributes equally to the contrast and the final contrast is $C = 10^{-10}$, which were our hypotheses. We also indicated here the cumulative contrasts when these constraints are injected as inputs of the end-to-end simulation, and despite an error on the final contrast of 3.75%, we can

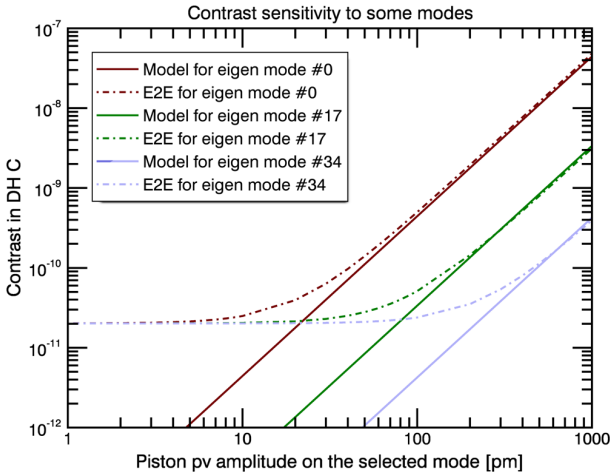

Fig. 12 Contrast as a function of the amplitude on three different piston modes, for both the E2E simulation and the matrix-based analytical model. The red curves correspond to the mode 0, which has the highest eigen value so the highest influence on the contrast. As a consequence, its constraints to reach a target contrast are tougher than the constraints obtained for any other mode. The green curves correspond to the intermediate piston mode 17, and the blue curves correspond to the mode with the lowest eigen value: as a consequence, its constraints are relaxed.

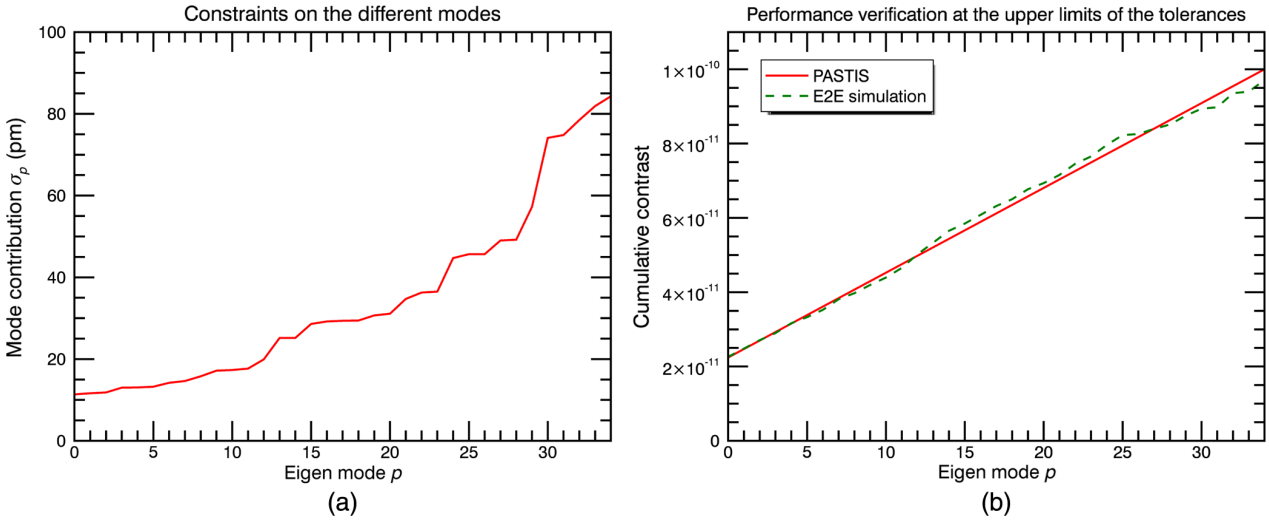

Fig. 11 (a) Contributions $(\sigma_p)_{p\in[0,n_{seg}-1]}$ on the different piston modes to reach a final target contrast of 10^{-10}, in the case where only local pistons on segments deteriorate the contrast. (b) Cumulative contrasts on these piston modes at their upper constraints to reach a final target contrast of 10^{-10}. In these two plots, only 35 modes are indicated as the mode with a very low eigen value corresponds to a global piston on the pupil and is chosen to not contribute to the final contrast.

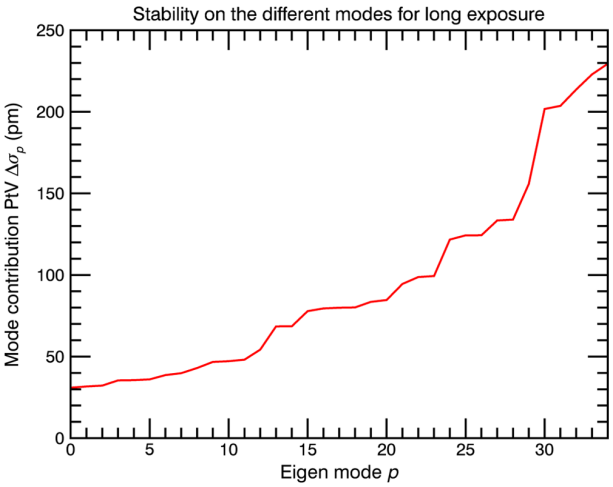

Fig. 13 Stability coefficients on the different piston modes to reach a final target stability on contrast of 10^{-10} on a long exposure, in the case where only local pistons on segments deteriorate the contrast.

Table 1 Absolute and stability constraints on three different modes for a contrast better than 10^{-10} stabilized at 10^{-10}.

Mode number p	0	17	34
Maximum mode contribution σ_p (pm)	11.36	29.37	84.30
Maximum stability mode contribution $\Delta\sigma_p$ (pm)	30.93	79.95	229.47

conclude that this method to compute the tolerances is relevant and useful.

In the general case, the mode contributions $(\sigma_p)_{p\in[0,n_{\text{seg}}-1]}$ both depend on the mode p and on the contrast to reach in each mode $(C_p)_{p\in[0,n_{\text{seg}}-1]}$. Figure 12 shows the contrast C_p as a function of the contribution σ_p for three different modes. The constraints clearly depend on the modes, the first modes requiring tighter constraints.

4.3.3 *Quasistatic stability*

In this section, the same inversion of the analytical model is applied to the contrast stability, which is ensured by the stability of the segment aberrations. The hypotheses and strategy were indicated in Sec. 4.2.

We then obtain the constraints per mode in stability indicated in Fig. 13. We mainly notice that the most constraining modes require a stability of around 30 pm.

In this example, for a contrast better than 10^{-10} stabilized at 10^{-10}, the constraints for the modes 0, 17, and 34 are shown in Table 1.

4.4 *Illustration in the Case of Local 45-deg Astigmatisms in the Pupil*

Now, we consider constraints on local 45-deg astigmatisms on the segments. Once again, the performance to achieve in the dark hole with the coronagraph only is $10^{-10} \pm 10^{-10}$.

A few selected eigen modes are shown in Fig. 14. Like in the piston case, the first eigen modes focus on the second ring, i.e., the only one not hidden by the Lyot stop and the least apodized.

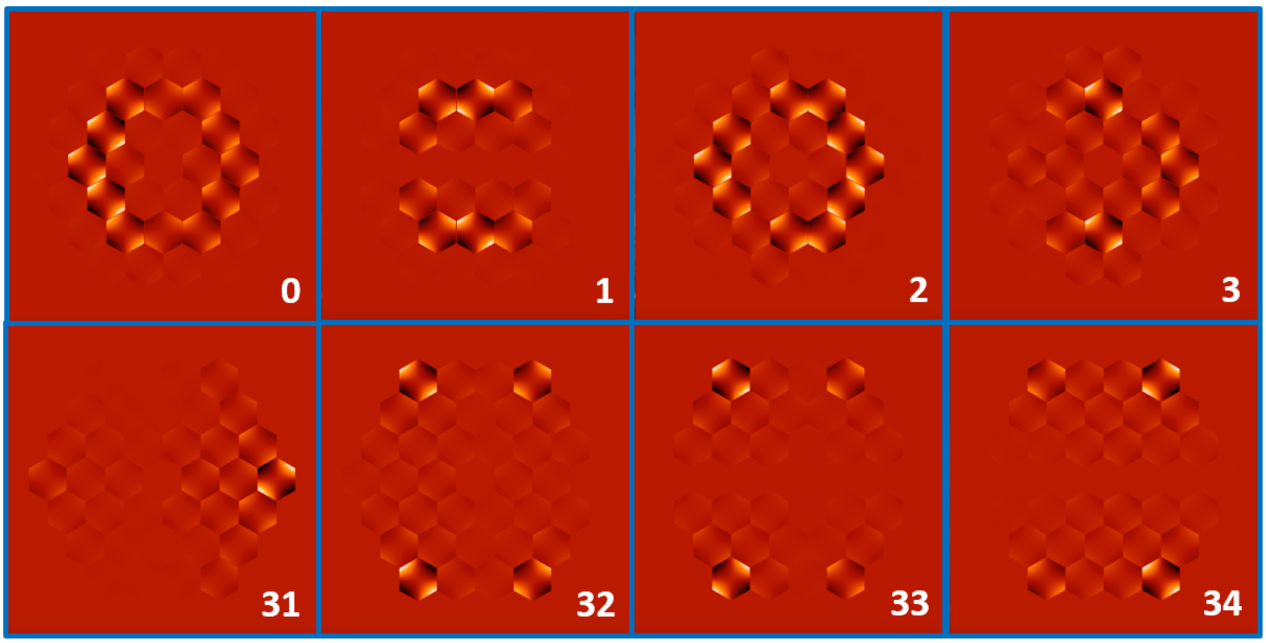

Fig. 14 Eigen modes in the local only 45-deg astigmatism case. The top line corresponds to the four modes with the highest eigen values, the bottom line to four of the modes with the lowest eigen values. On the top line, we can see that the segments with the most extreme 45-deg astigmatism coefficients correspond to the segments hidden by neither the apodizer nor the Lyot stop, so the segments that influence the contrast the most, which explains why they have the highest eigen values. On the opposite, the modes of the second line focus on the corner segments only, which are the segments the most hidden by both the Lyot stop and the apodizer.

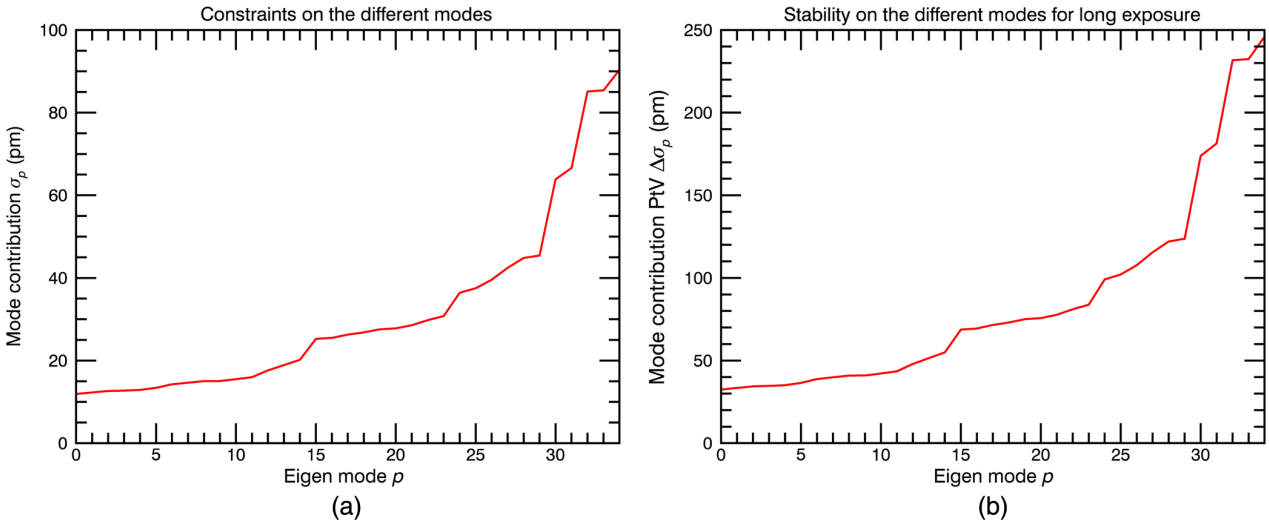

Fig. 15 (a) Contributions $(\sigma_p)_{p\in[0,n_{seg}-1]}$ on the different 45-deg astigmatism modes to reach a final target contrast of 10^{-10}, in the case where only local 45-deg astigmatisms on segments deteriorate the contrast. (b) Stability coefficients $(\Delta\sigma_p)_{p\in[0,n_{seg}-1]}$ on the different 45-deg astigmatism modes to reach a final target stability of 10^{-10} on a long exposure.

On the opposite, the last modes correspond to the corner segments, which are both the most hidden by the Lyot stop and the most apodized. We can conclude that the second ring, like in the piston case, requires the tightest constraints in manufacturing and alignment and might require special consideration in backplane design. This conclusion would not have been formulated with a traditional error budget based on numerous end-to-end simulations. It is here shown that another advantage of the model is its ability to build a comprehensive analysis of the impact of each perturbation term.

The numerical results in terms of sensibility analysis on the different modes are shown in Fig. 15. We can observe that the constraints are tighter or equal to the ones on piston on the first eigen modes, but looser on the last modes.

These last two applications are just some examples of the use of the analytical model for sensitivity analysis. They also illustrate the gain in time and in understanding that such a formal inversion would provide compared with multiple end-to-end simulations in error budgeting. They can also provide a better understanding of the constraint geometry of the primary mirror, to design, for example, an adequate backplane, edge sensor placement, or laser truss geometry.

5 Conclusions

In this paper, we have introduced an analytical model, PASTIS, i.e., the basis of a method for tolerancing of segmented telescopes with high-contrast instruments, both in terms of segment alignment and stability. The formalism has been validated for one kind of local Zernike polynomial at a time on the segments, using comparisons between its outputs and the images and contrasts determined from the simulation of an end-to-end propagation through a coronagraphic system. The error between the contrasts computed from the analytical model and from the end-to-end simulation is around 3% rms. The clear advantage of the analytical model is the reduction of computation time: to compute a contrast in the dark hole, an end-to-end simulation takes around 10^7 longer than the matrix-based analytical model PASTIS. Therefore, PASTIS enables complete error budget with a significant gain of time as a traditional error budget is based on tremendous contrast computations from phases selected thanks to a Monte Carlo distribution.

However, the primary advantage of this model is that the entire method presented here is based on a simple formal inversion based on a modal analysis. This process provides an easy and fast way to estimate the tolerancing for a given contrast, but also the constraints in terms of stability. It also provides a more comprehensive analysis of the system, with the eigen modes that affect the contrast the most and required the thinnest adjustment. A better understanding of the critical modes in the primary mirror can, for example, enable an optimization of the architecture of the backplane or of the positions of edge sensors.

The next step of this study is a generalization of this analytical model to a combination of Zernike polynomials, to understand the Zernike to Zernike dependency to contrast value. Furthermore, the static or quasistatic errors on the segments are not the only issue in high-contrast imaging. The telescope vibrations or the resonant modes of the segments are a main source of instability, and therefore are important factors in the limitation of the performance. As soon as the temporal aspect is considered, a full and time-consuming end-to-end simulation becomes inconvenient, and PASTIS shows its best advantage. Finally, we plan to compare its accuracy on other coronagraphs, for example, using a Vortex coronagraph instead of an APLC.

This formalism to describe segmented pupils and generate images and contrasts is adaptable to any segmented pupils, such as the ELTs, the Thirty Meters Telescopes, the JWST, or the HabEx and LUVOIR pupils. It can also be applied to non-hexagonal-segment pupils, such as the Giant Magellan Telescope. PASTIS enables a new, fast, and efficient method for static error budget and stability analysis for all segmented telescopes.

Appendix: The Impact of the Linear Term on the Contrast

In Eq. (21), the contrast is a sum of a constant term (the deep contrast, intrinsic to the coronagraph) and a quadratic term. However, in Eq. (5), the intensity, which the contrast derives from, is a sum of a constant term, a linear term, and a quadratic term. Why can the linear term not be taken into account, while the constant term can?

The linear term is called $L(\mathbf{u})$

$$\begin{aligned} L(\mathbf{u}) &= 2\Re\left[\hat{P}^*(\mathbf{u})i\hat{Z}_l(\mathbf{u})\sum_{k=1}^{n_{\text{seg}}} a_{k,l}e^{-i\mathbf{r_k}.\mathbf{u}}\right] \\ &= 2\Re\left[\sum_{k=1}^{n_{\text{seg}}} a_{k,l}\hat{P}^*(\mathbf{u})i\hat{Z}_l(\mathbf{u})e^{-i\mathbf{r_k}.\mathbf{u}}\right] \\ &= 2\sum_{k=1}^{n_{\text{seg}}} a_{k,l}\Re[\hat{P}^*(\mathbf{u})i\hat{Z}_l(\mathbf{u})e^{-i\mathbf{r_k}.\mathbf{u}}], \end{aligned} \tag{33}$$

since the coefficients $a_{k,l}$ are real.

- P is real and symmetrical, so its Fourier transform $\hat{P}$ is also real and symmetrical, and $\hat{P}^*$ is too.
- Furthermore, we have

$$\begin{aligned} ie^{-i\mathbf{r_k}.\mathbf{u}} &= i\,\cos(-\mathbf{r_k}.\mathbf{u}) + i^2\,\sin(-\mathbf{r_k}.\mathbf{u}) \\ &= i\,\cos(\mathbf{r_k}.\mathbf{u}) + \sin(\mathbf{r_k}.\mathbf{u}). \end{aligned} \tag{34}$$

- Z_l is necessary real but can be symmetrical or antisymmetrical. We study separately these two cases

If Z_l is real and symmetrical, then $\hat{Z}_l$ is real and symmetrical. Then

$$\Re[\hat{P}(\mathbf{u})i\hat{Z}_l(\mathbf{u})e^{-i\mathbf{r_k}.\mathbf{u}}] = \hat{P}(\mathbf{u})\hat{Z}_l(\mathbf{u})\sin(\mathbf{r_k}.\mathbf{u}). \tag{35}$$

In this case, as $\hat{P}(\mathbf{u})$ and $\hat{Z}_l(\mathbf{u})$ are the symmetrical and $\sin(\mathbf{r_k}.\mathbf{u})$ antisymmetrical, then L is antisymmetrical. As a result, the contrast resulting from computing its average on a symmetrical dark hole is null.

If Z_l is a real and antisymmetrical, then $\hat{Z}_l$ is imaginary and antisymmetrical. Then

$$\Re[\hat{P}(\mathbf{u})\hat{Z}_l(\mathbf{u})e^{-i\mathbf{r_k}.\mathbf{u}}] = -\hat{P}(\mathbf{u})\Im[\hat{Z}_l(\mathbf{u})]\cos(\mathbf{r_k}.\mathbf{u}), \tag{36}$$

where $\hat{P}(\mathbf{u})$ and $\cos(\mathbf{r_k}.\mathbf{u})$ are the symmetrical, $\Im[\hat{Z}_l(\mathbf{u})]$ is antisymmetrical, so L is once again antisymmetrical and its mean contrast on a symmetrical dark hole is null.

As a conclusion, in both cases, the linear term of the initial equation provides a null contrast.

Acknowledgments

This work was supported in part by the National Aeronautics and Space Administration under Grant Nos. NNX12AG05G and NNX14AD33G issued through the Astrophysics Research and Analysis (APRA) program (PI: R. Soummer) and by Jet Propulsion Laboratory subcontract No. 1539872 (Segmented-Aperture Coronagraph Design and Analysis; PI: R. Soummer). It is also partly funded by the French Aerospace Lab (ONERA) in the frame of the VASCO Research Project and by the Laboratoire d'Astrophysique de Marseille (LAM). The authors would also like to thank Gregory Brady for his valuable comments on this paper.

References

1. C. C. Stark et al., "A direct comparison of exo-Earth yields for starshades and coronagraphs," *Proc. SPIE* **9904**, 99041U (2016).
2. G. Ruane et al., "Deep imaging search for planets forming in the TW Hya protoplanetary disk with the Keck/NIRC2 vortex coronagraph," *Astron. J.* **154**, 73 (2017).
3. D. Mawet et al., "Characterization of the inner disk around HD 141569 A from Keck/NIRC2 L-band vortex coronagraphy," *Astron. J.* **153**, 44 (2017).
4. D. Mawet et al., "Keck planet imager and characterizer: concept and phased implementation," *Proc. SPIE* **9909**, 99090D (2016).
5. A. Boccaletti et al., "The mid-infrared instrument for the James Webb space telescope, V: predicted performance of the MIRI coronagraphs," *Publ. Astron. Soc. Pac.* **127**, 633–645 (2015).
6. J. E. Krist et al., "Hunting planets and observing disks with the JWST NIRCam coronagraph," *Proc. SPIE* **6693**, 66930H (2007).
7. A. Carlotti, R. Vanderbei, and N. J. Kasdin, "Optimal pupil apodizations of apertures for high-contrast imaging," *Opt. Express* **19**, 26796 (2011).
8. J. Mazoyer et al., "Capabilities of ACAD-OSM, an active method for the correction of aperture discontinuities," *Proc. SPIE* **10400**, 104000G (2017).
9. N. T. Zimmerman et al., "Lyot coronagraph design study for large, segmented space telescope apertures," *Proc. SPIE* **9904**, 99041Y (2016).
10. L. Pueyo and C. Norman, "High-contrast imaging with an arbitrary aperture: active compensation of aperture discontinuities," *Astrophys. J.* **769**, 102 (2013).
11. O. Guyon et al., "High performance Lyot and PIAA coronagraphy for arbitrarily shaped telescope apertures," *Astrophys. J.* **780**, 171 (2014).
12. J. Krist, B. Nemati, and B. Mennesson, "Numerical modeling of the proposed WFIRST-AFTA coronagraphs and their predicted performances," *J. Astron. Telesc. Instrum. Syst.* **2**, 011003 (2016).
13. F. Shi et al., "Low order wavefront sensing and control for WFIRST coronagraph," *Proc. SPIE* **9904**, 990418 (2016).
14. P. A. Lightsey et al., "Optical performance for the actively controlled James Webb space telescope," *Proc. SPIE* **7731**, 77310B (2010).
15. P. A. Lightsey, J. S. Knight, and G. Golnik, "Status of the optical performance for the James Webb space telescope," *Proc. SPIE* **9143**, 914304 (2014).
16. B. Macintosh et al., "Extreme adaptive optics for the thirty meter telescope," *Proc. SPIE* **6272**, 62720N (2006).
17. M. E. Kasper et al., "EPICS: the exoplanet imager for the E-ELT," *Proc. SPIE* **7015**, 70151S (2008).
18. R. Davies et al., "MICADO: the E-ELT adaptive optics imaging camera," *Proc. SPIE* **7735**, 77352A (2010).
19. S. P. Quanz et al., "Direct detection of exoplanets in the $3-10\ \mu$m range with E-ELT/METIS," *Int. J. Astrobiol.* **14**, 279–289 (2015).
20. N. Yaitskova, K. Dohlen, and P. Dierickx, "Analytical study of diffraction effects in extremely large segmented telescopes," *J. Opt. Soc. Am. A* **20**, 1563–1575 (2003).
21. J. T. Trauger and W. A. Traub, "A laboratory demonstration of the capability to image an earth-like extrasolar planet," *Nature* **446**, 771–773 (2007).
22. P. Baudoz et al., "Dark hole and planet detection: laboratory results using the self-coherent camera," *Proc. SPIE* **8446**, 84468C (2012).
23. J. Mazoyer et al., "High-contrast imaging in polychromatic light with the self-coherent camera," *Astron. Astrophys.* **564**, L1 (2014).
24. J. Dalcanton et al., "From cosmic birth to living earths: the future of UVOIR space astronomy," arXiv:1507.04779 (2015).
25. L. Pueyo et al., "The LUVOIR architecture 'A' coronagraph instrument," *Proc. SPIE* **10398**, 103980F (2017).
26. B. Mennesson et al., "The habitable exoplanet (HabEx) imaging mission: preliminary science drivers and technical requirements," *Proc. SPIE* **9904**, 99040L (2016).
27. H. P. Stahl, M. Postman, and W. S. Smith, "Engineering specifications for large aperture UVO space telescopes derived from science requirements," *Proc. SPIE* **8860**, 886006 (2013).

28. M. T. Stahl, S. B. Shaklan, and H. P. Stahl, "Preliminary analysis of effect of random segment errors on coronagraph performance," *Proc. SPIE* **9605**, 96050P (2015).
29. M. A. Greenhouse, "The JWST science instrument payload: mission context and status," *Proc. SPIE* **9904**, 990406 (2016).
30. M. Clampin, "Status of the James Webb space telescope (JWST)," *Proc. SPIE* **7010**, 70100L (2008).
31. P. J. Bordé and W. A. Traub, "High-contrast imaging from space: speckle nulling in a low-aberration regime," *Astrophys. J.* **638**, 488–498 (2006).
32. F. Malbet, J. W. Yu, and M. Shao, "High-dynamic-range imaging using a deformable mirror for space coronography," *Publ. Astron. Soc. Pac.* **107**, 386 (1995).
33. A. Quirrenbach, "Coronographic methods for the detection of terrestrial planets," arXiv:astro-ph/0502254 (2005).
34. C. Cavarroc et al., "Fundamental limitations on earth-like planet detection with extremely large telescopes," *Astron. Astrophys.* **447**, 397–403 (2006).
35. P. Janin-Potiron, P. Martinez, and M. Carbillet, "Analytical decomposition of Zernike and hexagonal modes over a hexagonal segmented optical aperture," *Appl. Opt.* (2018).
36. V. N. Mahajan and G.-M. Dai, "Orthonormal polynomials for hexagonal pupils," *Opt. Lett.* **31**, 2462–2464 (2006).
37. P. Janin-Potiron, "Active correction of pupil discontinuities on segmented telescopes for high contrast imaging and high angular resolution," Thesis, Université Côte d'Azur (2017).
38. M. Born and E. Wolf, *Principles of Optics: Electromagnetic Theory of Propagation, Interference and Diffraction of Light*, Cambridge University Press, Cambridge (1999).
39. P. G. Tuthill et al., "Michelson interferometry with the Keck I telescope," *Publ. Astron. Soc. Pac.* **112**, 555–565 (2000).
40. S. Lacour et al., "Sparse aperture masking at the VLT. I. Faint companion detection limits for the two debris disk stars HD 92945 and HD 141569," *Astron. Astrophys.* **532**, A72 (2011).
41. M. Postman et al., "Advanced technology large-aperture space telescope: science drivers and technology developments," *Opt. Eng.* **51**, 011007 (2012).
42. L. D. Feinberg et al., "A cost-effective and serviceable ATLAST 9.2m telescope architecture," *Proc. SPIE* **9143**, 914316 (2014).
43. B. Paul et al., "Simultaneous phase and amplitude retrieval with COFFEE: from theory to laboratory results," *Proc. SPIE* **9147**, 91479O (2014).
44. R. Soummer, C. Aime, and P. E. Falloon, "Stellar coronagraphy with prolate apodized circular apertures," *Astron. Astrophys.* **397**, 1161–1172 (2003).
45. M. N'Diaye, L. Pueyo, and R. Soummer, "Apodized pupil Lyot coronagraphs for arbitrary apertures. IV. Reduced inner working angle and increased robustness to low-order aberrations," *Astrophys. J.* **799**, 225 (2015).
46. M. N'Diaye et al., "Apodized Pupil Lyot coronagraphs for arbitrary apertures. V. Hybrid shaped pupil designs for imaging earth-like planets with future space observatories," *Astrophys. J.* **818**, 163 (2016).
47. H. P. Stahl, "Advanced mirror technology development (AMTD) project: overview and year four accomplishments," *Proc. SPIE* **9912**, 99120S (2016).
48. M. T. Stahl, H. P. Stahl, and S. B. Shaklan, "Contrast leakage as a function of telescope motion," in *Mirror Technology/SBIR/STTR Workshop* (2016).

Biographies for the authors are not available.

4.2.2 Case of segment-level higher order aberrations

The application of the PASTIS model developed so far remains quite restrictive, since only one Zernike polynomial is allowed on the segments. But the errors coming from a segmented aperture might contain higher orders, like tip-tilt (orientation of the segments), focus or astigmatism on each segment. First, these higher-order segment-level aberrations are not negligible compared to the piston case, but their contributions to the contrast are not simply additive (see later). These are the reasons why I chose to address this problematic in this thesis. I then propose to extend the PASTIS model to segment-level aberrations decomposed over several Zernike polynomials. This development will be illustrated with the case of classical phasing errors, ie. a combination of piston, tip, and tilt errors on the segments.

This section derives from the proceeding Leboulleux et al. (2018a), also available in the appendix B.

4.2.2.1 Formalism development

We use the expression of the phase of Eq. 9 of the article (see section 4.2), without simplifying it to the case of one single Zernike polynomial. We obtain the following general expression:

$$\hat{\phi}(\mathbf{u}) = \sum_{l=1}^{n_{zer}} \sum_{k=1}^{n_{seg}} a_{k,l} \hat{Z}_l e^{-i\mathbf{r_k}.\mathbf{u}} \tag{4.7}$$

Eq. 7 of the section 4.2 stipulates that $I(\mathbf{u}) = \left\| \hat{\phi}(\mathbf{u}) \right\|^2$. Combining this equation and Eq. 4.7 provides:

$$\begin{aligned} I(\mathbf{u}) &= [\sum_{l_1=1}^{n_{zer}} \sum_{k_1=1}^{n_{seg}} a_{k_1,l_1} \widehat{Z_{l_1}} e^{-i\mathbf{r_{k_1}}.\mathbf{u}}] \times [\sum_{l_2=1}^{n_{zer}} \sum_{k_2=1}^{n_{seg}} a_{k_2,l_2} \widehat{Z_{l_2}}^* e^{i\mathbf{r_{k_2}}.\mathbf{u}}] \\ &= \sum_{l_1=1}^{n_{zer}} \sum_{l_2=1}^{n_{zer}} \widehat{Z_{l_1}}.\widehat{Z_{l_2}}^* \sum_{k_1=1}^{n_{seg}} \sum_{k_2=1}^{n_{seg}} a_{k_1,l_1} a_{k_2,l_2} e^{i(\mathbf{r_{k_2}}-\mathbf{r_{k_1}}).\mathbf{u}} \end{aligned} \tag{4.8}$$

The Zernike polynomials are real and either even or odd, so their Fourier transform are either real or imaginary. Therefore, the envelopes $\widehat{Z_{l_1}}.\widehat{Z_{l_2}}^*$ are either real or imaginary. On the other hand, we have $e^{i(\mathbf{r_{k_2}}-\mathbf{r_{k_1}}).\mathbf{u}} = \cos((\mathbf{r_{k_2}}-\mathbf{r_{k_1}}).\mathbf{u}) + i\sin((\mathbf{r_{k_2}}-\mathbf{r_{k_1}}).\mathbf{u})$ and we know that the product of the envelope and $e^{i(\mathbf{r_{k_2}}-\mathbf{r_{k_1}}).\mathbf{u}}$ is real, since the intensity is real. We conclude that this expression is in practice sums of interference fringes between all pairs of segments, modulated by low-frequency envelopes.

By averaging this last equation over the dark hole and taking the calibration coefficients $(c_{k,l})_{k\in[1,n_{seg}]}$ into account, we obtain:

$$C = C_0 + AMA^t \tag{4.9}$$

where:

$$\begin{aligned} A &= \begin{bmatrix} A_1 & ... & A_{n_{Zer}} \end{bmatrix} \\ &= \begin{bmatrix} a_{1,1} & ... & a_{n_{seg},1} & ... & a_{1,n_{Zer}} & ... & a_{n_{seg},n_{Zer}} \end{bmatrix} \\ M &= \begin{bmatrix} M_{1,1} & ... & M_{1,n_{Zer}} \\ & ... & \\ M_{n_{Zer},1} & ... & M_{n_{Zer},n_{Zer}} \end{bmatrix} \end{aligned} \tag{4.10}$$

A is a concatenation of all the vectors A_l, while M is a block-diagonal matrix made of submatrices M_{l_1,l_2}, containing the coefficients:

$$\begin{aligned} M_{l_1,l_2}[k_1,k_2] &= m_{k_1,k_2,l_1,l_2} \\ &= c_{k_1,l_1} c_{k_2,l_2} \langle \widehat{Z_{l_1}} . \widehat{Z_{l_2}}^* e^{i(\mathbf{r_{k_2}} - \mathbf{r_{k_1}}).\mathbf{u}} \rangle_{DH} \end{aligned} \tag{4.11}$$

We find here an expression extremely similar to the equation 21 of the article, but generalized to the case of a combination of segment-level Zernike polynomials. The only difference is a longer A vector and a block matrix M. The conclusion of the article are therefore preserved, and the possible application to the error budget of a segmented telescope too. We propose a first application to combination of piston-tip-tilt errors in the next section.

4.2.2.2 Application to the case of segment-level pistons, tips, and tilts

We propose here an application of the previous formalism to the complete case of a phasing error, ie. including piston but also tip and tilt residuals.

The segments are not co-aligned and also present orientation errors one with another. Similarly to the case of phasing errors presented in the article, we first compare quickly the contrasts computed by PASTIS to the contrasts computed by the end-to-end simulations.

Fig. 4.2.1 provides a comparison between the contrasts computed by PASTIS and by the end-to-end simulation, in the case of cophasing errors combining local piston, tip, and tilt errors on the segments. We plot here the average contrasts computed from sets of 5 random phases, for sets from 1 pm to 1 nm rms. Each contrast is computed with both techniques: PASTIS (continuous red line) and the end-to-end simulation (dashed blut line). The error between all (not only averaged) PASTIS contrasts and end-to-end contrasts around 1.4% rms, computed from 1355 tests.

Fig. 4.2.3 indicates on a same plot the contributions to the contrast of the different Zernike polynomials: piston-tip-tilt, piston, tip, tilt, and tip-tilt. The wavefront error (in picometers rms) is obtained from computing the rms of the phase in the pupil mask only. We can notice that for a given rms error, the piston has a lower impact on the contrast than the tip and tilt. Indeed, between 20 pm and 1 nm, the piston-tip-tilt contrasts are in average 1.7 times higher than the piston only contrasts. Oppositely, on the same range, the tip and tilt contrasts are in average 1.2 times higher than the piston-tip-tilt contrasts, and 2.1 times

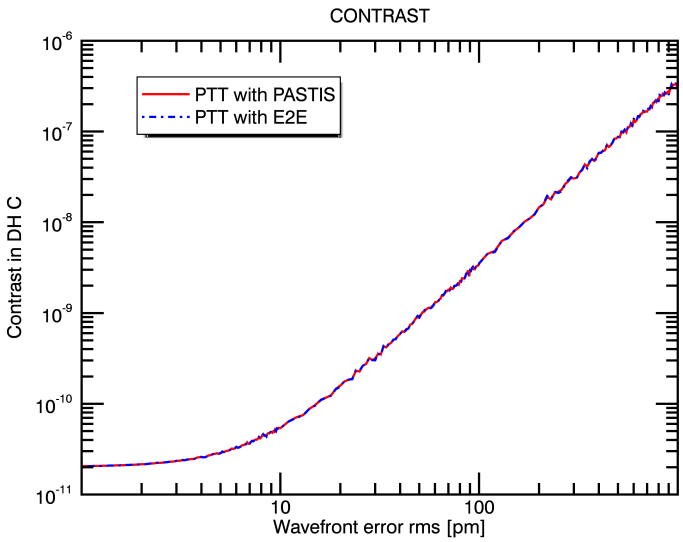

Figure 4.2.1: Contrast as a function of the rms piston-tip-tilt aberrations on the segments. It was computed through two methods: the end-to-end model (dashed blue lines) and PASTIS (continuous red lines). For each rms value, 5 random phases are selected, so 5 contrasts computed, and the average values of these 5 contrasts are plotted.

higher than the piston only contrasts. We can conclude that for a given wave-front error amplitude, the tip and tilt impact more significantly the final performance of the system, and so the control of the tip and tilt aberrations is more crucial than the control of the piston aberrations.

Fig. 4.2.3 indicates the relative contributions to the contrast of the different Zernike polynomials. For a given set of Zernike coefficients on all segments A, we compute the final contrast using PASTIS, but also the contrast that would have resulted from the piston only contribution (first 36 elements of A), tip only contribution (second 36 elements of A), tilt only contribution (last 36 elements of A), and tip-tilt contribution.

Several conclusions can be deduced from this plot. First, we can notice that the contrasts of each Zernike polynomial are not additive: the total contrast (all three Zernike polynomials taken into account) is smaller than the sum of the three independent contrasts (piston aberrations only, tip aberrations only, tilt aberrations only). This comes from cross-term between the Zernike polynomials, which correspond to non-diagonal blocks of the matrix M. If the contrast were additive, then the matrix M would only have diagonal blocks, which correspond to M_{piston}, M_{tip}, and M_{tilt}, and all non-diagonal blocks would be null.

Secondly, as in the previous plot, we notice a significant difference of impact between on one hand piston and on the other hand tip and tilt. Indeed, in average the contrasts from the piston contribution only represent 16.4% of the final contrasts, while the contrasts from the tip and tilt contributions respectively represent 52.3% and 51.5% of the final contrasts.

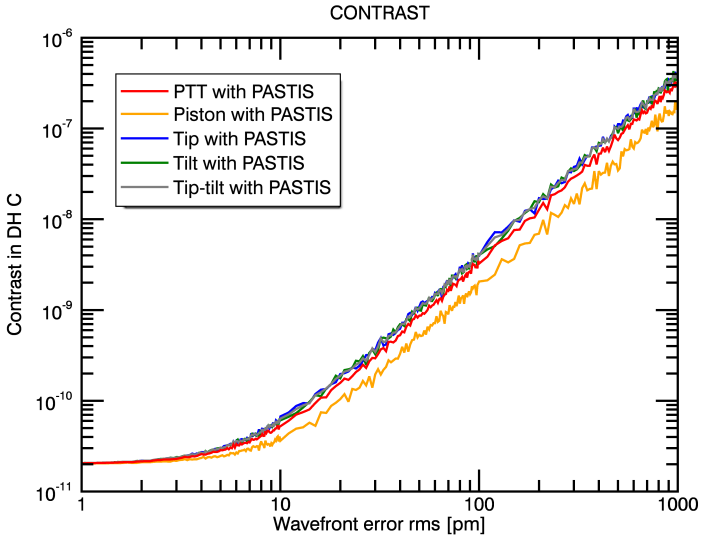

Figure 4.2.2: Contrast as a function of the rms piston-tip-tilt aberrations on the segments. 1355 random phases between 1 pm and 1 nm are considered and we compute from them the final contrasts (PTT, in red), with the contributions of the different Zernike polynomials: piston (green), tip (blue), tilt (orange), and tip-tilt combination (grey).

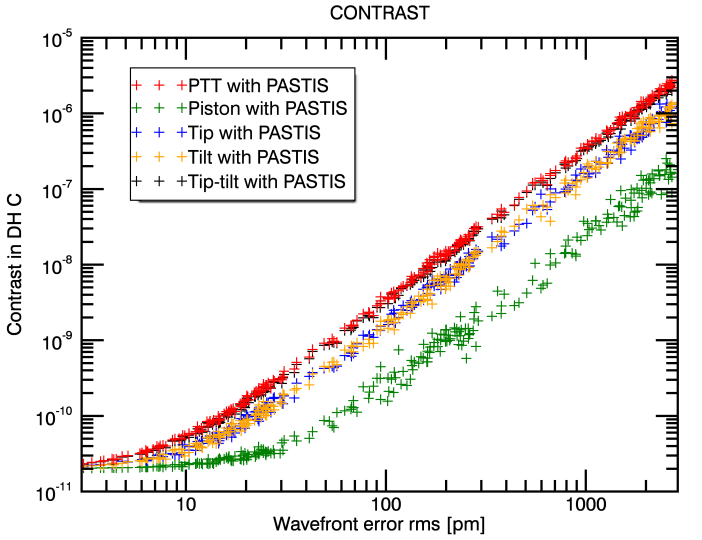

Figure 4.2.3: Contrast as a function of the rms piston-tip-tilt aberrations on the segments. 271 random phases between 1 pm and 1 nm are considered and we compute from them the final contrasts (PTT, in red), with the contributions of the different Zernike polynomials: piston (green), tip (blue), tilt (orange), and tip-tilt combination (grey).

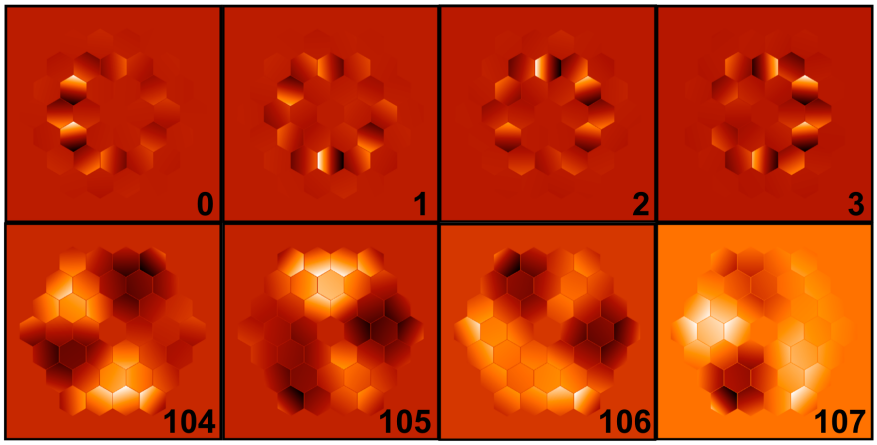

Figure 4.2.4: Some eigen modes in the piston-tip-tilt case. Top: the four modes with the highest eigen values. Tip and tilt errors appear to have a bigger impact on the contrast. Bottom: the four modes with the lowest eigen values, which correspond to low-order aberrations.

In average, the tip-tilt combination contributes by itself up to 93.7% to the final contrast. Once again, the sum is not equal to 100% because of the non-additivity of the contrasts, discussed in the previous paragraph. We can deduce here that the control of the tip-tilt is more crucial than the control of the piston, since the tip-tilt errors impact the contrast almost 6 times more than piston only errors.

This phenomenon can find an origin in the shapes of the different envelopes. Indeed, as seen in Fig. 4 of the JATIS article, the piston envelope has its maximum at the center of the PSF, ie. out of the dark hole. On the opposite, the tip and tilt envelopes both have two maxima, both located inside the dark hole. Since the degradation of the contrast is proportional to these envelopes, Zernike polynomials with envelopes higher in the dark hole should have a higher impact in the performance.

Once again, we can apply a Singular Value Decomposition on the matrix M in order to identify the eigen modes of the segmented apertures including piston tip and tilts and to provide a sensitivity analysis. We can derive the 3×36 eigen modes of the chosen telescope. This information enables a better understanding of the phasing structures that deteriorate the contrast the most. Fig. 4.2.4 gives some of these eigen modes for the chosen telescope, the top ones corresponding to the ones with the highest eigen values, so impacting the contrast the most, and the bottom ones corresponding to the ones with the smallest eigen values, so impacting the contrast the least. We can deduce from this figure that the control of the tip-tilt on the second ring, mainly for one every two segments, is primordial. On the opposite, the last modes indicate that the coronagraph is highly resistant to global low-order aberrations. Such an information can be determinant when it comes to choose a coronagraph between several options providing otherwise similar performance or to optimize the backplane architecture or the sensitivity of specific edge sensors to avoid the dominant modes.

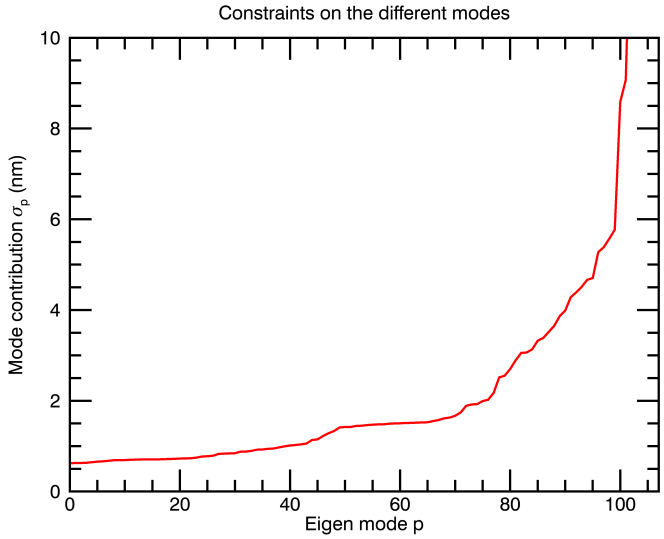

Figure 4.2.5: Contributions $(\sigma_p)_{p\in[0,n_{seg}-1]}$ on the different piston-tip-tilt modes to reach a final target contrast of 10^{-6}.

Like in the one single Zernike polynomial case of the JATIS article, it is also possible to obtain constraints to respect on each mode to achieve a target constraint. Fig. 4.2.5 provides the constraints per mode to achieve a contrast of 10^{-6} in the dark hole. We can notice that the 40 first modes are quite equivalent in term of constraints (between 0.5 nm and 1 nm rms), while the modes higher than 100^{th} seem less impacting when it comes to cophasing (constraints lower than 8 nm rms), and their constraints can be released.

4.2.3 Case of vibrating segments

A segmented telescope suffers from dynamic aberrations: the segments move at different temporal scale. The causes of such motions can be diverse: cryocoolers, motors, thermal drifts, or even resonance effects. They result in piston, tip, and tilt motions, but also in higher-order deformations (focus, astigmatism...). When a telescope' alignment constraints are of a few picometers as they are on LUVOIR, taking into account these motions is capital, and so is their modelization to understand and quantify their impact on the final performance.

Two main temporal scales can be identify when it comes to telescope and performance stability: motions that evolve by far faster than the exposure time and motions that evolve at the order of speed to lower than the exposure time. In this section, I focus on the first temporal scale, and I call the corresponding motions "vibrations". To take them into account in the model and performance estimation, I propose an extension of the PASTIS model based on an average over time. Indeed we will not consider a snapshot image or an

image obtained with static aberrations only, but an image integrated over an exposure time T_{exp}.

In this situation, PASTIS shows its main advantage. Indeed, the end-to-end simulation would require $T_{exp} \times F$ iterations to provide the contrast of one single long exposure image, where F corresponds to the number of images reconstructed by second to simulate the long exposure shot, while PASTIS, as we will see in this section, remains one single operation.

We also study one specific application, where all segments vibrate at the same frequency $f = 87.3$ Hz around the flat position but with different amplitudes and phase delays.

Once again, this section derives from the proceeding Leboulleux et al. (2018a), available on the appendix B.

4.2.4 Formalism development

In Eq. 21 of the article of section 4.2, we express the contrast as follows:

$$C = C_0 + a_l M_l a_l^t, \tag{4.12}$$

where A_l is the vector containing all the Zernike polynomial coefficients and M_l a constant matrix of the system. In the dynamical case, the Zernike coefficients depends on time and this equation becomes :

$$\begin{aligned} C(t) &= C_0 + A_l(t) M_l A_l(t)^t \\ &= C_0 + \sum_{k_1=1}^{n_{seg}} \sum_{k_2=1}^{n_{seg}} a_{k_1,l}(t) a_{k_2,l}(t) m_{k_1,k_2,l} \end{aligned} \tag{4.13}$$

where t is the time variable. After a long exposure time, the integrated image has a contrast C in the dark hole that corresponds to the average of the contrasts of all the intermediate images.

$$\begin{aligned} C &= \langle C(t) \rangle_{T_{exp}} \\ &= C_0 + \sum_{k_1=1}^{n_{seg}} \sum_{k_2=1}^{n_{seg}} \langle a_{k_1,l}(t) a_{k_2,l}(t) \rangle_{T_{exp}} m_{k_1,k_2,l} \end{aligned} \tag{4.14}$$

where T_{exp} is the exposure time. I can not go further with this expression without doing some assumptions on the temporal evolution of the Zernike coefficients. In the following section I will focus on correlated vibrations of segments. In this case, all segments vibrate around the flat position at the same frequency with a simple temporal phase difference between each other.

$$\forall k \in [1, n_{seg}], a_{k,l}(t) = \tilde{a}_{k,l} cos(ft + \phi_{k,l}) \tag{4.15}$$

In the appendix C, it is demonstrated that:

$$\forall (k_1, k_2) \in [1, n_{seg}]^2, \langle a_{k_1,l}(t) a_{k_2,l}(t) \rangle_{T_{exp}} = \frac{cos(\phi_{k_1,l} - \phi_{k_2,l})}{2} \tilde{a}_{k_1,l} \tilde{a}_{k_2,l} \tag{4.16}$$

Therefore, Eq. 4.14 becomes:

$$\begin{aligned} C &= C_0 + \sum_{k_1=1}^{n_{seg}} \sum_{k_2=1}^{n_{seg}} \tilde{a}_{k_1,l} \tilde{a}_{k_2,l} \frac{cos(\phi_{k_1,l} - \phi_{k_2,l})}{2} m_{k_1,k_2,l} \\ &= C_0 + \tilde{A}_l M'_l \tilde{A}_l^t \end{aligned} \tag{4.17}$$

where $\tilde{A}k, l$ contains all the vibration amplitudes for each mode and each segment $\tilde{a_{k,l}}$ and $\forall (i,j) \in [1, n_{seg}]^2, M'_l[i,j] = \frac{cos(\phi_{i,l} - \phi_{j,l})}{2} M_l[i,j]$.

4.2.4.1 Numerical application to segment piston vibrations

In this section we begin with a numerical validation of our formulae. We compare the contrast averaged over time using the Eq. 4.17 with the average contrast of consecutive contrasts computed with the static expression of PASTIS (Eq. 4.12).

The application case consists in piston-like vibrations of frequency $f = 87.3$Hz (this corresponds to the frequency of the deformation of the tests conducted on the JWST by Saif et al. (2017)). Each segment vibrate at the same frequency but with specific amplitudes and phase delay. The vibration amplitudes $\tilde{A}$ are random with a uniform distribution (rms$(\tilde{A}) = 100$ pm), and the vibration delays (ϕ_k) are random (uniform distribution) between $-\pi$ and π. The exposure time is $T_{exp} = 0.1$ s, which respects the condition of $T_{exp} >> 1/f$. Also, for numerical simulations we discretize the time and describe the temporal evolution with a $1/400$ second-long time step. For a Shannon sampling, 87×2 images per second would be enough, but we take a finer sampling to certify that the vibrations are well sampled and that the numerical simulation is realistic. Fig. 4.2.6 and table 4.2.1 present the results:

- the red curves: we consider the PSF integrated up to the time t of the abscissa, which mean the average PSF of all previous successive PSFs. The red curve corresponds to the contrast of this intermediate integrated PSF at the time t. This computation method is also called "Integrated E2E" in the table.

- the green curves: we compute the contrast of the "integrated PSF" at the time t with the integrated static PASTIS equation. This computation method is also called "Integrated PASTIS-STA" in the table.

- the grey curves are constant and correspond to the dynamic contrasts computed thanks to Eq. 4.17.

In the ideal case, ie. for a 0% error on the estimation of the contrast, the red and green curves should converge towards the grey curves. In practice, in our cases we have 0.03% error. This is probably due to the time sampling, since the equation of PASTIS-DYN results

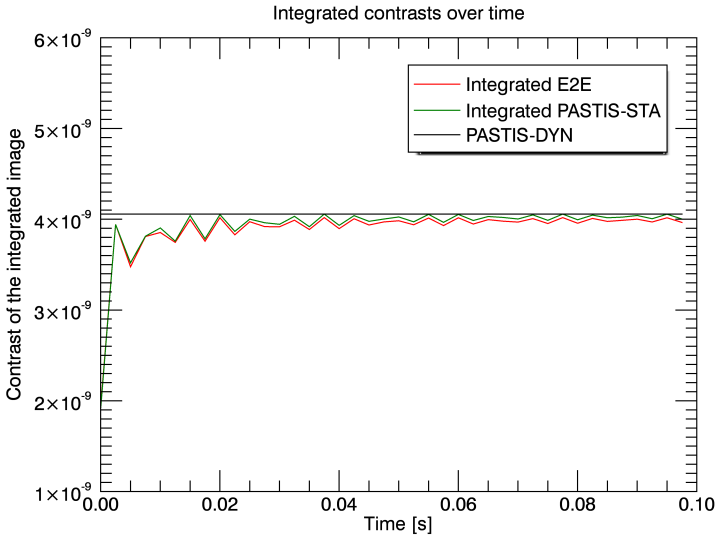

Figure 4.2.6: Example of temporal integration of the contrast, for piston-like vibrations. The segments vibrate at the frequency 87.3Hz and the amplitudes of the vibrations over all segments are 100pm. The red curve is the successive integrated contrasts computed with the E2E model. The green curve is the successive integrated contrasts computed with static PASTIS of Eq. 4.12. The grey curve is the integrated contrast computed directly from the averaged Eq. 4.17.

PASTIS-DYN	Integrated PASTIS-STA	Integrated E2E	Error between PASTIS-DYN and integrated E2E	Error between PASTIS-DYN and integrated PASTIS-STA
4.06×10^{-9}	4.00×10^{-9}	3.96×10^{-9}	2.31%	1.35%

Table 4.2.1: Contrasts and errors of the example introduced in Fig. 4.2.6.

from an absolute integration, while the integrated contrasts of the integrated PASTIS-STA and the integrated E2E results from the average of contrasts over a sampled time period, which brings a bias.

We know from the article of section 4.2 that there is a 3% error between the contrasts computed from end-to-end simulation and from PASTIS-STA, but the end-to-end simulations take 10^7 times longer to compute. Therefore, until the end of this section, we do not apply the end-to-end simulation anymore and compare PASTIS-DYN to the output of integrated PASTIS-STA only, considering that integrated PASTIS-STA provide outputs close enough to integrated end-to-end simulations.

I now apply the PASTIS-DYN equation to a concrete case of vibration of 87.3 Hz of the segments, correlated from one segment to another. Because I do not use the end-to-end model anymore but only the PASTIS equations, computations are really lighter and faster. Therefore I increase the exposure time: $T_{exp} = 5$ s to reduce as much as possible the bias due to the use of a finite and sampled time period.

We consider random $\tilde{A}$, with rms values between 1 pm and 1 nm. For each rms value, we randomly pick 1000 different amplitudes $\tilde{A}$ and 1000 different phase delays' sets (ϕ_k). To each of these configurations of segments' vibrations, we apply 1) integrated PASTIS-STA over the 5 seconds of T_{exp} and 2) PASTIS-DYN. For each rms value of $\tilde{A}$, we select the lowest contrasts computed with both methods, the mean contrasts, and the highest contrasts. Fig. 4.2.7 provides the results of this test: PASTIS-DYN gives the exact same computation than the integrated PASTIS-STA, with an error within the line's width or more precisely of $3.3 \times 10^{-5}\%$ rms, and for 1000 random sets of vibrations, the error between the outputs from PASTIS-DYN and integrated PASTIS-STA is $3.5 \times 10^{-4}\%$ rms.

Fig. 4.2.7 also indicates the contrasts that would have been obtained without vibrations (black line), ie. with equivalent (in terms of rms) static aberrations. We notice that after 20 pm, the averaged contrasts for vibrations are twice higher than the averaged contrasts for static aberrations, for equivalent wavefront error amplitudes. It then appears that vibration control are more critical than an absolute control of the static aberrations.

4.3 Application of PASTIS to JWST stability study

The JWST is the successor of the Hubble Space Telescope (HST). It is developed by NASA, with the participation of the European Space Agency (ESA) and the Canadian Space Agency (CSA). It is currently at the end of its realization phase and will be launched in Spring 2020. During its transition to its destination, which lasts around one month, the telescope is progressively deployed. Its destination is the L2 Lagrangian point of the Sun-Earth system, which is located at 1.5 million kilometers from Earth. One of the key steps between JWST deployment and its first light will be the cophasing of the primary mirror segments, which requires a complete and confident error budget.

Several studies are being conducted. For instance, at Goddard Space Flight Center (GSFC), experiments are being conducted on segment-level aberrations [Saif et al. (2017)],

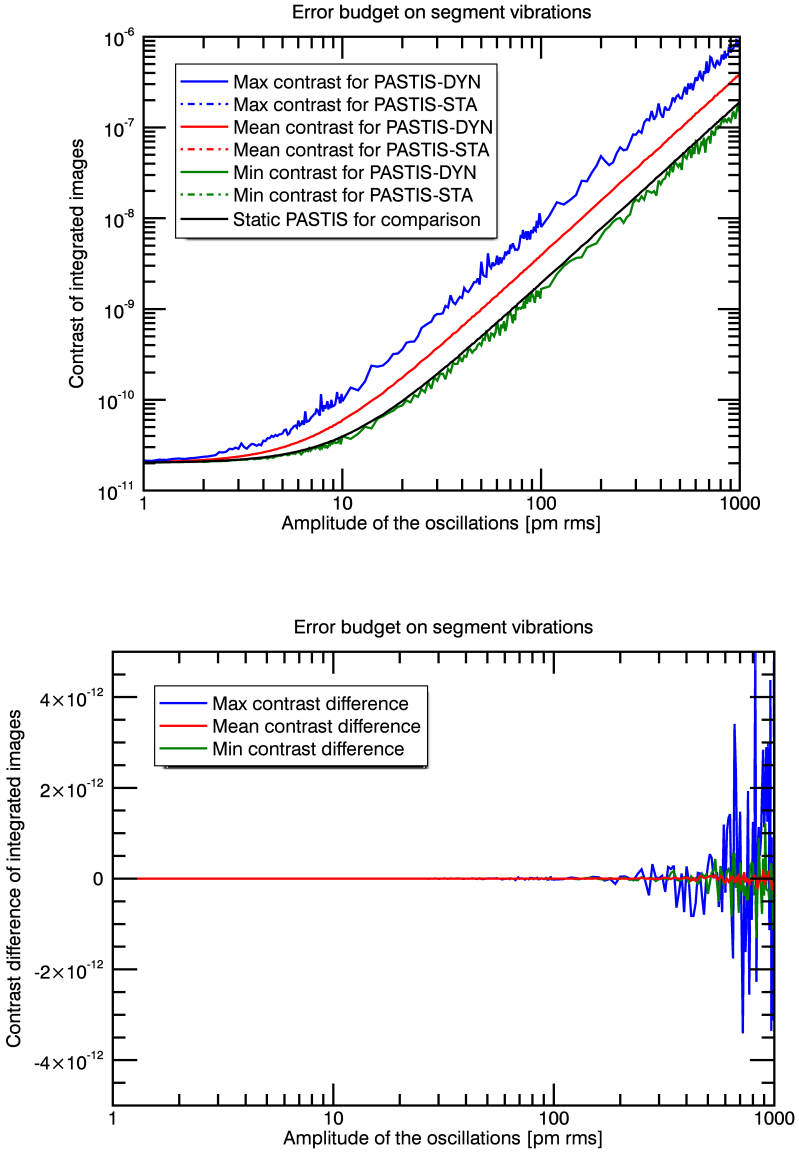

Figure 4.2.7: (Top) Contrast as a function of the rms piston-like vibrations on the segments. It was computed through two methods: the average of successive PASTIS-STA models (dashed lines) and the PASTIS-DYN model (continuous lines). For each rms value, 1000 random phases are selected, and we indicated the mean contrasts of this set (red), the minimum contrasts (green), and the maximum contrasts (blue). The black line indicates the static contrast $C_0 + \tilde{A}M\tilde{A}$ we would get if the vibrations amplitudes $\tilde{A}$ were static aberrations. (Bottom) Differences between the PASTIS-STA and PASTIS-DYN contrasts.

to be able to detect picometer-level dynamic terms on a segment of the JWST [Perrin et al. (2018)].

In parallel to these studies, the PASTIS procedure for error budgeting is currently being applied by Iva Laginja and Marshall Perrin on the JWST, to refine the constraints set on JWST primary mirror's alignment and stability. This section aims at mentioning this work, that is still ongoing. We first describe the telescope itself, before introducing the chosen application hypotheses for the PASTIS study. Since this is still an ongoing work, only preliminary results are provided here.

4.3.1 Description of the JWST

JWST was designed to fulfill different scientific objectives, including studying the exoplanets and perhaps the origin of life. Indeed, JWST is designed to 1) detect planets through the transit method and 2) image some exoplanets near bright stars using coronagraphs.

For this goal, working in the infrared light is interesting since it is the wavelength range where atmospheres have more features, which enables efficient spectroscopy. This is why JWST will provide infrared observations, more precisely between 0.6 and 28 μm (visible to middle IR). With a primary mirror of 6.5m diameter, it can enable to resolve objects down to 0.1 arcsecond which matters when it comes to detect faint objects such as exoplanets. Since a mirror of 6.5 m is too large to fit in the launcher, it is segmented in 18 identical hexagonal subapertures of 1.3 m width. With this segmentation, it can be folded in three sections for the launch.

JWST contains four instruments dedicated to science: NIRISS that can be combined with an NRM, NIRSPec (Near-InfraRed Spectrometer), MIRI working in mid-IR (5 to 28 μm) that will enable between others the observation and analysis of young exoplanets and their atmosphere and propose a coronagraphic mode, and NIRCam, that is also provided of several coronagraphs to image very faint objects located close to their star such as exoplanets or debris disks. A few of the coronagraphs of these instruments have been presented in Fig. 3.2.3 and 3.2.4.

4.3.2 Application

PASTIS is currently being applied on the JWST as part of the performance and stability study by Iva Laginja, a Research Instrument Analyst (RIA) of the telescope team at STScI.

It was decided to focus on the middle size round occulter of NIRCam (MASK335R), since the corresponding range of wavelengths (2.4 μm to 5 μm) is a particularity to JWST and will provide the most specific science cases. The corresponding FPM and Lyot stop are indicated in Fig.3.2.3 (b) and 3.2.4 (a).

Iva Laginja is translating all the PASTIS functions from IDL to Python, reducing the numbers of segments from 36 to 18, and working at a wavelength of 3.35μm for a dark hole between 6 and $10\lambda/D$. For the calibration step that requires an end-to-end model of the

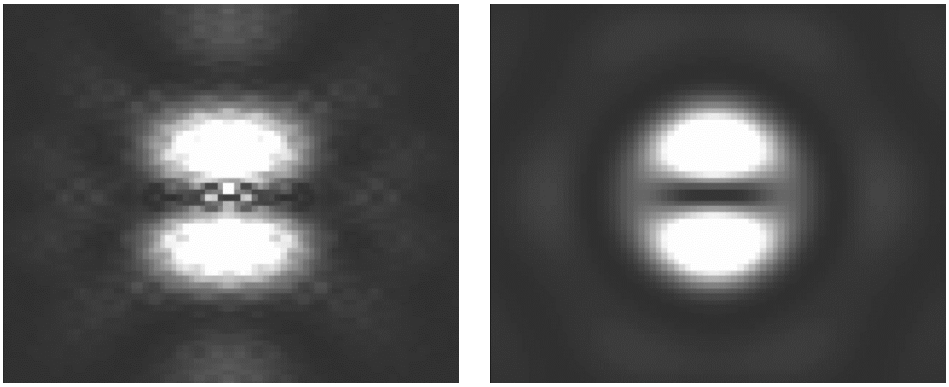

(a) (b)

Figure 4.3.1: PSFs when a 1 μm piston is applied on a segment computed from two different methods: (a) WebbPSF and (b) PASTIS.

optical system including the coronagraph, she is using WebbPSF, the PSF simulation tool of the JWST developed by Marshall Perrin and members of the telescope team at STScI. This tool enables to obtain a PSF from simulating any instrument and filter of JWST, in direct imaging, coronagraphy, and NRM mode, with and without aberrations in the Optical Telescope Element (OTE).

The application of PASTIS on the JWST is still under development. Fig. 4.3.1 indicates two different PSFs, when a 1 μm piston is applied on the same segment, but with two different tools: (a) WebbPSF and (b) PASTIS.

The main purpose of PASTIS being the computation of the contrast, further results with contrast curves such as the ones proposed in the article of section 4.2 should come soon.

4.4 Future developments

Error budget is a key part of the telescope and instrument design. PASTIS should facilitate this process and provide a better comprehension of the key factors on the system performance. However, as developed during this PhD, it has been applied to a specific case: a 36 hexagonal segment-primary mirror telescope combined with an APLC, designed to reach a contrast around 2×10^{-11}. Further studies need to be done, which fully subscribe in current research for future or ongoing telescopes.

First, further developments can be done, such as:

- a generalization of the dynamic case to any kind of segment motion. I am particularly interested in the case where the segments have geometrically correlated motions, ie. each segment motion impacts its closest neighbors'. Other cases where segments have non-correlated motions can also be addressed.

- estimation of the performance in the broadband case. The spectral bandwidth impacts

a lot the contrast, especially in the very high contrast regime, so this development seems quite mandatory. The broadband source case has been well developed in the Young experiment, which is quite parallel to the PASTIS algorithm, this should facilitate a lot the development of this application case.

- ELT and ground-based telescopes: these telescopes have in general larger primary mirrors, with sometimes more segments or larger segments. For instance, the ELT's primary mirror will be composed of 798 hexagonal segments of 1.4 m each for a total diameter of 39 m. On a completely different choice of design, the GMT primary mirror is made of 7 circular segments of 8.4 m each, for a total diameter of 24.5 m. The main common point of all these telescopes is the target contrast, by far more modest than in space high-contrast imaging and the presence of residual aberrations due to the atmospheric turbulence residual, not fully corrected by AO.

The analytical model of PASTIS can also be used in an optimisation process of the system, which means in a way to be inverted. What is the best system (coronagraph, apodizer, segment configuration), in terms of constraints releasing, that verifies a given contrast value or a given contrast stability? Such a perspective would require a complete kit of mathematical optimization tools and would result in new configurations of coronagraphic systems, efficient and less sensitive to segment-level aberrations. For instance, it can lead to optimize these different aspects:

- Segment configuration optimization: for a given primary mirror diameter, is it better to have many small segments or a few large segments? A first optimization would be to make the number and size of the segments vary.

- coronagraph optimization: no coronagraph was designed yet for many future applications (LUVOIR, HabEx...), and applying PASTIS to other coronagraphs than the APLC would be interesting to compare them, mainly in the process of optimizing the robustness of the whole telescope. In particular, we would like to use the Vortex coronagraph, that provides very promising performance.

- segment-level apodization: the last development I am really interested in corresponds to a modification of the coronagraph apodization itself. As we have seen before, with PASTIS, we show that the deterioration of contrast on the PSF is composed of an envelope that has, for piston aberrations, the shape of the PSF of one segment. Even for other low-order aberrations such as tip and tilt, it remains not too far from the PSF of one segment (see fig. 4 of the JATIS article). There should be a way to optimize the apodization of the generic segment to reduce the PSF of the segment in the dark hole, which would have the consequence of reducing the impact of aberrations on the final contrast. The telescope whose primary mirror is made of such segments would be hyper stable and less sensitive to aberrations!

The world is broken into fragments and pieces
That once were joined together in a unified whole
But now too many stand alone, there's too much separation
— Tracy Chapman

5

Experimental validation of focal-plane wavefront sensing for future space telescopes

As explained in chapter 2, several future telescopes will have at least one instrument dedicated to high-contrast imaging. The development and implementation of so challenging systems require laboratory tests for experimental validations. My experimental work fully subscribes in this experimental approach of the problematics of high-contrast imaging.

The first section of this chapter aims at describing the High-contrast imaging for Complex Aperture Telescopes testbed (HiCAT), specifically dedicated to experimental test and validation of so-far theoretical high-contrast imaging propositions for future missions, in particular for segmented telescopes.

As explained in the chapter 3, such propositions often combine coronagraphy, wavefront sensors, and wavefront control tools. Section 5.3 focuses on the experimental validation of the COFFEE wavefront sensor in the specific case of segmented apertures for the sub-aperture phasing.

5.1 Introduction

In this chapter, we want to demonstrate that the COFFEE sensor is able of measuring segmentation defects at levels required for high-contrast performance.

As a reminder, COFFEE is a sensor capable of estimating the wavefront aberrations with a high resolution. It constitutes an extension of the phase diversity technique to coronagraphic optical trains and it can be applied to the classical Lyot coronagraph, the R&R

coronagraph, the vortex coronagraph, the 4QPM coronagraph, and the APLC. As a consequence, this technique reunites several advantages for high-contrast imaging applications: it requires focal plane images so can work with the science camera, and there is no need to avoid or remove the coronagraph. More details about the COFFEE sensor can be found in the section 3.3.2.3.

Because of these specificities, COFFEE seems a good candidate for the measure of segmentation errors. It was decided to apply it to the HICAT testbed, described in the next section (section 5.2), since it constitutes a high performance demonstration testbed, dedicated to future space segmented telescopes. Because of the choice of optical components on HiCAT, its extremely precise alignment, and tight environment conditions, HiCAT is the optimal application tool to test high precision wavefront sensing for segmented apertures.

5.2 HiCAT testbed description

From 2013, HiCAT is being developed at the Russel B. Makidon Laboratory at STScI to investigate technologies for future space missions [N'Diaye et al. (2013a)]. Having participated to its alignment and tested the COFFEE sensor on HiCAT with a segmented aperture (see section 3.3), HiCAT is a key facility of my PhD. This section is dedicated to its description.

5.2.1 Goals of the testbed

HiCAT is designed to develop, test and validate solutions for future space telescopes with unfriendly apertures dedicated to high-contrast imaging, such as WFIRST or LUVOIR. The simulation of telescope pupil's complexity can include the central obstruction, the spiders, the segment gaps and the phasing errors, these components being easily replaceable with new components depending on the configuration tested.

To perform high-contrast imaging, HiCAT then includes a starlight and diffraction suppression system (Lyot coronagraphs or APLC) and wavefront sensing and wavefront control tools (deformable mirrors and phase retrieval camera). Some of these elements can also be easily replaced if different or new tests need to be done.

5.2.2 Optical and opto-mechanical design

As said earlier, HiCAT combines studies in coronagraphy, wavefront sensing and wavefront control, plus a simulated telescope with a complex pupil.

The final layout is presented in Fig. 5.2.1, the special components and their positions being listed in table 5.2.1 and the relay mirrors (focus-infinity and infinity-focus conjugations) being listed in table 5.2.2, where FP, PP, and OAP respectively stand for Focal Plane, Pupil Plane, and Off-Axis Parabola. It is a purely reflective testbed, except for the last imaging lenses. It is also designed to minimize the impact of its optical components on the final image and contrast, by reducing the sources of amplitude-induced errors from

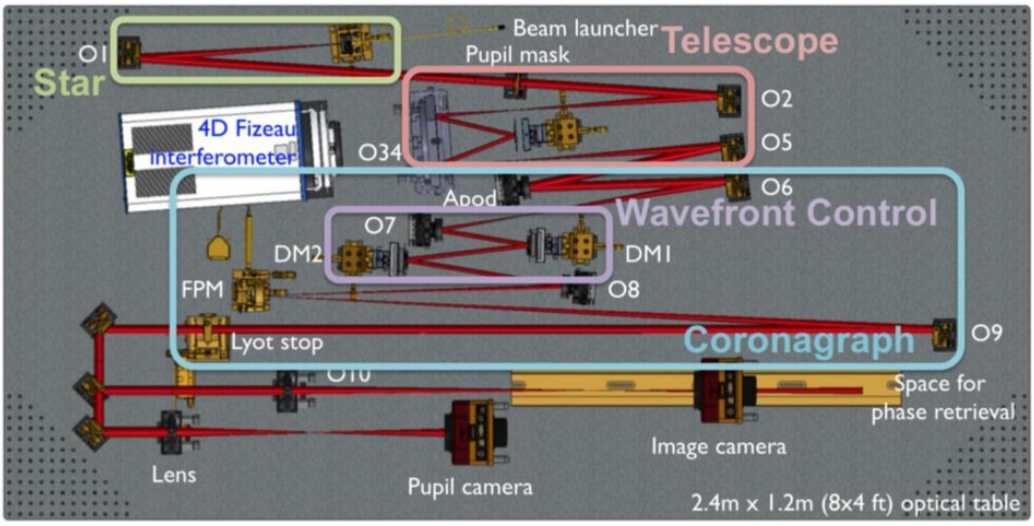

Figure 5.2.1: Optical and mechanical design of the HiCAT testbed. It was realized with the software Solidworks, the beam being exported from Zemax.

the propagation of out-of-pupil surfaces (Talbot effects). With this set up, the majority of the amplitude errors comes from the discontinuities in the pupil which should be corrected using apodization and wavefront control.

The star is simulated using a fiber source brought to infinity with an OAP. The source can be either a monochromatic light ($\lambda = 638$ nm) or a polychromatic light (600 to 680 nm).

The telescope is simulated using an entrance pupil mask (typically around 20 mm diameter) composed of the aperture shape, the central obstruction and the spiders, conjugated with a mirror that can be either flat (if the simulated telescope has a monolithic mirror) or segmented. In that case, we use a 37-segment Iris-AO MEMs DM with hexagonal segments that can be controlled in tip, tilt, and piston. The gaps between segments are between 10 and 12 μm and the full segmented mirror has an inscribed circle size of 7 mm.

The coronagraph is an APLC, whose apodizer can be replaced by a flat mirror to obtain a classical Lyot coronagraph. The apodizer is then easily replaceable and a couple of apodizers have already been tested: a WFIRST-like configuration (monolithic mirror, WFIRST central obstruction and spiders, and apodization optimized for this pupil) and a LUVOIR-like configuration (36 hexagonal segments, hexagonal central obstruction, spiders, apodization). The FPM is made of a reflective golden surface with a circular central hole, two diameters of holes being possible. The beam focal ratio at its location is set at F/80. Then the Lyot stop corresponds to a transmissive disk of diameter of 10 mm or 18 mm, or an iris of variable diameter. Both the FPM and the Lyot stop are motorized.

Different wavefront sensing tools can be used. First, a fold mirror can be set up between O8 and the FPM to deviate the beam towards another focal plane camera attached to a

Component	Location
fiber source	FP
Pupil mask	PP
Iris-AO segmented mirror	PP
Apodizer	PP
DM1	PP
DM2	/
FPM	FP
Lyot stop	PP
Image camera	FP
Pupil camera	PP

Table 5.2.1: All special components of HiCAT, ie. all components except for the infinity-focus and focus-infinity relay optics.

Component	Surface	Focal length (mm)
O1	OAP	478.3
O2	OAP	478.3
O34	Parabola (2 OAPs)	200.0
O5	OAP	478.3
O6	OAP	478.3
O7	Toric	215.3
O8	Toric	720.0
O9	Spheric	1,599.5

Table 5.2.2: All infinity-focus and focus-infinity relay mirrors.

rail, to perform phase diversity with the Optimized PhasE Retrieval Algorithm (OPERA) algorithm [Brady et al. (2018)]. However this sensor does not reconstruct the aberrations after O8, in particular in presence of the coronagraph, and reconstructs non-common path aberrations. Secondly, wavefront sensing algorithms including coronagraphs can run using the final image camera (see Fig. 5.2.1). This is the camera we used for the validation of COFFEE. This CMOS camera is the ASI1600mm from ZWO, its detector has 4656×3520 pixels, each of them having a size of 3.8 μm.

The wavefront control can be done with either one or two DMs: DM1 is set in a pupil plane while DM2 is out of pupil plane, to correct for both amplitude and phase aberrations. The DMs are Boston Micromachines deformable mirrors (kilo-DM), each of them with 952 actuators in a 9.9 mm (34 actuators) diameter disk. Both DMs are currently installed, but DM2 only is used since the calibration of DM1 needs to be redone.

After the alignment in 2014 and before the set up of the DMs (replaced by flat mirrors), the wavefront quality was around 13 nm rms over the entire testbed.

5.2.3 Environment constraints

For high-contrast imaging, performance is degraded by perturbations such as turbulence, dust, or vibrations. The DMs also induce drastic environment constraints, since they need to remain below 30% of humidity without any air flow.

This is why HiCAT is on a floating table, itself on a platform independent from the rest of the building to mitigate vibration effects. A box covers all the testbed to protect it from dust, particles, air flows, and parasite light. The box is located in a class 1000 clean room with temperate control in a 1°C range and humidity that is maintained under 40%. Inside the box, temperature and humidity sensors have been installed and a complementary dray air supply reduces the humidity to below 30%.

5.2.4 Current team and status

In the last couple of years, the HiCAT team grew up to combine different skills:

- the principal investigator of the Makidon laboratory, Rémi Soummer, began to work fully on the HiCAT testbed,

- Christopher Moriarty brought his strong skills in software development and version control to develop and manage the architecture of the HiCAT procedures,

- Keira Brooks developed all the DM calibration routines,

- Peter Petrone is an expert in metrology. He developed and set up the procedures to change some optics (such as the apodizer, DM2, and the Iris-AO) without losing the optical axis and misaligning the optics,

- Marshall Perrin is creating a simulation tool for HiCAT,

- Iva Laginja mainly works on the JWST Optical Simulation Testbed (JOST), dedicated to linear control and cophasing alignement tests for the JWST, but the codes she develops will directly be applied an HiCAT since some components, such as the cameras, are identical on both testbeds,

- Other people are also involved in the HiCAT project: Gregory Brady, Arturo Brito, Elodie Choquet, Tom Comeau, Sylvain Egron, A.J. Eldorado Riggs, Rob Gontrum, Johan Mazoyer, Mamadou N'Diaye, Laurent Pueyo, Anand Sivaramakrishnan, Kathryn St. Laurent, Ana Maria Valenzuela, students of JHU supervised by Nathan Scott, the LAM team...

As a result of their common effort, HiCAT can now simulate both monolithic and segmented telescopes, with or without the appropriate full APLCs. The speckle nulling procedure has been implemented and can be run in any given configuration, which provided first results of coronagraph/wavefront control combination. More precise results on HiCAT are described in Soummer et al. (2018).

5.3 Experimental results on wavefront sensing on segmented apertures

5.3.1 Objective of the experiment

Segmentation of the telescope primary mirrors generates various issues, including an increasing complexity of the alignment process. Indeed, in addition to the global alignment of the primary mirror, each segment has at least three degrees of freedom (piston, tip, tilt) that need to be aligned to achieve the target performance.

As described in section 3.3, numerous WFSs have been developed to reconstruct the wavefront aberrations and can be applied to segment phasing. In high-contrast imaging, focal plane sensors are preferably used, since they enable to reconstruct all aberrations from the entrance pupil to the science camera, while pupil plane wavefront sensors' reconstructions suffer from non-common path aberrations.

The sensor COFFEE (see section 3.3.2.3) belongs to this category of sensors, since it requires focal plane images. Another non negligible advantage of COFFEE is that it allows the presence of a coronagraph (classical Lyot coronagraph, APLC, R&R coronagraph, or 4QPM coronagraph), which makes it a strong candidate for high-contrast imaging instruments. It has already been validated on monolithic apertures in Paul et al. (2013) and Paul (2014) on SPHERE and on the MITHIC testbed. Lately Olivier Herscovici-Schiller and I validated it again on the MITHIC testbed to perform NLDH control (see section 6.2) and Olivier Herscovici-Schiller also applied it on the THD2 testbed [Herscovici-Schiller et al. (2018a)].

However, COFFEE has never been validated on bench nor in simulation on a segmented aperture. This is the motivation behind the experiment introduced in this section: using COFFEE on segmented apertures to reconstruct phasing errors, in particular in the presence of a coronagraph.

5.3.2 Conditions and tools

It has been chosen to conduct this experiment on the HiCAT testbed (see section 5.2) that reunites all necessary conditions, in particular the segmented aperture, a coronagraph, and a DM mandatory for the diversity phase. The optical conditions of the system are explained more in details in section 5.3.2.1.

The main steps of the experiment, from the images taken by the camera to the processed data, are detailed in sections 5.3.2.2, 5.3.2.3, and 5.3.2.4.

5.3.2.1 Optical conditions

The chosen source is a monochromatic light with a wavelength of $\lambda = 638$ nm.

On HiCAT, two pupil shapes are currently possible: monolithic when a flat mirror is used in the second pupil plane, and segmented when this flat mirror is replaced with 37-segment Iris-AO. For the purpose of the actual test, the segmented mirror is always set up. Similarly, the entrance pupil remains for the entire experience a circular mask of diameter 18 mm and the Lyot stop a circular pupil of diameter 15 mm. Since the pupil masks hides the outer ring of the Iris-AO, the number of fully visible segments reduces from 37 to 19. Depending if the Lyot coronagraph is on (coronagraphic imaging) or off (direct imaging), the reflective FPM is centered or drastically decentered from the optical axis.

To get the sampling on the camera, we compute the MTF of the system (modulus of the Fourier Transform of the PSF without FPM, see section 3.1.1.2). The size of the PSF image (in pixels) divided by the cutoff frequency of the MTF (also in pixels) provides the sampling on the camera. On HiCAT, the sampling on the camera is 13.3 ± 0.1 when the Lyot stop is set up, while 11.4 ± 0.1 when it is out. The ratio of these two values provides an estimation of the Lyot ratio: $85.6\% \pm 1.1\%$, more precise than the value deduced from the Lyot stop and entrance pupil diameters.

The Iris-AO is controlled using a GUI interface (see Fig. 5.3.1). For each segment, it is possible to enter commands of piston (in μm), tip, and tilt (in mrad). We can also upload at once the commands to all segments using a map of command vectors. A fast calibration of the Iris-AO is done before taking data to apply COFFEE.

For the piston calibration, we use the fact that an optical path difference of λ between two segments is optically equivalent to a flat. A piston of p nm in terms of Iris-AO surface implies an optical path difference of $2p$ nm because of the reflection of the mirror. Therefore, we take an image with coronagraph while the segmented mirror is flat, as a reference. The central segment is then displaced with a step of 1 nm until the PSF is recovered. We obtain that for a displacement of $p = 0.34$, the mirror is back to being optically equivalent to a flat mirror.

Eventually, to compute a precise estimation of the diameter of the FPM, we install a camera behind it, the detector being conjugated to the hole. When the FPM is well centered, we can then observe a PSF cropped after a few rings by the mask. We then use two different

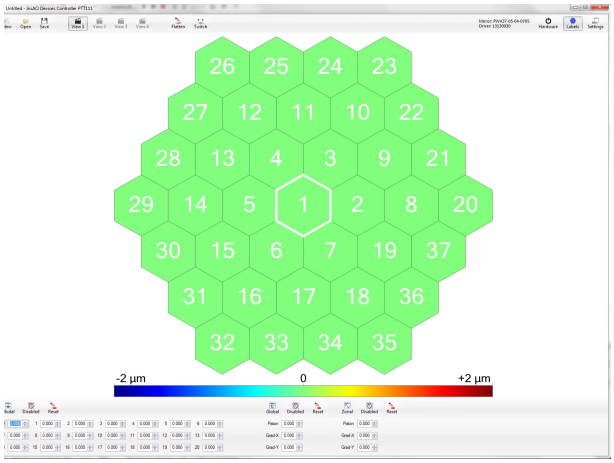

Figure 5.3.1: Iris-AO GUI interface, giving access to the piston, tip, and tilt positions of the 37 segments of the Iris-AO.

light expositions: by increasing the source intensity until saturating the inside of the hole (5.3.2 (a)), we can deduce a precise estimation in pixels of the hole diameter, and by adjusting the source intensity to obtain a non-saturated PSF (5.3.2 (b)), we can measure its FWHM, which provides an estimation of the resolution element λ/D in pixels. By dividing one with the other, we obtain that the hole of the FPM has a diameter of $7.2 \pm 0.9\lambda/D$.

5.3.2.2 Hardware control and pre-processing

To perform, COFFEE requires at least two images (see section 3.3.2.3): a focus image ("foc image" in Fig. 5.3.3) and a diversity image ("div image" in Fig. 5.3.3). In our case, the diversity image is obtained with applying a 300 nm pv focus on the DM (the focus was calibrated in front of a Fizeau interferometer), while the DM remains flat for the focus image.

Fig. 5.3.3 describes the successive pre-processing steps of this experiment. To increase the quality of the input images of COFFEE and reduce the noise, they result from a pre-processing step: each input image corresponds to the average of 400 images minus the average of 400 background images, the background images being taken when a motorized light trap blocks the beam ahead of the FPM. Furthermore, all images have 1424×1424 pixels with a sampling of either 11.4 ± 0.1 or 13.3 ± 0.1 depending if the Lyot stop is in or out of the optical path (see section 5.3.2.1).

Furthermore, for each application case, two configurations are considered: direct imaging and coronagraphic imaging ("direct" and "coron" in Fig. 5.3.3), depending if the FPM is out or in.

All these configurations (different DM phase application, FPM position control, light trap control, camera use, and image pre-processing) require a safe hardware control. On HiCAT,

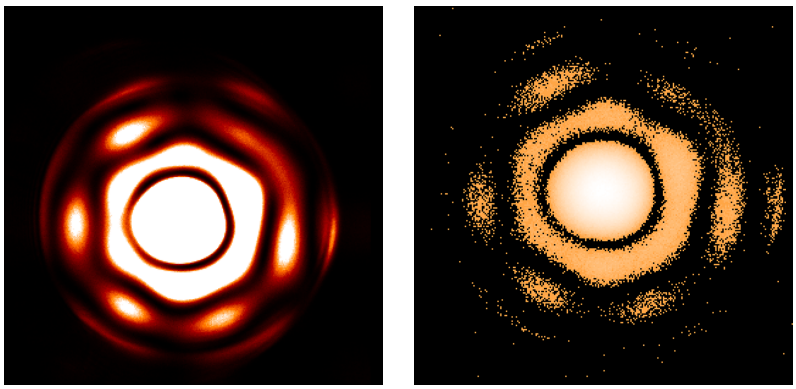

(a) (b)

Figure 5.3.2: Images of the PSF at the FPM plane, cropped by the mask. (a) Saturated image (linear scale) and (b) non-saturated image (logarithmic scale). In this case, the FPM diameter is estimated at $7.2 \pm 0.9\lambda/D$.

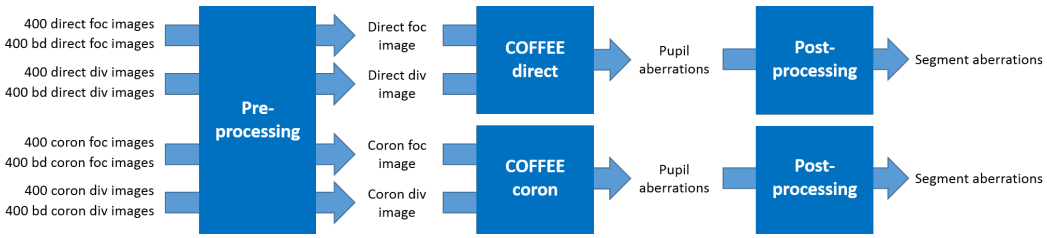

Figure 5.3.3: Structure of the data analysis process. "coron" stands for "coronagraphic", "bd" for "background", "foc" for "on focus" (the DM is flat), and "div" for "diversity".

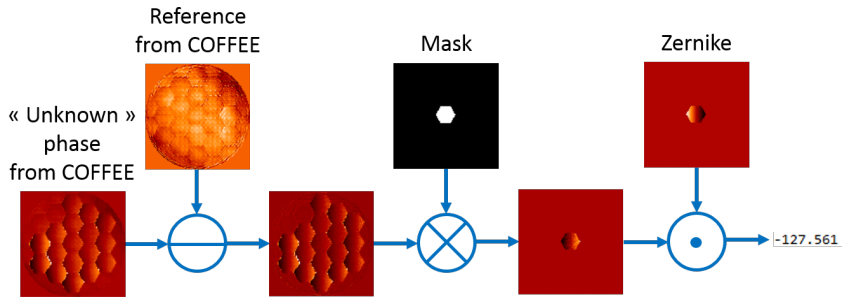

Figure 5.3.4: Post-processing to deduce the piston, tip, and tilt values on the different segments from the phases reconstructed by COFFEE. First, we subtract the reference phase (obtained with COFFEE when the Iris-AO is flattened) to the interest phase. The residual phase is multiplied with a hexagonal mask to isolate the interest segment. We apply a dot product to this segment phase with a calibrated Zernike polynomial on a similar support to deduce the aberration value, that can be compared to the command that has been sent to the Iris-AO.

it has been developed in object-oriented Python as a generic package: each hardware is a child class of a generic "instrument" parent class, and each action is a function. The entire hardware control and image pre-processing steps belong to this unified and generic software infrastructure [Moriarty et al. (2018)].

5.3.2.3 Phase reconstruction with COFFEE

The COFFEE algorithm corresponds to a generic version that works for different coronagraphs such has the APLC, the classical Lyot coronagraph, the R&R, 4QPM, or even no coronagraph. In our case, we apply it in the configurations of no coronagraph and a classical Lyot coronagraph.

As a reminder, in both configurations two are needed: one where the DM is flat, one where the DM has a known aberration (diversity phase). In our case, the diversity phase corresponds to a 300 nm pv focus.

From these two images, COFFEE deduces the upstream phase aberration (before the coronagraph) and the downstream phase aberration (after the coronagraph). The Iris-AO being in a pupil plane ahead of the coronagraph, it is sufficient for the objective of this experiment. As an information, with a third image, COFFEE could also reconstruct the amplitude aberrations of the system.

5.3.2.4 Post-processing

Fig. 5.3.4 presents the main steps of the post-processing applied on the COFFEE outputs. Since we are interested in reconstructing phasing errors on the Iris-AO, a known aberration is applied on the mirror. The objective is to find out what are the piston, tip, and tilt values applied on the segments.

To the phase deduced from COFFEE, we subtract a reference phase, also reconstructed by COFFEE but with the Iris-AO flattened. This enables in particular to remove global aberrations and reconstruction artifacts such as global tip and tilt, that do not interest us in our experiment. Then a hexagonal mask is put on each segment to get the aberration of the segment only. We apply a dot product between this local phase and a normalized tip or tilt to obtain the Zernike coefficient. To get the piston value, this last step is replaced by computing the average of the phase inside the mask.

5.3.3 Reconstruction of phasing errors without coronagraph

In this section, we focus on the data taken while the FPM is out of the optical train. The objective, in addition to validating COFFEE without coronagraph, is to set reference results with which we will compare the results obtained in presence of the coronagraph.

5.3.3.1 Examples of reconstructed phases

Fig. 5.3.5 introduces some phases reconstructed with COFFEE in direct configuration (no coronagraph), when known aberrations are applied on the segmented mirror. On the first column, the segmented mirror is flat, and the reconstructed phase corresponds to the reference phase that is subtracted from all phases in the first line to get the second line (residual phases). On the second column, the Iris-AO is flat, except for the central segment that has a 263 nm piston. On the third column, the Iris-AO is also flat, except for the central segment that has a 0.1 mrad tip. On the fourth column, several segments are tilted with values from 0.1 mrad to 0.26 mrad.

In all cases, the subtraction of the reference phases removes most of the global aberrations and reduces the segmentation pattern on flattened areas.

5.3.3.2 Application to a range of values

The objective here is to study the error of reconstruction of COFFEE for different kinds of phasing aberrations: piston, tip, and tilt.

To study piston aberrations, the Iris-AO remains flat, except for the central segment on which different piston values are applied: from 0 to around 600 nm. We compute with COFFEE the aberration phase for a set of around 26 images, and deduce the respective 26 piston value of the central segment. This set of values is compared to the command sent to the central segment of the Iris-AO. Fig. 5.3.6 illustrates this study.

We process similarly for the study of tip aberrations: the Iris-AO is still flat, except for the central segment on which seven tip commands from 0 to around 275 nm are successively applied. The results are indicated on Fig. 5.3.7 (left).

Because of the time-consuming process to take data and run the pre-processing step, for the study of tilt aberrations we compress the number of data to take: the Iris-AO is still flat,

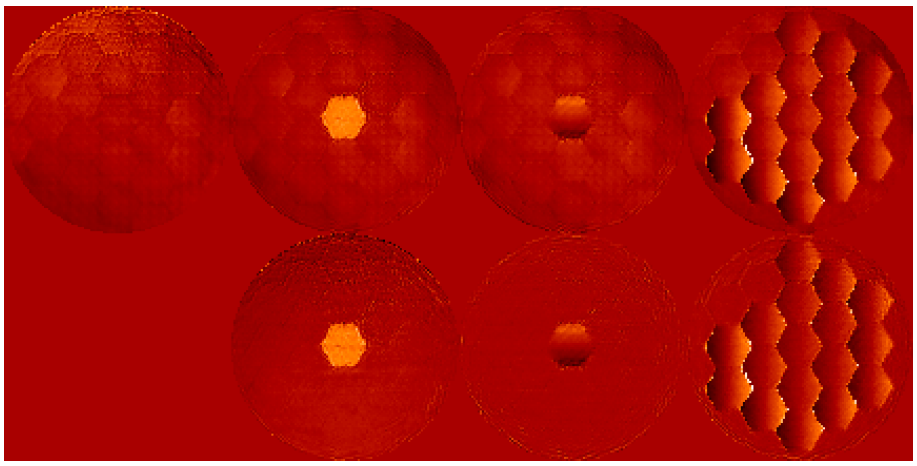

Figure 5.3.5: Some phases reconstructed with COFFEE in direct configuration. Top line: (first column) the Iris-AO is flat, this phase corresponds to the reference phase, (second column) the Iris-AO is flat, except for the central segment that has a 263 nm piston, (third column) the Iris-AO is flat, except for the central segment that has a 0.2 mrad tip, and (fourth column) the Iris-AO is flat, except for several segments that are tilted with values from 0.1 mrad to 0.26 mrad. Bottom line: top line subtracted by the reference phases.

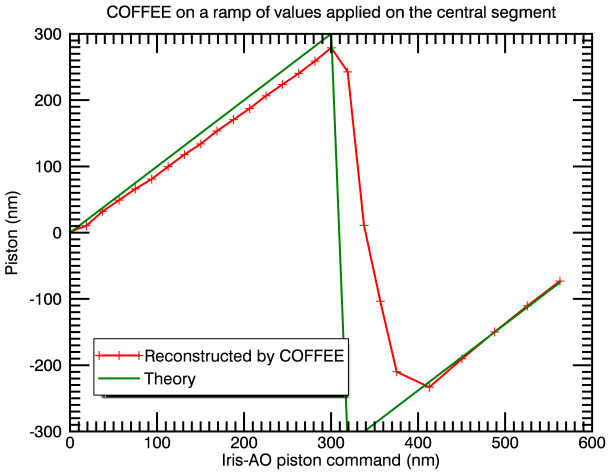

Figure 5.3.6: Piston values reconstructed by COFFEE vs expected piston values on the central segment, for a range of piston values from 0 to 560 nm. The theory curve corresponds to $y = x$ with a modulation of λ at $\lambda/2$.

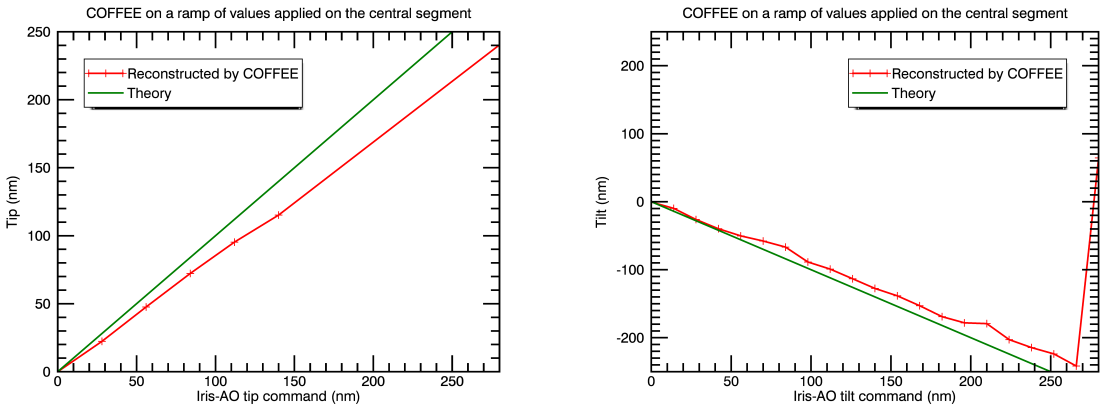

Figure 5.3.7: Values reconstructed by COFFEE vs expected values. (left) Tip case for a range of values from 0 to 275 nm pv and (right) tilt case for a range of values from 0 to 560 nm pv. The theory curves correspond to $y = x$ in the tip case and $y = -x$ in the tilt case.

except for tilt commands sent to the central segment and the two first ring segment, that take values between 0 and 560 nm, spread in 4 different sets of commands. Once the tilt values are recovered from the COFFEE reconstruction, we then obtain around 40 different tilt values, that can be compared to the commands sent to the Iris-AO, like in Fig. 5.3.7 (right).

5.3.3.3 Result analysis

For the piston case, the curve looks, as expected, like a piecewise linear function with a slope of 0.932 ± 0.006 and a y-intercept of -4.02 ± 0.97. The rms of the difference between the linear fit and the data from COFFEE is 1.97 nm. It is expected to find a piecewise linear function with a gap of λ (λ being the wavelength), since pistons with an offset of $n\lambda$ (n being an integer) have equivalent effects in the focal plane. Therefore, COFFEE reconstructs only phase aberrations in the range $[-\lambda/2, \lambda/2]$. The lack of reconstruction between 300 and 413 nm is due to λ-jumps inside the segment itself in the phases reconstructed by COFFEE.

For the tip and tilt cases, the curves look again linear, with a slope of 0.857 ± 0.009 (and a y-intercept of -0.98 ± 1.2) for the tip and a slope of 0.90 ± 0.01 (and a y-intercept of 1.3 ± 1.6) for the tilt. The rms error between the actual data and this fit is 1.68 nm for the tip, while 3.58 nm for the tilt. After a certain value (here around 270 nm), λ-jumps appear in the segment phase so the direct estimation of the tip and tilt is not possible anymore (see Fig. 5.3.8), more post-processing would be needed.

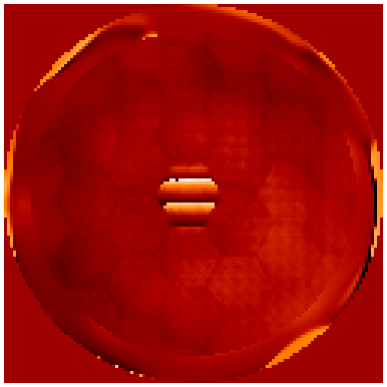

Figure 5.3.8: Phase reconstructed by COFFEE in the coronagraphic configuration when the Iris-AO is flat and a 1120 nm tip is applied on the central segment.

5.3.4 Reconstruction of phasing errors with coronagraph

In this section, we focus on the data taken while a $7.2\lambda/D$-large FPM and a Lyot stop are set in the optical train. The COFFEE algorithm is able of taking this into account.

5.3.4.1 Examples of reconstructed phases

We proceed with a similar strategy than in the previous section.

The bench aberrations are first calibrated with the IRIS-AO set to his best flat. This reference measurement is shown in Fig. 5.3.9 (top left): we can in particular recognize the high frequency print-through of the DM actuators, residual segments errors, and segments shapes.

Fig. 5.3.9 also introduces some phases reconstructed with COFFEE in coronagraphic configuration with phasing errors on the segments. The second measurement corresponds to the case where the Iris-AO is flat except for the central segment, where a 188 nm piston is applied, the third one the Iris-AO is flat except for the central segment that has a 0.2 mrad tip, and on the fourth column, several segments are tilted with values from 0.1 mrad to 0.26 mrad.

On all these phases, the hexagonal pattern can be clearly recognized. In the piston, tip, and tilt cases, we can also identify the moving segments, even if the reconstruction is not always as smooth as in the direct case. Some drawbacks and errors of reconstruction, showing the limits of COFFEE in coronagraphic mode can also be observed. They will be specifically addressed later in this chapter.

5.3.4.2 Application to a range of values

The objective here is to study the error of reconstruction of COFFEE for different kinds of phasing aberrations: piston, tip, and tilt.

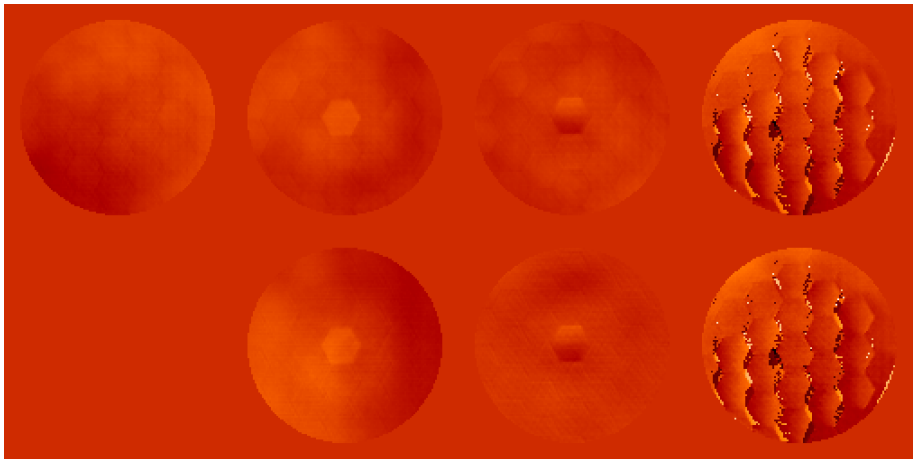

Figure 5.3.9: Some phases reconstructed with COFFEE in coronagraphic configuration. Top line: (First column) the Iris-AO is flat, (second column) the Iris-AO is flat, except for the central segment that has a 188 nm piston, (third column) the Iris-AO is flat, except for the central segment that has a 0.2 mrad tip, and (fourth column) the Iris-AO is flat, except for several segments that are tilted with values from 0.1 mrad to 0.26 mrad. Bottom line: top line subtracted by the reference phases.

To study piston aberrations, the Iris-AO remains flat, except for the central segment on which different piston values are applied: from 0 to around 600 nm. We compute with COFFEE the aberration phase for a set of around 26 images, and deduce the respective 26 piston value of the central segment. This set of values is compared to the command sent to the central segment of the Iris-AO. Fig. 5.3.10 illustrates this study. The reconstructed piston values seem strongly under-estimated, even if the general shape of the curve tend to follow the trend of the reference one (in green). An explanation of this difference is proposed in section 5.3.4.3.

We process similarly for the study of tip aberrations: the Iris-AO is still flat, except for the central segment on which seven tip commands from 0 to around 275 nm are successively applied. The results are indicated on Fig. 5.3.11 (left). For the study of tilt aberrations, the Iris-AO is still flat, except for tilt commands sent to the central segment and the two first ring segment, that take values between 0 and 560 nm, spread in 4 different sets of commands. Once the tilt values are recovered from the COFFEE reconstruction, we then obtain around 40 different tilt values, that can be compared to the commands sent to the Iris-AO, like in Fig. 5.3.11 (right). Similarly than for the piston case, the tip and tilt estimation seem strongly under estimated, which will be explained in section 5.3.4.3.

5.3.4.3 Analysis in the coronagraphic configuration

In this section, we analyze and explain the results described in the previous sections.

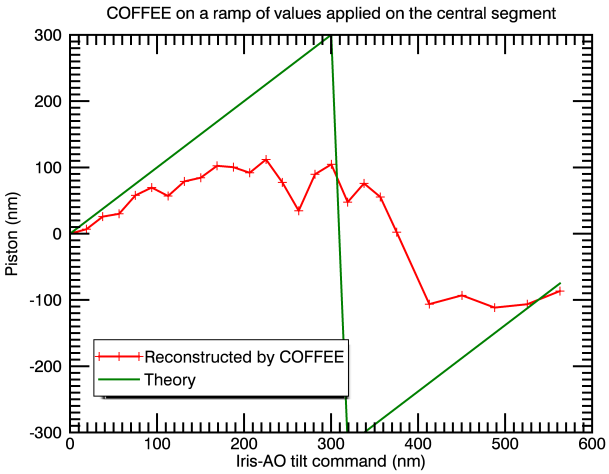

Figure 5.3.10: Reconstructed by COFFEE vs expected piston values on the central segment, for a range of piston values from 0 to 560 nm. The theory curves correspond to $y = x$ with a modulation of λ at $\lambda/2$.

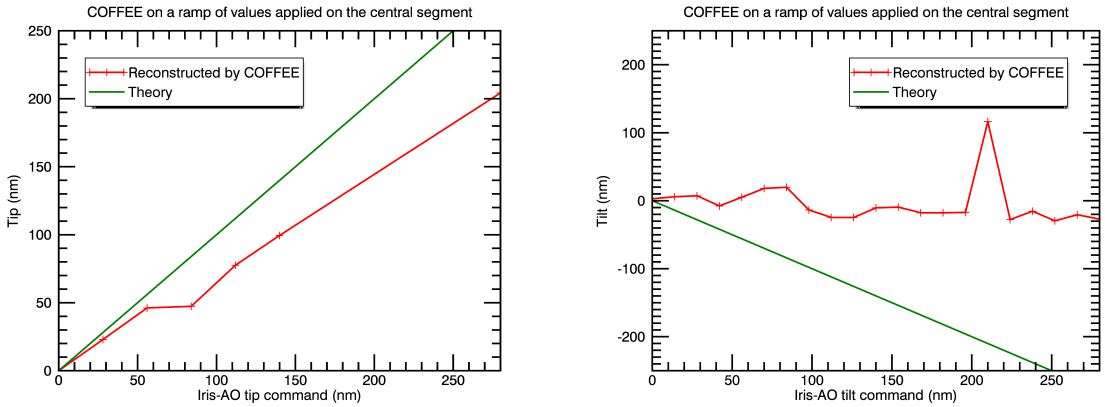

Figure 5.3.11: Reconstructed by COFFEE vs expected values on the central segment. (left) Tip case for a range of values from 0 to 275 nm and (right) tilt case for a range of values from 0 to 560 nm. The theory curves correspond to $y = x$ in the tip case and $y = -x$ in the tilt case.

5.3.4.3.1 Observations

In the coronagraphic configuration, COFFEE shows some difficulties to reconstruct low-order aberrations.

Indeed, while they should remain constant over the different reconstructions (only the central segment is displaced), we notice that they are modified between the reference phase and each of the measurements where commands are applied on the segments. Subtracting a reference to the phases does then not improve the estimation of the phase.

As a consequence, this evolution of the low-order aberrations disrupts the reconstruction of the segment-level pistons, which appears in Fig. 5.3.10.

5.3.4.3.2 FPM as a high-pass filter

The reconstruction issues pointed out before can be explained by seeing the FPm as a high-pass filter. Indeed, the FPM filters out the low frequency aberrations, such as, in our case, the reference or background phase or even low frequency components of the segment itself.

To illustrate this phenomenon, we simulate the PSFs (in focus and out of focus) that would be obtained with the HiCAT optical configuration with no aberration except for a sine phase. The sine phase is chosen at different frequencies: 2 cycles per pupil, which should be too large to pass the FPM, 3.5 cycles per pupil, that should be very close to the border of the FPM, and 15 cycles per pupil, that should fully pass the FPM. The in-focus PSFs are shown on the first line (1) of Fig. 5.3.12, and the corresponding phases, their low-frequency components (lower than the FPM), and their high-frequency components (higher than the FPM) are shown on the second line of the table of line (2).

Once these PSFs are simulated, they are used as inputs for COFFEE, which enables to reconstruct the aberration phases. The results are shown at the top line of the table of Fig. 5.3.12, line (2), including their low- and high-frequency components. The reconstruction error, ie. the difference between the reconstructed phases and the theoretical phases are indicated at the bottom line of the table of Fig. 5.3.12, line (2). In each case, we also plot the power spectral distributions (PSD) of the theoretical and reconstructed phases, visible on the line (3) of Fig. 5.3.12.

In table 5.3.1, we also indicate the rms values of the different phases (theoretical, COFFEE-reconstructed, and error, for the total aberrations, the low-frequency components, and the high-frequency components).

We can notice that in the high-frequency aberration case (15 cycles per pupil), the phase is well reconstructed. This kind of aberration fully passes the FPM, even if low-order patterns can be seen on the PSD, and rms of the error is minimal.

On the opposite, the reconstruction does not go well for low-order aberrations such as the 2 cycles per pupil case. The reconstructed phase is fully different than the theoretical

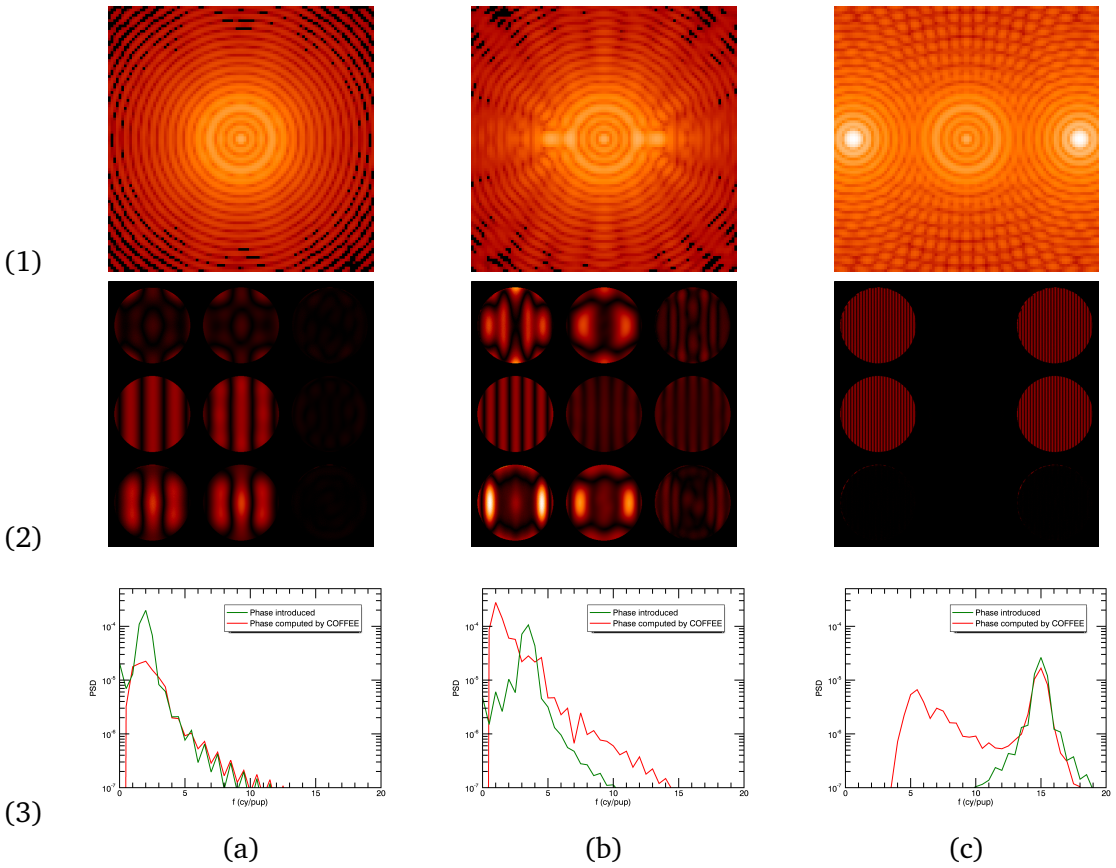

Figure 5.3.12: Comparison between theoretical phases and phases reconstructed by COFFEE for sine-like phases with three different spatial frequencies: (a) 2 cycles per pupil, (b) 3.5 cycles per pupil, and (c) 15 cycles per pupil. For each case, we show: (1) the PSF in the detector plane, (2) a table containing (first line) the phase reconstructed by COFFEE, its low-frequency components (lower than the FPM), and its high-frequency components (higher than the FPM), (second line) the theoretical phase to reconstruct, its low-frequency components, and its high-frequency components, and (third line) the differences between the two phases above, and (3) the power spectral distribution (PSD) of the theoretical phase and the phase reconstructed by COFFEE.

Freq	**Tot**			**Low-freq**			**High-freq**		
	Theory	Rec	Diff	Theory	Rec	Diff	Theory	Rec	Diff
2	0.24	0.14	0.29	0.23	0.11	0.29	0.072	0.076	0.021
3.5	0.24	0.31	0.44	0.17	0.26	0.34	0.18	0.18	0.13
15	0.24	0.24	0.040	0.0035	0.0049	0.0020	0.24	0.24	0.040

Table 5.3.1: RMS aberrations of the different phases of Fig. 5.3.12. For each frequency (2, 3.5, and 15 cycles per pupil), there are the rms values of the total, low-order component, and high-order component of the theoretical phase, the phase reconstructed by COFFEE (Rec), and the reconstruction error (Diff). The frequencies are indicated in cycles per pupil, and the aberrations values in radians rms.

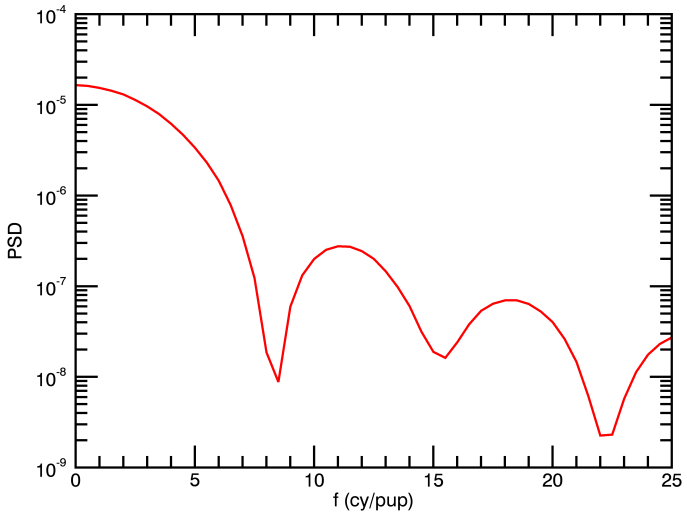

Figure 5.3.13: PSD of a flat phase with one segment unphased, at the same scale and dimensions than the Iris-AO as seen by COFFEE.

one, in terms of phase pattern and rms value, most of the error coming from low-frequency aberrations.

This test indicates that there exist some modes that are not visible by COFFEE, mainly when there are blocked by the FPM in the Fourier plane. Once again, the FPM acts like a high-pass filter and COFFEE shows its full capability for modes with higher spatial frequencies than the size of the FPM. On the opposite, it is left almost blind for spatial frequencies blocked by the FPM, ie. smaller than 3.5 cy/pup, in our case.

5.3.4.3.3 Conclusions

Fig. 5.3.13 indicates the theoretical PSD of a flat phase, except for the central segment. The PSD is higher below 6-7 cy/pup, ie. spatial frequencies that are mostly cut by the FPM. This means that phase patterns such as segments are lower-order variations such as the background phase can hardly be properly reconstructed.

We can also conclude that the smaller the FPM, the more exact the reconstruction by COFFEE is. Other data were taken on HiCAT with a smaller FPM, with a diameter of $4.4\lambda/D$ (instead of $7.2\lambda/D$), and random pistons values applied on the Iris-AO. Fig. 5.3.14 shows a first result with this FPM: on the left, the phase reconstructed by COFFEE subtracted by a reference phase (also computed with COFFEE), on the center the theoretical phase issued from the command sent to the Iris-AO, and on the right the difference between these two phases. These three phases are here on the same scale, which shows that they have similar

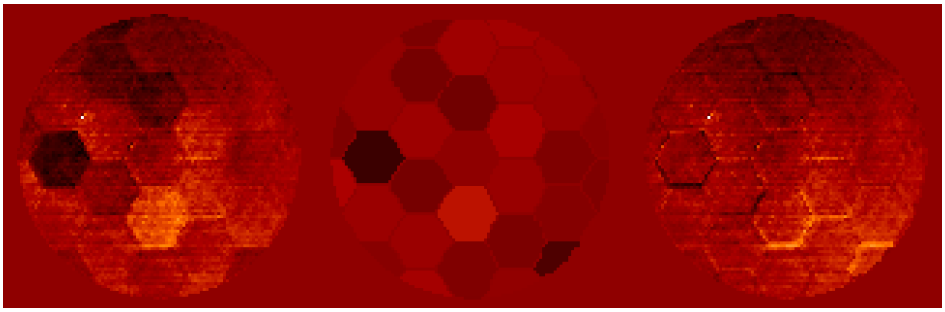

Figure 5.3.14: Comparison of (left) the phase reconstructed by COFFEE subtracted by a reference phase, also reconstructed by COFFEE, (center) the theoretical phase issued from the command sent to the Iris-AO, and (c) the reconstruction error phase, ie. the difference between the two previous phases, when random piston values are applied on the Iris-AO. The three phases are on the same scale.

amplitudes.

For future experimental tests, it would be then interesting to use this smaller mask on the HiCAT testbed, before running similar tests than the one conducted in this chapter. This FPM would allow a better demonstration of the COFFEE reconstruction of phasing errors of a segmented aperture.

It could also be interesting to numerically avoid the uncertainty on the low-order modes filtered by the coronagraph. This means setting up a regularization in the algorithm to reduce or even cancel the reconstruction on spatial frequencies lower than the FPM size. An equivalent solution has been proposed by Olivier Herscovici-Schiller, who was confronted to modes unseen by COFFEE on a 4QPM coronagraph [Herscovici-Schiller et al. (2018b)].

There's so many ways to act
And there's many shades of black
— Adele and The Raconteurs

6

From wavefront sensing to wavefront control

After the coronagraph and the wavefront sensor, the last ingredient of a typical high-contrast imaging instrument is the wavefront control. Numerous tools have been developed so far, described in 3.4. In particular, we introduced the NLDH technique, whose main advantage is to converge in less iterations than usual linear wavefront control methods. This fact is interesting when it comes to high-contrast performance, particularly hard to stabilize over long exposure times.

In this section, we propose to apply the NLDH technique to the case of segmented apertures. A short introduction is proposed in section 6.1, followed by a first experimental validation that was conducted on the MITHIC of the LAM (section 6.2). The NLDH algorithm remains valid in presence of a coronagraph (section 6.3), which makes it adapted to the case of high-contrast imaging instruments. I then ran several studies in simulation (section 6.4), to evaluate the performance of the NLDH technique when it comes to segmented telescopes: first, we compare the performance reached with a segmented aperture with the one reached with a monolithic aperture. We then study the impact of the DM type on the performance, to answer in particular the question of using the segmented primary mirror as wavefront corrector. As a third test, we compare the influence of the dark hole position on the final contrast. Eventually, we study the robustness of the algorithm to phasing errors of the primary mirror.

6.1 Reminders on the Non-Linear Dark Hole algorithm

The NLDH method [Paul (2014)] aims at cancelling or reducing the electric field in the focal plan of a coronagraphic instrument by sending commands to a DM located in the

pupil plane of the optical system. It has to be combined with a wavefront sensor since it requires an estimation of the aberrations in the system.

As explained in section 3.4, it is based on the minimization of the energy in the dark hole. It then requires a model of propagation of the wavefront errors through the optical system, ie. multiple Fourier transforms and multiplications with amplitude and/or phase masks.

Most of the other methods described in section 3.4 include a linearization of the model, only valid for small phase aberrations. In opposition to them, the NLDH controller has the specificity of using no model approximation and no low phase linearization. This means for instance that it remains valid on the whole range of aberrations, which is particularly interesting since most wavefront correction methods do not try to minimize the aberrations, but introduce more aberrations to cancel the electric field in a restricted area of the focal plane.

In addition, the NLDH algorithm can also take into account all aberrations of the optical system: the amplitude aberrations A, the upstream phase aberrations ϕ_{up} and the downstream phase aberrations ϕ_{do}, which makes it a particularly good candidate when it comes to non monolithic apertures and to coronagraphic systems.

Another non-negligible advantage of the NLDH algorithm is its convergence speed: the convergence loop is mostly done in the algorithm, which makes it extremely fast to converge and a couple of experimental iterations only are necessary to dig the dark hole. For high-contrast imaging instruments, very complex to stabilize over long exposure times, the convergence speed of the controller is a parameter to take into account.

6.2 First experimental validation of the Non Linear Dark Hole controller

During our respective PhDs, Olivier Herscovici-Schiller and I validated experimentally the NLDH algorithm on the MITHIC testbed. The objective was to obtain a decrease of the intensity in a selected dark hole.

In order to demonstrate its capacity to cancel out the diffraction residuals, we have decided to use it on a non-coronagraphic system. The goal is therefore to cancel out the light in a region of an airy pattern.

In this section, I first introduce the MITHIC testbed (section 6.2.1), before describing the conditions and results of this experiment (section 6.2.2).

6.2.1 MITHIC testbed description

The MITHIC testbed was developed at LAM in France in 2012 by N'Diaye et al. (2012) and later in Vigan et al. (2016). We used it during my PhD to test and validate the COF-

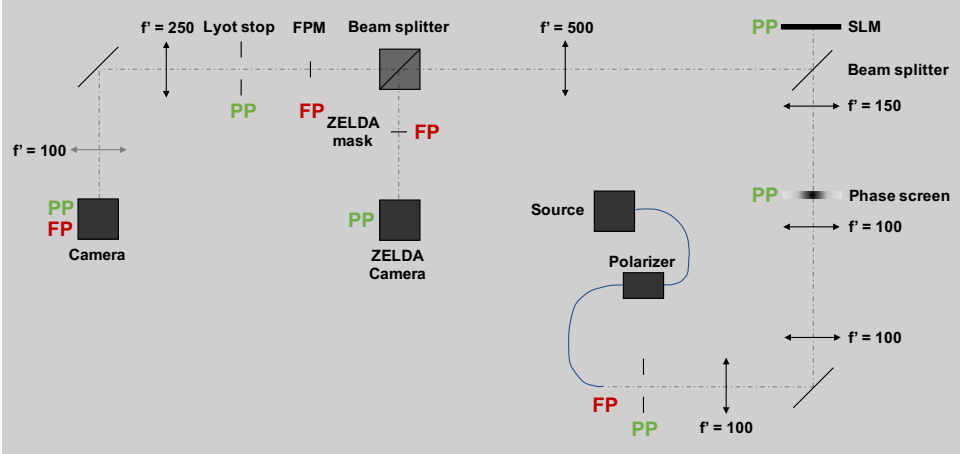

Figure 6.2.1: Scheme of the MITHIC testbed as used for this experiment.

FEE sensor combined with the NLDH control algorithm. The results being presented in section 6.2.2, we focus in this section on the description of the testbed.

6.2.1.1 Goals of the testbed

The MITHIC testbed was developed to test and validate methods for high-contrast imaging typically for ground-based telescopes such as the VLT, in particular wavefront sensing and wavefront control tools, optionally in presence of a coronagraph and/or simulated turbulences.

It was first used to experimentally validate the ZELDA sensor for phasing aberrations of segmented mirrors [N'Diaye et al. (2012)]. Even if more tests were done with segmented apertures [Vigan et al. (2016)], it can also be used for monolithic aperture applications.

6.2.1.2 Optical and opto-mechanical design

Fig. 6.2.1 corresponds to a scheme of the optical configuration of the MITHIC testbed. The pupil planes are spotted with PP, the focal planes with FP, and the focal lengths of the different lenses are indicated, all distances being in millimeters. Except for the Spatial Light Modulator (SLM), the entire testbed is transmissive.

The source corresponds to a superluminescent diode (SLED) that emits a light of wavelength $\lambda = 677$ nm, with a spectral width of 7.5 nm rms. In this thesis, we consider the light is monochromatic. The polarization direction of this light corresponding to the main direction of the SLM is selected with a polarizer + waveplate couple and emitted as a source point.

A diaphragm defines the entrance pupil and is conjugated through a lenses' triplet with a phase screen. This phase screen enables in particular to simulate segmentation and residual

turbulence effects, but we kept it clear in all our experimental tests.

This pupil is reimaged on the SLM by crossing a beam splitter. Even if half (75% in total) of the light is lost because of the beam splitter, it insures that the optical axis stays orthogonal to the SLM. Without this beam splitter, the beam would reach the SLM with a 45° angle. The SLM behaves like a high-density DM (792×600 pixels of $20 \times 20\mu$m), modifying the wavefront. It is composed of a matrix of liquid crystals whose orientation, which can be controlled by the user, created a phase difference. Even if the high density of actuators remains a good advantage, the SLM has also a very slow response and requires a polarized light.

After the SLM, the beam is divided into two paths. The first one is dedicated to the ZELDA sensor to reconstruct NCPA, and is made of a ZELDA mask located in the focal plane, and a ZELDA camera (Hamamatsu) in the pupil plane. The second one contains a R&R coronagraph composed of a Roddier mask ($1.1\lambda/D$) in the focal plane and a Lyot stop ($94 \pm 1\%$ in diameter of the entrance pupil) in the pupil plane. A Photometrics CoolSNAP HQ2 camera (1392×1040 pixels for a sampling of 9.43 ± 0.10) is set up at the end of this path, enabling to image either the focal plane or the pupil plane depending if a last imaging lens is in or out (grey lens in the scheme).

6.2.2 Experimental set up and validation

Olivier Herscovici-Schiller and I ran the first experimental validation of the NLDH algorithm on the MITHIC testbed. The goal of this test was to observe a decrease of the intensity in the defined dark hole, which in our case corresponds to a half-donut shape between 2 and $5\lambda/D$.

No coronagraph is set for this experiment and the PSF corresponds to the Airy pattern shown on Fig.6.2.2 (bottom-a). This PSF indicates that the testbed is well aligned with good-enough quality optics. This is verified with a Shack-Hartmann wavefront sensor that estimates the aberrations on the testbed around 10 nm rms. The contrast in the dark hole is then limited by the diffraction pattern more than by the speckles due to optical aberrations, and the NLDH controller will mainly dig into the diffraction rings, instead of correcting for wavefront aberrations.

As a sensor, we apply COFFEE that can reconstruct the phase aberrations needed for the NLDH algorithm to furnish the SLM command. COFFEE needing two different images, a 40 nm rms focus is set on the SLM for the second image.

After applying the NLDH algorithm, the command is sent to the SLM. It is not used in its full spatial capacity but to simulate a lower density DM composed of 41×41 actuators, like the SPHERE DM. The PSFs before and after application of the NLDH command are visible on Fig.6.2.2 (bottom), and the corresponding simulated PSFs on Fig.6.2.2 (top). As an information, the PSFs after correction were obtained after one single iteration. Fig. 6.2.3 indicates the radial averaged contrasts of the two PSFs of Fig.6.2.2 (bottom).

The first noticeable fact is that the dark hole shape can be clearly recognized and corre-

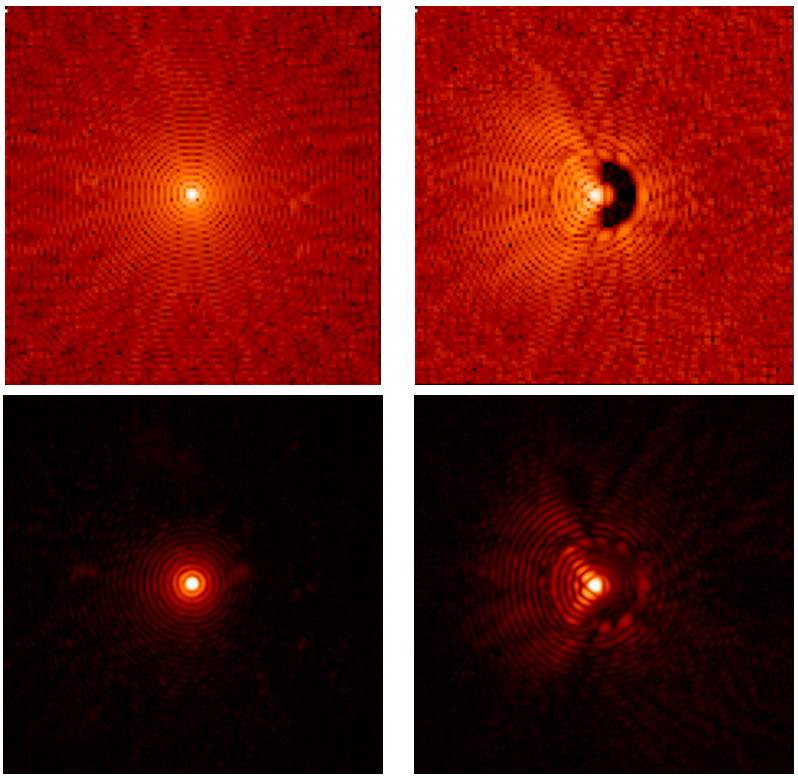

(a) (b)

Figure 6.2.2: PSFs (top) in simulation and (bottom) in laboratory, (a) before and (b) after NLDH control between 2 and $5\lambda/D$.

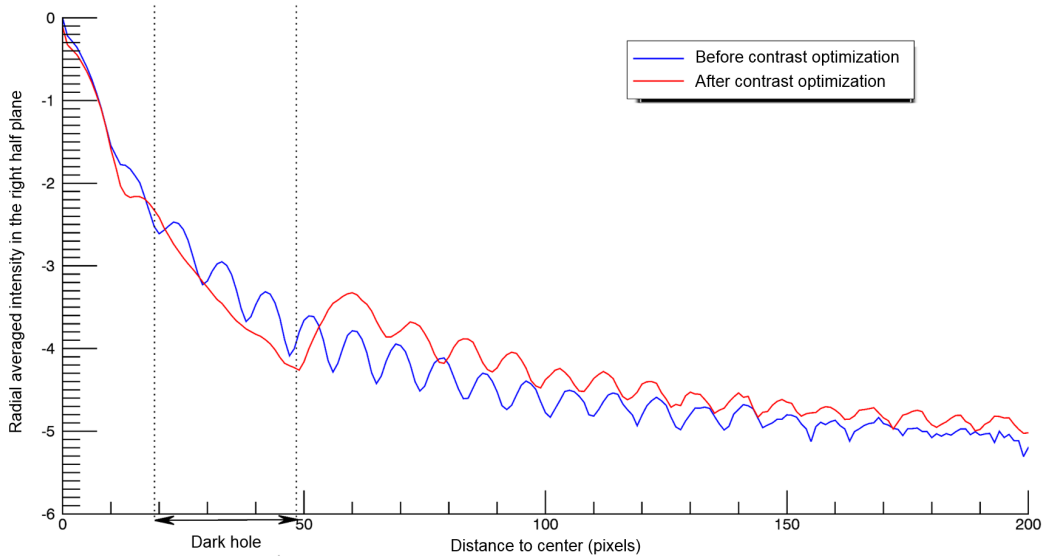

Figure 6.2.3: Radial averaged contrasts before (blue) and after (red) compensation with the NLDH controller. Credit: Olivier Herscovici-Schiller.

sponds to the one expected: half a donut between 2 and $5\lambda/D$. The repartition of intensity in the focal plane and in particular around the dark hole and on the symmetrical side of the dark hole is strongly modified, since the photons are ejected from the dark hole. The contrast in the dark hole after correction is 2.12×10^{-4} (1.77×10^{-4} rms), ie. 2.3 times better than before correction.

The difference of result between the simulation and the experimental data might come from an error in the optical system model. There exist also uncertainties in the orientation, position, and magnification of the map to apply on the SLM. We also noticed that the testbed components were not fully stable over time.

After this first experimental implementation of the NLDH algorithm, it has been tested and validated on the THD2 testbed by Olivier Herscovici-Schiller, in presence of a coronagraph [Herscovici-Schiller et al. (2018a)]. The next step is to apply this technique in presence of a coronagraph on a segmented aperture, which is a configuration proposed for instance by the HiCAT testbed.

6.3 Non Linear Dark Hole algorithm for high-contrast imaging

A specificity of the NLDH controller is its flexibility to the presence of a coronagraph [Paul (2014)]. This becomes a major quality when it comes to high-contrast imaging instruments, that often require coronagraphy.

The NLDH algorithm is based on a model of the optical system. This model just needs to

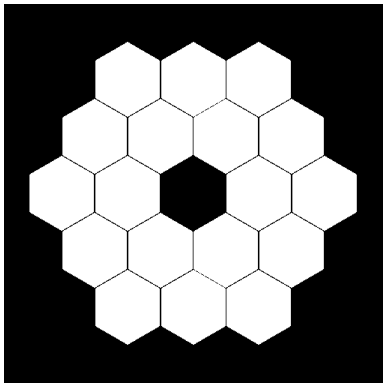

Figure 6.4.1: JWST pupil, used for this entire section. It is composed of 18 hexagonal segments plus an hexagonal central obstruction.

be modified so the NLDH algorithm works in presence of coronagraph (see section 3.2.2.2 for a model of light propagation through a coronagraph). All coronagraph models that the NLDH algorithm can call are based on one or multiple multiplications with a mask and Fourier transforms: the classical Lyot coronagraph, the APLC, the R&R coronagraph, and the 4QPM coronagraph.

In addition to the coronagraph, another parameter has to be taken into account: the segmentation of the pupil and the non-circular shape of the pupil, which can be challenging for the controller to compensate.

In the next section, we include these two new parameters into the NLDH algorithm: a coronagraph and a segmented pupil.

6.4 Non Linear Dark Hole algorithm on segmented apertures

In this section, we study the robustness of the NLDH algorithm to pupil segmentation, by mean of simulations. The objective is to answer the following questions:

- how deep can the NLDH suppress the diffraction residuals from a segmented aperture, compared to a more conventional monolithic circular pupil?

- is a segmented mirror of any help to improve the contrast?

- what is the robustness of the NLDH algorithm to phase aberrations?

We use a JWST-like pupil, composed of 18 hexagonal segments spread in two rings plus an hexagonal central obstruction (see Fig. 6.4.1). It is combined with a R&R coronagraph of size $1.06\lambda/D$, where $\lambda = 640$ nm. The control is done with a SPHERE-like DM with a continuous surface and composed of 41×41 actuators.

	Circular pupil	**Segmented pupil**
Contrast before correction	7.5×10^{-5}	1.1×10^{-4}
Contrast after correction	5.5×10^{-7}	9.2×10^{-7}
DM surface PV (nm)	308.7	627.9
DM surface RMS (nm)	51.7	41.8
Iteration number	46	100

Table 6.4.1: Comparison of NLDH performance between a circular aperture and a segmented aperture.

6.4.1 Comparison of performance between monolithic and segmented apertures

This section aims at comparing the performance reached with the NLDH technique for monolithic and segmented apertures. The considered monolithic pupil corresponds to the circumscribed disk of the studied segmented pupil.

We consider a dark hole half circular, between 4 and $10\lambda/D$. The system has no optical aberration, so the wavefront error is null, to focus only on the estimation of the ultimate performance of NLDH per aperture shape.

In this configuration, we run the NLDH algorithm similarly for both the monolithic and the segmented pupils. The final results are indicated in Fig.6.4.2 and table 6.4.1. In the circular pupil case the algorithm converges faster than in the segmented pupil case (46 vs 100 numerical iterations needed - once again, no hardware optical iteration is applied here), to reach a better contrast in the dark hole (5.5×10^{-7} vs 9.2×10^{-7}), with less effort to put on the DM surface (PV of 0.48λ vs 0.98λ). However, the initial contrast, before correction, was already better in the circular pupil case than in the segmented pupil case, so the contrast improvement is quite equivalent in both cases: the contrast is improved with a factor of 136 in the circular pupil case while with a factor of 120 in the segmented pupil case. The fact that the NLDH requires more iterations to compensate is normal: in the segmented aperture, more diffraction residuals have to be to cancelled out.

The PSD of both DM phases are plotted in Fig.6.4.3. In both cases (circular monolithic and segmented pupils), the PSDs show a clear increase right after 10 cy/pup, showing the rejection of photons out of the dark hole that goes from 4 to $10\lambda/D$.

6.4.2 Use of the segmented mirror for dark hole generation

In addition to the continuous surface DM, a second DM is added in the simulation, also in pupil plane, to contribute to the dark hole generation: a segmented mirror, composed of 18 hexagonal segments plus an hexagonal central obstruction. It is typically equivalent to the primary mirror of the telescope, used as a second wavefront corrector. The idea of this section is to study if these extra degrees of freedom improves the performance of the NLDH controller.

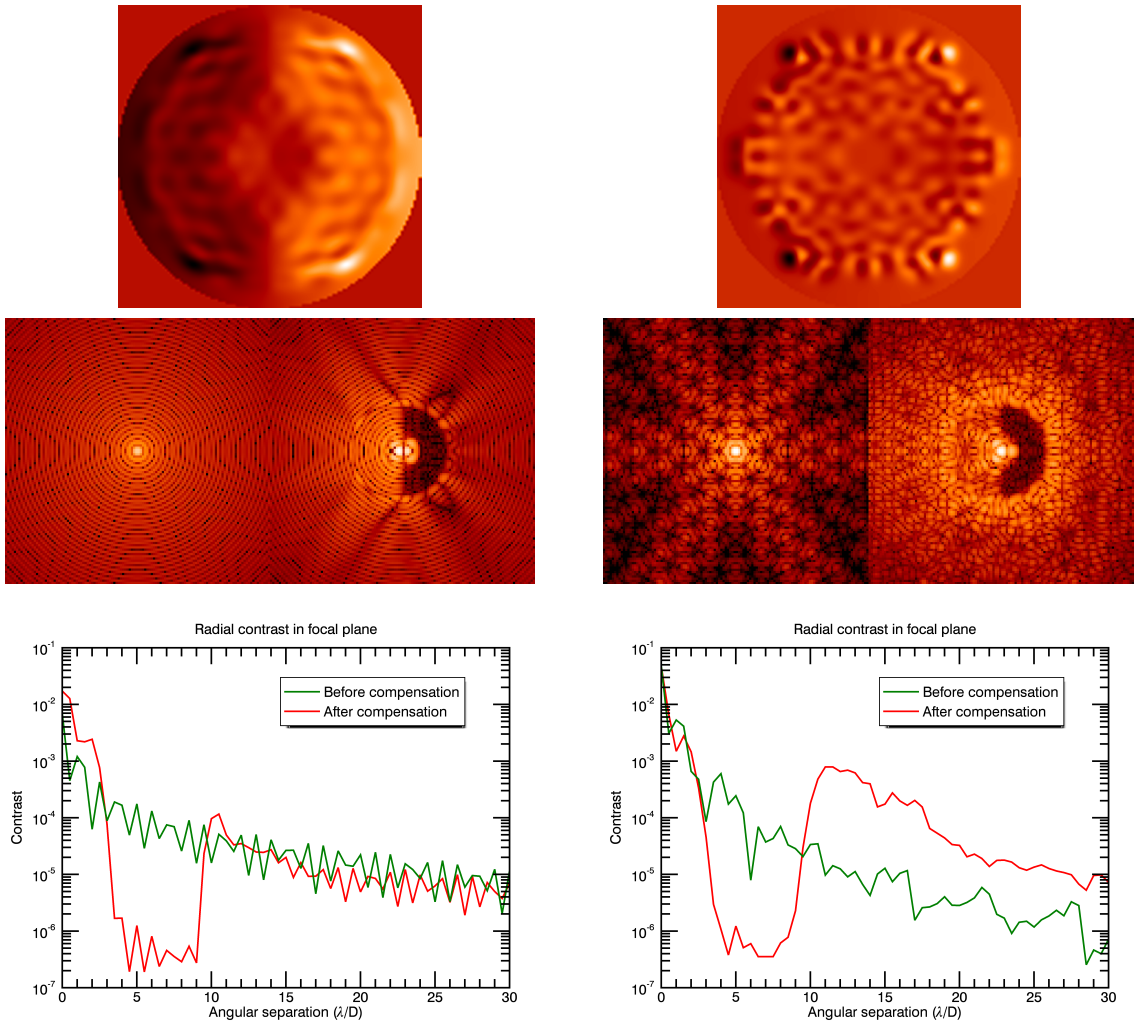

(a) (b)

Figure 6.4.2: Comparison of NLDH performance between (a) a circular aperture and (b) a segmented aperture. Top line: DM shape, middle line: (left) PSF before correction and (right) PSF after correction, bottom line: radial averages of the previous PSFs.

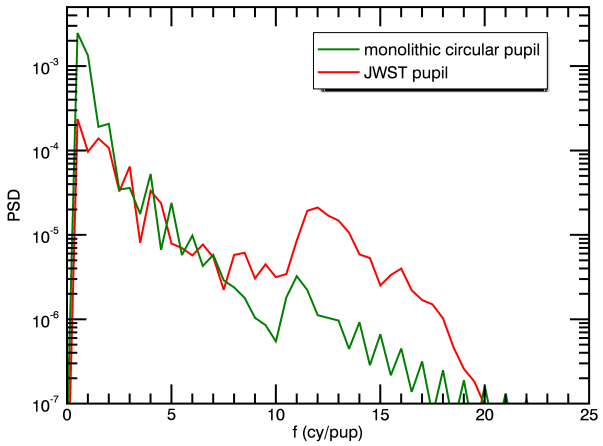

Figure 6.4.3: PSD of the DM phases for NLDH correction with a circular monolithic pupil and a segmented pupil.

	Cont DM only	**Seg mirror + cont DM**
Contrast after correction	9.2×10^{-7}	1.4×10^{-6}
Ratio before/after correction	120	78.6
Tot DM surface PV (nm)	627.9	638.7
Tot DM surface RMS (nm)	41.8	39.8
Iteration number	100	116

Table 6.4.2: Comparison of NLDH performance between the continuous DM only configuration and the continuous DM + segmented mirror configuration, the segments being controlled in piston only.

6.4.2.1 Segment piston control

I first consider that this new control device can only be controlled in piston, giving access to 18 new degrees of freedom. The table 6.4.2 proposes a comparison of performance criteria between the configuration with the continuous DM only and the configuration with both the continuous DM and the segmented mirror.

The two configurations propose quite similar results, even if a slight decrease of performance can be observed for the segmented mirror plus continuous DM configuration: the dark hole contrast is a bit worse and the algorithm takes longer to converge. In terms of effort on the DMs, on the one DM only case, the correction phase requires a quite higher deformation in the two DMs case than in the one DM case (639 nm pv vs 628 nm pv, 40 nm rms vs 42 nm rms), but this effort is spread between the two DMs, even if a clear preference for the continuous DM can be noticed (continuous DM: 597 nm pv and 43 nm rms, segmented mirror: 65 nm pv and 20 nm rms). The effort on the continuous DM remains globally equivalent.

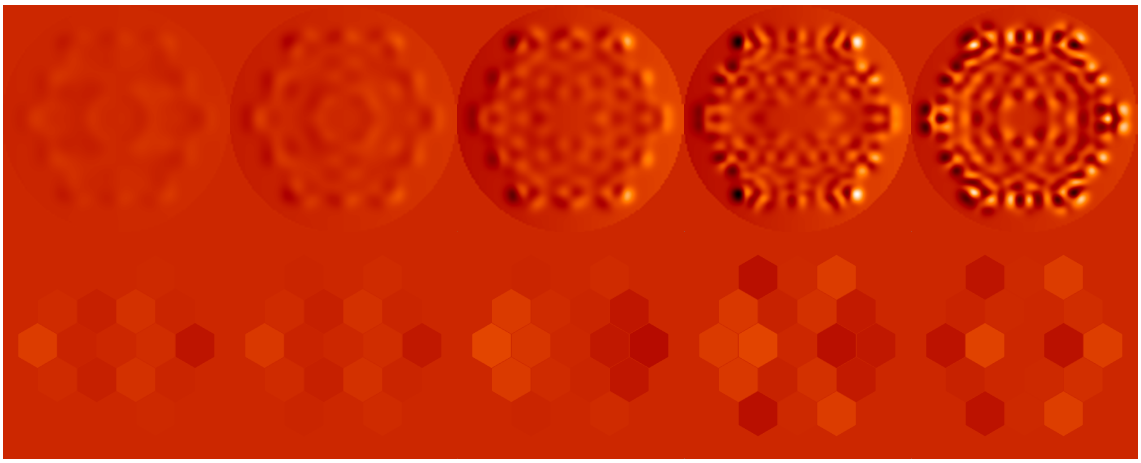

Figure 6.4.4: Comparison of NLDH performance with different convergence thresholds (from left to right: 1, 10^{-1}, 2×10^{-2}, 10^{-2}, and 10^{-3}), in the case where both a continuous surface DM and a segmented mirror are used for the correction. Top line: surface of the continuous DM, bottom line: surface of the segmented mirror. All phases are at the same scale.

Convergence threshold	**1**	$\mathbf{10^{-1}}$	$\mathbf{2 \times 10^{-2}}$	$\mathbf{10^{-2}}$	$\mathbf{10^{-3}}$
Contrast after correction	4.8×10^{-5}	2.4×10^{-5}	6.7×10^{-6}	1.4×10^{-6}	9.7×10^{-8}
Ratio b/a correction	2.3	4.6	16.4	78.6	1134
Cont DM surface PV (nm)	39.3	105.0	344.9	597.1	492.1
Cont DM surface RMS (nm)	5.8	13.1	30.6	43.1	54.5
Seg DM surface PV (nm)	47.0	41	73.6	64.7	59.8
Seg DM surface RMS (nm)	9.8	8.8	17.7	20.1	18.5
Iteration number	2	7	28	116	619

Table 6.4.3: Comparison of NLDH performance with different convergence thresholds, in the case where both a continuous surface DM and a segmented mirror are used for the correction. As a reminder, the contrast before correction is around 1.1×10^{-4}.

We could wonder why we do not obtain a better or at least an equal result or DM shape in these two configurations. The algorithm stops running when a certain convergence threshold is reached. Therefore, an explanation could be that since there are more degrees of freedom in the segmented mirror plus continuous DM configuration, another phase solution is proposed when the threshold is reached. Tightening this threshold makes the solutions of both configurations converge.

To illustrate this phenomenon, we run the algorithm with different convergence thresholds. Fig.6.4.4 and table 6.4.3 indicates the results of theses tests. We notice that without a surprise the final contrast in the dark hole improves with the convergence threshold, but also that the contribution of the segmented mirror decreases compared to the one of the continuous surface DM, until a certain threshold.

This effect can be explained with the spatial frequencies accessible by the segmented

	Cont DM only	**P-seg + cont DM**	**PTT-seg + cont DM**
Contrast after correction	9.2×10^{-7}	1.4×10^{-6}	2.7×10^{-6}
Ratio b/a correction	120	79	41
Tot DM surface PV (nm)	627.9	638.7	480.6
DM surface PV repartition (nm)	c: 627.9	c: 597.1 P: 64.7	c: 480.6 P: 54.5 TT: 2.5
Tot DM surface RMS (nm)	41.8	39.8	31.2
DM surface RMS repartition (nm)	c: 41.8	c: 43.1 P: 20.1	c: 31.1 P: 10.9 TT: 0.29
Iteration number	100	116	65

Table 6.4.4: Comparison of NLDH performance between the continuous DM only configuration, the continuous plus piston-controlled segmented mirrors, and the continuous plus piston-, tip-, and tilt-controlled segmented mirrors. P stands for piston, TT for tip and tilt, and c for continuous.

mirror: with at most 5 segments in a diameter, it cannot have a significant effect over $2.5\lambda/D$. Yet the chosen dark hole starts at $4\lambda/D$.

6.4.2.2 Segment piston, tip, and tilt control

We now add 36 more degrees of freedom, with access to the tip and tilt of all 18 segments. The dark hole is still between 4 and $10\lambda/D$ and the system has no optical aberration.

Fig.6.4.5 shows the phases to apply on the segmented and continuous DMs, the PSF with the dark hole generated by these commands, and the radial average of this PSF. The table 6.4.4 indicates the performance of the correction and the effort asked on the DMs.

We can notice that the contrast in the dark hole is a bit worse than with a continuous DM only (9.2×10^{-7}) or with access to the pistons of the segmented mirror in addition to the continuous DM (1.4×10^{-6}). Like in the previous case (piston-controlled segmented mirror and continuous DM), almost all the effort goes to the continuous DM, and even on the segmented mirror, almost no tip-tilt is applied. However, the command sent to the segmented mirror remains quite different from the piston-only case at equivalent threshold: the tips and tilts of the segments, even if they remain very small, gave access to an intermediate and faster solution.

To conclude these two tests, using a segmented mirror in addition to the continuous DM does not seem particularly interesting: at equivalent convergence thresholds, it is even a bit worse than using the continuous DM alone. More tests could be run with higher densities of segments or with a dark hole closer to the optical axis. However in this case the coronagraph needs to be specifically designed to provide a good enough contrast at small angular separations.

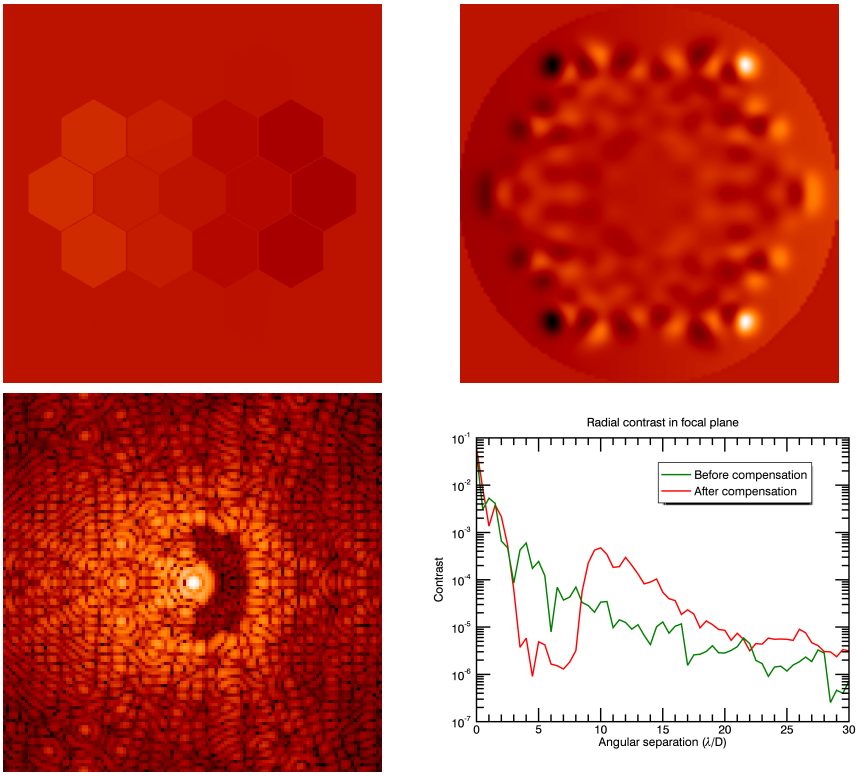

Figure 6.4.5: NLDH performance in the case where both a continuous surface DM and a segmented mirror are used for the correction, the segments being controlled in piston, tip, and tilt. Top line: surface of the segmented and continuous DMs (phases are at the same scale), bottom line: PSF after correction and its radial average.

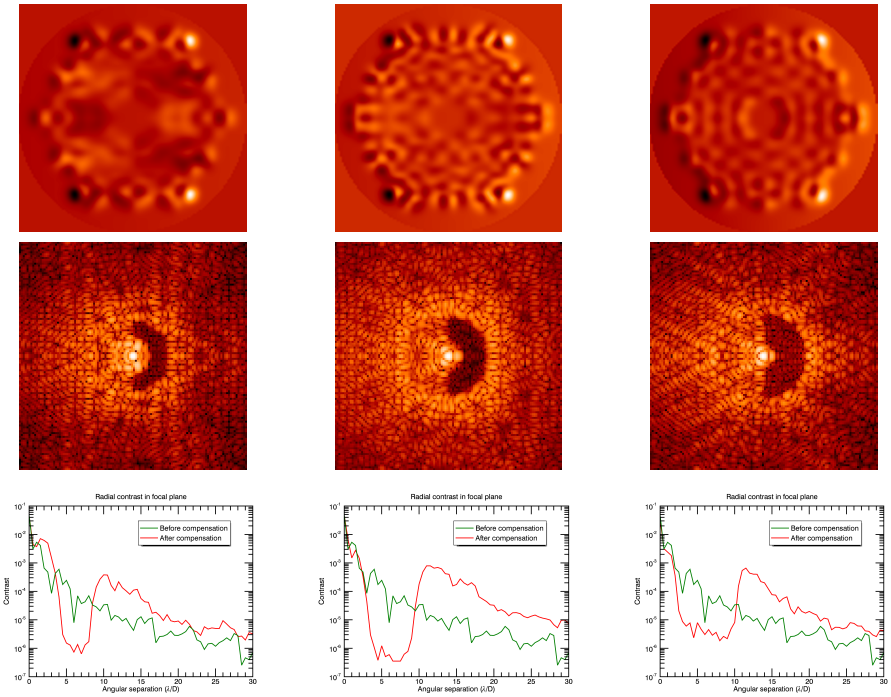

(a) (b) (c)

Figure 6.4.6: Comparison of NLDH performance with different dark hole sizes: (a) $5\lambda/D$ to $9\lambda/D$, (b) $4\lambda/D$ to $10\lambda/D$, and (c) $3\lambda/D$ to $11\lambda/D$. Top line: DM surface, middle line: PSF after correction, bottom line: radial averages before and after correction.

6.4.3 Impact of the dark hole shape on the NLDH performance

Several configurations exist when it comes to imaging an exoplanet: in some cases such as first detection, the area of high-contrast has to be as large as possible, while in some other cases, such as characterization of a known object, the area can be restricted. In general, we also want to observe very close to the star. These are the kind of problematic we address in this section: does the dark hole shape and position influence the performance of the controller?

A first test is done on modifying the surface of the considered dark hole. We study three different configurations: the dark hole goes from 5 to $9\lambda/D$, from 4 to $10\lambda/D$, and from 3 to $11\lambda/D$ (this last dark hole has an area twice larger than the first one). The results are indicated in Fig.6.4.6 and table 6.4.5. We can observe that the best contrast improvement is obtained for the middle case. However, it is also the solution that requires the most effort on the DM (0.98λ) and took the more numerical iterations to converge. It appears then that there is no clear correlation between the surface of the dark hole and the performance and efficiency of the algorithm: whatever area was chosen, the NLDH technique enabled to reach a contrast of the order of 10^{-6}, even at $3\lambda/D$!

	$5\lambda/D$ to $9\lambda/D$	**$4\lambda/D$ to $10\lambda/D$**	**$3\lambda/D$ to $11\lambda/D$**
Contrast before correction	8.9×10^{-5}	1.1×10^{-4}	1.1×10^{-4}
Contrast after correction	1.4×10^{-6}	9.2×10^{-7}	4.9×10^{-6}
Ratio before/after correction	64	120	22
DM surface PV (nm)	462.5	627.9	564.4
DM surface RMS (nm)	29.9	41.8	43.4
Iteration number	70	100	36

Table 6.4.5: Comparison of NLDH performance with different dark hole sizes.

	$4\lambda/D$ to $10\lambda/D$	**$15\lambda/D$ to $17.6\lambda/D$**
Contrast before correction	1.1×10^{-4}	9.5×10^{-6}
Contrast after correction	9.2×10^{-7}	5.7×10^{-9}
Ratio before/after correction	120	1656
DM surface PV (nm)	627.9	137.1
DM surface RMS (nm)	41.8	14.2
Iteration number	100	70

Table 6.4.6: Comparison of NLDH performance with different dark hole positions.

We now wonder how the position of the dark hole impacts the performance and efficiency of the algorithm. To study this phenomenon, we focus on two cases: a dark hole between 4 and $10\lambda/D$ and another one between 15 and $17.6\lambda/D$. These two dark holes have very close surfaces so the conclusions will be independent from the area covered by the dark hole. The results are shown in Fig.6.4.7 and table 6.4.6. In the case where the dark hole is further from the optical axis, the final contrast is by far better (final contrasts of 5.7×10^{-9} vs 9.2×10^{-7}), even relatively to the initial contrast (initial to final contrast ratios of 1656 vs 120). Furthermore, the effort on the DM is lower when the dark hole is further form the optical axis (0.21λ vs 0.98λ in peak-to-valley) and the algorithm converges faster (70 vs 100 iterations). It appears here clearly that the NLDH algorithm is more efficient the further from the optical axis the dark hole is, even regarding the fact that the initial contrast is already lower. A possible explanation to the phenomenon could be that less spatial frequencies have to be corrected so reached by the DM actuators ($2.6\lambda/D$ vs $6\lambda/D$).

To conclude, the distance between the dark hole and the optical axis seems to have the biggest impact on the efficiency of the NLDH algorithm, compared to the area covered by the dark hole. However, the dark hole is in general chosen as a function of the target object and more precisely its angular separation with the star, so dark holes close to the optical axis will be in practice often privileged.

6.4.4 Robustness to aberrations such as phasing errors

The ultimate performance depends on the phasing of the segments (see section 4). In high-contrast imaging, the constraints on the primary mirror alignment are extremely tight, and

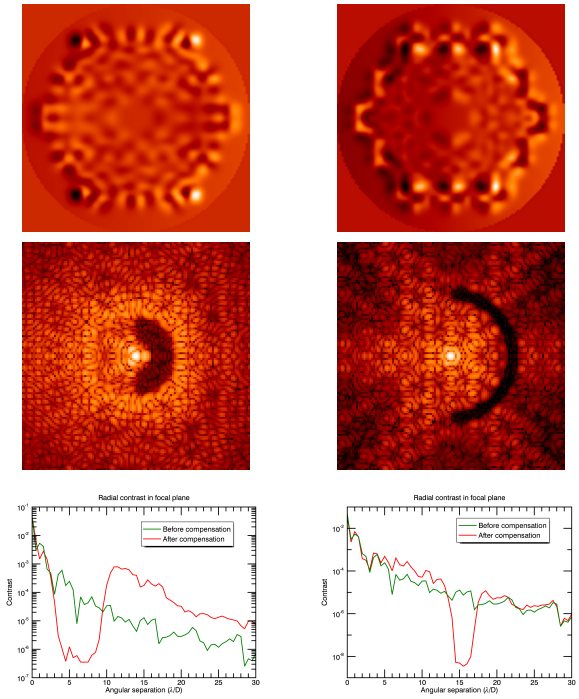

(a) (b)

Figure 6.4.7: Comparison of NLDH performance with different dark hole positions: (a) $4\lambda/D$ to $10\lambda/D$ and (b) $15\lambda/D$ to $17.6\lambda/D$.

Phasing error (nm rms)	**0**	**1**	**10**	**100**	**1000**
Contrast before correction ($\times 10^{-4}$)	1.1	1.19 ± 0.01	1.3 ± 0.12	23 ± 11	75 ± 15
Contrast after correction ($\times 10^{-7}$)	9.2	14 ± 3	7.2 ± 3.6	13 ± 5	13 ± 6
DM surface PV (nm)	627.9	667.0 ± 22	572.6 ± 97	978.3 ± 135	1245 ± 118
DM surface RMS (nm)	41.8	39.6 ± 1.9	43.1 ± 2.1	88.6 ± 23	189 ± 25
Iteration number	100	78 ± 13	122 ± 30	125 ± 38	150 ± 22

Table 6.4.7: Comparison of NLDH performance with different level of phasing errors (segment-level pistons). Each value, except for the no aberration case, corresponds to the average over a set of 5 different tests.

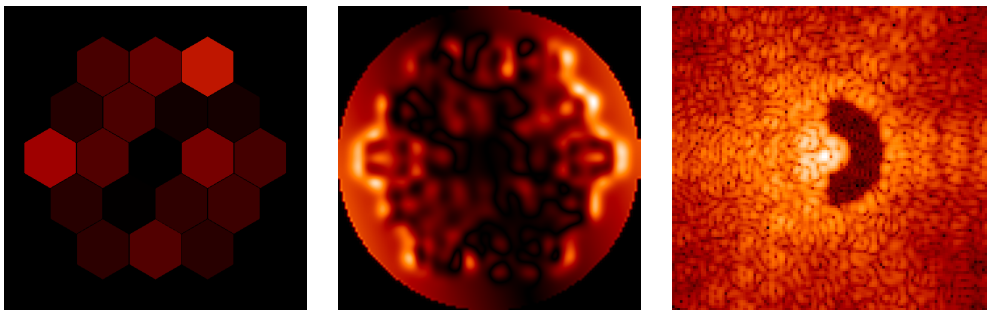

(a) (b) (c)

Figure 6.4.8: (a) Example of phasing error on the primary mirror of the telescope (segment-level pistons of 100 nm rms on the entire pupil), (b) Corresponding correction phase proposed by the NLDH algorithm (PV $= 1.5\lambda$, RMS $= 0.26\lambda$ on the DM), and (c) corresponding PSF, in presence of the phasing errors and the correction phase (C$= 1.85 \times 10^{-6}$). The dark hole goes from $4\lambda/D$ to $10\lambda/D$ and the phases (a) and (b) are at the same scale.

in general a wavefront controller is used to compensate also for these alignment precision errors. In this section, I study the robustness of the NLDH algorithm to piston-phasing errors on the segments, to verify if such a control method can be used to recover from a loss of performance due to phasing errors.

The results are indicated in table 6.4.7, for five different levels of aberrations: no aberration, 1 nm rms, 10 nm rms, 100 nm rms, and 1000 nm rms of piston errors. Except for the no aberration case, we select for each aberration level five random phases and run the NLDH algorithm. The results show that the performance can always be recovered, for a final contrast around 10^{-6}, whatever the level of aberration or original contrast in the dark hole is. However, the effort asked on the DM increases with the level of aberrations.

Fig.6.4.8 shows a phasing error on the telescope and the corresponding result computed by the NLDH algorithm. As noticed before, the final contrast is almost fully recovered, even with aberrations. Furthermore, we can notice that the DM correction phase does not correspond to the input aberrations: the DM is not directly compensating for the aberrations.

6.5 Conclusions

In this section, we focused on a promising wavefront control technique for high-contrast imaging instruments: the NLDH algorithm. Several studies were conducted to test its performance.

First, it was implemented for the first time on an experimental testbed, MITHIC, on the case of a circular and monolithic aperture, without coronagraph. This preliminary step was followed by the experimental validation of the NLDH controller on the THD2 testbed, in presence of a coronagraph, by Herscovici-Schiller et al. (2018a). The next step is now to apply it on a segmented aperture, which is doable on the HiCAT testbed, for instance.

To accompany the application of the NLDH algorithm on segmented apertures combined with a coronagraph, I conducted several studies in simulation:

- It appears that the NLDH algorithm remains efficient even when the monolithic aperture is replaced with a segmented aperture: the contrast is improved with a factor of 120 compared to the no-correction case, while 136 for the monolithic aperture case.

- The use of a segmented mirror does not improve the contrast in the final dark hole and almost all the correction phase is sent on the continuous surface rather than the segmented mirror (64.7 nm pv on the segmented mirror vs 597.1 nm pv on the continuous DM, for the piston + continuous DMs case).

- It also appears that the performance of the NLDH algorithm depends on the position of the dark hole more than on its surface: the further from the star the dark is, the better the performance (gain on the final contrast of 161 when the dark hole moves from 4 to $10\lambda/D$ to 15 to $17.6\lambda/D$).

- Eventually, the NLDH algorithm seems very robust to phasing aberrations, since from 0 to 1000 nm rms of segment-level pistons, it enables to reach equivalent contrasts in the dark hole. this is particularly interesting since the non linear specificity of this technique provides access to both low and high optical aberrations.

Such studies enable to understand the behavior of the NLDH controller and test its performance and limits in the presence of a segmented aperture combined with a coronagraph. However the results are so far very promising since this algorithm seems robust to segmentation and segmentation-related aberrations.

Nous avons tout dit, tout nous reste à dire
Il nous faudra tout délier

— Georges Moustaki

7 Conclusions and perspectives

Direct imaging of exoplanets, and more precisely of Earth-like planets provides several advantages compared to indirect detection methods. in particular, it enables the study of the spectrum and therefore the composition of its atmosphere, which informs about the possible presence of life markers on the planet.

However, imaging Earth-like planets is extremely challenging. Indeed this means being able to detect an object 10^{10} times less bright than its host star and within an angular separation of around 0.1". Several tools are being developed to achieve this goal: coronagraphs aims at removing the starlight while wavefront sensors reconstruct the wavefront aberrations and wavefront control algorithms, combined with deformable mirrors, reduce the speckles in a certain area of the focal plane called the dark hole.

In addition to the challenge brought by the star-planet system, another one has to be taken into account: future telescopes, in particular these dedicated to Earth-like planet imaging, tend to be segmented, and this segmentation impacts the PSF and the intensity in the dark hole, in addition to adding specific optical aberrations such as segment phasing errors or dynamic effects like vibrations and instabilities.

The goal of this thesis is to bring a refined comprehension of the process of high-contrast imaging through a segmented aperture. More precisely, I studied the robustness of a coronagraph to segment manufacturing and phasing errors and tested well-known algorithms of wavefront sensing and control on segmented telescopes in presence of a coronagraph.

In chapter 4, I describe the Pair-based Analytical model for Segmented Telescopes Imaging from Space (PASTIS) that I developed during my PhD. This model takes into account the specificities of the high-contrast imaging instruments (segmentation, coronagraph, segment-level optical aberrations) to analyze their performance and stability in presence of local

aberrations. Since it runs faster than any end-to-end simulation, it can be directly applied to error budgeting of segmented telescopes such as the LUVOIR telescope or the JWST. I personally applied PASTIS to a LUVOIR-like architecture, which allowed to identify specific modes of the primary mirror, based on combinations of segment-level aberrations. These modes can be classified as a function of their impact on the contrast, which informs about the critical shapes to avoid on the primary mirror and quantify the requirements on these configurations.

Beyond the developments proposed in this thesis, PASTIS still offers numerous directions of development (complex dynamic aberrations, broadband light, variation of coronagraph and segmentation architecture...) and applications (Keck telescope, ELT, GMT...). More excitingly, as a linear model PASTIS can be inverted in order to optimize the whole optical system (apodisor, focal plane mask, segmentation configuration...) with both the objectives of improving the contrast and releasing the constraints, which would lead to new configurations of coronagraphic systems, efficient and less sensitive to segment-level aberrations. In particular, I am really interested in studying segment-level apodisors: indeed, we proved with PASTIS that the shape of the segment impacts directly the level of contrast deterioration in presence of aberrations. Therefore, applying an apodization per segment will impact the robustness of the whole system to aberrations, leading to a release of the constraints on the system. The telescope whose primary mirror is conjugated with a segment-level apodisor would be hyper stable and less sensitive to aberrations!

In chapter 5, I present the experimental validation of the COFFEE (COronagraphic Focal-plane wave-Front Estimation for Exoplanet detection) wavefront sensor in the specific case of a segmented aperture, to reconstruct phasing errors. As an extension of the phase diversity algorithm to coronagraphic optical trains, COFFEE benefits from its advantages: an absolute measurement (no differential aberrations) and no need for additional hardware in the system, except for an image modulated by the deformable mirror. During my PhD, I applied COFFEE on the HiCAT testbed (High-contrast imager for Complex Aperture Telescopes) that combines a segmented aperture, a coronagraph, and a deformable mirror for wavefront control.

COFFEE was applied in two modes: without and with coronagraph on the optical train. Without coronagraph, the results are very promising and fit with the expectations. The coronagraphic case enabled to put into evidence a limit of COFFEE: it is blind to aberrations of lower order than the coronagraphic mask, that by definition filters them out. In our application case, the segments themselves are large enough to be considered as mostly low-order aberrations, and COFFEE had then some difficulties to reconstruct phasing aberrations. Taking that new constraint into account, new tests will be done in the future in presence of a better-suited coronagraph of smaller extension, which is anyway more adapted to the detection of planets close to their host star, and a control loop with COFFEE will be implemented to flatten the segmented mirror. This procedure might be interesting to compare to the baseline solution for the cophasing of the JWST segments once deployed.

In chapter 6, we apply the NLDH (Non Linear Dark Hole) technique in simulation to segmented apertures. Its main advantage is to converge faster than usual linear methods,

which is specifically interesting when it comes to high-contrast performance, particularly hard to stabilize over long exposure times. During my PhD, I ran several tests to analyze the performance, behavior, and limits of this technique, that had only been applied on circular monolithic apertures so far.

It appears from our studies that the segmentation does not significantly impact the final contrast in the dark hole, even if it slows down the convergence. We also proposed to use the primary mirror or a conjugated segmented mirror as part of the control process, but it did not show any significant advantage, except for absorbing a small fraction of the correction phase. As a third test, the position and shape of the dark hole seem to influence the performance of the algorithm, particularly when it comes to the distance between the dark hole and the star. I also showed that the NLDH technique enables even to recover or maintain the contrast without any loss in contrast when the segments have phasing errors, even if it requires a slower convergence and more effort on the DM.

The NLDH algorithm has been experimentally validated on monolithic pupils, first without coronagraph on the Marseille Imaging Testbed for HIgh Contrast (MITHIC) testbed and more recently on the Très haute Dynamique (THD2) testbed. The next step is to validate it on a segmented aperture combined with a coronagraph, which could typically be done on the HiCAT testbed.

A

Development of the computations for the Young experiment in broadband light

We demonstrate here the expression of the channelled spectrum, generated by the Young experiment in broadband light.

$$
\begin{aligned}
I(M) &= \frac{1}{\Delta\upsilon}\int_{\upsilon_0-\frac{\Delta\upsilon}{2}}^{\upsilon_0+\frac{\Delta\upsilon}{2}} I(M,\upsilon)\,\mathrm{d}\upsilon \\
&= \frac{2E_0^2}{\Delta\upsilon}\int_{\upsilon_0-\frac{\Delta\upsilon}{2}}^{\upsilon_0+\frac{\Delta\upsilon}{2}} 1+\cos(2\pi\theta\frac{a\upsilon}{c})\,\mathrm{d}\upsilon \\
&= 2E_0^2(1+\frac{1}{\Delta\upsilon}\int_{\upsilon_0-\frac{\Delta\upsilon}{2}}^{\upsilon_0+\frac{\Delta\upsilon}{2}} \cos(2\pi\theta\frac{a\upsilon}{c})\,\mathrm{d}\upsilon) \\
&= 2E_0^2\left(1+\frac{c}{2\pi\theta a\Delta\upsilon}[\sin(2\pi\theta\frac{a\upsilon}{c})]_{\upsilon_0-\frac{\Delta\upsilon}{2}}^{\upsilon_0+\frac{\Delta\upsilon}{2}}\right) \\
&= 2E_0^2\left(1+\frac{c}{2\pi\theta a\Delta\upsilon}\left(\sin(2\pi\theta(\upsilon_0+\frac{\Delta\upsilon}{2})\frac{a}{c})-\sin(2\pi\theta(\upsilon_0-\frac{\Delta\upsilon}{2})\frac{a}{c})\right)\right) \\
&= 2E_0^2\left(1+\frac{c}{\pi\theta a\Delta\upsilon}\sin\left(\pi\theta\Delta\upsilon\frac{a}{c}\right)\cos\left(2\pi\theta\upsilon_0\frac{a}{c}\right)\right) \\
&= 2E_0^2\left(1+\mathrm{sinc}\left(\pi\theta\Delta\upsilon\frac{a}{c}\right)\cos\left(2\pi\theta\upsilon_0\frac{a}{c}\right)\right)
\end{aligned}
\tag{A.1}
$$

B

Leboulleux et al. 2018, proceeding for the SPIE conference

Sensitivity analysis for high-contrast imaging with segmented space telescopes

Lucie Leboulleux[abc], Laurent Pueyo[a], Jean-François Sauvage[bc], Thierry Fusco[bc], Johan Mazoyer[ad], Anand Sivaramakrishnan[ad], Mamadou N'Diaye[e], Rémi Soummer[a]

[a] Space Telescope Science Institute, 3700 San Martin Drive, Baltimore, MD 21218, USA
[b] Aix Marseille Université, CNRS, LAM (Laboratoire d´Astrophysique de Marseille) UMR 7326, 13388, Marseille, France
[c] Office National d´Etudes et de Recherches Aérospatiales, 29 Avenue de la Division Leclerc, 92320 Châtillon, France
[d] Department of Physics and Astronomy, Johns Hopkins University, Baltimore, MD, USA
[e] Observatoire de Nice Côte d´Azur, Boulevard de l´Observatoire, 06304 Nice, France

ABSTRACT

Direct imaging and spectroscopy of Earth-like planets will require high-contrast imaging at very close angular separation: 1e10 star to planet flux ratio at a few tenths of an arcsecond. Large telescopes in space are necessary to provide sufficient collecting area and angular resolution to achieve this goal. In the static case, coronagraphic instrument designs combined with wavefront control techniques have been optimized for segmented on-axis telescope geometries, but the extreme wavefront stability required at very high contrast of the order of tens of picometers remains one of the main challenges. Indeed, cophasing errors and instabilities directly contribute to the degradation of the final image contrast. A systematic understanding is therefore needed to quantify and optimize the static and dynamic constraints on segment phasing. We present an analytical model: Pair-based Analytical model for Segmented Telescopes Imaging from Space (PASTIS), which enables quasi-instantaneous analytical evaluations of the impact of segment-level aberrations and phasing on the image contrast. This model is based on a multiple sum of Young interference fringes between pairs of segments and produces short and long exposure coronagraphic images with a segmented telescope in presence of local phase aberrations on each segment. PASTIS matches end-to-end numerical simulations with high-fidelity (3% rms error on the contrast). Moreover, the model can be inverted by dint of a projection on the singular modes of the phase to provide constraints on each Zernike polynomial for each segment. These singular modes provide information on the contrast sensitivity to segment-level phasing errors in the pupil, which can be used to derive constraints on both static and dynamic mitigation strategies (e.g. backplane geometry or segment vibration sensing and control). The few most sensitive modes can be well identified and must be controlled at the level of tens of picometers, while the least sensitive modes in the hundreds of picometers. This novel formalism enables a fast and efficient sensitivity analysis for any segmented telescopes, in both static and dynamic modes.

Keywords: Segmented telescope, cophasing, exoplanet, high-contrast imaging, error budget

1. INTRODUCTION

Achieving direct imaging and spectroscopy of Earth-like planets means being able to resolve smaller and fainter objects, a typical objective being to image planets with a 10^{-10} planet-to-star contrast and a 0.1 arcsec angular separation. Different solutions and tools have been developed to achieve this goal, such as sending telescopes to space (to null the impact of the atmospheric turbulence), increasing of the size of the primary mirror (to perform high-resolution images), combined with coronagraphs (to remove the starlight) and deformable mirrors (to perform wavefront control). To fit these large telescopes into the launch vehicle, they have to be folded and therefore segmented.

Further author information, send correspondence to Lucie Leboulleux: E-mail: leboulleux@stsci.edu, Telephone: 1 410 338 2881

Recent developments in coronagraphy and wavefront control start to absorb the effect of the diffraction due to the segmentation and to the spiders on the final image and contrast: for instance, apodized pupil Lyot coronagraphs (APLCs)[1–3] and Phase-Induced Amplitude Apodization (PIAA) coronagraphs[4] and the Active Compensation of Aperture Discontinuities (ACAD-OSM)[5,6] are now optimized to compensate for these effects. However, such solutions only correct for amplitude discountinuities and do not take into account the case where all segments are not perfectly aligned.

Indeed segmentation generates other issues, such as cophasing errors or segment unstabilities. Their impact on the coronagraphic Point Spread Function (PSF) quality needs to be studied, in particular to set up manufacturing and stability constraints for a viable mission. The traditional method is based on an end-to-end model of the optical system, on which a numerous amount of aberration phases are applied and propagated.[7,8] Because of the numerous factors that impact the contrast (local/global aberrations, phasing errors, segment vibrations, thermal drift...), this error budget is extremely time- and computer-consuming.

We developed a tool called the Pair-based Analytical model for Segmented Telescopes Imaging from Space (PASTIS) that enables a fast error-budget for any segmented pupil.[9,10] This model is mainly dedicated to space telescopes, such as the James Webb Space Telescope (JWST),[11,12] the Large Ultra-Violet Optical Infrared (LUVOIR) telescope[13,14] or the Habitable Exoplanet Imaging Mission (HabEx),[15] but can also been applied to ground-based segmented telescopes such as the Extremely Large Telescopes (ELTs).[16–19]

PASTIS enables to express directly the contrast of a coronagraphic image as a function of the Zernike coefficients of the segments' aberrations. This model can be inverted on the basis of the singular modes of the wavefront to directly provide the requirements in segment phasing, alignment, polishing, and stability to perform a target contrast. It was developed in a previous paper[10] in the static case where only one kind of Zernike polynomial is present on the segments. In this proceeding, we develop PASTIS to two other cases, more general: the general case where the segment-level aberrations are decomposed on several Zernike polynomials and the dynamic case, where the segments are impacted by vibrations that deteriorate the contrast.

Section 2 provides reminders about the PASTIS model and its main conclusions, for static errors of one single Zernike polynomial. This section also provides the basics for the developments of the next sections. In section 3, we extend this formalism to combinations of Zernike polynomials and apply it to segment phasing errors (piston, tip, and tilt). Finally in section 4, we develop PASTIS to dynamic segment aberrations, and apply it to the case of all segments vibrating at the same frequency.

2. REMINDERS ABOUT PASTIS FOR ONE SINGLE ZERNIKE POLYNOMIAL

The development of the Pair-based Analytical model for Segmented Telescopes Imaging from Space for one kind of Zernike polynomial applied on the pupil is described in a previosu paper.[10] This section consists of a summary of the main results of these papers, from the theoretical development of the model to its validation. It provides the needed basics for the extensions proposed further in this proceeding.

2.1 Theory

2.1.1 Hypotheses

We consider a segmented telescope, composed of identical segments. Behind the telescope, a coronagraph enables high-contrast imaging in the dark hole.

PASTIS is developed under different hypotheses.

First of all, we only consider small segment-level phase aberrations on the primary mirror. This means that:

- the amplitude aberrations are neglected

- other sources of aberrations such as downstream aberrations or the effect of the secondary mirror are also neglected

- global aberrations on the primary mirror of the telescope are sampled as a sum of segment-level aberrations[20]

- we consider only residual phase errors.

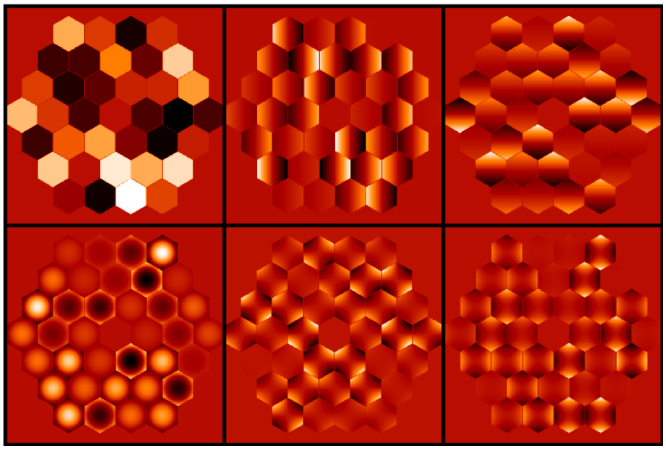

Figure 1. Typical examples of phase errors for the section 2, where only one single Zernike polynomial is considered at a time. Top line from left to right: piston, tip, and tilt. Bottom line from left to right: focus, 45°-astigmatism, and 0°-astigmatism.

These hypotheses are kept in this entire proceeding.

Furthermore, in this section, the pupil phase aberrations are simplified to the case of one single Zernike polynomial present on the segments. For instance, it can correspond to segment-level piston aberrations only, if the segments are not well phased, or to segment-level focus aberrations only if the segments have focus-like polishing errors (See Fig. 1).

2.1.2 Expression of the model

The phase ϕ is expressed as a sum between the segment-level phases, each of them being expressed on the basis of Zernike polynomials $(Z_l)_{l\in[1,n_{zer}]}$ defined on a generic segment shape:

$$\phi(\mathbf{r}) = \sum_{l=1}^{n_{zer}} \sum_{k=1}^{n_{seg}} a_{k,l} Z_l(\mathbf{r} - \mathbf{r_k}), \tag{1}$$

where:

- n_{seg} is the number of segments
- $(a_{k,l})_{k\in[1,n_{seg}]}$ are the local Zernike coefficients of Z_l
- where $\mathbf{r}$ is the position vector in the primary mirror plane (pupil plane)
- $\mathbf{r_k}$ the position vector from the center of the pupil to the center of the k-th segment.

In this section, we simplify this formula using one single Zernike polynomial.

Furthermore, we approximate the intensity in the dark hole I as:

$$I(\mathbf{u}) = \left\| \widehat{\phi}(\mathbf{u}) \right\|^2 \tag{2}$$

where $\mathbf{u}$ is the position vector in the detector plane (focal plane) and $\hat{f}$ is the Fourier Transform of the function f.

We then obtain that the intensity in the dark hole is a sum of interference fringes, similar to the Young experiment, between all pairs of segment, modulated by a low-frequency envelope. This envelope depends only on the considered Zernike polynomial, defined on a segment.

$$I(\mathbf{u}) = \left\| \widehat{Z}_l(\mathbf{u}) \right\|^2 \times \Big(\sum_{k=1}^{n_{seg}} c_{k,l}^2 a_{k,l}^2 + \sum_{k_1=1}^{n_{seg}} \sum_{k_2=1, k_2\neq k_1}^{n_{seg}} c_{k_1,l} a_{k_1,l} c_{k_2,l} a_{k_2,l} \cos((\mathbf{r_{k_2}} - \mathbf{r_{k_1}}).\mathbf{u}) \Big) \tag{3}$$

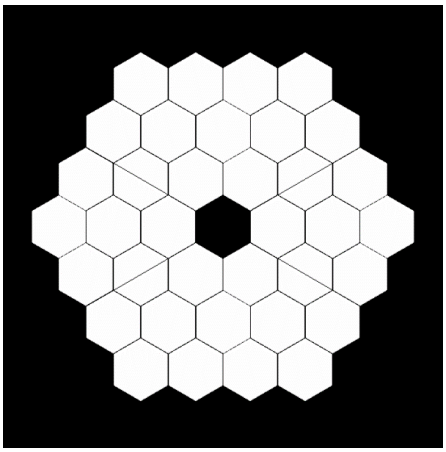

Figure 2. Pupil used for all applications in this proceeding, composed of 36 hexagonal segments. It is also one of the pupils of the Segmented Coronagraph Design and Analysis (SCDA) study.[3]

$(c_{k,l})_{k\in[1,n_{seg}]}$ are calibration coefficients, added here to take into account the coronagraph. They are obtained in a calibration step and strongly related to the apodization ratio of the segments.

This expression can be averaged to get the contrast in the dark hole:

$$C = C_0 + \sum_{k_1=1}^{n_{seg}} \sum_{k_2=1}^{n_{seg}} a_{k_1,l} a_{k_2,l} m_{k_1,k_2,l} \tag{4}$$

where C_0 is the deep contrast of the coronagraph, ie. the best contrast the coronagraph can achieve, without aberrations, and $\forall (k_1,k_2) \in [1,n_{seg}]^2, m_{k_1,k_2,l} = \langle \left\| \widehat{Z}_l(\mathbf{u}) \right\|^2 c_{k_1,l} c_{k_2,l} \cos((\mathbf{r_{k_2}} - \mathbf{r_{k_1}}).\mathbf{u}) \rangle_{DH}$, $\langle f \rangle_{DH}$ corresponding to the mean value of the function f over the dark hole. This equation is equivalent to:

$$C = C_0 + A_l M_l A_l^t \tag{5}$$

where the vector A_l contains all the coefficients $(a_{k,l})_{k\in[1,n_{seg}]}$, and $\forall (i,j) \in [1,n_{seg}]^2, M_l(i,j) = m_{i,j,l}$.

2.2 Application

2.2.1 Chosen application case

The PASTIS model is adaptable to all segmented pupils. For this proceeding, we choose to apply it to the 36-segment pupil presented in Fig. 2, with a monolithic source at 640nm.

It is combined with an Apodized Pupil Lyot Coronagraph (APLC) that enables a contrast of a few 10^{-11} in a dark hole between $4\lambda/D$ and $9\lambda/D$, without aberrations. The impact of the coronagraph on the final image is illustrated in Fig. 3.

In the application section, the end-to-end simulation corresponds to an explicit computation of the electric field from plane to plane using a Fourier formalism and the different masks composing the APLC.

2.2.2 Validation of PASTIS

In Fig. 4 we can find the contrasts computed from both PASTIS and the end-to-end simulation, for piston aberrations from 1pm to 10nm rms on the segments. For each rms piston value, 250 random phases are tested, providing 250 contrasts with the end-to-end simulation and 250 contrasts with PASTIS. From these two sets, we plot the minimum contrast, the maximum contrast, and the average contrast.

For all phases used for these curves, PASTIS provides an estimation of the contrast with an error around 3% rms. But the main advantage of PASTIS remains that the plots have been 10^7 times faster to obtain the the ones from the end-to-end simulation.

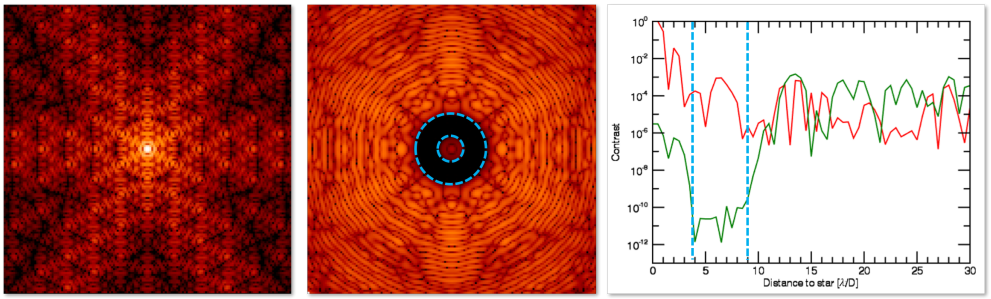

Figure 3. Left: PSF of the SCDA pupil (see Fig.2), obtained with an end-to-end numerical simulation with no coronagraph and aberrations. Center: PSF of the same SCDA pupil, obtained with an end-to-end numerical simulation with coronagraph and without aberrations. Right: Cut along the horizontal radius of the two previous PSFs (red: without APLC, green: with APLC). The two blue dashed lines correspond to the limits of the dark hole.

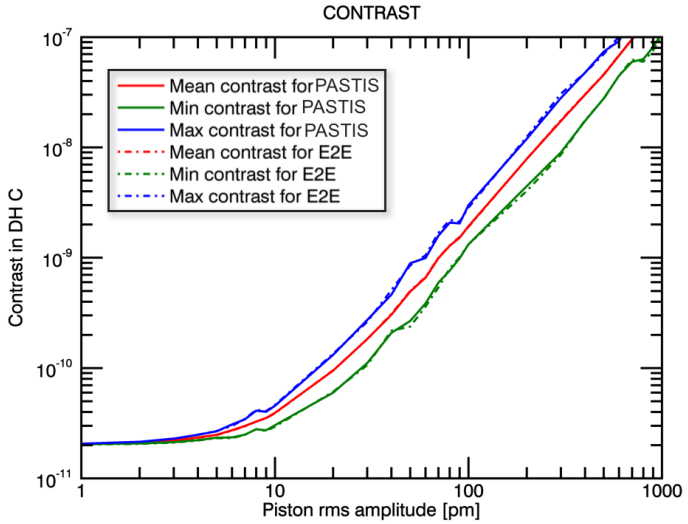

Figure 4. Contrast as a function of the rms piston aberrations on the segments. It was computed through two methods: the end-to-end model (dashed lines) and PASTIS (continuous lines). For each rms piston value, 250 random phases are selected, so 250 contrasts computed, and the minimum, average, and maximum values are plotted.

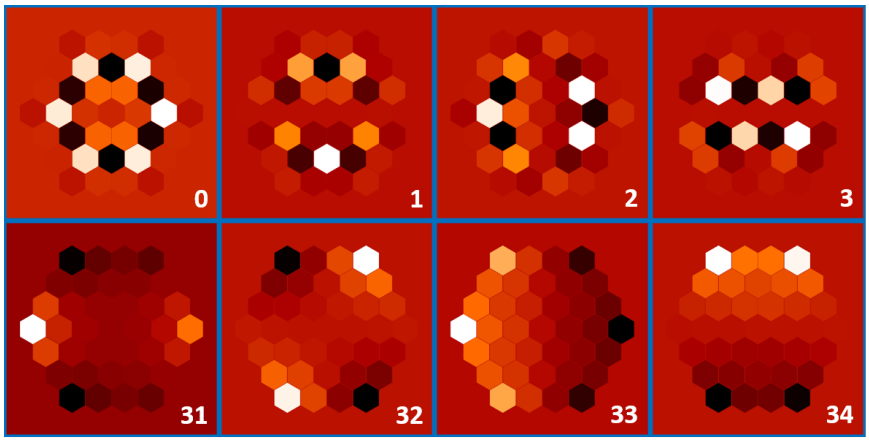

Figure 5. Some eigen modes in the piston case. Top: the four modes with the highest eigen values. We can notice that the segments the most concerned by these modes belong to the second ring, ie. are the least hidden by the coronagraph (apodizer and Lyot stop). Bottom: the four modes with the lowest eigen values. We can recognize discrete versions of low-order Zernike polynomials (astigmatisms, tip, and tilt).

As a comparison, similar results can be found in the studies of Stahl et al.,[21] later completed in Stahl et al.,[22] using end-to-end simulations.

2.3 Stability analysis

The objective of an error budget is to define constraints that enable to fulfill a certain performance. In our case, we want to set up constraints in terms of rms error on the segments to get a target contrast C. From Fig. 4 we can for instance derive from a target contrast the rms error for piston-like segments' phasing. However, we propose another approach, which takes into account the segment-dependant contribution to the contrast.

It is based on a projection of the phase on the eigen modes of the system. Indeed, by applying a Singular Value Decomposition (SVD) on the matrix M_l, we can obtain the eigen values $(\lambda_{p,l})_{p\in[1,n_{seg}]}$ and eigen modes $(U_{p,l})_{p\in[1,n_{seg}]}$ of the system. Fig. 5 illustrates a few modes issued from M_{piston}: the four modes with the highest eigen values (so impacting the contrast the most), and the four modes with the lowest eigen values (impacting the contrast the least). We can notice that the modes with the highest eigen values are made of aberrations located on the second ring of segments, ie. the least hidden by the optical components (apodizer and Lyot stop), while the modes with the lowest eigen values correspond to discretized global low order Zernike polynomials: the two astigmatisms (31 and 32) and the tip-tilt (33 and 34). It is known that in the design process, the apodizer has been optimized to be robust the tip-tilt misalignments, and this robustness is confirmed here. The 35-th mode, not represented in Fig. 5, has an almost null eigen value, and corresponds to a global piston of the primary mirror, which is known for not affecting the contrast.

The eigen modes form a basis of orthonormal vectors, so the final contrast due to a Zernike coefficients vector A is exactly the sum of the contrasts due to the projections of A on the different eigen modes:

$$C = \sum_{p=0}^{n_{seg}-1} C_p \tag{6}$$

Then, to get a contribution to contrast smaller than C_p on the p-th mode, the projection of the phase on this mode has to be smaller than

$$\sigma_p = \sqrt{\frac{C_p}{\lambda_{p,l}}}. \tag{7}$$

We call σ_p the contribution of the phase to the mode p.[10]

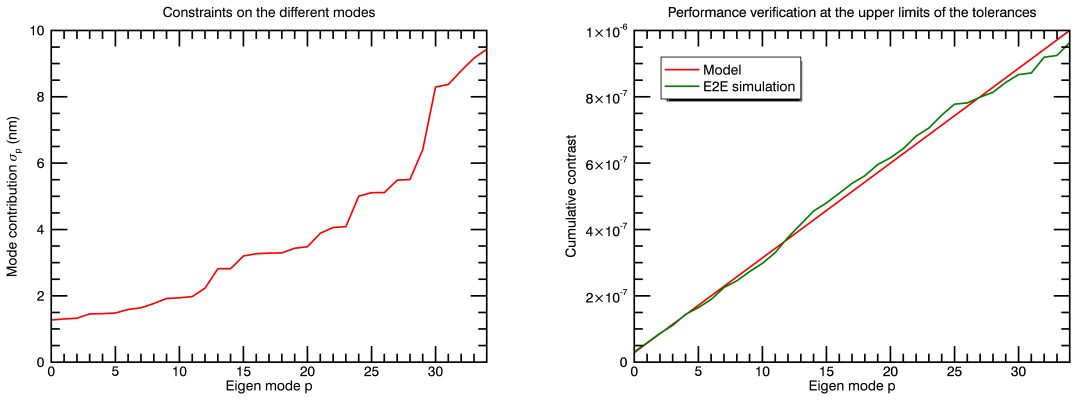

Figure 6. Left: Contributions $(\sigma_p)_{p\in[0,n_{seg}-1]}$ on the different piston modes to reach a final target contrast of 10^{-6}, in the case where only local pistons on segments deteriorate the contrast. Right: Cumulative contrasts on these piston modes at their upper constraints to reach a final target contrast of 10^{-6}. In these two plots, only 35 modes are indicated, since the mode with a very low eigen value corresponds to a global piston on the pupil and is chosen to not contribute to the final contrast.

For applications, we consider that all modes contribute equally to the contrast, ie. all the C_p are equal, and that $C = 10^{-6}$. From the previous equation, we then derive the results of Fig. 6: (a) indicates the mode contributions $(\sigma_p)_{p\in[0,n_{seg}-1]}$ that generate such contrasts and (b) shows the cumulative contrasts generated by these constraints: both plots issued from PASTIS and the end-to-end simulation are almost linear and the error on the final contrast is 3.75%. We can conclude that this method to compute the tolerances is relevant.

3. ZERNIKE POLYNOMIAL COMBINATION

The previous section introduced the PASTIS model for a simple application case: the aberrations are static and composed of the same Zernike polynomial on all segments. In this new section, we study the case where the segment-level aberrations are more complex, being composed of several Zernike polynomials. As an example, we will focus on classic phasing errors, ie. a combination of piston, tip, and tilt aberrations.

3.1 Theory

We use the expression of the phase of Eq. 1, without simplifying it to the case of one single Zernike polynomial. We obtain in the general case:

$$\widehat{\phi}(\mathbf{u}) = \sum_{l=1}^{n_{zer}} \sum_{k=1}^{n_{seg}} a_{k,l} \widehat{Z}_l e^{-i\mathbf{r_k}.\mathbf{u}} \tag{8}$$

Combining this equation and Eq 2 provides:

$$\begin{aligned} I(\mathbf{u}) &= [\sum_{l_1=1}^{n_{zer}} \sum_{k_1=1}^{n_{seg}} a_{k_1,l_1} \widehat{Z_{l_1}} e^{-i\mathbf{r_{k_1}}.\mathbf{u}}] \times [\sum_{l_2=1}^{n_{zer}} \sum_{k_2=1}^{n_{seg}} a_{k_2,l_2} \widehat{Z_{l_2}}^* e^{i\mathbf{r_{k_2}}.\mathbf{u}}] \\ &= \sum_{l_1=1}^{n_{zer}} \sum_{l_2=1}^{n_{zer}} \widehat{Z_{l_1}}.\widehat{Z_{l_2}}^* \sum_{k_1=1}^{n_{seg}} \sum_{k_2=1}^{n_{seg}} a_{k_1,l_1} a_{k_2,l_2} e^{i(\mathbf{r_{k_2}}-\mathbf{r_{k_1}}).\mathbf{u}} \end{aligned} \tag{9}$$

Since the intensity in the dark hole is real, $e^{i(\mathbf{r_{k_2}}-\mathbf{r_{k_1}}).\mathbf{u}} = \cos((\mathbf{r_{k_2}}-\mathbf{r_{k_1}}).\mathbf{u}) + i\sin((\mathbf{r_{k_2}}-\mathbf{r_{k_1}}).\mathbf{u})$, and the envelopes $\widehat{Z_{l_1}}.\widehat{Z_{l_2}}^*$ are either real or imaginary, this expression is in practice sums of interference fringes between all pairs of segments, modulated by low-frequency envelopes.

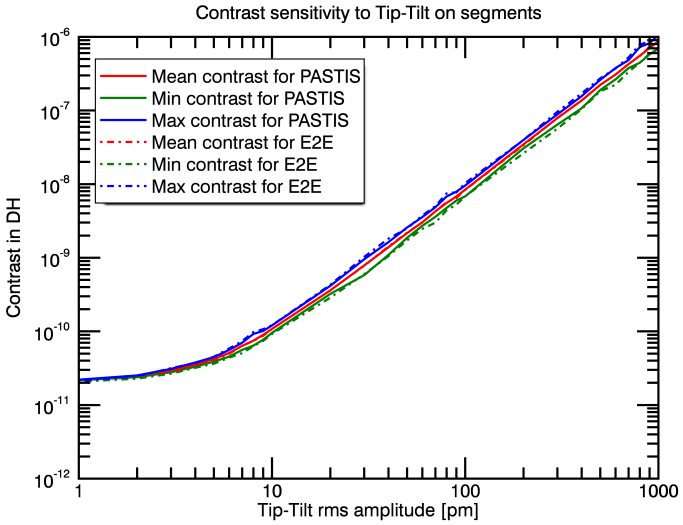

Figure 7. Contrast as a function of the rms piston-tip-tilt aberrations on the segments. It was computed through two methods: the end-to-end model (dashed lines) and PASTIS (continuous lines). For each rms value, 250 random phases are selected, so 250 contrasts computed, and the minimum, average, and maximum values are plotted.

By averaging this expression and taking the calibration coefficients $(c_{k,l})_{k\in[1,n_{seg}]}$ into account, we obtain:

$$C = C_0 + AMA^t \tag{10}$$

where:

$$\begin{aligned} A &= \begin{bmatrix} A_1 & \dots & A_{n_{Zer}} \end{bmatrix} \\ &= \begin{bmatrix} a_{1,1} & \dots & a_{n_{seg},1} & \dots & a_{1,n_{Zer}} & \dots & a_{n_{seg},n_{Zer}} \end{bmatrix} \\ M &= \begin{bmatrix} M_{1,1} & \dots & M_{1,n_{Zer}} \\ & \dots & \\ M_{n_{Zer},1} & \dots & M_{n_{Zer},n_{Zer}} \end{bmatrix} \end{aligned} \tag{11}$$

A is a concatenation of all the vectors A_l, while M is a block-diagonal matrix made of submatrices M_{l_1,l_2}, containing the coefficients:

$$\begin{aligned} M_{l_1,l_2}[k_1,k_2] &= m_{k_1,k_2,l_1,l_2} \\ &= c_{k_1,l_1} c_{k_2,l_2} \langle \widehat{Z_{l_1}} . \widehat{Z_{l_2}}^* e^{i(\mathbf{r_{k_2}} - \mathbf{r_{k_1}}).\mathbf{u}} \rangle_{DH} \end{aligned} \tag{12}$$

3.2 Application to the case of segment-level pistons, tips, and tilts

PASTIS in the case of Zernike polynomials' combination can be validated with a comparison with an end-to-end simulation. We use the same application case than described in section 2.2.1.

Fig. 7 provides a comparison between the results from PASTIS and from the end-to-end simulation, in the case of cophasing errors combining local piston, tip, and tilt errors on the segments. Like in Fig. 4, we plot here the minimum contrasts, the maximum contrasts, and the average contrasts computed from sets of 250 random phases, for sets from 1pm to 10nm rms. Once again, each contrast is computed with both techniques: PASTIS and the end-to-end simulation. As a conclusion, PASTIS still enables a huge gain of time for an error of around 9%.

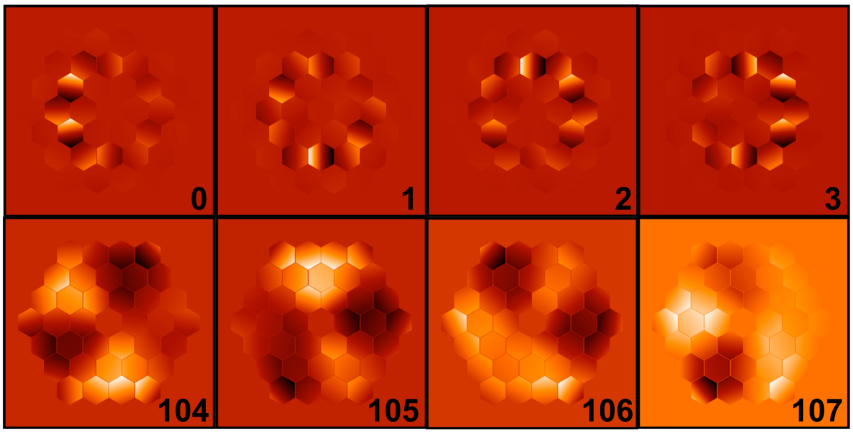

Figure 8. Some eigen modes in the piston-tip-tilt case. Top: the four modes with the highest eigen values. Tip and tilt errors appear to have a bigger impact on the contrast. Bottom: the four modes with the lowest eigen values, which correspond to low-order aberrations.

Once again, we can apply a Singular Value Decomposition on the matrix M enabling the computation of the contrast for piston, tip, and tilt aberrations. We can derive the 3×36 eigen modes of the chosen telescope. This information enables a better understanding of the phasing structures that deteriorate the contrast the most. It is then possible to optimize the backplane architecture or the sensitivity of specific edge sensors to avoid the dominant modes. For instance, Fig. 8 gives some of these eigen modes for the chosen telescope, the top ones corresponding to the ones with the highest eigen values, so impacting the contrast the most, and the bottom ones corresponding to the ones with the smallest eigen values, so impacting the contrast the least. We can deduce from this figure that the control of the tip-tilt on the second ring, mainly for one every two segments, is primordial. On the opposite, the last modes indicate that the coronagraph is highly resistant to global low-order aberrations. Such an information can be determinant when it comes to choose a coronagraph between several options providing otherwise similar performance.

Like in the one single Zernike polynomial case, it is also possible to quantify the relative importance of these eigen modes, or to obtain constraints to respect on each mode to achieve a target constraints. Fig. 9 provides for instance the constraints per mode to achieve a contrast of 10^{-6} in the dark hole. We can notice that the 40 first modes are quite equivalent in term of constraints (between 0.5nm and 1nm rms), while the modes higher than the 100^{th} one seem negligible when it comes to cophasing (constraints higher than 8nm rms).

4. DYNAMICAL CASE EXTENSION

In the previous sections, only static aberrations were considered. However, multiple dynamical factors generate vibrations or segments' motions: cryocoolers, motors, thermal drifts, or even resonance effects. Therefore, we do not consider a snapshot image or an image obtained with static aberrations only, but an image integrated over an exposure time T_{exp}, obtained from successive images taken at a frame rate $F = 400$ Hz.

In this situation, PASTIS shows its main advantage. Indeed, the end-to-end simulation would require $T_{exp} \times F$ iterations to provide the contrast of one single long exposure image, while PASTIS, as we will see in this section, remains one single operation.

We also study one specific application, where all segments vibrate at the same frequency $f = 87.3$Hz around the flat position but with different amplitudes and phase delays.

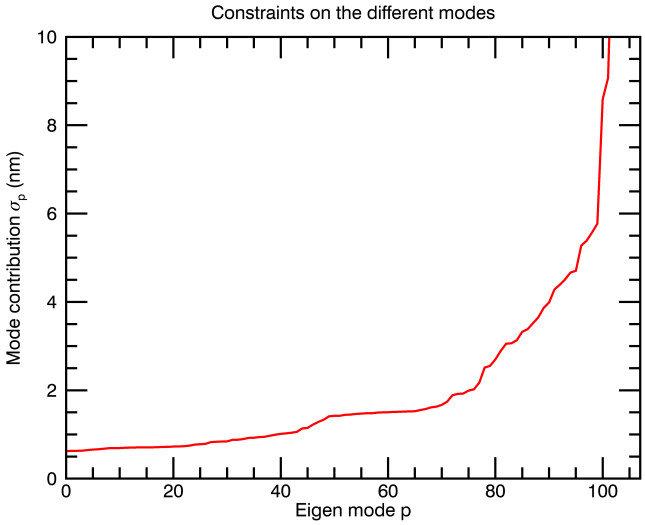

Figure 9. Contributions $(\sigma_p)_{p\in[0,n_{seg}-1]}$ on the different piston-tip-tilt modes to reach a final target contrast of 10^{-6}.

4.1 Theory for the generic case

In Eq. 5, we express the contrast as a function of the vector A_l, containing all the Zernike polynomial coefficients, and the matrix M_l which is a constant of the system. In the dynamical case, this equation becomes:

$$\begin{aligned} C(t) &= C_0 + A_l(t) M_l A_l(t)^t \\ &= C_0 + \sum_{k_1=1}^{n_{seg}} \sum_{k_2=1}^{n_{seg}} a_{k_1,l}(t) a_{k_2,l}(t) m_{k_1,k_2,l} \end{aligned} \tag{13}$$

where t is the time variable. After a long exposure time, the integrated image has a contrast C in the dark hole that corresponds to the average of the contrasts of all the intermediate images.

$$\begin{aligned} C &= \langle C(t) \rangle_{T_{exp}} \\ &= C_0 + \sum_{k_1=1}^{n_{seg}} \sum_{k_2=1}^{n_{seg}} \langle a_{k_1,l}(t) a_{k_2,l}(t) \rangle_{T_{exp}} m_{k_1,k_2,l} \end{aligned} \tag{14}$$

where T_{exp} is the exposure time.

4.2 Application to the case where all segments vibrate at the same frequency

4.2.1 Theory

In this case, all segments vibrate around the flat position:

$$\forall k \in [1, n_{seg}], a_{k,l}(t) = \tilde{a}_k cos(ft + \phi_k) \tag{15}$$

In the appendix A, it is demonstrated that:

$$\forall (k_1, k_2) \in [1, n_{seg}]^2, \langle a_{k_1,l}(t) a_{k_2,l}(t) \rangle_{T_{exp}} = \frac{cos(\phi_{k_1} - \phi_{k_2})}{2} \tilde{a}_{k_1} \tilde{a}_{k_2} \tag{16}$$

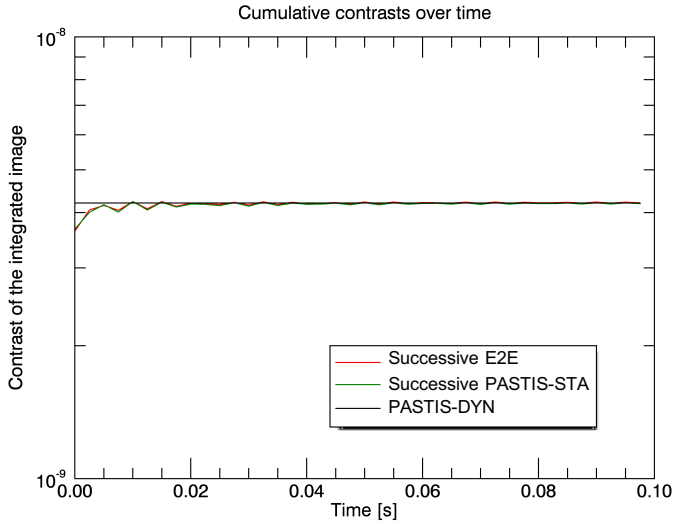

Figure 10. Example of temporal integration of the contrast, for piston-like vibrations. The segments vibrate at the frequency 87.3Hz and the amplitudes of the vibrations over all segments are 100pm. Furthermore: 1) to obtain the red curve, we compute the integrated PSF up to the time at the abscissa, then compute the contrast of this integrated PSF; this integrated contrast should converge towards the value computed in Eq. 17, 2) to obtain the green curve, we compute the contrast from the static PASTIS model at each time sample and average it up to the time at the abscissa, 3) the grey curve is constant and corresponds to the final contrast computed from Eq. 17.

Therefore, Eq. 14 becomes:

$$\begin{aligned} C &= C_0 + \sum_{k_1=1}^{n_{seg}} \sum_{k_2=1}^{n_{seg}} \tilde{a}_{k_1} \tilde{a}_{k_2} \frac{cos(\phi_{k_1} - \phi_{k_2})}{2} m_{k_1,k_2,l} \\ &= C_0 + \tilde{A} M' \tilde{A}^t \end{aligned} \tag{17}$$

where $\tilde{A}$ contains all the vibration amplitudes $\tilde{a_k}$ and $\forall (i,j) \in [1, n_{seg}]^2, M'[i,j] = \frac{cos(\phi_i - \phi_j)}{2} M_l[i,j]$.

4.2.2 Application

We apply now this result for piston-like vibrations of frequency $f = 87.3$Hz. The vibration amplitudes $\tilde{A}$ are random but with an rms value of 100pm, and the vibration delays (ϕ_k) are random between $-\pi$ and π. The exposure time is $T_{exp} = 0.1$s. Also, we sample the time and consider that 400 images are taken by seconds. Fig. 10 and table 1 present the results:

- the red curves: we consider the PSF integrated up to the time t of the abscissa, which mean the average PSF of all previous successive PSFs. The red curve corresponds to the contrast of this intermediate integrated PSF at the time t. This computation method is also called "Successive E2E" in the table.

- the green curves: at the time t, we compute the contrasts of all images taken before thanks to the static PASTIS model as presented in section 2. The green curve corresponds to the average of these contrasts at the time t. This computation method is also called "Successive PASTIS-STA" in the table.

- the grey curves are constant and correspond to the dynamic contrasts computed thanks to Eq. 17.

In the ideal case, ie. for a 0% error on the estimation of the contrast, the red and green curves should converge towards the grey curves. In practice, in our cases we have 0.03% error.

We know from section 2.2.2 that there is a 3% error between the contrasts computed from end-to-end simulation and from PASTIS-STA, but the end-to-end simulations take 10^7 times longer to compute. Therefore, until

PASTIS-DYN	Successive PASTIS-STA	Successive E2E	Error between PASTIS-DYN and successive E2E	Error between PASTIS-DYN and successive PASTIS-STA
4.21×10^{-9}	4.20×10^{-9}	4.21×10^{-9}	0.03%	0.36%

Table 1. Contrasts and errors of the example introduced in Fig. 10.

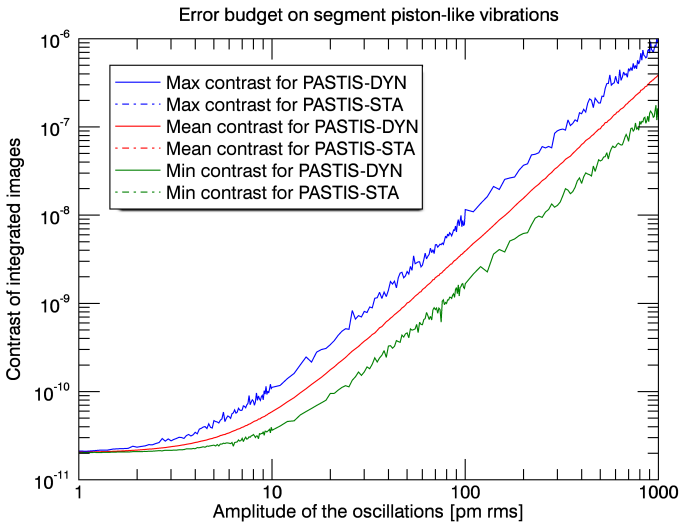

Figure 11. Contrast as a function of the rms piston-like vibrations on the segments. It was computed through two methods: the average of successive PASTIS-STA models (dashed lines) and the PASTIS-DYN model (continuous lines). For each rms value, 1000 random phases are selected.

the end of this section, we do not apply the end-to-end simulation anymore and compare PASTIS-DYN to the output of successive PASTIS-STA only, considering that successive PASTIS-STA provide outputs close enough to successive end-to-end simulations.

We now set $T_{exp} = 5$s. We consider random $\tilde{A}$, with rms values between 1 pm and 1 nm. For each rms value, we randomly pick 1000 different amplitudes $\tilde{A}$ and 1000 different phase delays' sets (ϕ_k). To each of these configurations of segments' vibrations, we apply 1) successive PASTIS-STA over the 5 seconds of T_{exp} and 2) PASTIS-DYN. For each rms value of $\tilde{A}$, we select the lowest contrasts computed with both methods, the mean contrasts, and the highest contrasts. Fig. 11 provides the results of this test: the outputs from PASTIS-DYN cannot be identified from the ones from the successive PASTIS-STA. To quantify the error of PASTIS-DYN compared to the output of successive PASTIS-STA, there is a 1.80×10^{-5}% rms error between the two mean curves, and for 1000 random sets of vibrations, the error between the outputs from PASTIS-DYN and successive PASTIS-STA is 8.30×10^{-5}% rms.

5. CONCLUSIONS

In this proceeding, we have introduced an analytical model called PASTIS. It was demonstrated in Leboulleux et al. (2017)[9] and Leboulleux et al. (2018)[10] in the case of one single static Zernike polynomial, summarized in section 2. This proceeding mainly extends the use of PASTIS to more complex situations: the segment-level aberrations are static combinations of several Zernike polynomials and dynamical effects such as vibrations also affect the system.

In the first of these two cases, we obtained a very good correlation between the results from the end-to-end simulation and PASTIS, with an rms error of around 9%. We could also identify the eigen modes of the phasing aberrations made of local piston, tip, and tilt and in particular the eigen modes that impact the contrast the

most. We could also quantify the relative impacts of these modes and provide absolute constraints to respect in order to maintain a target contrast.

As a second application case, we focused on segments' instabilities, in particular vibrations. When the temporal dimension is considered, PASTIS is particularly interesting, since it is extremely faster to compute than an end-to-end simulation. We noticed that this gain of computation time can be even more improved by reducing the successive contrast computations in one single operation, even after a long exposure time. We obtained very low errors in the contrasts when comparing the output of this one single operation (PASTIS-DYN), the average of the successive contrasts over time computed with PASTIS as presented in section 2 (PASTIS-STA), and the contrast of image obtained from successive end-to-end simulations and integrated over the exposure time (E2E).

In all theses cases, PASTIS provides not only a significant gain of time with a low error, but also a better comprehension of the system and its robustness. Knowing the eigen modes of the segmented primary mirror and their relative sensitivities to contrast enables to optimize the system, for instance the choice of edge sensors for segment's positioning or the architecture of the backplane structure.

Other parameters can also be optimized, such as the number of segments, their sizes and shapes, and the coronagraph itself, the objective being to get an optimal system that combines an absolute performance enabling exo-Earth imaging and a robustness to static and dynamic perturbations. PASTIS will enable a fast testing of these parameters in the path to make the next generation of space telescopes both performant and robust.

To diversify its applications and the used configurations, PASTIS is also currently being applied to the JWST for stability studies[23] and should be tested in laboratory on the High-contrast imager for Complex Aperture Telescopes (HiCAT) testbed at the Space Telescope Science Institute (STScI).[24]

ACKNOWLEDGMENTS

This work is supported in part by the National Aeronautics and Space Administration under Grants NNX12AG05G and NNX14AD33G issued through the Astrophysics Research and Analysis (APRA) program (PI: R. Soummer) and by Jet Propulsion Laboratory subcontract No.1539872 (Segmented-Aperture Coronagraph Design and Analysis; PI: R. Soummer).
It is also partly funded by the French Aerospace Lab (ONERA) in the frame of the VASCO Research Project and by the Laboratoire d'Astrophysique de Marseille (LAM).

APPENDIX A.

We demonstrate here that $\forall (k_1, k_2) \in [1, n_{seg}]^2, \langle a_{k_1,l}(t) a_{k_2,l}(t) \rangle_{T_{exp}} = \frac{\tilde{a}_{k_1} \tilde{a}_{k_2}}{2} \cos(\phi_{k_1} - \phi_{k_2})$ for $T_{exp} >> 1/f$.

$$\begin{aligned}
\langle a_{k_1,l}(t) a_{k_2,l}(t) \rangle_{T_{exp}} &= \frac{1}{T_{exp}} \int_0^{T_{exp}} \tilde{a}_{k_1} \tilde{a}_{k_2} \cos(f_{k_1} t + \phi_{k_1}) \cos(f_{k_2} t + \phi_{k_2}) \, \mathrm{d}t \\
&= \frac{1}{T_{exp}} \int_0^{T_{exp}} \tilde{a}_{k_1} \tilde{a}_{k_2} \frac{1}{2} (\cos(\phi_{k_1} - \phi_{k_2}) + \cos(2ft + \phi_{k_2} + \phi_{k_1})) \, \mathrm{d}t \\
&= \frac{\tilde{a}_{k_1} \tilde{a}_{k_2}}{2T_{exp}} \left(\int_0^{T_{exp}} \cos(\phi_{k_1} - \phi_{k_2}) \mathrm{d}t + \int_0^{T_{exp}} \cos(2ft + \phi_{k_2} + \phi_{k_1})) \, \mathrm{d}t \right. \\
&= \frac{\tilde{a}_{k_1} \tilde{a}_{k_2}}{2T_{exp}} (T_{exp} \cos(\phi_{k_1} - \phi_{k_2}) + 0)
\end{aligned} \tag{18}$$

since $T_{exp} >> 1/f$. We obtain:

$$\langle a_{k_1,l}(t) a_{k_2,l}(t) \rangle_{T_{exp}} = \frac{\tilde{a}_{k_1} \tilde{a}_{k_2}}{2} \cos(\phi_{k_1} - \phi_{k_2}) \tag{19}$$

REFERENCES

[1] Carlotti, A., Vanderbei, R., and Kasdin, N. J., "Optimal pupil apodizations for arbitrary apertures," *ArXiv e-prints* (Aug. 2011).

[2] N'Diaye, M., Pueyo, L., and Soummer, R., "Apodized Pupil Lyot Coronagraphs for Arbitrary Apertures. IV. Reduced Inner Working Angle and Increased Robustness to Low-order Aberrations," *Astrophysical Journal* **799**, 225 (Feb. 2015).

[3] Zimmerman, N. T., N'Diaye, M., St. Laurent, K. E., Soummer, R., Pueyo, L., Stark, C. C., Sivaramakrishnan, A., Perrin, M., Vanderbei, R. J., Kasdin, N. J., Shaklan, S., and Carlotti, A., "Lyot coronagraph design study for large, segmented space telescope apertures," in [*Space Telescopes and Instrumentation 2016: Optical, Infrared, and Millimeter Wave*], *Proc. SPIE* **9904**, 99041Y (July 2016).

[4] Guyon, O., Hinz, P. M., Cady, E., Belikov, R., and Martinache, F., "High Performance Lyot and PIAA Coronagraphy for Arbitrarily Shaped Telescope Apertures," *Astrophysical Journal* **780**, 171 (Jan. 2014).

[5] Pueyo, L. and Norman, C., "High-contrast Imaging with an Arbitrary Aperture: Active Compensation of Aperture Discontinuities," *Astrophysical Journal* **769**, 102 (June 2013).

[6] Mazoyer, J., Pueyo, L., N'Diaye, M., Fogarty, K., Leboulleux, L., Egron, S., and Norman, C., "Capabilities of ACAD-OSM, an active method for the correction of aperture discontinuities," *ArXiv e-prints* (Oct. 2017).

[7] Stahl, H. P., Postman, M., and Smith, W. S., "Engineering specifications for large aperture UVO space telescopes derived from science requirements," in [*UV/Optical/IR Space Telescopes and Instruments: Innovative Technologies and Concepts VI*], *Proc. SPIE* **8860**, 886006 (Sept. 2013).

[8] Stahl, M. T., Shaklan, S. B., and Stahl, H. P., "Preliminary analysis of effect of random segment errors on coronagraph performance," in [*Techniques and Instrumentation for Detection of Exoplanets VII*], *Proc. SPIE* **9605**, 96050P (Sept. 2015).

[9] Leboulleux, L., Sauvage, J.-F., Pueyo, L., Fusco, T., Soummer, R. N'Diaye, M., and St. Laurent, K., "Sensitivity analysis for high-contrast missions with segmented telescopes," in [*Techniques and Instrumentation for Detection of Exoplanets VIII*], *Proc. SPIE* **10400** (2017).

[10] Leboulleux, L., Sauvage, J. F., Pueyo, L., Fusco, T., Mazoyer, J., Soummer, R., Sivaramakrishnan, A., N'Diaye, M., and Fauvarque, O., "Pair-based Analytical model for Segmented Telescopes Imaging from Space (PASTIS) for sensitivity analysis," *Journal of Astronomical Telescopes, Instruments, and Systems (submitted)* (2018).

[11] Greenhouse, M. A., "The JWST science instrument payload: mission context and status," in [*Space Telescopes and Instrumentation 2016: Optical, Infrared, and Millimeter Wave*], *Proc. SPIE* **9904**, 990406 (July 2016).

[12] Clampin, M., "Status of the James Webb Space Telescope (JWST)," in [*Space Telescopes and Instrumentation 2008: Optical, Infrared, and Millimeter*], *Proc. SPIE* **7010**, 70100L (July 2008).

[13] Dalcanton, J., Seager, S., Aigrain, S., Battel, S., Brandt, N., Conroy, C., Feinberg, L., Gezari, S., Guyon, O., Harris, W., Hirata, C., Mather, J., Postman, M., Redding, D., Schiminovich, D., Stahl, H. P., and Tumlinson, J., "From Cosmic Birth to Living Earths: The Future of UVOIR Space Astronomy," *ArXiv e-prints* (July 2015).

[14] Pueyo, L., Zimmerman, N., Bolcar, M., Groff, T., Stark, C., Ruane, G., Jewell, J., Soummer, R., St. Laurent, K., Wang, J., Redding, D., Mazoyer, J., Fogarty, K., Juanola-Parramon, R., Domagal-Goldman, S., Roberge, A., Guyon, O., and Mandell, A., "The LUVOIR architecture "A" coronagraph instrument," in [*Society of Photo-Optical Instrumentation Engineers (SPIE) Conference Series*], *Society of Photo-Optical Instrumentation Engineers (SPIE) Conference Series* **10398**, 103980F (Sept. 2017).

[15] Mennesson, B., Gaudi, S., Seager, S., Cahoy, K., Domagal-Goldman, S., Feinberg, L., Guyon, O., Kasdin, J., Marois, C., Mawet, D., Tamura, M., Mouillet, D., Prusti, T., Quirrenbach, A., Robinson, T., Rogers, L., Scowen, P., Somerville, R., Stapelfeldt, K., Stern, D., Still, M., Turnbull, M., Booth, J., Kiessling, A., Kuan, G., and Warfield, K., "The Habitable Exoplanet (HabEx) Imaging Mission: preliminary science drivers and technical requirements," in [*Space Telescopes and Instrumentation 2016: Optical, Infrared, and Millimeter Wave*], *Proc. SPIE* **9904**, 99040L (July 2016).

[16] Macintosh, B., Troy, M., Doyon, R., Graham, J., Baker, K., Bauman, B., Marois, C., Palmer, D., Phillion, D., Poyneer, L., Crossfield, I., Dumont, P., Levine, B. M., Shao, M., Serabyn, G., Shelton, C., Vasisht, G., Wallace, J. K., Lavigne, J.-F., Valee, P., Rowlands, N., Tam, K., and Hackett, D., "Extreme adaptive optics for the Thirty Meter Telescope," in [*Society of Photo-Optical Instrumentation Engineers (SPIE) Conference Series*], *Proc. SPIE* **6272**, 62720N (June 2006).

[17] Kasper, M. E., Beuzit, J.-L., Verinaud, C., Yaitskova, N., Baudoz, P., Boccaletti, A., Gratton, R. G., Hubin, N., Kerber, F., Roelfsema, R., Schmid, H. M., Thatte, N. A., Dohlen, K., Feldt, M., Venema, L., and Wolf, S., "EPICS: the exoplanet imager for the E-ELT," in [*Adaptive Optics Systems*], *Proc. SPIE* **7015**, 70151S (July 2008).

[18] Davies, R., Ageorges, N., Barl, L., Bedin, L. R., Bender, R., Bernardi, P., Chapron, F., Clenet, Y., Deep, A., Deul, E., Drost, M., Eisenhauer, F., Falomo, R., Fiorentino, G., Förster Schreiber, N. M., Gendron, E., Genzel, R., Gratadour, D., Greggio, L., Grupp, F., Held, E., Herbst, T., Hess, H.-J., Hubert, Z., Jahnke, K., Kuijken, K., Lutz, D., Magrin, D., Muschielok, B., Navarro, R., Noyola, E., Paumard, T., Piotto, G., Ragazzoni, R., Renzini, A., Rousset, G., Rix, H.-W., Saglia, R., Tacconi, L., Thiel, M., Tolstoy, E., Trippe, S., Tromp, N., Valentijn, E. A., Verdoes Kleijn, G., and Wegner, M., "MICADO: the E-ELT adaptive optics imaging camera," in [*Ground-based and Airborne Instrumentation for Astronomy III*], *Proc. SPIE* **7735**, 77352A (July 2010).

[19] Quanz, S. P., Crossfield, I., Meyer, M. R., Schmalzl, E., and Held, J., "Direct detection of exoplanets in the 3-10 μm range with E-ELT/METIS," *International Journal of Astrobiology* **14**, 279–289 (Apr. 2015).

[20] Janin-Potiron, P., Martinez, P., and Carbillet, M., "Analytical decomposition of Zernike and hexagonal modes over an hexagonal segmented optical aperture," *Applied Optics (submitted)* (2018).

[21] Stahl, H. P., "Advanced Mirror Technology Development (AMTD) project: overview and year four accomplishments," in [*Advances in Optical and Mechanical Technologies for Telescopes and Instrumentation II*], *Proc. SPIE* **9912**, 99120S (July 2016).

[22] Stahl, M. T., Stahl, H. P., and Shaklan, S. B., "Contrast Leakage as a function of telescope motion," *Mirror Technology Days* (2016).

[23] Perrin, M., "Updated optical modeling of JWST coronagraph performance, contrast, and stability," in [*Space Telescopes and Instrumentation 2018: Optical, Infrared, and Millimeter Wave*], *SPIE paper 10698-8 in these proceedings* (2018).

[24] Soummer, R., "High-contrast imager for complex aperture telescopes (HiCAT): 5. rst results with segmented-aperture coronagraph and wavefront control," in [*Space Telescopes and Instrumentation 2018: Optical, Infrared, and Millimeter Wave*], *SPIE paper 10698-59 in these proceedings* (2018).

C

Development of the computation of the average of the product of the cosine functions at same frequency

We demonstrate here that $\forall (k_1, k_2) \in [1, n_{seg}]^2, \langle a_{k_1,l}(t) a_{k_2,l}(t) \rangle_{T_{exp}} = \frac{\tilde{a}_{k_1} \tilde{a}_{k_2}}{2} \cos(\phi_{k_1} - \phi_{k_2})$ for $T_{exp} >> 1/f$.

$$
\begin{aligned}
\langle a_{k_1,l}(t) a_{k_2,l}(t) \rangle_{T_{exp}} &= \frac{1}{T_{exp}} \int_0^{T_{exp}} \tilde{a}_{k_1} \tilde{a}_{k_2} \cos(f_{k_1} t + \phi_{k_1}) \cos(f_{k_2} t + \phi_{k_2}) \, \mathrm{d}t \\
&= \frac{1}{T_{exp}} \int_0^{T_{exp}} \tilde{a}_{k_1} \tilde{a}_{k_2} \frac{1}{2} (\cos(\phi_{k_1} - \phi_{k_2}) + \cos(2ft + \phi_{k_2} + \phi_{k_1})) \, \mathrm{d}t \\
&= \frac{\tilde{a}_{k_1} \tilde{a}_{k_2}}{2T_{exp}} \left(\int_0^{T_{exp}} \cos(\phi_{k_1} - \phi_{k_2}) \mathrm{d}t + \int_0^{T_{exp}} \cos(2ft + \phi_{k_2} + \phi_{k_1})) \, \mathrm{d}t \right. \\
&= \frac{\tilde{a}_{k_1} \tilde{a}_{k_2}}{2T_{exp}} (T_{exp} \cos(\phi_{k_1} - \phi_{k_2}) + 0)
\end{aligned}
\tag{C.1}
$$

since $T_{exp} >> 1/f$. We obtain:

$$
\langle a_{k_1,l}(t) a_{k_2,l}(t) \rangle_{T_{exp}} = \frac{\tilde{a}_{k_1} \tilde{a}_{k_2}}{2} \cos(\phi_{k_1} - \phi_{k_2}) \tag{C.2}
$$

D

High-contrast imaging testbeds over the world

The last decade saw the emergence of multiple optical testbeds over the world, dedicated to validation of specific coronagraphs, wavefront sensors, and wavefront control techniques for future instruments or telescopes. Some of these testbeds even take into account the difficulties brought by the primary mirror segmentation.

All testbeds have different purposes, working at different wavelengths for different pupils, telescopes, or missions. They can provide spectroscopy, NRM, coronagraphy, different DMs, different wavefront sensors... All these differences make each of them unique. A good description and comparison of the different high-contrast imaging testbeds can be very useful to learn about their differences, for instance in case a specific algorithm or technique has to be tested. It is important here to emphasize the work of Nemanja Jovanovic and other researchers from the Leiden workshop on high-contrast imaging, who provided a very useful comparison table between many different testbeds [Jovanovic et al. (2018)].

Iva Laginja, Keira Brooks, Rebecca Jensen-Clem, and I have been working on a platform on the different high-contrast imaging testbeds over the world. The website is now published and can be found on https://sites.google.com/view/highcontrastlabs/home. It was created to get an overview on what is happening on the different testbeds, and to facilitate communication and information sharing.

As a non-exhaustive list, the website can be used to:

- share/find through a github link codes and softwares for a specific task, such as the DM calibration, the communication with the camera, a specific wavefront sensing algorithm, etc,

- have an easy comparison of the different testbeds, in order to find out which one would be the most adapted to test a specific wavefront sensing/control/coronagraph only tested

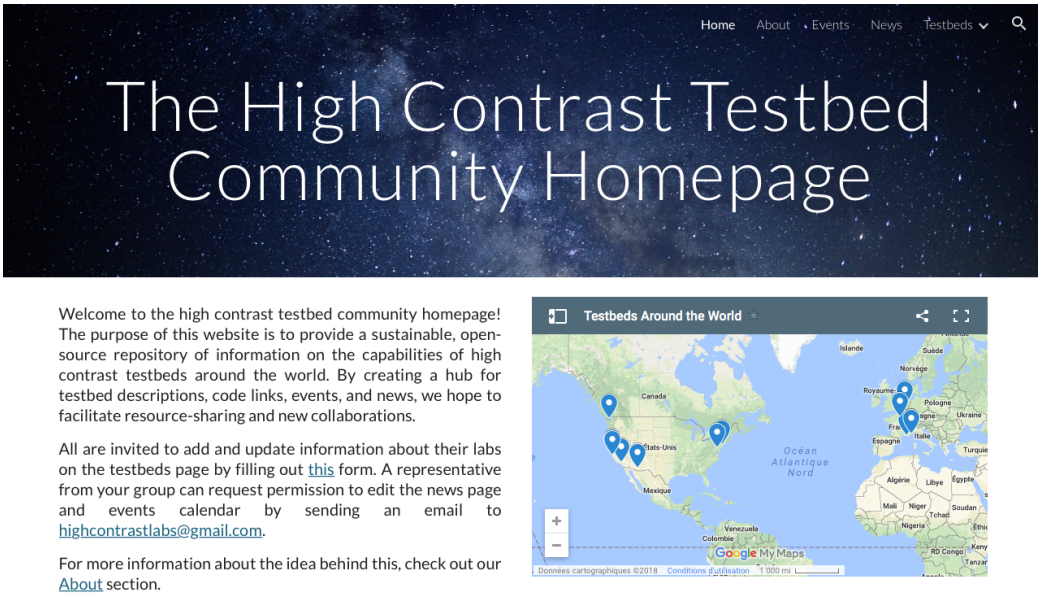

Figure D.0.1: Homepage of the high-contrast community website.

in simulation so far,

- contact a person of a specific lab to discuss about a potential position, giving a seminar, etc,

- find out which events concerning high-contrast imaging facilities are being organized.

To answer to these problematics, different pages have been created: Home, About, Events, News, and Testbeds. The Home section is shown in Fig. D.0.1 and welcomes and guides the visitor. The About section informs about why the website was created and how it can evolve. The Events section provides a calendar of the events organized on high-contrast imaging. This page will eventually be automatized. In the News section, we want a feed of articles about what is happening on the different testbeds to appear. This section is not fully optimized and automatized yet. Finally, the Testbeds pages correspond to descriptions of the different testbeds. For now 11 testbeds (HCIL from Princeton University, HCST from Caltech, HiCAT and JOST from STScI, HOT from ESO, MITHIC from LAM, New earth Lab from the National research Council of Canada, SCExAO from the Subaru telescope, SPEED from the Laboratoire Lagrange, THD2 from the Observatoire de Paris, and VODCA from Liège University) appear on the website, and the user can easily add another testbed by filling a form.

The four of us are quite new at this kind of projects, so there is a lot to improve, in addition to all the tasks that still need to be done. We created a google account and an email address (highcontrastlabs@gmail.com) to manage the platform and communicate with the users and so far it is going quite well. We had for now very good feedbacks from the community and are curious to see how this platform will evolve.

E

Leboulleux et al. 2016, proceeding for the SPIE conference

High-contrast imager for Complex Aperture Telescopes (HiCAT). 4. Status and wavefront control development

Lucie Leboulleux[abc], Mamadou N'Diaye[a], A J Eldorado Riggs[d], Sylvain Egron[abc], Johan Mazoyer[a], Laurent Pueyo[a], Elodie Choquet[ef], Marshall D. Perrin[a], Jeremy Kasdin[d], Jean-François Sauvage[bc], Thierry Fusco[bc], and Rémi Soummer[a]

[a] Space Telescope Science Institute, 3700 San Martin Drive, Baltimore, MD 21218, USA
[b] Aix Marseille Université, CNRS, LAM (Laboratoire d'Astrophysique de Marseille) UMR 7326, 13388, Marseille, France
[c] Office National d'Etudes et de Recherches Aérospatiales, 29 Avenue de la Division Leclerc, 92320 Châtillon, France
[d] Princeton University, Department of Mechanical and Aerospace Engineering, Engineering Quadrangle, Princeton, NJ 08544, USA
[e] Jet Propulsion Laboratory, California Institute of Technology, 4800 Oak Grove Drive, MS 169-506, Pasadena, CA 91109, USA
[f] Hubble Fellow

ABSTRACT

Segmented telescopes are a possible approach to enable large-aperture space telescopes for the direct imaging and spectroscopy of habitable worlds. However, the increased complexity of their aperture geometry, due to their central obstruction, support structures and segment gaps, makes high-contrast imaging very challenging.
The High-contrast imager for Complex Aperture Telescopes (HiCAT) was designed to study and develop solutions for such telescope pupils using wavefront control and starlight suppression. The testbed design has the flexibility to enable studies with increasing complexity for telescope aperture geometries starting with off-axis telescopes, then on-axis telescopes with central obstruction and support structures (e.g. the Wide Field Infrared Survey Telescope [WFIRST]), up to on-axis segmented telescopes e.g. including various concepts for a Large UV, Optical, IR telescope (LUVOIR), such as the High Definition Space Telescope (HDST). We completed optical alignment in the summer of 2014 and a first deformable mirror was successfully integrated in the testbed, with a total wavefront error of 13nm RMS over a 18mm diameter circular pupil in open loop. HiCAT will also be provided with a segmented mirror conjugated with a shaped pupil representing the HDST configuration, to directly study wavefront control in the presence of segment gaps, central obstruction and spider.
We recently applied a focal plane wavefront control method combined with a classical Lyot coronagraph on HiCAT, and we found limitations on contrast performance due to vibration effect. In this communication, we analyze this instability and study its impact on the performance of wavefront control algorithms. We present our Speckle Nulling code to control and correct for wavefront errors both in simulation mode and on testbed mode. This routine is first tested in simulation mode without instability to validate our code. We then add simulated vibrations to study the degradation of contrast performance in the presence of these effects.

Keywords: exoplanets, high-contrast imaging, wavefront sensing, wavefront control, Speckle Nulling, vibration analysis

1. INTRODUCTION

The next generation of space telescopes for direct imaging and spectroscopy of exoplanets includes telescopes with a monolithic mirror, such as the Wide Field Infrared Survey Telescope (WFIRST),[1] and Large Ultra-Violet

Further author information, send correspondence to Lucie Leboulleux: E-mail: leboulleux@stsci.edu, Telephone: 1 410 338 2881

Optical Infrared (LUVOIR) telescopes with segmented primary mirror, like ATLAST[2,3] or HDST.[4] Because of the complexity of their pupils, high-contrast imaging becomes more challenging, including starlight suppression with coronagraphy and wavefront sensing and wavefront control for contrast stability in the presence of vibrations.

The High-contrast imager for Complex Aperture Telescopes (HiCAT) testbed has been developed to enable studies on starlight suppression, wavefront sensing (WFS), and wavefront control (WFC) for such unfriendly pupils. New coronagraph designs for any kind of aperture that are based on the Apodized Pupil Lyot Coronagraph (APLC)[5,6] are currently developed on simulation and will then be implemented on the testbed. Furthermore, new high-contrast methods will be implemented and tested, such as pupil remapping techniques (e.g. Active Control of Aperture Discontinuities [ACAD][7–9]) that use two deformable mirrors (DMs) to convert complex pupils into friendly apertures for coronagraphy.

In previous papers, we presented the overall goals and design of HiCAT[10,11] and described its assembly and integration including the installation and first tests with single Boston Micromachines deformable mirror (DM).[12]

In this communication, we report on progress and challenges since then. In particular we describe the detection and analysis of instability that prevents us from implementing high-contrast imaging codes on HiCAT. From these studies, we derive a new DM mount design and the implementation of a Speckle Nulling code in simulation, without and with instability.

In Section 2, we present the main features of our testbed and our first wavefront control tests. We show that the preliminary results did not reach the desired contrast levels because of the instability issues that were detected during our experiments. In Section 3, we analyze the point spread function (PSF) motion that was observed on the testbed and we derive conclusions on the instability issues. Finally, in Section 4, we present the results of our simulations on wavefront control using a single DM and a classical Lyot coronagraph, including instability effects.

2. HICAT TESTBED IMPLEMENTATION AND STATUS

2.1 Optical and opto-mechanical designs

The detailed optical design of the testbed was presented in N'Diaye et al.[10] and it will at the end simulate a complex aperture telescope on which the starlight will be suppressed thanks to an APLC and wavefront control, using two DMs. The design goal was to minimize amplitude-induced errors due to Talbot effects. In addition, the access to several pupil and focal planes enables the correction of phase errors induced by aperture diffraction. As shown in Fig. 1, the HiCAT testbed is provided with a starlight suppression system, based on the APLC architecture. This includes a reflective apodizer,[13] a reflective Focal Plane Mask (FPM), which currently has a 334 micrometer size hole at its center, and a Lyot Stop. Both the Lyot Stop and the FPM are motorized and can be controlled from a computer. The final design of the apodizer is still under development as part of our ongoing coronagraph optimization studies,[6] so it is currently replaced with a high quality flat mirror and the full starlight suppression system is currently equivalent to a Lyot coronagraph.
Two DMs (Boston kilo-DM) enable wavefront sensing and control studies on HiCAT. The first one has been set up in a pupil plane in 2014-2015 and allows first studies to be driven.[12] The second one, out of pupil plane, is not installed yet and is currently replaced by a high quality flat mirror.
Furthermore, since HiCAT should be able to simulate a telescope with a complex geometry pupil, it can be featured with a pupil mask similar to the WFIRST pupil, including the spider and the central obstruction. It will also be provided with a segmented mirror (SM), conjugated with the previous complex pupil to simulate an ATLAST/HDST-like primary mirror. This mirror is an Iris-AO SM with 36 segments.
At the very end of the testbed, a beam splitter sends the beam to two cameras, CamF and CamP, respectively installed at a focal plane and at a pupil plane.

The testbed is fully aligned with an excellent wavefront quality of 13nm RMS over a 18mm diameter circular pupil[11] and now includes all the convergent and flat mirrors, the beam launcher, the pupil mask, the first DM (DM1) which is set in a pupil plane, the FPM, the Lyot Stop, and the two cameras. To reduce the stray light, it also has an enclosure, several black screens and laser beam dumps.

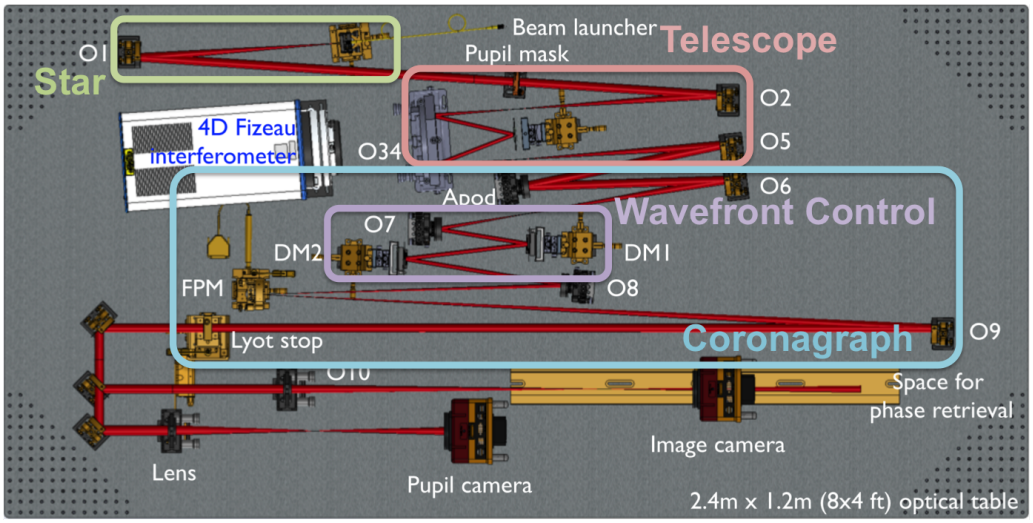

Figure 1. HiCAT testbed design done with the software Solidworks, the beam is exported from Zemax. The telescope is simulated by a pupil mask, the segmented mirror and off-axis parabolas. The segmented mirror is conjugated with the pupil mask to form a segmented pupil with central obstruction and spider struts. The off-axis parabolas set the telescope aperture. The wavefront control is done with two deformable mirrors. The coronagraph is composed of an apodizer, a focal plane mask and a Lyot stop.

It will also have to be upgraded with the WFIRST-like pupil mask, the SM conjugated with the previous complex pupil to simulate a ATLAST/HDST-like primary mirror, the apodizer that is currently being designed and a second Boston kilo-DM, out of pupil plane.

2.2 Wavefront sensing and wavefront control implementation

In 2015, a first Speckle Nulling code was implemented on the HiCAT testbed, using DM1. It enabled the suppression of a speckle in our final image. For more details about this first implementation, please see N'Diaye et al. 2015.[12]
After this first step, we tested a Focal Plane Wavefront Control (FPWC) code[14] but we did not manage to produce a dark hole with the expected contrast because of some Point Spread Function (PSF) drifts between the different exposures.

3. INSTABILITY ANALYSIS

In this section, we present our instability analysis and introduce a new DM mount design, that should be an important improvement compared to the current one.

3.1 PSF motion analysis

The idea here is to characterize the motion effect on recorded videos and, depending on the kind of motion or shape changing we observe, to find both the source of the vibration and its support on the testbed. For example, the motor driver could be the origin of the vibration, but it does not have an real direct influence on the beam, unless an optical component is loose. In the following sections, we present our main tests and the derived conclusions.

The criteria to characterize the motion are:
- the amplitude of the motion around an average position as a function of the time
- the direction of the motion (the motion could follow only the Y-axis, for example)
- the spectrum of the motion.

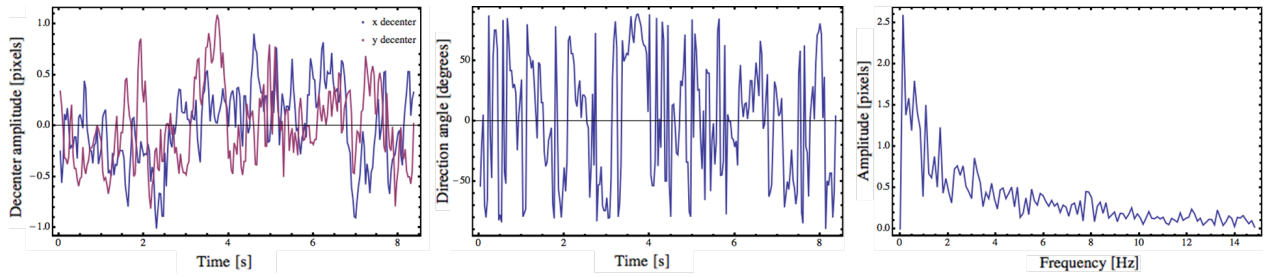

Figure 2. Analysis of the PSF motion when HiCAT is at rest (all the hardware is on, the enclosure is closed and the camera is at the end of the testbed). Left: distance in pixels of the PSF from the mean position as a function of time. Center: direction of the motion on the detector as a function of time. No privileged direction appears here. Right: Spectrum of the motion. The motion is obviously a low frequency movement, there is no high frequency peak.

Our tests were done using a Thorlabs CMOS camera, that can take monochrome videos at a frame rate from 25 fps to 250 fps with a 1280 x 1024 pixel detector, where each pixel is a 5.20 μm square. In addition, the small size of the camera (48.6 mm $\times$ 44 mm $\times$ 25.7 mm) facilitates access to the different planes of study.

3.1.1 HiCAT at rest

As a reference comparison for the following tests, if HiCAT is at rest, so in normal running conditions (hardwares are on and the enclosure is closed), we obtain the results shown in Fig. 2. No main direction of motion could be obtained from the video analysis and only frequencies below 2 Hz seem to appear. Indeed, above 2 Hz, we cannot see any specific peak in the spectrum.

Furthermore, we realigned all the frames from a video, where the coronagraph is set, and we noticed after realignment that the PSF was not moving anymore, except that the shape of the core of the coronagraphic PSF was modified with time. This observation made us conclude that there is at least one optical component moving before the FPM.

3.1.2 Which optical components are most unstable?

To find out which optical component could be responsible for the beam direction to change in the testbed, two sets of tests were done.

First, we set the camera at the end of the testbed, at the focal plane and gently tap every optical component that appears on Fig. 1 except for DM1. The idea here is to check if tapping has an influence on the PSF motion. The three main results from these first tests are given in Fig. 3 and tapping every other optical component has no effect on the PSF instability. For these three optics, so DM2, the apodizer and the Iris AO (actually flat mirrors), we do observe an important change of the amplitude and spectrum of the PSF motion.

As a second set of test, we put successively the camera at each of the five focal planes of the testbed and compare the amplitude of the PSF motion normalized by the value of the focal length until this focal plane, which is equivalent of getting a value of the amplitude of the motion angle of the beam instead of the metric amplitude of the PSF. In theses conditions, the amplitude values can be compared even if the camera is set at different focal planes.
Without a surprise, the further the camera is from the entrance of the testbed, the worse the amplitude is. We mainly observe the most significant difference between the two focal planes situated right before and right after the two DMs and the mirror O8: the average motion values are multiplied by 3.20 between these two successive focal planes. These three optical components, DM1 and DM2 and O8, then become principal suspects.

As a final test, since our two previous tests were never done on DM1 that is too easily damageable, we built a spare mount, similar to DM1 mount, and set it up in the beam path of the testbed to study its stability as well. We can conclude from the results we obtain that tapping this mount has a huge influence on the PSF motion amplitude (the average value of the motion amplitude is multiplied by 4.87), which means that DM1 is unstable too and can also be considered as a suspect of the PSF motion.

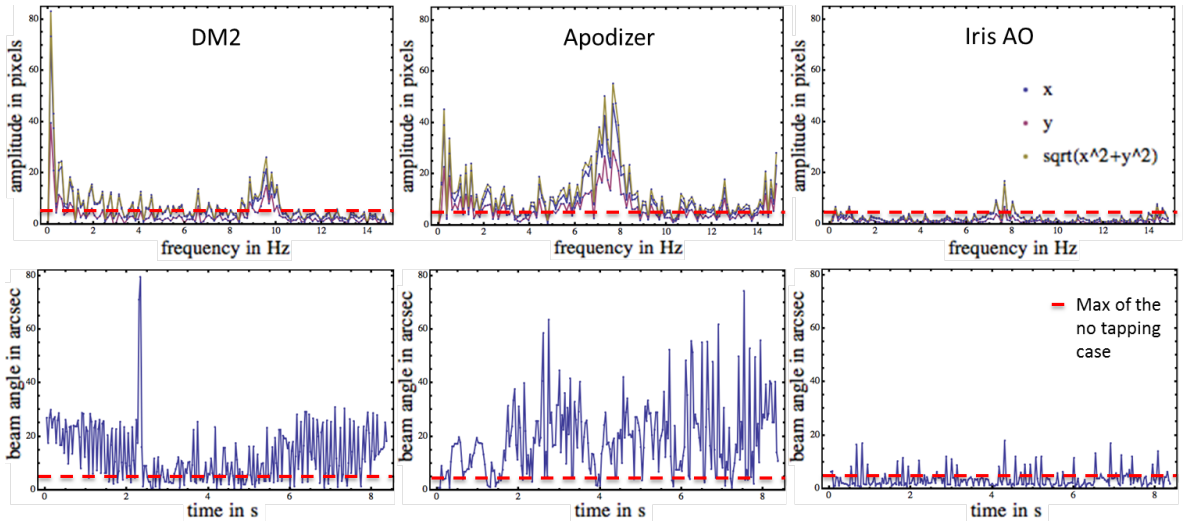

Figure 3. Temporal amplitude (top) and spectra (bottom) of the PSF motion obtained from a video acquisition when tapping three optical components. Left: the flat mirror replacing DM2, middle: the flat mirror replacing the apodizer, right: the flat mirror replacing the Iris-AO segmented mirror. The red lines correspond to the maximum value obtained without tapping.

3.1.3 Which source(s) drive(s) the instability?

This test consists in turning off one by one every possible source of motion in the testbed environment, such as the camera fans, the drivers or the air supply and taking videos at the end of the testbed.
After analysing the different recorded videos, we reached the conclusion that the motor driver and mainly the camera fans were responsible for the PSF motion. For the cameras turned off, the average motion amplitude indeed decreased by a factor of 1.45 and if the motor driver is turned off, it is decreased by a factor of 1.26.

3.1.4 Conclusion on vibration analysis

In conclusion, the motor driver and the camera fans seem responsible for the motion of the PSF and this motion of the sources can be transmitted to the beam train thanks to different possible loose or unstable optics: the two DMs, the flat mirror replacing the SM, and the apodizer.
All these optics are located before the FPM, which makes sense since when the coronagraph is on, the shape of the core of the PSF is changing.
This study still gives a large panel of suspects and careful checking of the assembly and mounting screws for all testbed optomechanics did not result in any improvements in stability. Rather it appears that one or more mount designs themselves are insufficiently stable.

3.2 Mechanical improvement on the DM mount

As we showed in the previous part, DM1 seems to be the most likely source of the vibration effect, which can easily be explained since the current mount is really cantilevered. After this analysis, it was decided to re-design this mount to make it as stable as possible.
The main constraints that have to be respected are the radius of curvature of the goniometer, the beam height (both of them have to correspond to the DM center) and the mount stability. We finally reach the global design presented in Fig. 4, where all the components are set above each other, following a vertical axis that makes the global structure really more stable than the current one.

4. SPECKLE NULLING SIMULATION TESTS

To study the instability phenomenon, we decided to focus on a well-known procedure: the Speckle Nulling method.

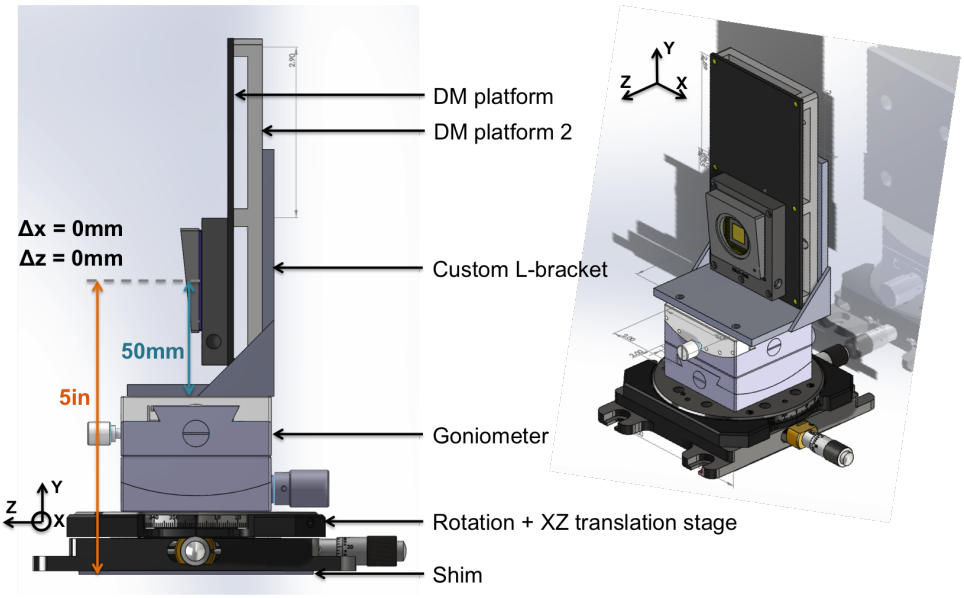

Figure 4. Solidworks design of the mount. Both the center of curvature of the goniometer and the beam height have an origin that corresponds to the DM center. The components are set one above each other, which guarantees better stability than the current cantilevered mount design.

Since Brown and Burrows[15] set the typical requirements in term of contrast for exoplanet detection, the theoretical feasibility of starlight subtraction in a so-called dark hole thanks to a DM has been proven.[16] This approach has been simplified with linearization of the equations to become the Speckle Nulling algorithm which has already several times been experimentally tested and has proven its efficiency and its robustness in broadband light.[17,18] A first generalization of this method (Speckle Field Nulling), which is based on minimization of the speckle energy in all over the dark hole thanks to a Fast-Fourier-Transform-based (FFT) algorithm, has been developed.[19] In opposition to these estimation-free approaches, model-based techniques are developed and implemented. They separate estimation and control for a faster correction, such as the Self-Coherent Camera (SCC)[20] and the COronagraphic Focal-plane waveFront Estimation for Exoplanet detection (COFFEE)[21] for the estimation, or the Electric Field Conjugation (EFC)[14,22] and the Stroke Minimization,[23] including even multiple DMs to enable symmetric correction in the dark hole (both amplitude and phase aberration correction).
In this section, we describe in the first part the Speckle Nulling code that is applied in simulation mode in the case of a circular aperture and the results we obtain. In the second part, we add random tip-tilt vibrations in the pupil plane of our simulated system and study the influence of this perturbation on the results.

4.1 Simulation without perturbation

4.1.1 Theory and code

We wrote a code that is split in different parts, to separate the simulation-only sections from the sections common to the simulation mode and to the on-testbed mode. The simulation-only sections are equivalent on the testbed to an image acquisition and therefore contain a simulated Lyot coronagraph similar to the HiCAT configuration. A visual description of the code is given in Fig. 5.

The Speckle Nulling method does not uniformly correct the image in the all dark hole. It typically focuses on the correction of the n brightest speckles of the dark hole. For example, if we only want to correct for one single speckle, the Speckle Nulling method selects the brightest speckle of the dark hole and computes its intensity I and its position (u_x, u_y), according to the center of the PSF.
Since one speckle in the field is equivalent to a sine function of the wavefront surface in the pupil plane, we are looking for an equation of the unknown error phase in the pupil plane such as:

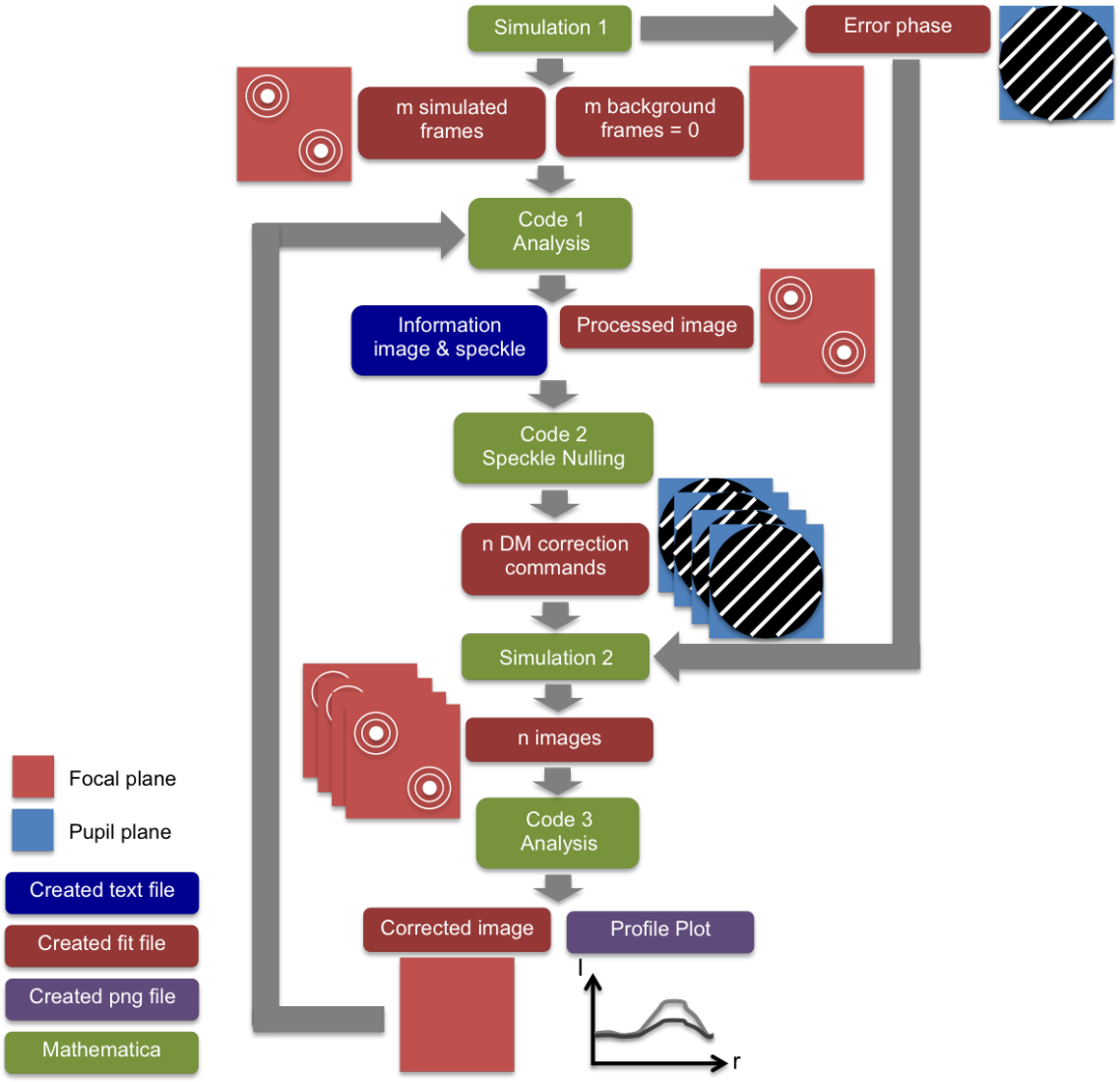

Figure 5. Diagram of our Speckle Nulling code. The code has been written to work in two different modes: with simulated data or experimental images on the testbed. Simulations 1 and 2 are dedicated to the simulation mode only while Codes 1, 2 and 3 are common to the simulation mode and the on-testbed mode. Simulation 1 sets up all the useful input for the rest of the procedure: a fake flat command of the DM, an "unknown" phase error (here: a sine function), background frames and image plane frames obtained with a Lyot coronagraph. Code 1 computes the characteristics of the selected speckle (spatial frequency and amplitude) and takes the average background-subtracted image. Code 2 generates n commands to the DM to probe different spatial phases of the selected speckle. Simulation 2 computes the coronagraphic images in the presence of unknown phase for each of the n commands applied on the DM. Finally, Code 3 analyses the coronagraphic images to determine the phase and the corresponding DM command that allow us to obtain the best correction of the selected speckle.

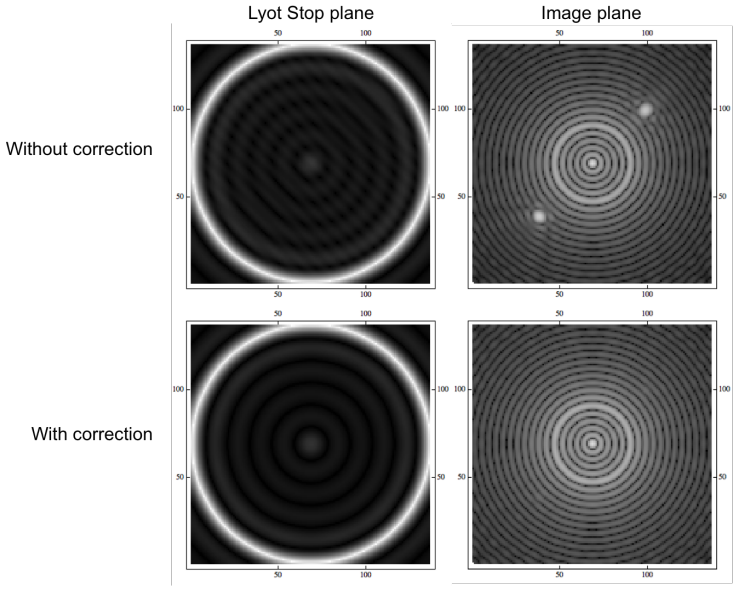

Figure 6. First results obtained with the Speckle Nulling code with simulated images before and after correction of a pair of speckles (top and bottom). Left: Images in the relayed pupil plane of the coronagraph before application of the Lyot stop. Right: Coronagraphic images in the final image plane.

$$\Phi = A \times \sin(\phi_0 + 2\pi \times (f_x x + f_y y)) \tag{1}$$

where A is the amplitude of the sine, ϕ_0 is the origin phase and f_x and f_y are the spatial frequencies of the phase and can easily be computed from the position (u_x, u_y) of the speckle.

Furthermore, to estimate the amplitude of the sine function, we add a calibration step before the correction. A known sine function is applied on the DM surface and we simulate the resulting image in the focal plane behind the coronagraph. This image has two symmetrical speckles, and we can get their intensity. According to this value and the amplitude of the sine command sent to the DM, we have a conversion factor from the DM command to the intensity of the image points.

$$A = C \times A_0 \times \sqrt{\frac{I}{I_0}} \tag{2}$$

where A is the calculated amplitude, A_0 is the amplitude of the calibration sine command, C is the conversion factor, I is the intensity of the speckle that has to be corrected, and I_0 is the intensity of the calibration speckle.

The main problem is finding the spatial phase ϕ_0. As explained in Fig. 5, it is found by testing different possible spatial phases and selecting thanks to an interpolation the one that gives the best results on the corrected image.

4.1.2 Results

We apply the procedure described before on a simulated coronagraph with a Lyot Stop size equal to 0.99 times the pupil size. In this case, since we are working on simulated data, we fix the DM size to 136 actuators, so 4 times larger than our real DM. The error phase is set as shown on Fig. 6 on the top left image and we just have access to the top right image, which is the input of the routine.

We can also observe the results that we obtain after applying the Speckle Nulling code with the best correction to the images. As we can see, the correction was very efficient: in this case, the value of the speckle changed

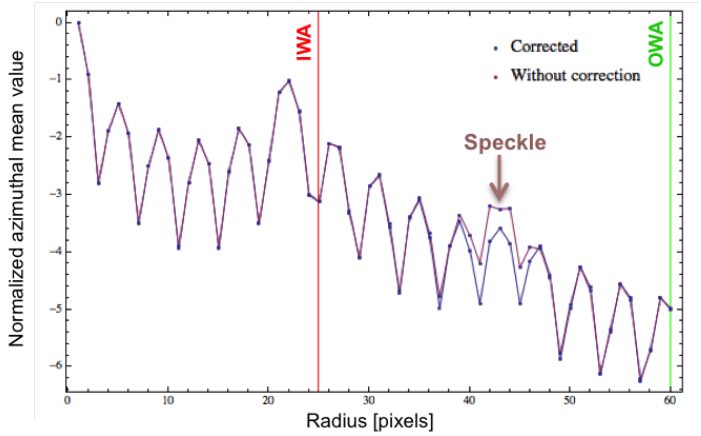

Figure 7. Azimuthal averaged intensity profiles of the coronagraphic images in log scale for the initial image (purple) and the corrected image (blue) that are displayed in Figure 6. The IWA and OWA of the controlled region are represented with vertical lines. The attenuation of the intensity is observed at the speckle location (44 pixels).

from 0.6898 to 0.01247 and on the corrected image, no speckle is visible. If we look at Fig. 7, the absence of speckle on the corrected image also clearly appears.

We also notice that on the simulated resulting phase in the pupil plane, issued from both the error phase and the correction phase, we can observe a non uniform phenomenon. This is due to the Moiré effect (frequency folding), which results from the difference between the spatial frequencies from the error phase and from the correction phase. Let's set the error phase has $(f_x, f_y) = (21, 21)$ as a spatial frequency and the frequency computed thanks to our Speckle Nulling code is (f'_x, f'_y). The difference between the error phase frequencies and the correction frequencies is responsible from this Moiré effect and creates another periodic pattern in our pupil plane at a frequency $(\frac{|f_x - f'_x|}{2}, \frac{|f_y - f'_y|}{2})$. This effect is negligible, since at the scale of the pupil plane, we just have a tiny fraction of this new period.

4.2 Simulation with perturbation

In this part, we add fake random vibration in the pupil plane before the coronagraph, that is equivalent of the DM plane.

4.2.1 Vibration simulation

Simulated vibratory perturbation can be applied on different components, such as the DM, the FPM or the Lyot Stop. Since on HiCAT the motion most likely comes from a component located before the FPM, we simulate vibrations in the DM plane.
To do so, we generate a vector of n random tip values and a vector of n random tilt values, in a certain range. We can then compute the n corresponding wavefronts in the DM plane and we add them to our phase error. After that, we can simulate the n images behind the coronagraph that are used as an input of the procedure.
We apply random vibration before summing the input images and also before applying the correction phases tested on the DM.

Except for these two extra steps, the code is applied similarly than in the previous case. We describe in the following part the results we obtain.

4.2.2 Results

As shown on Fig. 8, the vibration effect is clearly visible both before and after correction. In average, the correction is still doable, the vibration does not prevent the code from working.
The main effects of the vibration are that we can obtain random results, sometimes really good and sometimes really bad, which is due to the fact that after correction, we take a single snapshot and the random tip-tilt can

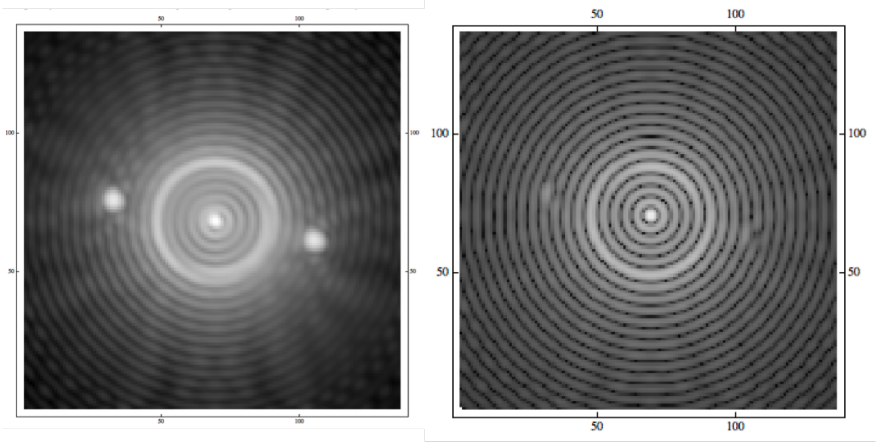

Figure 8. Coronagraphic images without and with correction, in presence of vibration. Left: Averaged image of 10 frames with random tip and tilt within the amplitude range $[-0.01\lambda, +0.01\lambda]$. Right: one single snapshot after correction, with a similar random tip-tilt vibration. In both images, the tip and tilt aberrations are visible with the asymmetry of the diffraction rings that are produced by the Lyot coronagraph. As the correction is applied at a certain position, it does not necessarily correspond to the right speckle location since a tip-tilt is added. The correction is therefore less efficient than in the case we work without vibration.

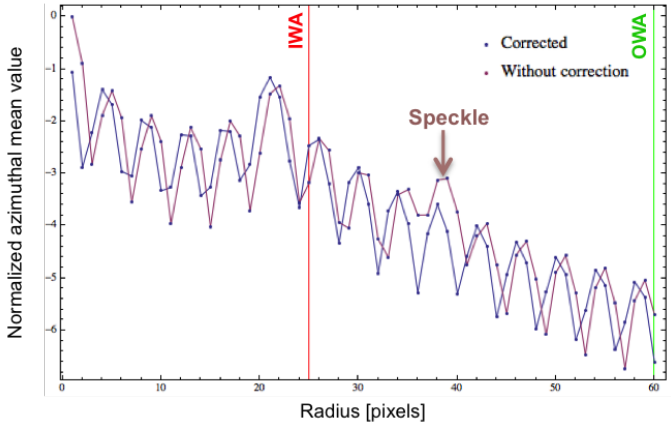

Figure 9. Azimuthal averaged intensity profiles of the simulated coronagraphic images in log scale for the noncorrected image (purple) and the corrected image (blue) that are displayed in Figure 8. The IWA and OWA of the controlled region are represented with vertical lines. A shift of the diffraction rings is observed between the two cases. The attenuation of the speckle at its location is less important than the reduction observed in the absence of vibration in Figure 7.

be small or important. Furthermore, the translation of the pattern appears on the azimuthal plot. Indeed, we observe both a translation of the rings and a smoothing of the values, as shown on Fig. 9.

The image 10 indicates the performance depending on the vibration amplitude maximum range.
For every maximum range, we apply the code 5 times and obtain a set of 5 speckle values after correction. We then look at the minimum obtained value, which corresponds to the best performance, the average value and the maximum value (worst correction). As shown on the plot 10, the higher the instability amplitude is, the more random the results are, even if in every case we can still obtain very good results (the minimum value is quite constant).

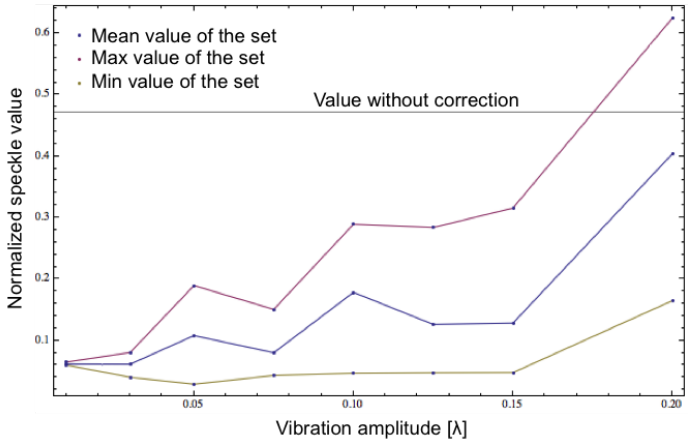

Figure 10. Intensity of the speckle after correction as a function of the maximum vibration amplitude. For every maximum range, we apply the code 5 times and obtain a set of 5 speckle values after correction. From this analysis, we retrieve the minimum obtained value, which corresponds to the best performance (yellow curve), the average value (blue curve) and the maximum value that corresponds to the worst correction (pink curve).

5. CONCLUSIONS

The HiCAT testbed will enable high-contrast imaging studies for telescopes with segmented apertures, spiders and/or central obstruction, such as WFIRST or HDST. It is designed as a coronagraph completed with two deformable mirrors to perform wavefront control and address both phase and amplitude aberrations. This year, we implemented first wavefront control codes that led us to detect an instability issue with drifts that were observed on the PSF. This issue needs to be solved to pursue our wavefront control studies. Thanks to the PSF motion analysis, we obtained strong suspects that could cause this instability. Further studies will be done thanks to an accelerometer to confirm our initial guess. In the meanwhile, a new DM mount has been designed and should provide an important improvement in terms of testbed stability.
In parallel, we coded a preliminary version of a Speckle Nulling code that gives good results in simulation mode, even in presence of pupil plane instability. Without vibration, a given speckle is fully removed after correction. In presence of vibration, we obtain a reduction of the speckle intensity in almost every case. This code will further be applied on the testbed to correct for the speckles in the chosen dark zone.
Our code will also be adapted to the case of a segmented mirror to study the effects of segments that vibrate independently on contrast performance.

REFERENCES

[1] Spergel, D., Gehrels, N., Baltay, C., Bennett, D., Breckinridge, J., Donahue, M., Dressler, A., Gaudi, B. S., Greene, T., Guyon, O., Hirata, C., Kalirai, J., Kasdin, N. J., Macintosh, B., Moos, W., Perlmutter, S., Postman, M., Rauscher, B., Rhodes, J., Wang, Y., Weinberg, D., Benford, D., Hudson, M., Jeong, W.-S., Mellier, Y., Traub, W., Yamada, T., Capak, P., Colbert, J., Masters, D., Penny, M., Savransky, D., Stern, D., Zimmerman, N., Barry, R., Bartusek, L., Carpenter, K., Cheng, E., Content, D., Dekens, F., Demers, R., Grady, K., Jackson, C., Kuan, G., Kruk, J., Melton, M., Nemati, B., Parvin, B., Poberezhskiy, I., Peddie, C., Ruffa, J., Wallace, J. K., Whipple, A., Wollack, E., and Zhao, F., "Wide-Field InfrarRed Survey Telescope-Astrophysics Focused Telescope Assets WFIRST-AFTA 2015 Report," *ArXiv e-prints* (Mar. 2015).

[2] Postman, M., Brown, T., Sembach, K., Giavalisco, M., Traub, W., Stapelfeldt, K., Calzetti, D., Oegerle, W., Michael Rich, R., Phillip Stahl, H., Tumlinson, J., Mountain, M., Soummer, R., and Hyde, T., "Advanced Technology Large-Aperture Space Telescope: science drivers and technology developments," *Optical Engineering* **51**, 011007 (Jan. 2012).

[3] Feinberg, L. D., Jones, A., Mosier, G., Rioux, N., Redding, D., and Kienlen, M., "A Cost-effective and Serviceable ATLAST 9.2m Telescope Architecture," *SPIE* **9143**, 1–11 (2014).

[4] Dalcanton, J., Seager, S., Aigrain, S., Battel, S., Brandt, N., Conroy, C., Feinberg, L., Gezari, S., Guyon, O., Harris, W., Hirata, C., Mather, J., Postman, M., Redding, D., Schiminovich, D., Stahl, H. P., and Tumlinson, J., "From Cosmic Birth to Living Earths: The Future of UVOIR Space Astronomy," *ArXiv e-prints* (July 2015).

[5] N'Diaye, M., Pueyo, L., and Soummer, R., "Apodized Pupil Lyot Coronagraphs for Arbitrary Apertures. IV. Reduced Inner Working Angle and Increased Robustness to Low-order Aberrations," *Astrophysical Journal* **799**, 225 (Feb. 2015).

[6] N'Diaye, M., Soummer, R., Pueyo, L., Carlotti, A., Stark, C. C., and Perrin, M. D., "Apodized Pupil Lyot Coronagraphs for Arbitrary Apertures. V. Hybrid Shaped Pupil Designs for Imaging Earth-like planets with Future Space Observatories," *Astrophysical Journal* **818**, 163 (Feb. 2016).

[7] Pueyo, L. and Norman, C., "High-contrast Imaging with an Arbitrary Aperture: Active Compensation of Aperture Discontinuities," *Astrophysical Journal* **769**, 102 (June 2013).

[8] Mazoyer, J., Pueyo, L., Norman, C., N'Diaye, M., and Soummer, R., "Correcting for the effects of pupil discontinuities with the ACAD method," *SPIE* **9904** (2016).

[9] Mazoyer, J., Pueyo, L., Norman, C., N'Diaye, M., van der Marel, R. P., and Soummer, R., "Active compensation of aperture discontinuities for WFIRST-AFTA: analytical and numerical comparison of propagation methods and preliminary results with a WFIRST-AFTA-like pupil," *Journal of Astronomical Telescopes, Instruments, and Systems* **2** (Mar. 2016).

[10] N'Diaye, M., Choquet, E., Pueyo, L., Elliot, E., Perrin, M., Wallace, J., Groff, T., Carlotti, A., Mawet, D., Sheckells, M., Shaklan, S., Macintosh, B., Kasdin, N. J., and Soummer, R., "High-contrast imager for Complex Aperture Telescopes (HiCAT): 1. Testbed design," in [*SPIE*], **8864** (Sept. 2013).

[11] N'Diaye, M., Choquet, E., Egron, S., Pueyo, L., Leboulleux, L., Levecq, O., Perrin, M. D., Elliot, E., Wallace, J. K., Hugot, E., Marcos, M., Ferrari, M., Long, C. A., Anderson, R., DiFelice, A., and Soummer, R., "High-contrast Imager for Complex Aperture Telescopes (HICAT): II. Design overview and first light results," in [*SPIE*], **9143**, 27 (Aug. 2014).

[12] N'Diaye, M., Mazoyer, J., Choquet, E., Pueyo, L., Perrin, M. D., Egron, S., Leboulleux, L., Levecq, O., Carlotti, A., Long, C. A., Lajoie, R., and Soummer, R., "High-contrast imager for complex aperture telescopes (HiCAT): 3. first lab results with wavefront control," in [*SPIE*], **9605**, 12 (Sept. 2015).

[13] Balasubramanian, K., Wilson, D., White, V., Muller, R., Dickie, M., Yee, K., Ruiz, R., Shaklan, S., Cady, E., Kern, B., Belikov, R., Guyon, O., and Kasdin, N. J., "High contrast internal and external coronagraph masks produced by various techniques," in [*Society of Photo-Optical Instrumentation Engineers (SPIE) Conference Series*], **8864**, 1 (Sept. 2013).

[14] Riggs, A. J. E., Kasdin, N. J., and Groff, T. D., "Recursive starlight and bias estimation for high-contrast imaging with an extended Kalman filter," *Journal of Astronomical Telescopes, Instruments, and Systems* **2**(1), 011017 (2016).

[15] Brown, R. A. and Burrows, C. J., "On the feasibility of detecting extrasolar planets by reflected starlight using the Hubble Space Telescope," *Icarus* **87**, 484–497 (Oct. 1990).

[16] Malbet, F., Yu, J. W., and Shao, M., "High-Dynamic-Range Imaging Using a Deformable Mirror for Space Coronography," **107**, 386 (Apr. 1995).

[17] Trauger, J. T., Burrows, C., Gordon, B., Green, J. J., Lowman, A. E., Moody, D., Niessner, A. F., Shi, F., and Wilson, D., "Coronagraph contrast demonstrations with the high-contrast imaging testbed," in [*Optical, Infrared, and Millimeter Space Telescopes*], Mather, J. C., ed., *SPIE* **5487**, 1330–1336 (Oct. 2004).

[18] Belikov, R., Give'on, A., Trauger, J. T., Carr, M., Kasdin, N. J., Vanderbei, R. J., Shi, F., Balasubramanian, K., and Kuhnert, A., "Toward 10 ^{10} contrast for terrestrial exoplanet detection: demonstration of wavefront correction in a shaped-pupil coronagraph," in [*Society of Photo-Optical Instrumentation Engineers (SPIE) Conference Series*], *SPIE* **6265**, 626518 (June 2006).

[19] Bordé, P. J. and Traub, W. A., "High-Contrast Imaging from Space: Speckle Nulling in a Low-Aberration Regime," *ApJ* **638**, 488–498 (Feb. 2006).

[20] Mazoyer, J., Baudoz, P., Galicher, R., and Rousset, G., "High-contrast imaging in polychromatic light with the self-coherent camera," *AAJ* **564**, L1 (Apr. 2014).

[21] Paul, B., Sauvage, J.-F., Mugnier, L. M., Dohlen, K., Fusco, T., and Ferrari, M., "Simultaneous phase and amplitude retrieval with COFFEE: from theory to laboratory results," in [*Ground-based and Airborne Instrumentation for Astronomy V*], *SPIE* **9147**, 91479O (July 2014).

[22] Give'on, A., Kern, B. D., and Shaklan, S., "Pair-wise, deformable mirror, image plane-based diversity electric field estimation for high contrast coronagraphy," in [*Techniques and Instrumentation for Detection of Exoplanets V*], *SPIE* **8151**, 815110 (Oct. 2011).

[23] Pueyo, L., Kay, J., Kasdin, N. J., Groff, T., McElwain, M., Give'on, A., and Belikov, R., "Optimal dark hole generation via two deformable mirrors with stroke minimization," *Appl. Opt.* **48**, 6296–6312 (Nov 2009).

F

Leboulleux et al. 2016, proceeding for the ICSO conference

ICSO 2016

International Conference on Space Optics

Biarritz, France

18–21 October 2016

Edited by Bruno Cugny, Nikos Karafolas and Zoran Sodnik

Comparison of wavefront control algorithms and first results on the high-contrast imager for complex aperture telescopes (hicat) testbed

L. Leboulleux

M. N'Diaye

J. Mazoyer

L. Pueyo

et al.

esa icso proceedings cnes

International Conference on Space Optics — ICSO 2016, edited by Bruno Cugny, Nikos Karafolas, Zoran Sodnik, Proc. of SPIE Vol. 10562, 105622Z · © 2016 ESA and CNES
CCC code: 0277-786X/17/$18 · doi: 10.1117/12.2296154

COMPARISON OF WAVEFRONT CONTROL ALGORITHMS AND FIRST RESULTS ON THE HIGH-CONTRAST IMAGER FOR COMPLEX APERTURE TELESCOPES (HICAT) TESTBED

L. Leboulleux[1,2,3], M. N'Diaye[3], J. Mazoyer[3], L. Pueyo[3], M. Perrin[3], S. Egron[1,2,3], E. Choquet[4,5], J.-F. Sauvage[1,2], T. Fusco[1,2], R. Soummer[3]. Contact: lucie.leboulleux@lam.fr.
[1] ONERA, 29 Avenue de la Division Leclerc, 92320 Châtillon, France. [2] Aix Marseille Université, CNRS, LAM (Laboratoire d'Astrophysique de Marseille) UMR 7326, 13388, Marseille, France. [3] Space Telescope Science Institute, 3700 San Martin Drive, Baltimore, MD 21218, USA. [4] Jet Propulsion Laboratory, California Institute of Technology, 4800 Oak Grove Drive, MS 169-506, Pasadena, CA 91109, USA. [5]Hubble Fellow.

I. INTRODUCTION:

The next generation of space telescopes for direct imaging and spectroscopy of exoplanets includes telescopes with a monolithic mirror, such as the Wide Field Infrared Survey Telescope (WFIRST) [1] and Large Ultra-Violet Optical Infrared (LUVOIR) telescopes with segmented primary mirror, like ATLAST [2, 3] or HDST [4]. Because of the complexity of their pupils, high-contrast imaging becomes more challenging. Furthermore, space telescopes have huge requirements in term of contrast stability in the presence of vibrations.

The High-contrast imager for Complex Aperture Telescopes (HiCAT) testbed has been developed to enable studies on different components of high-contrast imaging, meaning starlight suppression, wavefront sensing (WFS), and wavefront control (WFC) for such unfriendly pupils. New coronagraph designs are currently developed in simulation [5, 6, 7] for a next implementation on the testbed. The wavefront control of HiCAT will also consist in two deformable mirrors (DM) pupil-remapping techniques (e.g. Active Control of Aperture Discontinuities [ACAD] [8, 9, 10]), that convert complex pupils into friendly apertures for coronagraphy.

In this communication, in section II we introduce the HiCAT testbed, focusing on its objectives and in particular the studies it will enable and the requirements that were deduced from these goals. These requirements led to a final design and environment, that we also present here, before describing its current status.

In section III, we present different well-known wavefront control methods, in particular their prerequisites.

II. HICAT TESTBED:

The HiCAT testbed is currently being developed at the Space Telescope Science Institute (STScI), more precisely at the Russel B. Makidon Laboratory. This facility is dedicated to the development of technologies for future space missions. In particular, HiCAT is designed to provide an integrated solution for high-contrast imaging for unfriendly aperture geometries in space, such as HDST or ATLAST-like pupils. In the section, we will describe the objectives of this optical bench, its final optical and opto-mechanical design that was deduced from these requirements, the environment constraints, and finally the current status of the project.

A. Goals of the testbed

The HiCAT tesbed was designed to develop methods for high-contrast imaging, including a starlight and diffraction suppression system and wavefront sensing and control tools. These techniques have to be applied in complex-aperture case telescopes, which includes segment gaps, spiders and central obstruction.

Its initial contrast goal in air is 10^{-7} in a dark hole limited by $3\lambda/D$ and $10\lambda/D$ (where λ is the wavelength and D is the aperture diameter) in a 2% bandpass, in the visible, assuming a single Boston Micromachines-deformable mirror (DM), which should be improved to higher contrast after implementation of wavefront control methods.

To reach this contrast ratio, the testbed is designed to minimize the impact of its optical components on its final contrast, with focus on the sources of amplitude-induced errors from the propagation of out-of-pupil surfaces. To limit that effect, known as the Talbot effect, we place a requirement on the contrast contribution of amplitude errors to be one order of magnitude fainter than the total contrast, i.e. 10^{-8}. The goal is that, by minimizing the amplitude-induced errors due to the Talbot effect, the majority of the amplitude errors comes from the discontinuities in the pupil, such as the segment gaps, the spiders or the central obstruction and will be corrected using wavefront control and wavefront shaping.

Since HiCAT was designed to compensate for both amplitude errors due to its complex entrance pupil and phase errors due to surface errors and non-homogeneous reflectivities of the optical components, two Boston-DM are planned to be used. This is why this value of contrast should be then really improved after setting up the second DM in the optical path.

Such a theoretical limit for the contrast is significantly better than the requirement. We are therefore quite confident than the ultimate performance on HiCAT will satisfy the requirement, even with complex apertures (central obstruction, spiders and segments) and in large spectral broadband operations.

But HiCAT also includes a coronagraph for starlight and diffraction-effect suppression, which is designed considering the contrast as a metric to optimize.

B. Optical and opto-mechanical design

The HiCAT testbed is designed to achieve these goals, performing high-contrast imaging in the case of unfriendly apertures. Therefore, it combines studies in coronagraphy, wavefront sensing and wavefront control, plus a simulated telescope with a complex pupil. The final layout is presented in Fig.1 and is explained in details in [7, 11, 12]. It is a purely reflective testbed, except for the last imaging lenses.

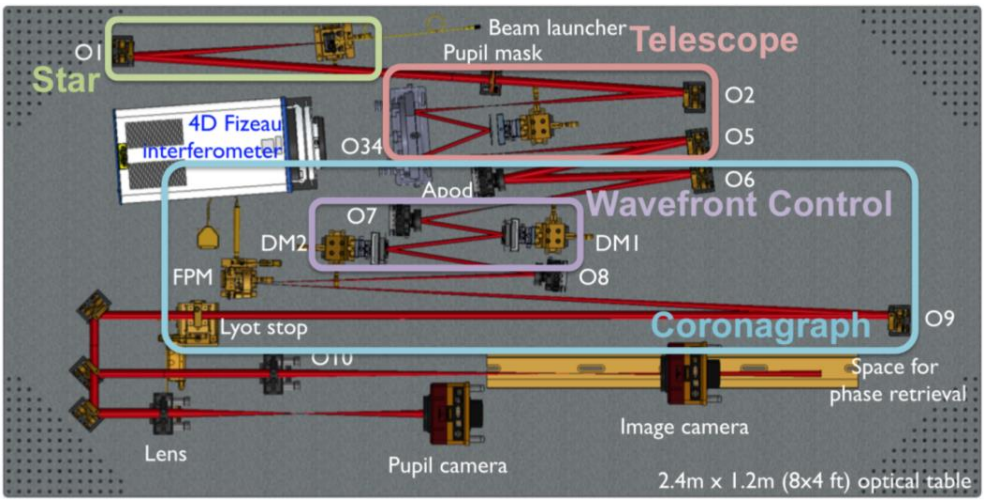

Fig. 1. Optical and mechanical design of the HiCAT testbed, realized with the software Solidworks, the beam is exported from Zemax. The telescope is simulated by a pupil mask, the segmented mirror and off-axis parabolas. The segmented mirror is conjugated with the pupil mask to form a segmented pupil with central obstruction and spider struts. The off-axis parabolas set the telescope aperture. The wavefront control is done with two deformable mirrors. The coronagraph is composed of an apodizer, a focal plane mask and a Lyot stop.

The telescope is simulated using:

- A non-circular entrance pupil mask with central obstruction and spiders to define an aperture shape. Its size is set the 20 mm to enable small details to be represented with good precision (such as the spider) and the use of 1inch optics.
- A 37-segment Iris-AO MEMs deformable mirror with hexagonal segments that can be controlled in tip, tilt, and piston. The gaps between segments are between 10 and 12 µm and the full segmented mirror has an inscribed circle size of 7 mm. This component is conjugated to the entrance pupil mask.

Together, these two components provide a segmented pupil similar to ATLAST. The segmented mirror can also be replaced with a high-quality flat mirror to give the possibility of studying AFTA-like pupils.

The chosen coronagraph is a Apodized Pupil Lyot Coronagraph (APLC), which combines a classical Lyot coronagraph with entrance pupil apodization [8, 9, 10]. This type of coronagraph is currently implemented in the exoplanet direct imagers P1640, GPI, and SPHERE. It is then composed of:

- An apodizer, located in a pupil plane, so conjugated with the two optical components previously presented.
- A reflective focal plane mask (FPM), with a 334 µm diameter central hole. The beam focal ratio at its location is set at F/80.
- A Lyot Stop, with a diameter equal to the entrance pupil. We also have another possible Lyot Stop of 10 mm.

Both the FPM and the Lyot Stop are motorized and can be controlled from a computer.

The final design of the apodizer is still under development, and the testbed is currently equipped with a Lyot coronagraph, the apodizer being replaced by a high-quality mirror. For more details about the investigations on coronagraph designs, please see [7]. Furthermore, thanks to the hole in the FPM, part of the beam can be reused and this coronagraph is compatible with a low-order wavefront sensor [13, 14, 15].

Finally, the wavefront sensing and control system includes:

- Two Boston Micromachines deformable mirrors (kilo-DM), named DM1 and DM2, each of them with 952 actuators in a 9.9 mm diameter disk. DM1 is calibrated and set in a pupil plane [7], and DM2, currently replaced by a flat mirror, is located out of pupil. It will enable active correction for aperture discontinuities (ACAD) and both amplitude and phase control.
- A focal plane camera (CamF), with a motorized translation stage along the optical axis. This translation stage will allow phase diversity applications [16, 17].

The testbed also includes a pupil plane camera (CamP), a 4D AccuFiz interferometer for alignment and wavefront measurements, and convergent mirrors.

Combining all these components, the total wavefront error (WFE) in the testbed is 150 nm RMS without the correction from the DMs. This enables the use of $\lambda/20$ surface error optics and an alignment tolerance of 100 to 500 µm, depending on the optic.

C. Environment constraints

To limit air turbulence and dust on the optical components, which would degrade the contrast performance, HiCAT is located in a class 1000 clean room with temperate control in a 1°C range and humidity that is maintained under 40%. Furthermore, the testbed is on a floating table, which is on a platform independent from the rest of the building, to remove vibration effects. A box covers all the testbed to protect it from dust and particles.

In addition to these first protections, the deformable mirrors have stronger constraints, in particular about humidity (below 30%), which lead to the installation of temperature and humidity sensors and a complementary dry air system inside the box containing the optical bench.

This air supply may create unwanted turbulence effects in the bench box, that might make the wavefront more unstable and so high-contrast imaging implementation more challenging. This is why we plan to make this supply external by limiting the humidity in the entire room below 30%, which would minimize the turbulence inside the box.

D. Timeline and first results

The HiCAT testbed was fully aligned in Summer 2014, except for the three deformable mirrors (2 Boston-DMs and the Iris-AO segmented mirror) and the apodizer. This alignment resulted in a wavefront errors of 12±3 nm RMS (instead of the 150 nm RMS required in section B) over an 18mm circular pupil, after passing through an optical train of 15 components. Fig. 2 shows the direct and coronagraphic images obtained at the end of the testbed after this alignment. The direct image corresponds to a nice Airy diffraction pattern, with seven visible rings. Furthermore, the coronagraphic image shows a lot of speckles, that result from the residual wavefront errors of the testbed, and was not optimized at that time since the FPM and the Lyot Stop were not optimally centered yet.

In 2015, the first DM was calibrated and integrated into the testbed, and replaced a flat mirror located in a pupil plane. After alignment of the DM, we obtained a wavefront error of 13±3 nm RMS, which makes us hope for very good results after implementation of wavefront control.

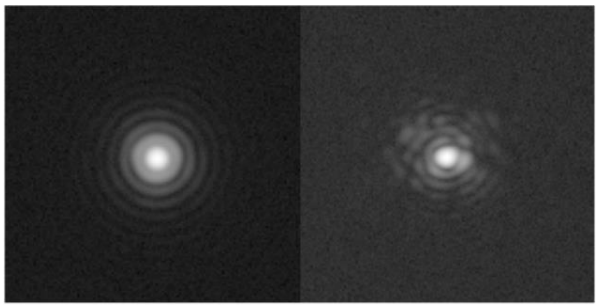

Fig. 2. Direct and coronagraphic PSF obtained at the end of the HiCAT testbed, in log scale, but not on the same dynamical range. The camera was not precisely aligned yet. A 18mm circular pupil was used, combined with a 10mm Lyot Stop. The source gives a monochromatic light at λ=640nm.

Unfortunately, the first wavefront control tests could not be achieved, due to an instability issue, that is described in [18]. The resolution of this problem is currently on going, and once it will be solved, the wavefront control implementation will go on, leading to the installation of the second DM to apply also the ACAD method.

Furthermore, the apodizer design studies is on-going and gives very promising results and an apodizer should be added to the optical bench.

III. WAVEFRONT SENSING AND WAVEFRONT CONTROL: THE WAY TO HIGH-CONTRAST:

Since Brown and Burrows set [19] the typical requirements in term of contrast for exoplanet detection, the theoretical feasibility of starlight subtraction in a so-called dark hole thanks to a DM has been proven [20]. Since 1995, several methods have been developed and have proven their efficiency. For a faster correction, most of them separate estimation and control of the wavefront, using complementary sensing methods such as the Self-Coherent Camera (SCC) [21] and the COronagraphic Focal-plane waveFront Estimation for Exoplanet detection (COFFEE) [22]. In this section, we introduce different well-known wavefront control algorithms.

A. Speckle Nulling

The Speckle Nulling (SN) is the first algorithm that was developed and has already several times been experimentally tested and has proven its efficiency and its robustness in broadband light [23, 24].

It is an estimation-free approach, that only uses the image on the science camera. Furthermore, this method typically focuses on the correction of the brightest speckle in the dark hole. This is why it has to be applied many times in a row to correct for speckles in the entire dark hole.

It is based on the relationship between one speckle in a focal plane and a sine error phase in a pupil plane, where the DM is located. This is why a speckle on the science camera plane will be corrected by applying a sine command on the DM surface, such as:

$$\varphi_{DM} = A \times \sin(\varphi_0 + 2\pi \times (f_x x + f_y y)) \quad (1)$$

where A is the amplitude of the sine, φ_0 is the origin phase and f_x and f_y are the spatial frequencies of the phase and can easily be computed from the position (α, β) of the speckle.

Since the relationship between the electric fields in DM plane and in science camera plane is linear, the links are easy between position of the speckle and frequencies of the sine function and between intensity in the image and amplitude of the sine function. This second step also implies to acquire a flux reference prior to the SN to get the DM response. This algorithm is illustrated in Fig. 3 and explained in details in [18]. The main issue is to find the phase offset φ_0. This is done by testing different phase offsets and selecting thanks to an interpolation the one that gives the best results on the corrected image in term of speckle extinction.

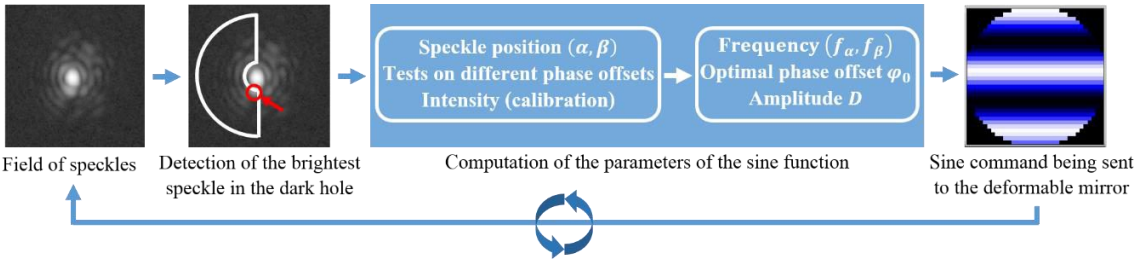

Fig. 3. SN algorithm principle. The coronagraphic PSF is used as an input. In the desired dark hole, the brightest speckle is selected. Thanks to its position, the frequency of the optimal correction sine function is computed. The amplitude of the correction function is obtained thanks to a calibration step and the intensity of the speckle. The optimal phase offset is deduced from test commands that are sent to the DM before selection of the most efficient one. After correction of the speckle, the second brightest speckle is selected in the dark hole, and the algorithm is applied again.

This algorithm is interesting since it does not need any prerequisite, except for a fast calibration of the deformable mirror and a reference flux calibration. However, this method has some drawbacks, such as the absence of physical constraints on the DM: by adding as many sine commands as speckles in the dark hole, huge actuator strokes can be produced, which is not realistic. Furthermore, the correction is very slow, since one speckle is corrected at each step of the control loop. Many hundreds of thousands of correction iterations are necessary to correct for the electric field in the entire dark hole, which is not compatible with space missions. This is why, after this first test, we want to focus on other methods, which are directly correcting for the wavefront in the entire dark hole.

B. Speckle Field Nulling

The Speckle Field Nulling (SFN) algorithm [25] brings an improvement to the SN as it proposes an enhanced convergence speed. This method is a generalization of the previous one and is based on the minimization of the speckle energy in all over the dark hole.

The electric field E in the pupil plane can be expressed as:

$$\forall (x,y) \in Pup, E(x,y) = P(x,y) \times e^{A(x,y)+i\varphi(x,y)+i\varphi_{DM}(x,y)} \quad (2)$$

where P is the pupil function, A is the amplitude aberration, φ is the phase aberration, and φ_{DM} is the phase correction, equivalent to the DM surface equation. If we consider the amplitude aberrations as negligible and the correction efficient enough so that $\varphi + \varphi_{DM}$ is small, then we have the following linearization:

$$\forall (x,y) \in Pup, E(x,y) \approx P(x,y) \times (1 + i\varphi(x,y) + i\varphi_{DM}(x,y)) \quad (3)$$

After passing through the coronagraph, modeled here as a linear function $\boldsymbol{\mathcal{C}}$, the electric field in the detector plane E_f can be expressed as following:

$$\forall (\alpha,\beta) \in DH, E_f(\alpha,\beta) \approx \boldsymbol{\mathcal{C}}\{P(x,y)\} + i\boldsymbol{\mathcal{C}}\{P(x,y)\varphi(x,y)\} + i\boldsymbol{\mathcal{C}}\{P(x,y)\varphi_{DM}(x,y)\} \quad (4)$$

where $\boldsymbol{\mathcal{C}}\{P\}$ is the image of the star, $i\boldsymbol{\mathcal{C}}\{P\varphi\}$ corresponds to the field of speckles, and $i\boldsymbol{\mathcal{C}}\{P\varphi_{DM}\}$ is the correction brought by the DM as seen in the detector plane. Since the image of the star is cancelled by the coronagraph, this expression becomes:

$$\forall (\alpha,\beta) \in DH, E_f(\alpha,\beta) \approx i\boldsymbol{\mathcal{C}}\{P(x,y)\varphi(x,y)\} + i\boldsymbol{\mathcal{C}}\{P(x,y)\varphi_{DM}(x,y)\} \quad (5)$$

Furthermore, the DM surface can be expressed as the sum of the contribution of its different actuators, meaning:

$$\forall (x,y) \in Pup, \varphi_{DM}(x,y) = \sum_{k=1}^{N}\sum_{l=1}^{N} a_{kl} f_{kl}(x,y) \quad (6)$$

where $(a_{kl})_{(k,l)\in[\![1,N]\!]^2}$ are the actuator strokes and $(f_{kl})_{(k,l)\in[\![1,N]\!]^2}$ are the influence functions of the DM, obtained by calibration.

Furthermore, since the objective of this method is to obtain:

$$\forall (\alpha,\beta) \in DH, E_f(\alpha,\beta) = 0 \quad (7)$$

by combining this equation with (4) and (5), we finally get:

$$\sum_{k=1}^{N}\sum_{l=1}^{N} a_{kl}\boldsymbol{\mathcal{C}}\{Pf_{kl}\} = -\boldsymbol{\mathcal{C}}\{P\varphi\} \quad (8)$$

This corresponds to a linear system in (a_{kl}) and can easily be solved using Singular Value Decomposition (SVD) or Fourier Expansion.

This algorithm proposes a good improvement in term of computing speed from the previous method, since the electric field is corrected in the entire dark hole at once. However, it requires a preliminary pupil plane wavefront sensing step and is based on a model for the coronagraph, that needs to be realistic, and a complex calibration of the deformable mirror. Furthermore, once again, there is no constraint on the deformable mirror, which means big strokes can be produced.

C. Electric Field Conjugation

The Electric Field Conjugation algorithm (EFC) is well described in [26, 27]. This algorithm needs an estimation of the amplitude of the electric field in the focal plane. As in the previous method, the objective is to satisfy the requirement of (6).

This approach is also based on the expression of the electric field in the pupil plane, given in (2), but the linearization is different, since we consider that a small correction phase is applied:

$$\forall (x,y) \in Pup, E(x,y) \approx P(x,y) \times e^{A(x,y)+i\varphi(x,y)}(1 + i\varphi_{DM}(x,y)) \quad (9)$$

After passing through the coronagraph, the electric field becomes:

$$\forall(\alpha,\beta) \in DH, E_f(\alpha,\beta) \approx \boldsymbol{\mathcal{C}}\{Pe^{A+i\varphi}\} + i\boldsymbol{\mathcal{C}}\{P\varphi_{DM}\} \tag{10}$$

A preliminary calibration step furnishes the relation between the voltages v applied on the DM and the electric field on the detector plane. This relationship is modeled thanks to a so-called interaction matrix G, defined as:

$$\boldsymbol{\mathcal{C}}\{P\varphi_{DM}\} = Gv \tag{11}$$

By combining this equation, (10) and the criterion (6), we then get:

$$\boldsymbol{\mathcal{C}}\{Pe^{A+i\varphi}\} + iGv = 0 \tag{12}$$

which is equivalent to:

$$v = G^{\dagger}(i\boldsymbol{\mathcal{C}}\{Pe^{A+i\varphi}\}) \tag{13}$$

where the generalized inverse matrix of G, $G^{\dagger}$, can be obtained by SVD. Finally, since v is necessary real, we have:

$$v = \begin{bmatrix}\boldsymbol{\mathcal{Re}}\{G\}\\ \boldsymbol{\mathcal{Im}}\{G\}\end{bmatrix}^{\dagger}\begin{bmatrix}\boldsymbol{\mathcal{Re}}\{i\boldsymbol{\mathcal{C}}\{Pe^{A+i\varphi}\}\}\\ \boldsymbol{\mathcal{Im}}\{i\boldsymbol{\mathcal{C}}\{Pe^{A+i\varphi}\}\}\end{bmatrix} \tag{14}$$

where $\boldsymbol{\mathcal{C}}\{Pe^{A+i\varphi}\}$ is the electric field in the image plane, obtained thanks to wavefront sensing.

This algorithm, such as the previous one, needs to be complemented with a wavefront estimator, and is based on a calibration of the deformable mirror. There is again no constraint on the DM strokes, and the linearization of the correction phase implies that it has to remain small. But, in opposition to the SFN method, it does nto require any model for the coronagraph.

D. Stroke Minimization

The problem of these last three methods is that they do not take into account the physical constraints of the deformable mirror, in particular the limited strokes of the actuators. The last algorithm we introduce here, named Stroke Minimization (SM), answers to this issue. The idea here is to minimize the quadratic sum of the actuator strokes, $\frac{1}{2}\sum_{k=1}^{N}\sum_{l=1}^{N} {a_{kl}}^2$, regardless a constraint in contrast:

$$\varepsilon \leq 10^{-C} \tag{15}$$

where ε corresponds to the total energy in the dark hole and is defined as:

$$\varepsilon \equiv \langle E_f, E_f \rangle = \iint_{DH} |E_f(\alpha,\beta)|^2 \delta\alpha\delta\beta \tag{16}$$

To combine these two requirements, we define a criterion, named ε_M and defined as:

$$\varepsilon_M = \frac{1}{2}\sum_{k=1}^{N^2} {a_k}^2 + \mu \times (\varepsilon - 10^{-C}) \tag{17}$$

where μ is a weighting parameter that needs to be optimized.

In practice, μ is set at a small value. ε_M is minimized by setting its derivative to 0 and we obtain a value for the actuator strokes $(a_{kl})_{(k,l)\in[\![1,N]\!]^2}$. Then, if the contrast constraint is respected, the algorithm is finished, if not, the value of μ is increased, which is equivalent to increasing the importance of the contrast constraint in the criterion ε_M, and the algorithm is applied again, until the requirements are satisfied.

To have a complete description of this algorithm, its formalism, and results, please refer to [28].

Even if this algorithm is more complex than the previous ones and requires a calibration step and a wavefront sensing, it is very efficient and if the wavefront estimation is well done, it can be also very fast. It also takes into account the physical limitations of the DM, but its main advantage is that it can include multiple DMs to enable symmetric correction in the dark hole, by correcting for both amplitude and phase aberrations, which is not possible with one single DM.

E. Non-linear Dark Hole

In opposition to these methods that are all using a linearization of the electric field, another algorithm was developed, the so-called Non-Linear Dark Hole (NLDH) [29]. The idea of this method is the minimization of the energy ε in the dark hole, as defined in (16). Without any linearization, this energy is equal to:

$$\varepsilon = \left\| \mathcal{C}\{P \times e^{A+i\varphi+i\varphi_{DM}}\} \right\|^2 \tag{18}$$

where:

$$\varphi_{DM} = Fv \tag{19}$$

F contains the influence functions $(f_{kl})_{(k,l)\in[\![1,N]\!]^2}$.

This energy is minimized to obtain an optimal voltage vector v thanks to a numerical minimization based on the Variable Metric with Limited Memory and Bounds (VMLM-B) method [29]. The key point to optimize the minimization is to compute the analytical expression of the gradient of the coronagraphic PSF with respect to the aberrations upstream of the coronagraphic mask. The computation of this term $\delta\varepsilon/\delta\varphi$ is explicitly detailed in the thesis of B. Paul, appendix B.0.3.

IV. CONCLUSIONS AND PERSPECTIVES:

The HiCAT testbed will enable high-contrast imaging studies for telescopes with segmented apertures, spiders and/or central obstruction. It is designed as a coronagraph completed with two deformable mirrors to perform wavefront sensing and wavefront control and address both phase and amplitude aberrations.

In parallel to this experimental study, we plan to focus on simulation of several well-known wavefront control algorithms, that we introduced in the second part of this paper. Even if SN is the only one that does not need any wavefront estimation and limits the number of prerequisites (no need of a model for the coronagraph, and a fast single calibration step), it is the longest to converge for a correction on the entire dark hole. This is why, after this first test, it appears necessary to focus on other methods, such as SFN, EFC, SM, and NLDH. As indicated in Fig. 4, these methods require wavefront estimation, a calibration of the deformable mirror actuators with the knowledge of the influence functions or the interaction matrix, and a realistic model for the coronagraph, in the cases of SFN and NLDH.

The objective now is comparing the performance in contrast of these different methods, but also their requirements and their robustness to realistic space-like environment conditions, such as jitter. After this study, a method should be selected to be implemented on the HiCAT testbed for further studies.

Criteria\Method	Speckle Nulling	Speckle Field Nulling	Electric Field Conjugation	Stroke Minimization	Non linear Dark Hole
Wavefront sensing needed		✖	✖ Electric field in focal plane	✖	✖
Use of a model for the coronagraph		✖			✖
Use of a calibration for the deformable mirror	✖	✖			✖
Use of a calibration Pupil -> Focal plane	✖		✖	✖	

Fig. 4. Prerequisites of the different wavefront control algorithms that have been introduced in this paper. In opposition to the last four algorithms, the SN does not need any estimation, but this is the slowest method. The five options require a calibration of the deformable mirror actuators with the knowledge of the influence functions or the interaction matrix, and also a realistic model for the coronagraph, in the case of SFN or NLDH.

REFERENCES

[1] D. Spergel, N. Gehrels, C. Baltay, D. Bennett, J. Breckinridge, et al., *Wide-Field InfrarRed Survey Telescope-Astrophysics Focused Telescope Assets WFIRST-AFTA 2015 Report*, ArXiv e-prints, March 2015.

[2] M. Postman, T. Brown, K. Sembach, M. Giavalisco, W. Traub, et al., "Advanced Technology Large-Aperture Space Telescope: science drivers and technology developments", *Optical Engineering*, 51, 011007, January 2012.
[3] L. D. Feinberg, A. Jones, G. Mosier, N. Rioux, D. Redding, and M. Kienlen, "A Cost-effective and Serviceable ATLAST 9.2m Telescope Architecture", *SPIE 9143*, 1-11, 2014.
[4] J. Dalcanton, S. Seager, S. Aigrain, S. Battel, N. Brandt, et al., "From Cosmic Birth to Living Earths: The Future of UVOIR Space Astronomy", ArXiv e-prints, July 2015.
[5] M. N'Diaye, L. Pueyo, and R. Soummer, "Apodized Pupil Lyot Coronagraphs for Arbitrary Apertures. IV. Reduced Inner Working Angle and Increased Robustness to Low-order Aberrations", *Astrophysical Journal* 799, 225, February 2015.
[6] M. N'Diaye, R. Soummer, L. Pueyo, A. Carlotti, C. Stark, and M. D. Perrin, "Apodized Pupil Lyot Coronagraphs for Arbitrary Apertures. V. Hybrid Shaped Pupil Designs for Imaging Earth-like planets with Future Space Observatories", *Astrophysical Journal* 818, 163, February 2016.
[7] M. N'Diaye, J. Mazoyer, E. Choquet, L. Pueyo, M. D. Perrin, et al., "High-contrast imager for complex aperture telescopes (HiCAT): 3. First lab results with wavefront control", *SPIE*, 9605, 12, September 2015.
[8] L. Pueyo and C. Norman, "High-contrast Imaging with an Arbitrary Aperture: Active Compensation of Aperture Discontinuities", *Astrophysical Journal* 769, 102, June 2013.
[9] J. Mazoyer, L. Pueyo, C. Norman, M. N'Diaye, and R. Soummer, "Correcting for the effects of pupil discontinuities with the ACAD method", *SPIE* 9904, 2016.
[10] J. Mazoyer, L. Pueyo, C. Norman, M. N'Diaye, R. P. van der Marel, and R. Soummer, "Active compensation of aperture discontinuities for WFIRST-AFTA: analytical and numerical comparison of propagation methods and preliminary results with a WFIRST-AFTA-like pupil", *Journal of Astronomical Telescopes, Instruments, and Systems 2*, March 2016.
[11] M. N'Diaye, E. Choquet, L. Pueyo, E. Elliot, M. D. Perrin, et al., "High-contrast imager for Complex Aperture Telescopes (HiCAT): 1. Testbed design", *SPIE*, 8864, September 2013.
[12] M. N'Diaye, E. Choquet, S. Egron, L. Pueyo, L. Leboulleux, et al., "High-contrast Imager for Complex Aperture Telescopes (HICAT): II. Design overview and first light results", *SPIE*, 9143, 27, August 2014.
[13] J. K. Wallace, S. Rao, R. M. Jensen-Clem, and G. Serabyn, "Phase-shifting Zernike interferometer wavefront sensor", *SPIE*, 8126, September 2011.
[14] M. N'Diaye, K. Dohlen, T. Fusco, K. El Hadi, R. Soummer, et al., "Lab results of the circular phase mask concepts for high-contrast imaging of exoplanets", *SPIE*, 8450, September 2012.
[15] M. N'Diaye, K. Dohlen, T. Fusco, and B. Paul, "Calibration of quasi-static aberrations in exoplanet direct-imaging instruments with a Zernike phase-mask sensor", *Astron. & Astrophys.*, 555, A94, July 2013.
[16] B. H. Dean and C. W. Bowers, "Diversity selection for phase-diverse phase retrieval", *Journal of the Optical Society of America* A 20, pp. 1490-1504, August 2003.
[17] J.-F. Sauvage, L. Mugnier, B. Paul, and R. Villecroze, "Coronagraphic phase diversity: a simple focal plane sensor for high-contrast imaging", *Optics Letters* 37, p. 4808, December 2012.
[18] L. Leboulleux, M. N'Diaye, A. J. Eldorado Riggs, S. Egron, J. Mazoyer, "High-contrast imager for Complex Aperture Telescopes (HiCAT). 4. Status and wavefront control development", *SPIE*, July 2016.
[19] R. A. Brown and C. J. Burrows, "On the feasibility of detecting extrasolar planets by reflected starlight using the Hubble Space Telescope", *Icarus* 87, 484-497, October 1990.
[20] F. Malbet, J. W. Yu, M. and Shao, "High-Dynamic-Range Imaging Using a Deformable Mirror for Space Coronography", 107, 386, April 1995.
[21] J. Mazoyer, P. Baudoz, R. Galicher, and G. Rousset, "High-contrast imaging in polychromatic light with the self-coherent camera", *AAJ* 564, L1, April 2014.
[22] B. Paul, J.-F. Sauvage, L. M. Mugnier, K. Dohlen, T. Fusco, et al., "Simultaneous phase and amplitude retrieval with COFFEE: from theory to laboratory results", *SPIE* 9147, 91479O, July 2014.
[23] J. T. Trauger, C. Burrows, B. Gordon, J. J. Green, A. E. Lowman, et al., "Coronagraph contrast demonstrations with the high-contrast imaging testbed", *SPIE* 5487, 1330-1336, October 2004.
[24] R. Belikov, A. Give'on, J. T. Trauger, M. Carr, N. J. Kasdin, et al., "Toward 10^{10} contrast for terrestrial exoplanet detection: demonstration of wavefront correction in a shaped-pupil coronagraph", *SPIE* 6265, 62651, June 2006.
[25] P. J. Bordé and W. A. Traub, "High-Contrast Imaging from Space: Speckle Nulling in a Low-Aberration Regime", *ApJ* 638, 488-498, February 2006.
[26] A. J. E. Riggs, N. J. Kasdin, and T. D. Groff, "Recursive starlight and bias estimation for high-contrast imaging with an extended Kalman filter", *JATIS* 2(1), 011017, 2016.
[27] A. Give'on, B. D. Kern, and S. Shaklan, "Pair-wise, deformable mirror, image plane-based diversity electric field estimation for high contrast coronagraphy", *SPIE* 8151, 815110, October 2011.
[28] L. Pueyo, J. Kay, N. J. Kasdin, T. D. Groff, M. McElwain, et al., "Optimal dark hole generation via two deformable mirrors with stroke minimization", *Appl. Opt.* 48, 6296-6312, November 2009.
[29] B. Paul, "Mesure de front d'onde post-coronographique à haute précision pour l'imagerie à haut contraste : application sol et espace", PhD thesis, September 2014.

G

Leboulleux et al. 2017, proceeding for the SPIE conference

Sensitivity analysis for high-contrast missions with segmented telescopes

Lucie Leboulleux[abc], Jean-François Sauvage[bc], Laurent Pueyo[a], Thierry Fusco[bc], Rémi Soummer[a], Mamadou N'Diaye[d], Kathryn St.Laurent[a]

[a] Space Telescope Science Institute, 3700 San Martin Drive, Baltimore, MD 21218, USA
[b] Aix Marseille Université, CNRS, LAM (Laboratoire d´Astrophysique de Marseille) UMR 7326, 13388, Marseille, France
[c] Office National d´Etudes et de Recherches Aérospatiales, 29 Avenue de la Division Leclerc, 92320 Châtillon, France
[d] Observatoire de Nice Côte d´Azur, Boulevard de l´Observatoire, 06304 Nice, France

ABSTRACT

Segmented telescopes enable large-aperture space telescopes for the direct imaging and spectroscopy of habitable worlds. However, the increased complexity of their aperture geometry, due to their central obstruction, support structures, and segment gaps, makes high-contrast imaging very challenging.
In this context, we present an analytical model that will enable to establish a comprehensive error budget to evaluate the constraints on the segments and the influence of the error terms on the final image and contrast. Indeed, the target contrast of 10^{10} to image Earth-like planets requires drastic conditions, both in term of segment alignment and telescope stability. Despite space telescopes evolving in a more friendly environment than ground-based telescopes, remaining vibrations and resonant modes on the segments can still deteriorate the contrast.
In this communication, we develop and validate the analytical model, and compare its outputs to images issued from end-to-end simulations.

Keywords: Segmented telescope, cophasing, exoplanet, high-contrast imaging, error budget

1. INTRODUCTION

The next generation of space telescopes for direct imaging and spectroscopy of exoplanets includes telescopes with a monolithic mirror, such as the Wide Field Infrared Survey Telescope (WFIRST)[1] and studies for telescopes with segmented primary mirrors, such as the Large Ultra-Violet Optical Infrared (LUVOIR) telescope[2,3] or the Habitable Exoplanet Imaging Mission (HabEx).[4] Even current and future ground-based telescopes have segmented apertures, such as the Keck telescopes[5,6] or the coming Extremely Large Telescopes (ELTs).[7–10] Unfortunately, the increased complexity of their aperture geometry, due to their central obstruction, support structures, and segment gaps, makes high-contrast imaging very challenging.
Indeed, to observe a habitable world, two constraints have to be respected. First, in a planetary system with a probable Earth-like planet, the ratio between the star photon flux and the planet photon flux, which is called the contrast, is higher than 10^{10}. Secondly, the angular separation between the star and the planet is smaller than 0.1 arcsec. Therefore, the region of interest is restricted to a so-called dark hole, a region centered on the star with a very high star-to-planet contrast. These two goals, the contrast and the angular separation, are extremely challenging to achieve, mainly in a segmented pupil configuration, which generates huge diffraction effects.
This performance is still far from being reached, since the best contrast achieved in laboratories corresponds to a few 10^9, obtained on the High-Contrast Imaging Testbed (HCIT) with a circular aperture.[11] A contrast of a few 10^8 was also reached on the Très Haute Dynamique (THD) bench below 0.5 arcsec,[12,13] which would allow

Further author information, send correspondence to Lucie Leboulleux: E-mail: leboulleux@stsci.edu, Telephone: 1 410 338 2881

the detection of young exo-Jupiters. But since this performance is reached on a clear aperture, the desired 10^{10} is still far from being achieved, particularly with segmented apertures.
To get a sufficient contrast stability, the studies for the chosen optical systems need to be completed with an error budget. Since numerous factors can degrade the performance of the system and since the objective is extremely challenging, a comprehensive error budget is essential in order to make the right decisions early enough in the system design process. The most traditional method for tolerancing is based on multiple end-to-end propagation simulations of the system.[14] At each iteration, an aberration or a group of aberrations is applied to a segment or a group of segments and propagated through the simulated optical system. This method is extremely time-consuming and is both pupil- and system-dependant.
We propose an alternative method, faster and adaptable to all segmented pupils, such as the James Webb Space Telescope (JWST),[15,16] the ELTs,[7–10] the HabEx mission,[4] or the LUVOIR telescope.[2,3] This new method is based on an analytical model to directly express the focal plane image and its contrast as a function of the Zernike coefficients applied to the segments. This analytical model requires then to be inverted to obtain the upper constraints in cophasing and stability that need to be respected to achieve the desired contrast. In this paper, we focus only on the development of the analytical model and on its validation, the inversion of the model and its application to tolerancing being the studies of future work.
In Section 2, we introduce this analytical model, which is based on a perfect coronagraph to model high-contrast performance and a segment-based model of the pupil. In Section 3, we apply this model to a LUVOIR-like pupil. In particular, its outputs are compared to images issued from an end-to-end simulation, where the LUVOIR-like pupil is combined first with a perfect coronagraph, then with an Apodized Lyot Coronagraph (APLC) that enables a 10^{10} contrast in a circular dark hole from $4\lambda/D$ to $10\lambda/D$.

2. ANALYTICAL MODEL

This section aims at introducing and developing the formalism needed for the analytical model.

2.1 Pupil model

To make the variable use easier, we define $\vec{r}$ the position vector in the pupil plane and $\vec{u}$ the one in the detector plane (focal plane). The upstream pupil of the system is called P and is made of identical segments of generic shape S. The pupil is defined as follow:

$$P(\vec{r}) = \sum_{k=1}^{n_{seg}} S(\vec{r} - \vec{r_k}) \tag{1}$$

where, as shown in Fig. 1, $\vec{r_k}$ stands for the position vector pointing from the center of the central obstruction to the center of the segment number k. n_{seg} corresponds to the number of segments ($n_{seg} = 36$ for this LUVOIR-like pupil).

2.2 Phase aberration model

The phase aberration, called ϕ, can be expressed as the sum of a global phase aberration and local phase aberrations on the different segments:

$$\phi(\vec{r}) = \sum_{l=0}^{n_{zer}} a_l Z_{g,l}(\vec{r}) + \sum_{(k,l)=(1,0)}^{(n_{seg},n_{zer})} a_{k,l} S(\vec{r} - \vec{r_k}) \times Z_l(\vec{r} - \vec{r_k}) \tag{2}$$

where $(Z_{g,l})_{l\in[0,n_{zer}]}$ corresponds to the Zernike basis on the entire pupil and $(Z_l)_{l\in[0,n_{zer}]}$ corresponds to the Zernike basis on one segment.
Thanks to the telescope alignment and a first cophasing of the primary mirror, the main global and local aberrations can be removed, so only residual aberrations are left. Furthermore, by segmenting the residual global aberrations on the pupil, they can be seen as local aberrations. Therefore, for the rest of this communication, only residual local aberrations are considered:

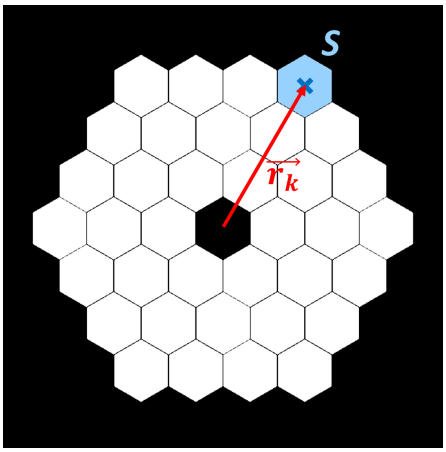

Figure 1. Definitions of the vectors $\vec{r_k}$ and of the shape of a generic segment S on a segmented pupil. In red, we can see the vector $\vec{r_{36}}$, from the center of the pupil to the 36th segment.

$$\phi(\vec{r}) = \sum_{(k,l)=(1,0)}^{(n_{seg},n_{zer})} a_{k,l} S(\vec{r} - \vec{r_k}) \times Z_l(\vec{r} - \vec{r_k}) \tag{3}$$

2.3 Imaging model

In case of phase aberration only, the electric field in the pupil plane can be expressed as:

$$E(\vec{r}) = P(\vec{r}) \times e^{i\phi(\vec{r})} \tag{4}$$

Since the aberrations are small, we get:

$$E(\vec{r}) = P(\vec{r}) \times (1 + i\phi(\vec{r})) \tag{5}$$

In the hypothesis of a perfect coronagraph, which is not realistic when the performance is limited by the coronagraph design, the amplitude of the electric field generated by the star can be removed,[17–19] which corresponds to the constant term 1 in the previous formula. Then, in the final detector plane, the amplitude of the electric field becomes:

$$E_f(\vec{u}) = i\widehat{P\phi}(\vec{u}) \tag{6}$$

where $\hat{f}$ is the Fourier Transform of the function f.

2.4 Imaging with phase aberration

By combining the equations 3 and 6, we obtain:

$$\begin{aligned} E_f(\vec{u}) &= i \sum_{(k,l)=(1,0)}^{(n_{seg},n_{zer})} a_{k,l} \widehat{(SZ_l)(\vec{r} - \vec{r_k})} \\ &= i \sum_{(k,l)=(1,0)}^{(n_{seg},n_{zer})} a_{k,l} \widehat{(SZ_l)}(\vec{u}) e^{-i\vec{r_k}.\vec{u}} \\ &= i \sum_{l=0}^{n_{zer}} \widehat{(SZ_l)}(\vec{u}) \sum_{k=1}^{n_{seg}} a_{k,l} e^{-i\vec{r_k}.\vec{u}} \end{aligned} \tag{7}$$

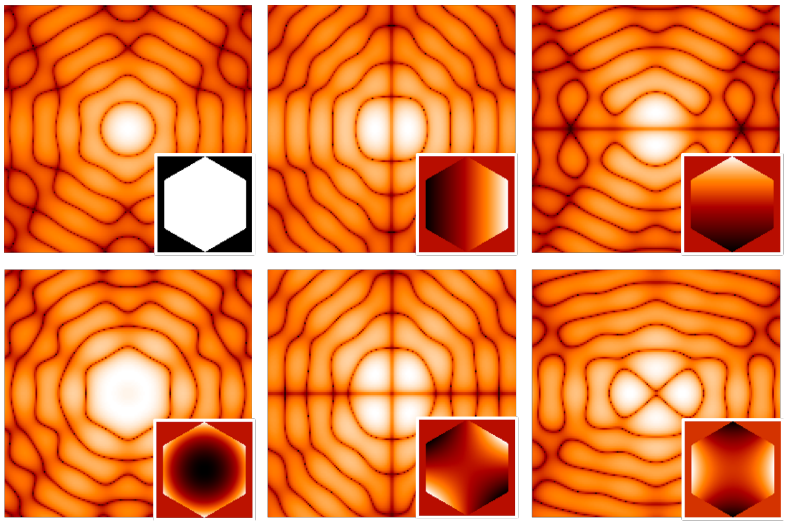

Figure 2. Envelopes corresponding to the first Zernikes. Top left: piston, top center: tip, top right: tilt, bottom left: focus, bottom center: 45° astigmatism, bottom right: 0° astigmatism. These envelopes will be multiplied to interference fringes between all the pairs of segments of the pupil.

Because $\widehat{(SZ_l)}(\vec{u})$ does not depend on k.

As we can see in this equation, every Zernike polynomial, Z_l, present on a segment acts on the final image plane as an envelope only, which does not depend on the segment positioning at all. Fig. 2 illustrates the envelopes for the first Zernikes.
The segments only indirectly act on the global coefficient of this envelope, $i\sum_{k=1}^{n_{seg}} a_{k,l}e^{-i\vec{r_k}.\vec{u}}$, which is influenced by the positions of the segments $\vec{r_k}$ and the local Zernike coefficients $a_{k,l}$.

2.5 Case of one single Zernike on the segments

In this case, only one Z_l is applied on the segments, even if they can still have different coefficients. The electric field in the image plane can then be expressed as:

$$E_f(\vec{u}) = i\widehat{SZ_l}(\vec{u}) \sum_{k=1}^{n_{seg}} a_{k,l}e^{-i\vec{r_k}.\vec{u}} \tag{8}$$

The intensity becomes:

$$\begin{aligned} I(\vec{u}) &= (i\widehat{SZ_l}(\vec{u}) \sum_{k=1}^{n_{seg}} a_{k,l}\exp(-i\vec{r_k}.\vec{u})) \times (-i\widehat{SZ_l}^*(\vec{u}) \sum_{k=1}^{n_{seg}} a_{k,l}\exp(i\vec{r_k}.\vec{u})) \\ &= \left\|\widehat{SZ_l}(\vec{u})\right\|^2 \sum_{k_1=1}^{n_{seg}}\sum_{k_2=1}^{n_{seg}} a_{k_1,l}a_{k_2,l}e^{i(\vec{r_{k_2}}-\vec{r_{k_1}}).\vec{u}} \end{aligned} \tag{9}$$

Since the intensity is real, $\sum_{k_1=1}^{n_{seg}}\sum_{k_2=1}^{n_{seg}} a_{k_1,l}a_{k_2,l}e^{i(\vec{r_{k_2}}-\vec{r_{k_1}}).\vec{u}}$ is real, and therefore:

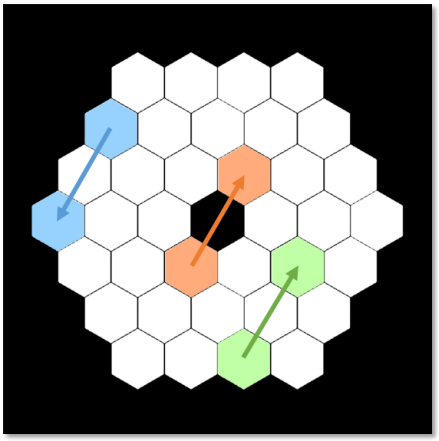

Figure 3. Illustration of some redundant oriented pairs that correspond to one single non-redundant pair. 42 oriented pairs generate exactly the same interference fringes than the pair $\vec{r_{16}} - \vec{r_{28}}$ (blue), for example the pairs $\vec{r_{25}} - \vec{r_{12}}$ (orange) and $\vec{r_{14}} - \vec{r_{3}}$ (green). Since these 42 pairs have the same effect in the detector plane, they can all be replaced by one single pair, called the non-redundant pair.

$$\begin{aligned} I(\vec{u}) &= \left\|\widehat{SZ_l}(\vec{u})\right\|^2 \times \Big(\sum_{k=1}^{n_{seg}} a_{k,l}^2 + \Re\Big(\sum_{k_1=1}^{n_{seg}} \sum_{k_2=1, k_2\neq k_1}^{n_{seg}} a_{k_1,l} a_{k_2,l} e^{i(\vec{r_{k_2}} - \vec{r_{k_1}}).\vec{u})} \\ &= \left\|\widehat{SZ_l}(\vec{u})\right\|^2 \times \Big(\sum_{k=1}^{n_{seg}} a_{k,l}^2 + \sum_{k_1=1}^{n_{seg}} \sum_{k_2=1, k_2\neq k_1}^{n_{seg}} a_{k_1,l} a_{k_2,l} \cos((\vec{r_{k_2}} - \vec{r_{k_1}}).\vec{u})\Big) \end{aligned} \tag{10}$$

It appears here that studying the effect of random values of the same Zernike on all the segments is equivalent to studying the interference effects on each pair of segments and summing them.
n_{NRP} represents the number of non-redundant segment pairs and $(\vec{b_q})_{q\in[1,n_{NRP}]}$ the basis of non-redundant segment pairs. In the case of the LUVOIR-like pupil, which contains 36 segments, there are 1260 possible oriented pairs of segments (obtained with the binomial coefficient $2 \times C_{36}^2$), but $n_{NRP} = 63$. In the case of JWST, there are 306 pairs of segments in total, but only 30 non-redundant pairs of segments. The Fig. 3 illustrates the redundancy of some pairs of segments.

Then we can write:

$$I(\vec{u}) = \left\|\widehat{SZ_l}(\vec{u})\right\|^2 \times \Big(\sum_{k=1}^{n_{seg}} a_{k,l}^2 + 2\sum_{q=1}^{n_{NRP}} A_q \cos(\vec{b_q}.\vec{u})\Big) \tag{11}$$

where, for $q \in [1, n_{NRP}]$, $A_q = \sum_{(k_1,k_2)} a_{k_1,l} a_{k_2,l}$ and the couples (k_1, k_2) are all the couples that verify the relation $\vec{r_{k_2}} - \vec{r_{k_1}} = \pm\vec{b_q}$.
We can conclude that it is possible to obtain a relation between the final image, a certain baseline, and the Zernike coefficients applied on each segment of the baseline.

3. APPLICATION TO THE LUVOIR GEOMETRY

In this section, we apply the analytical model previously developed to the LUVOIR-like pupil and compare the results given by the model to an end-to-end simulation designed to respect the high-contrast conditions.

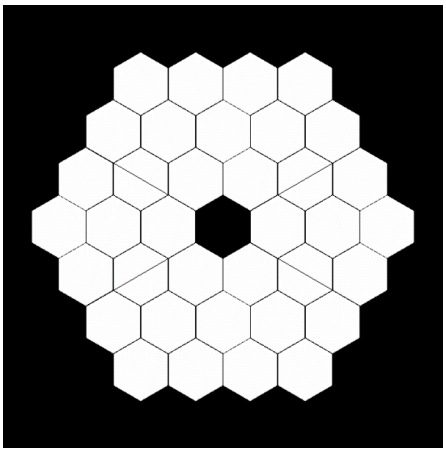

Figure 4. Pupil of a LUVOIR-like telescope, chosen for this study. It is made of 36 segments, a hexagonal central obstruction, and spiders.

3.1 Choice of pupil and end-to-end simulation

The LUVOIR-like pupil chosen for this study is formed of 36 identical hexagonal segments and a hexagonal central obstruction (see Fig. 4).[20,21]
In the following sections, we compare the outputs of the analytical model, exactly computed from the formula 13, and the outputs of the end-to-end simulation using the LUVOIR-like pupil. Two coronagraphs are used in the end-to-end simulation: a perfect coronagraph that fully removes the starlight,[17–19] and a realistic coronagraph, an APLC,[22–24] specially designed for the LUVOIR-like pupil to obtain a contrast higher than 10^{10} in the dark region, ie. between $4\lambda/D$ and $10\lambda/D$.
The APLC is a system of an Apodizer, located in a pupil plane, a Focal Plane Mask (FPM), in a focal plane, and a Lyot Stop, in a pupil plane (see Fig. 5). This configuration and the design of these different components enable to obtain an extremely high contrast in the dark hole, needed to image Earth-like planets (see Fig. 6). Since this area corresponds to the conditions of the theoretical model, we look at the images and performance in this area only and compare them to the outputs of the model. In our case, the interest region corresponds to a circular zone between $4\lambda/D$ and $10\lambda/D$.
Here we can derive the first difference between the results from the model and from the end-to-end simulation with an APLC: the contrast with no aberration in the first case is the absolute zero, and around 10^{10} in the second case. On the opposite, the end-to-end simulation with a perfect coronagraph also gives absolute zero.

3.2 Comparison between analytical model and end-to-end simulation for piston aberrations on the segments

Since the analytical model is based on the same theory than the perfect coronagraph with removal of the starlight (eq.5 to 6), we first compare the output from the end-to-end simulation with a perfect coronagraph and the output from the analytical model.
Two cases are compared here: case where two segments only are not well-phased, which should generate clear interference fringes and case where three segments are not well-phased. These configurations have been chosen since they generate clear patterns in the dark hole. The results are shown in the top two rows of Fig. 7. Obviously, there is a strong similarity between the PSF resulting from the end-to-end simulation and the one resulting from the analytical model. The rms values of these images are indicated in table 1 and confirm such a similitude between the two images. In Fig. 7, on the right, the cross sections of the two PSF on their 33rd rows are also plotted: they are similar to each other.

Now that the perfect coronagraph case has been verified, the analytical model is compared to a realistic coronagraph, the APLC described before. Like in the perfect coronagraph case, we begin with the two-segment

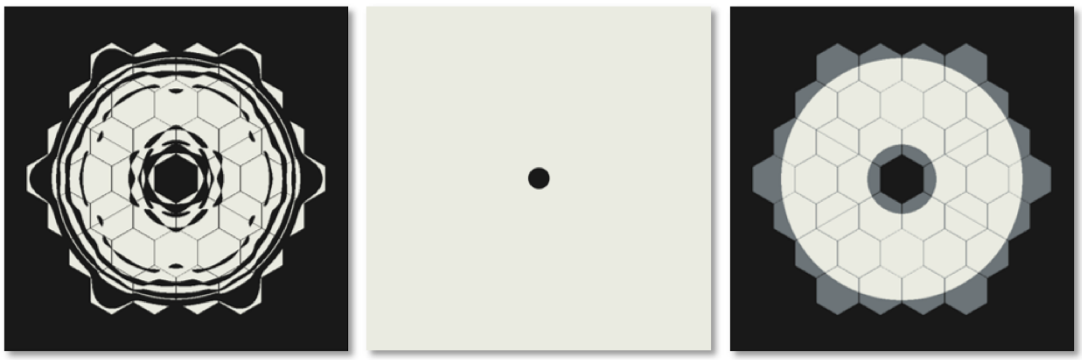

Figure 5. Optical masks used in the end-to-end simulation. The apodizer (left) is located in the first pupil plane, the focal plane mask (center) on the following focal plane, and the Lyot Stop (circular aperture on the right, here superposed with the entrance pupil) on the last pupil plane. Together, these three components form a so-called Apodized Lyot Coronagraph (APLC).

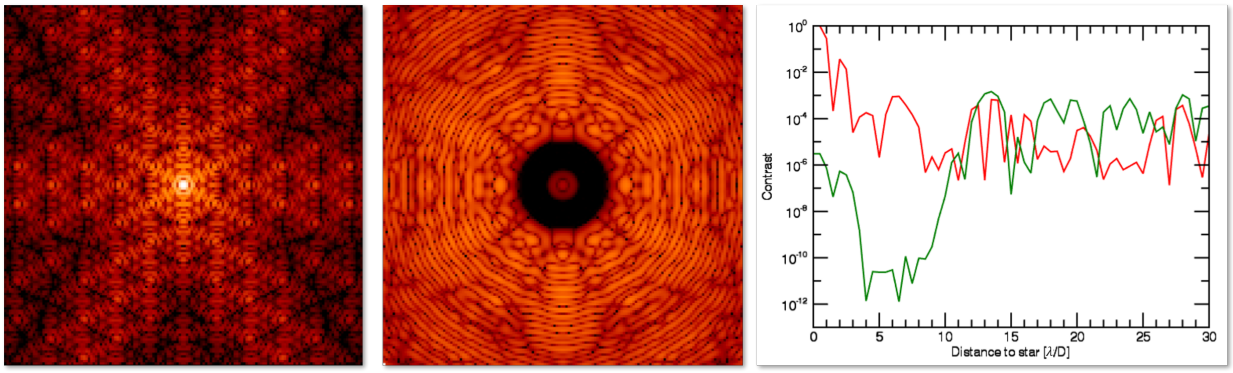

Figure 6. Left: PSF in presence of the LUVOIR-like pupil. Center: Same PSF, but in presence of the APLC. Right: Cut along a radius of the two previous PSF (red: without APLC, green: with APLC). We can observe that the APLC brings a huge correction in the interest region, ie. between $4\lambda/D$ and $10\lambda/D$.

Configuration	Method	RMS
Configuration 1	End-to-end simulation with perfect coronagraph	9.69×10^{-6}
	Analytical model	9.67×10^{-6}
Configuration 2	End-to-end simulation with perfect coronagraph	1.13×10^{-5}
	Analytical model	1.12×10^{-5}
Configuration 3	End-to-end simulation with APLC	3.24×10^{-6}
	Analytical model	4.12×10^{-6}
Configuration 4	End-to-end simulation with APLC	8.02×10^{-6}
	Analytical model	8.90×10^{-6}

Table 1. RMS values of the outputs from the end-to-end simulations and from the analytical model for four different configurations. Configuration 1 refers to the first lines of Fig. 7, Configuration 2 to the second line, Configuration 3 to the third line and Configuration 4 to the bottom line. Thanks to the normalisation, the outputs from both methods, in each configuration, have the same extrema.

and three-segment configurations. The results are illustrated in Fig. 7 and numerical values are given in table 1. Once again, we can see a very close similitude between the PSF issued from the analytical model, and the ones issued from the end-to-end simulation.

A phase is now generated with random piston aberrations from 0 to 15nm on the segments and propagated through two end-to-end simulations: one using the perfect coronagraph, one using the APLC. The same phase is applied in the analytical model. The phase and PSF are illustrated in Fig. 8. Once again, the images present the same patterns, even if the similitude is better between the analytical model and the propagation through a perfect coronagraph than between the analytical model and the propagation through the APLC.

A traditional error budget aims to quantify the deterioration of the contrast with the rms piston phase applied on the segments. To illustrate this effect, Fig. 9 indicates on the left the radial contrast as a function of the angular separation, in the dark hole only, for different rms piston values applied on the segments. These curves were only obtained using the analytical model and require further studies to be adjusted. We can recognize the characteristic shape of the piston envelope, which was shown in Fig. 2. The grey zone below 10^{10} is due to the limitation of a realistic coronagraph, which is not taken into account in the analytical model. The second plot in Fig. 9, also issued from the analytical model only, indicates the mean contrast in the dark region as a function of the rms piston values applied on the segments. This plot, once well-normalized, will quantify the actual constraints on piston cophasing of the segments, even if the formalism inversion mentioned in the introduction should give a faster and more accurate result, non-redundant-bases- and segment-dependant.

The application of the analytical model to piston aberrations on segments has been validated. In the next section, we generalize the application to other Zernikes.

3.3 Comparison between analytical model and end-to-end simulation for other aberrations

In this section, we compare the PSF and their cross-section at the 33rd row issued from the analytical model and the end-to-end simulation with an APLC, when tip, focus, and 0-astigmatism are applied on segments. The aberrations are only applied on one pair of segments, since the patterns are then really well-defined in the dark region.
Fig. 10 illustrates the results from this study. The envelopes are visible in Fig. 2, even if the scale does not match that of the PSF (150 pixels vs 40 pixels). In the tip case, the envelope creates a dark vertical line crossing the center of the PSF, which also appears in the PSF or the cross-sections at the top of Fig. 10. In the focus case, the envelope has a ring shape, which is also visible in the two PSF in the middle of Fig. 10. Finally, in the 0-astigmatism, the envelope has a bow-tie shape, which becomes a cross after being cut by the dark hole. This effect also clearly appears in the image issued from the end-to-end simulation.
These preliminary images show that the analytical model is still reliable when it comes to other Zernikes. The next step is a generalization of the model to a combination of Zernikes, to avoid studying them separately.

4. CONCLUSIONS

This paper aims at introducing an analytical model that is the basis of a new method for error budgets, both in static and dynamic modes. The formalism has been validated, using comparisons with both a perfect coronagraph and a realistic coronagraph. Its only limitation for now is the coronagraph: the analytical model takes into account a simplified model for the coronagraph, so adapting this formalism to a realistic coronagraph will probably add a calibration step in the process. For example, we know that the apodisation of the APLC does have an effect on the amplitudes of the interference fringes.
The next step of this study is a generalization of this analytical model to a combination of Zernikes. Then, the formula will be reversed to obtain this time the Zernike coefficients as a function of the desired contrast. This inversion method is based on the hypothesis that all the non-redundant baselines equally contribute to the final contrast deterioration. This process will enable a fast and complete error budget for any segmented pupil.
The static or quasi-static errors on the segments are not the only issue in high-contrast imaging. The telescope

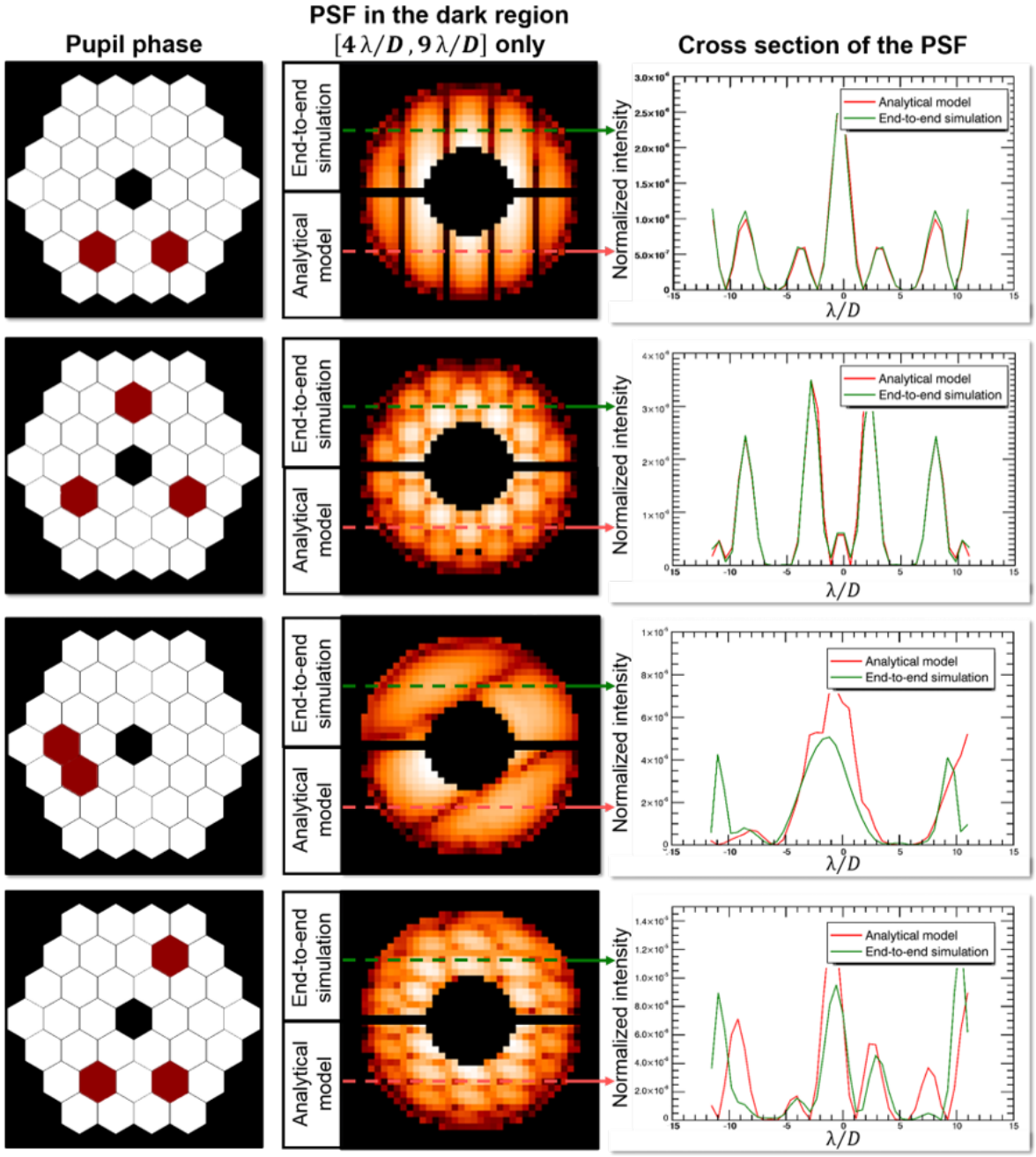

Figure 7. Results when identical piston values are applied on some segments of the pupil. Top two rows: comparison between the output from the end-to-end simulation with a perfect coronagraph and the output from the analytical model. Bottom two rows: comparison between the output from the end-to-end simulation with a realistic coronagraph (Apodized Lyot Coronagraph) and the output from the analytical model. On each row, left: phase applied on the pupil, where the white segments have no piston and the red segments have a 15nm piston applied on them. Center: Comparison of the PSF resulting from the end-to-end simulation and from the analytical model in the dark hole only. A central symmetry should be observed. Because of a small issue that has not been fixed yet, the amplitude of the analytical model output has been adjusted so its maximum fits the maximum of the end-to-end simulation PSF. Right: Cross section at the 33rd line of the end-to-end simulation and analytical model outputs.

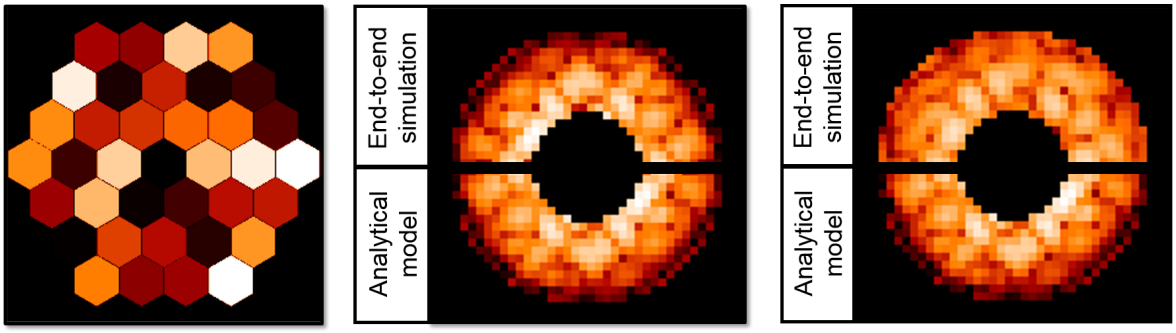

Figure 8. Results with the same random piston phase applied on the segmented pupil. Left: Phase applied on the segments. The piston coefficients are in the 0nm to 15nm range. Center: Combination of the PSF resulting from the end-to-end simulation in the perfect coronagraph case (top) and from the analytical model case (bottom). Right: Combination of the PSF resulting from the end-to-end simulation in the APLC case (top) and from the analytical model case (bottom). Once again, the amplitude of the analytical model output has been adjusted so its maximum fits the maximum of the end-to-end simulation PSF. A central symmetry should be observed.

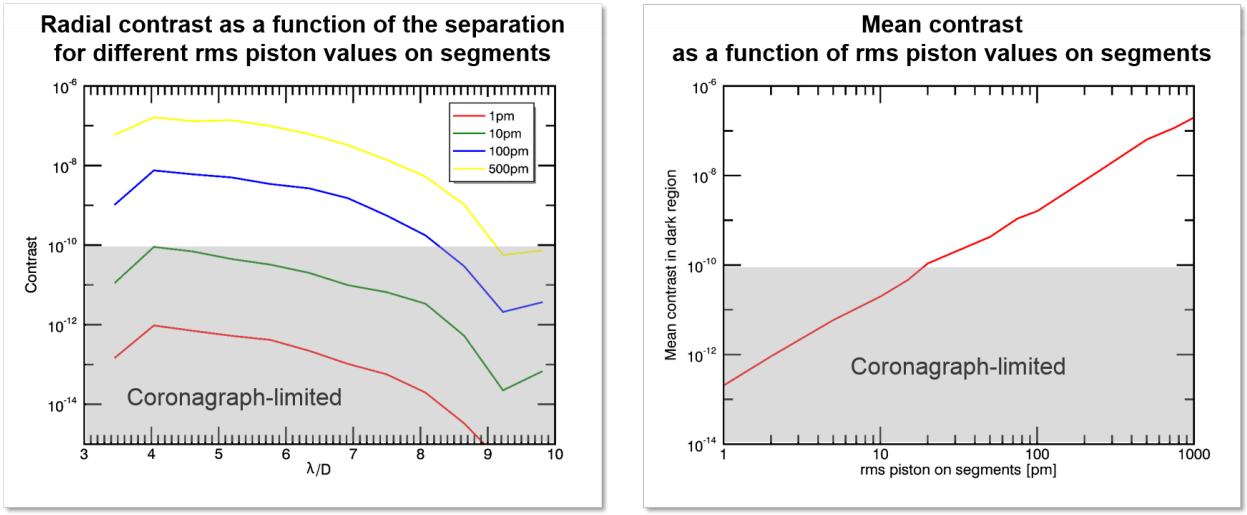

Figure 9. Results from the analytical model only. Left: Radial contrast as a function of the angular separation for different rms piston values applied on the segments. Right: Mean contrast in the dark region as a function of the rms piston values on the segments. In these two graphs, the grey zone corresponds to the performance limited by the coronagraph. Since the analytical model is based on a perfect coronagraph, it gives an absolute zero with no aberration, which is not realistic. The grey zone indicates where this artefact of the model appears.

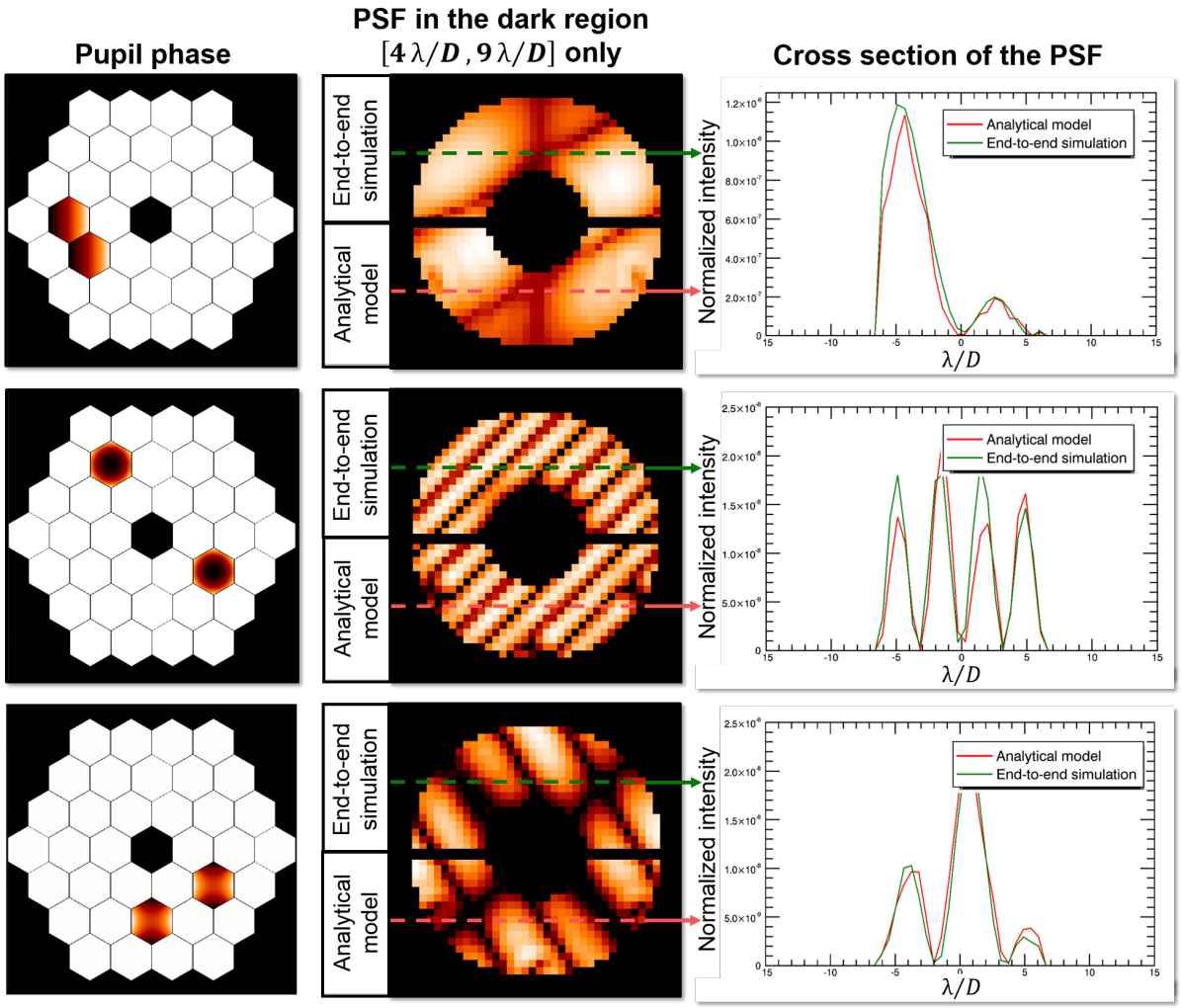

Figure 10. comparison between the output from the end-to-end simulation with an APLC and the output from the analytical model when identical Zernike coefficients are applied on one pair of segments. Top row: comparison when a tip is applied on two segments. Center row: comparison when a focus is applied on two segments. Bottom row: comparison when a 0-astigmatism is applied on two segments. On each row, left: phase applied on the pupil, where the white segments have no aberration. Center column: Comparison of the PSF resulting from the end-to-end simulation and from the analytical model in the dark hole only. A central symmetry should be observed. Because of a small issue that has not been fixed yet, the amplitude of the analytical model output has been adjusted so its maximum fits the maximum of the end-to-end simulation PSF. Right: Cross section at the 33rd line of the end-to-end simulation and analytical model outputs.

vibrations or the resonant modes of the segments also generate instability issues, which are important factors in the limitation of the performance. This formalism needs then to be applied on the dynamic case, where only the Zernike coefficients are time-dependant.
Such a new formalism to describe segmented pupils and generate images is very fast to compute. It is also adaptable to any segmented pupils, such as the Extremely Large Telescopes, the Thirty Meters Telescopes, the James Webb Space Telescope or the new HabEx and LUVOIR pupils. It can even been applied to non-hexagonal-segment pupils, such as the Giant Magellan Telescope. Such an analytical model enables a new, fast, and efficient method in static error budget and stability analysis for all segmented telescopes.

ACKNOWLEDGMENTS

This work is supported in part by the National Aeronautics and Space Administration under Grants NNX12AG05G and NNX14AD33G issued through the Astrophysics Research and Analysis (APRA) program (PI: R. Soummer) and by Jet Propulsion Laboratory subcontract No.1539872 (Segmented-Aperture Coronagraph Design and Analysis; PI: R. Soummer).
It is also partly funded by the French Aerospace Lab (ONERA) in the frame of the VASCO Research Project and by the Laboratoire d'Astrophysique de Marseille (LAM).

REFERENCES

1. D. Spergel, N. Gehrels, C. Baltay, D. Bennett, J. Breckinridge, M. Donahue, A. Dressler, B. S. Gaudi, T. Greene, O. Guyon, C. Hirata, J. Kalirai, N. J. Kasdin, B. Macintosh, W. Moos, S. Perlmutter, M. Postman, B. Rauscher, J. Rhodes, Y. Wang, D. Weinberg, D. Benford, M. Hudson, W.-S. Jeong, Y. Mellier, W. Traub, T. Yamada, P. Capak, J. Colbert, D. Masters, M. Penny, D. Savransky, D. Stern, N. Zimmerman, R. Barry, L. Bartusek, K. Carpenter, E. Cheng, D. Content, F. Dekens, R. Demers, K. Grady, C. Jackson, G. Kuan, J. Kruk, M. Melton, B. Nemati, B. Parvin, I. Poberezhskiy, C. Peddie, J. Ruffa, J. K. Wallace, A. Whipple, E. Wollack, and F. Zhao, "Wide-Field InfrarRed Survey Telescope-Astrophysics Focused Telescope Assets WFIRST-AFTA 2015 Report," *ArXiv e-prints* , Mar. 2015.
2. J. Dalcanton, S. Seager, S. Aigrain, S. Battel, N. Brandt, C. Conroy, L. Feinberg, S. Gezari, O. Guyon, W. Harris, C. Hirata, J. Mather, M. Postman, D. Redding, D. Schiminovich, H. P. Stahl, and J. Tumlinson, "From Cosmic Birth to Living Earths: The Future of UVOIR Space Astronomy," *ArXiv e-prints* , July 2015.
3. L. Pueyo, "The LUVOIR coronagraph instrument: definition and design," in *UV/Optical/IR Space Telescopes and Instruments: Innovative Technologies and Concepts VIII*, *SPIE paper 10398-15 in these proceedings*, 2017.
4. B. Mennesson, S. Gaudi, S. Seager, K. Cahoy, S. Domagal-Goldman, L. Feinberg, O. Guyon, J. Kasdin, C. Marois, D. Mawet, M. Tamura, D. Mouillet, T. Prusti, A. Quirrenbach, T. Robinson, L. Rogers, P. Scowen, R. Somerville, K. Stapelfeldt, D. Stern, M. Still, M. Turnbull, J. Booth, A. Kiessling, G. Kuan, and K. Warfield, "The Habitable Exoplanet (HabEx) Imaging Mission: preliminary science drivers and technical requirements," in *Space Telescopes and Instrumentation 2016: Optical, Infrared, and Millimeter Wave*, *Presented at the Society of Photo-Optical Instrumentation Engineers (SPIE) Conference* **9904**, p. 99040L, July 2016.
5. S. M. Adkins, I. S. McLean, M. P. Fitzgerald, J. E. Larkin, H. A. Lewis, C. Martin, D. Mawet, J. X. Prochaska, and P. Wizinowich, "New developments in instrumentation at the W. M. Keck Observatory," in *Ground-based and Airborne Instrumentation for Astronomy VI*, *Presented at the Society of Photo-Optical Instrumentation Engineers (SPIE) Conference* **9908**, p. 990805, Aug. 2016.
6. M. M. Colavita, P. L. Wizinowich, R. L. Akeson, S. Ragland, J. M. Woillez, R. Millan-Gabet, E. Serabyn, M. Abajian, D. S. Acton, E. Appleby, J. W. Beletic, C. A. Beichman, J. Bell, B. C. Berkey, J. Berlin, A. F. Boden, A. J. Booth, R. Boutell, F. H. Chaffee, D. Chan, J. Chin, J. Chock, R. Cohen, A. Cooper, S. L. Crawford, M. J. Creech-Eakman, W. Dahl, G. Eychaner, J. L. Fanson, C. Felizardo, J. I. Garcia-Gathright, J. T. Gathright, G. Hardy, H. Henderson, J. S. Herstein, M. Hess, E. E. Hovland, M. A. Hrynevych, E. Johansson, R. L. Johnson, J. Kelley, R. Kendrick, C. D. Koresko, P. Kurpis, D. Le Mignant, H. A. Lewis, E. R. Ligon, W. Lupton, D. McBride, D. W. Medeiros, B. P. Mennesson, J. D. Moore, D. Morrison,

C. Nance, C. Neyman, A. Niessner, C. G. Paine, D. L. Palmer, T. Panteleeva, M. Papin, B. Parvin, L. Reder, A. Rudeen, T. Saloga, A. Sargent, M. Shao, B. Smith, R. F. Smythe, P. Stomski, K. R. Summers, M. R. Swain, P. Swanson, R. Thompson, K. Tsubota, A. Tumminello, C. Tyau, G. T. van Belle, G. Vasisht, J. Vause, F. Vescelus, J. Walker, J. K. Wallace, U. Wehmeier, and E. Wetherell, "The Keck Interferometer," *Publications of the Astronomical Society of the Pacific* **125**, p. 1226, Oct. 2013.

7. B. Macintosh, M. Troy, R. Doyon, J. Graham, K. Baker, B. Bauman, C. Marois, D. Palmer, D. Phillion, L. Poyneer, I. Crossfield, P. Dumont, B. M. Levine, M. Shao, G. Serabyn, C. Shelton, G. Vasisht, J. K. Wallace, J.-F. Lavigne, P. Valee, N. Rowlands, K. Tam, and D. Hackett, "Extreme adaptive optics for the Thirty Meter Telescope," in *Society of Photo-Optical Instrumentation Engineers (SPIE) Conference Series*, *Presented at the Society of Photo-Optical Instrumentation Engineers (SPIE) Conference* **6272**, p. 62720N, June 2006.
8. M. E. Kasper, J.-L. Beuzit, C. Verinaud, N. Yaitskova, P. Baudoz, A. Boccaletti, R. G. Gratton, N. Hubin, F. Kerber, R. Roelfsema, H. M. Schmid, N. A. Thatte, K. Dohlen, M. Feldt, L. Venema, and S. Wolf, "EPICS: the exoplanet imager for the E-ELT," in *Adaptive Optics Systems*, *Presented at the Society of Photo-Optical Instrumentation Engineers (SPIE) Conference* **7015**, p. 70151S, July 2008.
9. R. Davies, N. Ageorges, L. Barl, L. R. Bedin, R. Bender, P. Bernardi, F. Chapron, Y. Clenet, A. Deep, E. Deul, M. Drost, F. Eisenhauer, R. Falomo, G. Fiorentino, N. M. Förster Schreiber, E. Gendron, R. Genzel, D. Gratadour, L. Greggio, F. Grupp, E. Held, T. Herbst, H.-J. Hess, Z. Hubert, K. Jahnke, K. Kuijken, D. Lutz, D. Magrin, B. Muschielok, R. Navarro, E. Noyola, T. Paumard, G. Piotto, R. Ragazzoni, A. Renzini, G. Rousset, H.-W. Rix, R. Saglia, L. Tacconi, M. Thiel, E. Tolstoy, S. Trippe, N. Tromp, E. A. Valentijn, G. Verdoes Kleijn, and M. Wegner, "MICADO: the E-ELT adaptive optics imaging camera," in *Ground-based and Airborne Instrumentation for Astronomy III*, *Presented at the Society of Photo-Optical Instrumentation Engineers (SPIE) Conference* **7735**, p. 77352A, July 2010.
10. S. P. Quanz, I. Crossfield, M. R. Meyer, E. Schmalzl, and J. Held, "Direct detection of exoplanets in the 3-10 μm range with E-ELT/METIS," *International Journal of Astrobiology* **14**, pp. 279–289, Apr. 2015.
11. J. T. Trauger and W. A. Traub, "A laboratory demonstration of the capability to image an Earth-like extrasolar planet," *Nature* **446**, pp. 771–773, Apr. 2007.
12. P. Baudoz, J. Mazoyer, M. Mas, R. Galicher, and G. Rousset, "Dark hole and planet detection: laboratory results using the self-coherent camera," in *Ground-based and Airborne Instrumentation for Astronomy IV*, *Presented at the Society of Photo-Optical Instrumentation Engineers (SPIE) Conference* **8446**, p. 84468C, Sept. 2012.
13. J. Mazoyer, P. Baudoz, R. Galicher, and G. Rousset, "High-contrast imaging in polychromatic light with the self-coherent camera," *Astronomy & Astrophysics* **564**, p. L1, Apr. 2014.
14. M. T. Stahl, "Effects of space telescope primary mirror segment errors on coronagraph instrument performance," in *UV/Optical/IR Space Telescopes and Instruments: Innovative Technologies and Concepts VIII*, *SPIE paper 10398-16 in these proceedings*, 2017.
15. M. A. Greenhouse, "The JWST science instrument payload: mission context and status," in *Space Telescopes and Instrumentation 2016: Optical, Infrared, and Millimeter Wave*, *Presented at the Society of Photo-Optical Instrumentation Engineers (SPIE) Conference* **9904**, p. 990406, July 2016.
16. M. Clampin, "Status of the James Webb Space Telescope (JWST)," in *SPIE*, **7010**, Aug. 2008.
17. F. Malbet, J. W. Yu, and M. Shao, "High-Dynamic-Range Imaging Using a Deformable Mirror for Space Coronography," *Publications of the Astronomical Society of the Pacific* **107**, p. 386, Apr. 1995.
18. A. Quirrenbach, "Coronographic Methods for the Detection of Terrestrial Planets," *ArXiv Astrophysics e-prints* , Feb. 2005.
19. C. Cavarroc, A. Boccaletti, P. Baudoz, T. Fusco, and D. Rouan, "Fundamental limitations on Earth-like planet detection with extremely large telescopes," *Astronomy & Astrophysics* **447**, pp. 397–403, Feb. 2006.
20. M. Postman, T. Brown, K. Sembach, M. Giavalisco, W. Traub, K. Stapelfeldt, D. Calzetti, W. Oegerle, R. Michael Rich, H. Phillip Stahl, J. Tumlinson, M. Mountain, R. Soummer, and T. Hyde, "Advanced Technology Large-Aperture Space Telescope: science drivers and technology developments," *Optical Engineering* **51**, pp. 011007–011007, Jan. 2012.

21. L. D. Feinberg, A. Jones, G. Mosier, N. Rioux, D. Redding, and M. Kienlen, "A cost-effective and serviceable ATLAST 9.2m telescope architecture," in *Space Telescopes and Instrumentation 2014: Optical, Infrared, and Millimeter Wave*, *Presented at the Society of Photo-Optical Instrumentation Engineers (SPIE) Conference* **9143**, p. 914316, Aug. 2014.
22. R. Soummer, C. Aime, and P. E. Falloon, "Stellar coronagraphy with prolate apodized circular apertures," *Astronomy & Astrophysics* **397**, pp. 1161–1172, Jan. 2003.
23. M. N'Diaye, L. Pueyo, and R. Soummer, "Apodized Pupil Lyot Coronagraphs for Arbitrary Apertures. IV. Reduced Inner Working Angle and Increased Robustness to Low-order Aberrations," *Astrophysical Journal* **799**, p. 225, Feb. 2015.
24. M. N'Diaye, R. Soummer, L. Pueyo, A. Carlotti, C. C. Stark, and M. D. Perrin, "Apodized Pupil Lyot Coronagraphs for Arbitrary Apertures. V. Hybrid Shaped Pupil Designs for Imaging Earth-like planets with Future Space Observatories," *Astrophysical Journal* **818**, p. 163, Feb. 2016.

References

Aime, C., Soummer, R., and Ferrari, A. (2002). Total coronagraphic extinction of rectangular apertures using linear prolate apodizations. *A&A*, 389, 334.

Akondi, V., Castillo, S., and Vohnsen, B. (2014). Multi-faceted digital pyramid wavefront sensor. *Optics Communications*, 323, 77.

Angel, J. R. P. (1994). Ground-based imaging of extrasolar planets using adaptive optics. *Nature*, 368, 203.

Arney, G. N., Crooke, J., Domagal-Goldman, S. D., Fischer, D., Peterson, B., Schmidt, B. E., and Stdt, T. L. T. (2017). The LUVOIR Decadal Mission Concept. *AGU Fall Meeting Abstracts*, .

Baglin, A. (2003). COROT: A minisat for pionnier science, asteroseismology and planets finding. *Advances in Space Research*, 31, 345.

Baranne, A., Queloz, D., Mayor, M., Adrianzyk, G., Knispel, G., Kohler, D., Lacroix, D., Meunier, J.-P., Rimbaud, G., and Vin, A. (1996). ELODIE: A spectrograph for accurate radial velocity measurements. *A&AS*, 119, 373.

Baron, F., Mocoeur, I., Cassaing, F., and Mugnier, L. M. (2008). Unambiguous phase retrieval as a cophasing sensor for phased array telescopes. *Journal of the Optical Society of America A*, 25, 1000.

Baudoz, P., Boccaletti, A., Baudrand, J., and Rouan, D. (2006). The Self-Coherent Camera: a new tool for planet detection. In Aime, C. and Vakili, F., editors, *IAU Colloq. 200: Direct Imaging of Exoplanets: Science Techniques*, pages 553–558.

Baudoz, P., Galicher, R., Patru, F., Dupuis, O., and Thijs, S. (2018). Status and performance of the THD2 bench in multi-deformable mirror configuration. *ArXiv e-prints*, .

Baudoz, P., Mazoyer, J., Mas, M., Galicher, R., and Rousset, G. (2012). Dark hole and planet detection: laboratory results using the self-coherent camera. In *Ground-based and Airborne Instrumentation for Astronomy IV*, volume 8446 of *Proc. SPIE*, page 84468C.

Baudoz, P., Rabbia, Y., Gay, J., Rossi, E., Petro, L., Casey, S. C., Bely, P. Y., Burg, R., MacKenty, J. W., Fleury, B., and Madec, P.-Y. (1998). First results with the Achromatic Interfero Coronograph. In Bonaccini, D. and Tyson, R. K., editors, *Adaptive Optical System Technologies*, volume 3353 of *Proc. SPIE*, pages 455–462.

Belikov, R., Give'on, A., Trauger, J. T., Carr, M., Kasdin, N. J., Vanderbei, R. J., Shi, F., Balasubramanian, K., and Kuhnert, A. (2006). Toward 10 ^{10} contrast for terrestrial exoplanet detection: demonstration of wavefront correction in a shaped-pupil coronagraph. In *Society of Photo-Optical Instrumentation Engineers (SPIE) Conference Series*, volume 6265 of *Proc. SPIE*, page 626518.

Beuzit, J.-L., Feldt, M., Dohlen, K., Mouillet, D., Puget, P., Wildi, F., Abe, L., Antichi, J., Baruffolo, A., Baudoz, P., Boccaletti, A., Carbillet, M., Charton, J., Claudi, R., Downing, M., Fabron, C., Feautrier, P., Fedrigo, E., Fusco, T., Gach, J.-L., Gratton, R., Henning, T., Hubin, N., Joos, F., Kasper, M., Langlois, M., Lenzen, R., Moutou, C., Pavlov, A., Petit, C., Pragt, J., Rabou, P., Rigal, F., Roelfsema, R., Rousset, G., Saisse, M., Schmid, H.-M., Stadler, E., Thalmann, C., Turatto, M., Udry, S., Vakili, F., and Waters, R. (2008). SPHERE: a 'Planet Finder' instrument for the VLT. In *Ground-based and Airborne Instrumentation for Astronomy II*, volume 7014 of *Proc. SPIE*, page 701418.

Bloemhof, E. E. and Wallace, J. K. (2003). Phase contrast techniques for wavefront sensing and calibration in adaptive optics. In Tyson, R. K. and Lloyd-Hart, M., editors, *Astronomical Adaptive Optics Systems and Applications*, volume 5169 of *Proc. SPIE*, pages 309–320.

Boccaletti, A., Lagage, P.-O., Baudoz, P., Beichman, C., Bouchet, P., Cavarroc, C., Dubreuil, D., Glasse, A., Glauser, A. M., Hines, D. C., Lajoie, C.-P., Lebreton, J., Perrin, M. D., Pueyo, L., Reess, J. M., Rieke, G. H., Ronayette, S., Rouan, D., Soummer, R., and Wright, G. S. (2015). The Mid-Infrared Instrument for the James Webb Space Telescope, V: Predicted Performance of the MIRI Coronagraphs. *PASP*, 127, 633.

Bond, I. A., Rattenbury, N. J., Skuljan, J., Abe, F., Dodd, R. J., Hearnshaw, J. B., Honda, M., Jugaku, J., Kilmartin, P. M., Marles, A., Masuda, K., Matsubara, Y., Muraki, Y., Nakamura, T., Nankivell, G., Noda, S., Noguchi, C., Ohnishi, K., Reid, M., Saito, T., Sato, H., Sekiguchi, M., Sullivan, D. J., Sumi, T., Takeuti, M., Watase, Y., Wilkinson, S., Yamada, R., Yanagisawa, T., and Yock, P. C. M. (2002). Study by MOA of extrasolar planets in gravitational microlensing events of high magnification. *MNRAS*, 333, 71.

Bordé, P. J. and Traub, W. A. (2006). High-Contrast Imaging from Space: Speckle Nulling in a Low-Aberration Regime. *ApJ*, 638, 488.

Born, M. and Wolf, E. (1999). *Principles of Optics: Electromagnetic Theory of Propagation, Interference and Diffraction of Light (7th Edition)*. Cambridge University Press, 7th edition.

Borucki, W. J. (2017). Kepler: A Brief Discussion of the Mission and Exoplanet Results. *Proceedings of the American Philosophical Society*, 161, 38.

Brady, G. R., Moriarty, C., Petrone, P., Laginja, I., Brooks, K., Comeau, T., Leboulleux, L., and Soummer, R. (2018). Phase-retrieval-based wavefront metrology for high contrast coronagraphy. volume 10698 of *Proc. SPIE*.

Brandl, B. R., Agócs, T., Aitink-Kroes, G., Bertram, T., Bettonvil, F., van Boekel, R., Boulade, O., Feldt, M., Glasse, A., Glauser, A., Güdel, M., Hurtado, N., Jager, R., Kenworthy, M. A.,

Mach, M., Meisner, J., Meyer, M., Pantin, E., Quanz, S., Schmid, H. M., Stuik, R., Veninga, A., and Waelkens, C. (2016). Status of the mid-infrared E-ELT imager and spectrograph METIS. In *Ground-based and Airborne Instrumentation for Astronomy VI*, volume 9908 of *Proc. SPIE*, page 990820.

Brandl, B. R., Feldt, M., Glasse, A., Guedel, M., Heikamp, S., Kenworthy, M., Lenzen, R., Meyer, M. R., Molster, F., Paalvast, S., Pantin, E. J., Quanz, S. P., Schmalzl, E., Stuik, R., Venema, L., and Waelkens, C. (2014). METIS: the mid-infrared E-ELT imager and spectrograph. In *Ground-based and Airborne Instrumentation for Astronomy V*, volume 9147 of *Proc. SPIE*, page 914721.

Butler, R. P., Vogt, S. S., Laughlin, G., Burt, J. A., Rivera, E. J., Tuomi, M., Teske, J., Arriagada, P., Diaz, M., Holden, B., and Keiser, S. (2017). The LCES HIRES/Keck Precision Radial Velocity Exoplanet Survey. *AJ*, 153, 208.

Cady, E., Balasubramanian, K., Gersh-Range, J., Kasdin, J., Kern, B., Lam, R., Mejia Prada, C., Moody, D., Patterson, K., Poberezhskiy, I., Riggs, A. J. E., Seo, B.-J., Shi, F., Tang, H., Trauger, J., Zhou, H., and Zimmerman, N. (2017). Shaped pupil coronagraphy for WFIRST: high-contrast broadband testbed demonstration. In *Society of Photo-Optical Instrumentation Engineers (SPIE) Conference Series*, volume 10400 of *Society of Photo-Optical Instrumentation Engineers (SPIE) Conference Series*, page 104000E.

Carlotti, A., N'Diaye, M., Pueyo, L., and Mawet, D. (2014). Three possible types of coronagraphs for the E-ELT PCS instrument. In *Ground-based and Airborne Instrumentation for Astronomy V*, volume 9147 of *Proc. SPIE*, page 91479D.

Cavarroc, C., Boccaletti, A., Baudoz, P., Fusco, T., and Rouan, D. (2006). Fundamental limitations on Earth-like planet detection with extremely large telescopes. *A&A*, 447, 397.

Chauvin, G., Desidera, S., Lagrange, A.-M., Vigan, A., Gratton, R., Langlois, M., Bonnefoy, M., Beuzit, J.-L., Feldt, M., Mouillet, D., Meyer, M., Cheetham, A., Biller, B., Boccaletti, A., D'Orazi, V., Galicher, R., Hagelberg, J., Maire, A.-L., Mesa, D., Olofsson, J., Samland, M., Schmidt, T. O. B., Sissa, E., Bonavita, M., Charnay, B., Cudel, M., Daemgen, S., Delorme, P., Janin-Potiron, P., Janson, M., Keppler, M., Le Coroller, H., Ligi, R., Marleau, G. D., Messina, S., Mollière, P., Mordasini, C., Müller, A., Peretti, S., Perrot, C., Rodet, L., Rouan, D., Zurlo, A., Dominik, C., Henning, T., Menard, F., Schmid, H.-M., Turatto, M., Udry, S., Vakili, F., Abe, L., Antichi, J., Baruffolo, A., Baudoz, P., Baudrand, J., Blanchard, P., Bazzon, A., Buey, T., Carbillet, M., Carle, M., Charton, J., Cascone, E., Claudi, R., Costille, A., Deboulbe, A., De Caprio, V., Dohlen, K., Fantinel, D., Feautrier, P., Fusco, T., Gigan, P., Giro, E., Gisler, D., Gluck, L., Hubin, N., Hugot, E., Jaquet, M., Kasper, M., Madec, F., Magnard, Y., Martinez, P., Maurel, D., Le Mignant, D., Möller-Nilsson, O., Llored, M., Moulin, T., Origné, A., Pavlov, A., Perret, D., Petit, C., Pragt, J., Puget, P., Rabou, P., Ramos, J., Rigal, R., Rochat, S., Roelfsema, R., Rousset, G., Roux, A., Salasnich, B., Sauvage, J.-F., Sevin, A., Soenke, C., Stadler, E., Suarez, M., Weber, L., Wildi, F., Antoniucci, S., Augereau, J.-C., Baudino, J.-L., Brandner, W., Engler, N., Girard, J., Gry,

C., Kral, Q., Kopytova, T., Lagadec, E., Milli, J., Moutou, C., Schlieder, J., Szulágyi, J., Thalmann, C., and Wahhaj, Z. (2017). Discovery of a warm, dusty giant planet around HIP 65426. *A&A*, 605, L9.

Chauvin, G., Lagrange, A.-M., Dumas, C., Zuckerman, B., Mouillet, D., Song, I., Beuzit, J.-L., and Lowrance, P. (2004). A giant planet candidate near a young brown dwarf. Direct VLT/NACO observations using IR wavefront sensing. *A&A*, 425, L29.

Close, L. M., Males, J. R., Kopon, D. A., Gasho, V., Follette, K. B., Hinz, P., Morzinski, K., Uomoto, A., Hare, T., Riccardi, A., Esposito, S., Puglisi, A., Pinna, E., Busoni, L., Arcidiacono, C., Xompero, M., Briguglio, R., Quiros-Pacheco, F., and Argomedo, J. (2012). First closed-loop visible AO test results for the advanced adaptive secondary AO system for the Magellan Telescope: MagAO's performance and status. In *Adaptive Optics Systems III*, volume 8447 of *Proc. SPIE*, page 84470X.

Codona, J. L. (2004). Exoplanet imaging with the Giant Magellan Telescope. In Bonaccini Calia, D., Ellerbroek, B. L., and Ragazzoni, R., editors, *Advancements in Adaptive Optics*, volume 5490 of *Proc. SPIE*, pages 379–388.

Codona, J. L., Kenworthy, M. A., Hinz, P. M., Angel, J. R. P., and Woolf, N. J. (2006). A high-contrast coronagraph for the MMT using phase apodization: design and observations at 5 microns and 2 λ/D radius. In *Society of Photo-Optical Instrumentation Engineers (SPIE) Conference Series*, volume 6269 of *Proc. SPIE*, page 62691N.

Currie, T., Guyon, O., Tamura, M., Kudo, T., Jovanovic, N., Lozi, J., Schlieder, J. E., Brandt, T. D., Kuhn, J., Serabyn, E., Janson, M., Carson, J., Groff, T., Kasdin, N. J., McElwain, M. W., Singh, G., Uyama, T., Kuzuhara, M., Akiyama, E., Grady, C., Hayashi, S., Knapp, G., Kwon, J.-m., Oh, D., Wisniewski, J., Sitko, M., and Yang, Y. (2017). Subaru/SCExAO First-light Direct Imaging of a Young Debris Disk around HD 36546. *ApJL*, 836, L15.

Currie, T., Kasdin, N. J., Groff, T. D., Lozi, J., Jovanovic, N., Guyon, O., Brandt, T., Martinache, F., Chilcote, J., Skaf, N., Kuhn, J., Pathak, P., and Kudo, T. (2018). Laboratory and On-sky Validation of the Shaped Pupil Coronagraphs Sensitivity to Low-order Aberrations With Active Wavefront Control. *PASP*, 130, 044505.

Davies, R., Schubert, J., Hartl, M., Alves, J., Clénet, Y., Lang-Bardl, F., Nicklas, H., Pott, J.-U., Ragazzoni, R., Tolstoy, E., Agocs, T., Anwand-Heerwart, H., Barboza, S., Baudoz, P., Bender, R., Bizenberger, P., Boccaletti, A., Boland, W., Bonifacio, P., Briegel, F., Buey, T., Chapron, F., Cohen, M., Czoske, O., Dreizler, S., Falomo, R., Feautrier, P., Förster Schreiber, N., Gendron, E., Genzel, R., Glück, M., Gratadour, D., Greimel, R., Grupp, F., Häuser, M., Haug, M., Hennawi, J., Hess, H. J., Hörmann, V., Hofferbert, R., Hopp, U., Hubert, Z., Ives, D., Kausch, W., Kerber, F., Kravcar, H., Kuijken, K., Lang-Bardl, F., Leitzinger, M., Leschinski, K., Massari, D., Mei, S., Merlin, F., Mohr, L., Monna, A., Müller, F., Navarro, R., Plattner, M., Przybilla, N., Ramlau, R., Ramsay, S., Ratzka, T., Rhode, P., Richter, J., Rix, H.-W., Rodeghiero, G., Rohloff, R.-R., Rousset, G., Ruddenklau, R., Schaffenroth, V., Schlichter, J., Sevin, A., Stuik, R., Sturm, E., Thomas, J., Tromp, N.,

Turatto, M., Verdoes-Kleijn, G., Vidal, F., Wagner, R., Wegner, M., Zeilinger, W., Ziegler, B., and Zins, G. (2016). MICADO: first light imager for the E-ELT. In *Ground-based and Airborne Instrumentation for Astronomy VI*, volume 9908 of *Proc. SPIE*, page 99081Z.

de Wit, J., Wakeford, H. R., Gillon, M., Lewis, N. K., Valenti, J. A., Demory, B.-O., Burgasser, A. J., Burdanov, A., Delrez, L., Jehin, E., Lederer, S. M., Queloz, D., Triaud, A. H. M. J., and Van Grootel, V. (2016). A combined transmission spectrum of the Earth-sized exoplanets TRAPPIST-1 b and c. *Nature*, 537, 69.

Dohlen, K., Morris, T., Piqueras Lopez, J., Calcines-Rosario, A., Costille, A., Dubbeldam, M., El Hadi, K., Fusco, T., Llored, M., Neichel, B., Pascal, S., Sauvage, J.-F., Vola, P., Clarke, F., Schnetler, H., Bryson, I., and Thatte, N. (2018). Opto-mechanical designs for the HARMONI Adaptive Optics systems. *ArXiv e-prints*, .

Enya, K., Kotani, T., Haze, K., Aono, K., Nakagawa, T., Matsuhara, H., Kataza, H., Wada, T., Kawada, M., Fujiwara, K., Mita, M., Takeuchi, S., Komatsu, K., Sakai, S., Uchida, H., Mitani, S., Yamawaki, T., Miyata, T., Sako, S., Nakamura, T., Asano, K., Yamashita, T., Narita, N., Matsuo, T., Tamura, M., Nishikawa, J., Kokubo, E., Hayano, Y., Oya, S., Fukagawa, M., Shibai, H., Baba, N., Murakami, N., Itoh, Y., Honda, M., Okamoto, B., Ida, S., Takami, M., Abe, L., Guyon, O., Bierden, P., and Yamamuro, T. (2011). The SPICA coronagraphic instrument (SCI) for the study of exoplanets. *Advances in Space Research*, 48, 323.

Esposito, S., Riccardi, A., Pinna, E., Puglisi, A. T., Quirós-Pacheco, F., Arcidiacono, C., Xompero, M., Briguglio, R., Busoni, L., Fini, L., Argomedo, J., Gherardi, A., Agapito, G., Brusa, G., Miller, D. L., Guerra Ramon, J. C., Boutsia, K., and Stefanini, P. (2012). Natural guide star adaptive optics systems at LBT: FLAO commissioning and science operations status. In *Adaptive Optics Systems III*, volume 8447 of *Proc. SPIE*, page 84470U.

Fanson, J., McCarthy, P. J., Bernstein, R., Angeli, G., Ashby, D., Bigelow, B., Bouchez, A., Burgett, W., Chauvin, E., Contos, A., Figueroa, F., Gray, P., Groark, F., Laskin, R., Millan-Gabet, R., Rakich, A., Sandoval, R., Pi, M., and Wheeler, N. (2018). Overview and status of the Giant Magellan Telescope project. In *Society of Photo-Optical Instrumentation Engineers (SPIE) Conference Series*, volume 10700 of *Society of Photo-Optical Instrumentation Engineers (SPIE) Conference Series*, page 1070012.

Fauvarque, O., Neichel, B., Fusco, T., and Sauvage, J.-F. (2015). Variation around a pyramid theme: optical recombination and optimal use of photons. *Optics Letters*, 40, 3528.

Fauvarque, O., Neichel, B., Fusco, T., Sauvage, J.-F., and Girault, O. (2017). General formalism for Fourier-based wave front sensing: application to the pyramid wave front sensors. *Journal of Astronomical Telescopes, Instruments, and Systems*, 3, 019001.

Fortier, A., Beck, T., Benz, W., Broeg, C., Cessa, V., Ehrenreich, D., and Thomas, N. (2014). CHEOPS: a space telescope for ultra-high precision photometry of exoplanet transits. In *Space Telescopes and Instrumentation 2014: Optical, Infrared, and Millimeter Wave*, volume 9143 of *Proc. SPIE*, page 91432J.

Fusco, T., Petit, C., Rousset, G., Sauvage, J.-F., Dohlen, K., Mouillet, D., Charton, J., Baudoz, P., Kasper, M., Fedrigo, E., Rabou, P., Feautrier, P., Downing, M., Gigan, P., Conan, J.-M., Beuzit, J.-L., Hubin, N., Wildi, F., and Puget, P. (2006). Design of the extreme AO system for SPHERE, the planet finder instrument of the VLT. In *Society of Photo-Optical Instrumentation Engineers (SPIE) Conference Series*, volume 6272 of *Proc. SPIE*, page 62720K.

Fusco, T., Sauvage, J.-F., Mouillet, D., Costille, A., Petit, C., Beuzit, J.-L., Dohlen, K., Milli, J., Girard, J., Kasper, M., Vigan, A., Suarez, M., Soenke, C., Downing, M., N'Diaye, M., Baudoz, P., Sevin, A., Baruffolo, A., Schmid, H.-M., Salasnich, B., Hugot, E., and Hubin, N. (2016). SAXO, the SPHERE extreme AO system: on-sky final performance and future improvements. In *Adaptive Optics Systems V*, volume 9909 of *Proc. SPIE*, page 99090U.

Gaia Collaboration, Brown, A. G. A., Vallenari, A., Prusti, T., de Bruijne, J. H. J., Babusiaux, C., and Bailer-Jones, C. A. L. (2018). Gaia Data Release 2. Summary of the contents and survey properties. *ArXiv e-prints*, .

Gaia Collaboration, Prusti, T., de Bruijne, J. H. J., Brown, A. G. A., Vallenari, A., Babusiaux, C., Bailer-Jones, C. A. L., Bastian, U., Biermann, M., Evans, D. W., and et al. (2016). The Gaia mission. *A&A*, 595, A1.

Galicher, R., Baudoz, P., Delorme, J.-R., Mawet, D., Bottom, M., Dupuis, O., Reess, J.-M., and Bernardi, P. (2018). Self-Coherent Camera At The Palomar Observatory. In *Fifth International Conference on Adaptive Optics for Extremely Large Telescopes*.

Galicher, R., Guyon, O., Otsubo, M., Suto, H., and Ridgway, S. (2005). Laboratory Demonstration and Numerical Simulations of the Phase-Induced Amplitude Apodization. *PASP*, 117, 411.

Give'on, A., Kern, B., Shaklan, S., Moody, D. C., and Pueyo, L. (2007). Broadband wavefront correction algorithm for high-contrast imaging systems. In *Astronomical Adaptive Optics Systems and Applications III*, volume 6691 of *Proc. SPIE*, page 66910A.

Give'on, A., Kern, B. D., and Shaklan, S. (2011). Pair-wise, deformable mirror, image plane-based diversity electric field estimation for high contrast coronagraphy. In *Techniques and Instrumentation for Detection of Exoplanets V*, volume 8151 of *Proc. SPIE*, page 815110.

Gonsalves, R. A. (1982). Phase retrieval and diversity in adaptive optics. *Optical Engineering*, 21, 829.

Graham, J. R., Macintosh, B., Doyon, R., Gavel, D., Larkin, J., Levine, M., Oppenheimer, B., Palmer, D., Saddlemyer, L., Sivaramakrishnan, A., Veran, J.-P., and Wallace, K. (2007). Ground-Based Direct Detection of Exoplanets with the Gemini Planet Imager (GPI). *ArXiv e-prints*, .

Groff, T., Chilcote, J., Brandt, T., Kasdin, N. J., Galvin, M., Loomis, C., Rizzo, M., Knapp, G., Guyon, O., Jovanovic, N., Lozi, J., Currie, T., Takato, N., and Hayashi, M. (2017).

First light of the CHARIS high-contrast integral-field spectrograph. In *Society of Photo-Optical Instrumentation Engineers (SPIE) Conference Series*, volume 10400 of *Society of Photo-Optical Instrumentation Engineers (SPIE) Conference Series*, page 1040016.

Groff, T. D. and Kasdin, J. N. (2013). Kalman filtering techniques for focal plane electric field estimation. *Journal of the Optical Society of America A*, 30, 128.

Guisard, S., Noethe, L., and Spyromilio, J. (2000). Performance of active optics at the VLT. In Dierickx, P., editor, *Optical Design, Materials, Fabrication, and Maintenance*, volume 4003 of *Proc. SPIE*, pages 154–164.

Guyon, O. (2003). Phase-induced amplitude apodization of telescope pupils for extrasolar terrestrial planet imaging. *A&A*, 404, 379.

Guyon, O., Hinz, P. M., Cady, E., Belikov, R., and Martinache, F. (2014). High Performance Lyot and PIAA Coronagraphy for Arbitrarily Shaped Telescope Apertures. *ApJ*, 780, 171.

Guyon, O., Pluzhnik, E. A., Galicher, R., Martinache, F., Ridgway, S. T., and Woodruff, R. A. (2005). Exoplanet Imaging with a Phase-induced Amplitude Apodization Coronagraph. I. Principle. *ApJ*, 622, 744.

Guyon, O., Pluzhnik, E. A., Ridgway, S. T., Woodruff, R. A., Blain, C., Martinache, F., and Galicher, R. (2006). The Phase-Induced Amplitude Coronagraph (PIAA). In Aime, C. and Vakili, F., editors, *IAU Colloq. 200: Direct Imaging of Exoplanets: Science Techniques*, pages 385–392.

Herscovici-Schiller, O., Mugnier, L. M., Baudoz, P., Galicher, R., Sauvage, J.-F., Patru, F., Leboulleux, L., Vigan, A., Dohlen, K., Fusco, T., Pueyo, L. A., Soummer, R., Le Duigou, J.-M., Shiri, R. S., Sivaramakrishnan, A., St. Laurent, K., Valenzuela, A. M., and Zimmerman, N. T. (2018a). Towards the experimental validation of the non-linear dark hole on the THD bench. volume 10703 of *Proc. SPIE*.

Herscovici-Schiller, O., Mugnier, L. M., Baudoz, P., Galicher, R., Sauvage, J.-F., and Paul, B. (2018b). Experimental validation of joint phase and amplitude wave-front sensing with coronagraphic phase diversity for high-contrast imaging. *A&A*, 614, A142.

Hinkley, S., Oppenheimer, B. R., Zimmerman, N., Brenner, D., Parry, I. R., Crepp, J. R., Vasisht, G., Ligon, E., King, D., Soummer, R., Sivaramakrishnan, A., Beichman, C., Shao, M., Roberts, Jr., L. C., Bouchez, A., Dekany, R., Pueyo, L., Roberts, J. E., Lockhart, T., Zhai, C., Shelton, C., and Burruss, R. (2011). A New High Contrast Imaging Program at Palomar Observatory. *PASP*, 123, 74.

Janin-Potiron, P., N'Diaye, M., Martinez, P., Vigan, A., Dohlen, K., and Carbillet, M. (2017). Fine cophasing of segmented aperture telescopes with ZELDA, a Zernike wavefront sensor in the diffraction-limited regime. *A&A*, 603, A23.

Jovanovic, N., Absil, O., Baudoz, P., Beaulieu, M., Bottom, M., Cady, E., Carlomagno, B., Carlotti, A., Doelman, D., Fogarty, K., Galicher, R., Guyon, O., Haffert, S., Huby, E., Jewell, J., Keller, C., Kenworthy, M. A., Knight, J., Kuhn, J., Miller, K., Mazoyer, J., N'Diaye, M., Por, E., Pueyo, L., Eldorado Riggs, A., Ruane, G., Sirbu, D., Snik, F., Wallace, J. K., Wilby, M., and Ygouf, M. (2018). Review of high-contrast imaging systems for current and future ground-based and space-based telescopes II. Common path wavefront sensing/control and Coherent Differential Imaging. *ArXiv e-prints*, .

Jovanovic, N., Guyon, O., Martinache, F., Clergeon, C., Singh, G., Kudo, T., Newman, K., Kuhn, J., Serabyn, E., Norris, B., Tuthill, P., Stewart, P., Huby, E., Perrin, G., Lacour, S., Vievard, S., Murakami, N., Fumika, O., Minowa, Y., Hayano, Y., White, J., Lai, O., Marchis, F., Duchene, G., Kotani, T., and Woillez, J. (2014). Development and recent results from the Subaru coronagraphic extreme adaptive optics system. In *Ground-based and Airborne Instrumentation for Astronomy V*, volume 9147 of *Proc. SPIE*, page 91471Q.

Jovanovic, N., Martinache, F., Guyon, O., Clergeon, C., Singh, G., Kudo, T., Garrel, V., Newman, K., Doughty, D., Lozi, J., Males, J., Minowa, Y., Hayano, Y., Takato, N., Morino, J., Kuhn, J., Serabyn, E., Norris, B., Tuthill, P., Schworer, G., Stewart, P., Close, L., Huby, E., Perrin, G., Lacour, S., Gauchet, L., Vievard, S., Murakami, N., Oshiyama, F., Baba, N., Matsuo, T., Nishikawa, J., Tamura, M., Lai, O., Marchis, F., Duchene, G., Kotani, T., and Woillez, J. (2015). The Subaru Coronagraphic Extreme Adaptive Optics System: Enabling High-Contrast Imaging on Solar-System Scales. *PASP*, 127, 890.

Kasdin, N. J., Belikov, R., Beall, J., Vanderbei, R. J., Littman, M. G., Carr, M., and Give'on, A. (2005). Shaped pupil coronagraphs for planet finding: optimization, manufacturing, and experimental results. In Coulter, D. R., editor, *Techniques and Instrumentation for Detection of Exoplanets II*, volume 5905 of *Proc. SPIE*, pages 128–136.

Kasdin, N. J., Vanderbei, R. J., Spergel, D. N., and Littman, M. G. (2003). Extrasolar Planet Finding via Optimal Apodized-Pupil and Shaped-Pupil Coronagraphs. *ApJ*, 582, 1147.

Kenworthy, M., Quanz, S., Meyer, M., Kasper, M., Girard, J., Lenzen, R., Codona, J., and Hinz, P. (2010a). A New Coronagraph for NAOS-CONICA – the Apodising Phase Plate. *The Messenger*, 141, 2.

Kenworthy, M. A., Codona, J. L., Hinz, P. M., Angel, J. R. P., Heinze, A., and Sivanandam, S. (2007). First On-Sky High-Contrast Imaging with an Apodizing Phase Plate. *ApJ*, 660, 762.

Kenworthy, M. A., Quanz, S. P., Meyer, M. R., Kasper, M. E., Lenzen, R., Codona, J. L., Girard, J. H., and Hinz, P. M. (2010b). An apodizing phase plate coronagraph for VLT/NACO. In *Ground-based and Airborne Instrumentation for Astronomy III*, volume 7735 of *Proc. SPIE*, page 773532.

Krist, J. E., Balasubramanian, K., Muller, R. E., Shaklan, S. B., Kelly, D. M., Wilson, D. W., Beichman, C. A., Serabyn, E., Mao, Y., Echternach, P. M., Trauger, J. T., and Liewer,

K. M. (2010). The JWST/NIRCam coronagraph flight occulters. In *Space Telescopes and Instrumentation 2010: Optical, Infrared, and Millimeter Wave*, volume 7731 of *Proc. SPIE*, page 77313J.

Kuchner, M. J. and Traub, W. A. (2002). A Coronagraph with a Band-limited Mask for Finding Terrestrial Planets. *ApJ*, 570, 900.

Leboulleux, L., N'Diaye, M., Mazoyer, J., Pueyo, L., Perrin, M., Egron, S., Choquet, E., Sauvage, J.-F., Fusco, T., and Soummer, R. (2017). Comparison of wavefront control algorithms and first results on the high-contrast imager for complex aperture telescopes (hicat) testbed. In *Society of Photo-Optical Instrumentation Engineers (SPIE) Conference Series*, volume 10562 of *Society of Photo-Optical Instrumentation Engineers (SPIE) Conference Series*, page 105622Z.

Leboulleux, L., Pueyo, L., Sauvage, J.-F., Fusco, T., Mazoyer, J., Sivaramakrishnan, A., N'Diaye, M., and Soummer, R. (2018a). Sensitivity analysis for high-contrast imaging with segmented space telescopes. In *Society of Photo-Optical Instrumentation Engineers (SPIE) Conference Series*, volume 10698 of *Society of Photo-Optical Instrumentation Engineers (SPIE) Conference Series*, page 106986H.

Leboulleux, L., Sauvage, J.-F., Pueyo, L., Fusco, T., Soummer, R., Mazoyer, J., Sivaramakrishnan, A., N'Diaye, M., and Fauvarque, O. (2018b). Pair-based Analytical model for Segmented Telescopes Imaging from Space for sensitivity analysis. *Journal of Astronomical Telescopes, Instruments, and Systems*, 4, 035002.

Léger, A., Rouan, D., Schneider, J., Barge, P., Fridlund, M., Samuel, B., Ollivier, M., Guenther, E., Deleuil, M., Deeg, H. J., Auvergne, M., Alonso, R., Aigrain, S., Alapini, A., Almenara, J. M., Baglin, A., Barbieri, M., Bruntt, H., Bordé, P., Bouchy, F., Cabrera, J., Catala, C., Carone, L., Carpano, S., Csizmadia, S., Dvorak, R., Erikson, A., Ferraz-Mello, S., Foing, B., Fressin, F., Gandolfi, D., Gillon, M., Gondoin, P., Grasset, O., Guillot, T., Hatzes, A., Hébrard, G., Jorda, L., Lammer, H., Llebaria, A., Loeillet, B., Mayor, M., Mazeh, T., Moutou, C., Pätzold, M., Pont, F., Queloz, D., Rauer, H., Renner, S., Samadi, R., Shporer, A., Sotin, C., Tingley, B., Wuchterl, G., Adda, M., Agogu, P., Appourchaux, T., Ballans, H., Baron, P., Beaufort, T., Bellenger, R., Berlin, R., Bernardi, P., Blouin, D., Baudin, F., Bodin, P., Boisnard, L., Boit, L., Bonneau, F., Borzeix, S., Briet, R., Buey, J.-T., Butler, B., Cailleau, D., Cautain, R., Chabaud, P.-Y., Chaintreuil, S., Chiavassa, F., Costes, V., Cuna Parrho, V., de Oliveira Fialho, F., Decaudin, M., Defise, J.-M., Djalal, S., Epstein, G., Exil, G.-E., Fauré, C., Fenouillet, T., Gaboriaud, A., Gallic, A., Gamet, P., Gavalda, P., Grolleau, E., Gruneisen, R., Gueguen, L., Guis, V., Guivarc'h, V., Guterman, P., Hallouard, D., Hasiba, J., Heuripeau, F., Huntzinger, G., Hustaix, H., Imad, C., Imbert, C., Johlander, B., Jouret, M., Journoud, P., Karioty, F., Kerjean, L., Lafaille, V., Lafond, L., Lam-Trong, T., Landiech, P., Lapeyrere, V., Larqué, T., Laudet, P., Lautier, N., Lecann, H., Lefevre, L., Leruyet, B., Levacher, P., Magnan, A., Mazy, E., Mertens, F., Mesnager, J.-M., Meunier, J.-C., Michel, J.-P., Monjoin, W., Naudet, D., Nguyen-Kim, K., Orcesi, J.-L., Ottacher, H., Perez, R., Peter, G., Plasson, P., Plesseria, J.-Y., Pontet, B., Pradines, A., Quentin, C., Reynaud, J.-L.,

Rolland, G., Rollenhagen, F., Romagnan, R., Russ, N., Schmidt, R., Schwartz, N., Sebbag, I., Sedes, G., Smit, H., Steller, M. B., Sunter, W., Surace, C., Tello, M., Tiphène, D., Toulouse, P., Ulmer, B., Vandermarcq, O., Vergnault, E., Vuillemin, A., and Zanatta, P. (2009). Transiting exoplanets from the CoRoT space mission. VIII. CoRoT-7b: the first super-Earth with measured radius. *A&A*, 506, 287.

Lenzen, R., Hartung, M., Brandner, W., Finger, G., Hubin, N. N., Lacombe, F., Lagrange, A.-M., Lehnert, M. D., Moorwood, A. F. M., and Mouillet, D. (2003). NAOS-CONICA first on sky results in a variety of observing modes. In Iye, M. and Moorwood, A. F. M., editors, *Instrument Design and Performance for Optical/Infrared Ground-based Telescopes*, volume 4841 of *Proc. SPIE*, pages 944–952.

Lozi, J., Guyon, O., Jovanovic, N., Goebel, S., Pathak, P., Skaf, N., Sahoo, A., Norris, B., Martinache, F., N'Diaye, M., Mazin, B., Walter, A. B., Tuthill, P., Kudo, T., Kawahara, H., Kotani, T., Ireland, M., Cvetojevic, N., Huby, E., Lacour, S., Vievard, S., Groff, T. D., Chilcote, J. K., Kasdin, J., Knight, J., Snik, F., Doelman, D., Minowa, Y., Clergeon, C., Takato, N., Tamura, M., Currie, T., Takami, H., and Hayashi, M. (2018). Scexao, an instrument with a dual purpose: perform cutting-edge science and develop new technologies.

Luger, R., Sestovic, M., Kruse, E., Grimm, S. L., Demory, B.-O., Agol, E., Bolmont, E., Fabrycky, D., Fernandes, C. S., Van Grootel, V., Burgasser, A., Gillon, M., Ingalls, J. G., Jehin, E., Raymond, S. N., Selsis, F., Triaud, A. H. M. J., Barclay, T., Barentsen, G., Howell, S. B., Delrez, L., de Wit, J., Foreman-Mackey, D., Holdsworth, D. L., Leconte, J., Lederer, S., Turbet, M., Almleaky, Y., Benkhaldoun, Z., Magain, P., Morris, B. M., Heng, K., and Queloz, D. (2017). A seven-planet resonant chain in TRAPPIST-1. *Nature Astronomy*, 1, 0129.

Lyon, R. G., Clampin, M., Woodruff, R. A., Vasudevan, G., Thompson, P., Petrone, P., Madison, T., Rizzo, M., Melnick, G., and Tolls, V. (2010). Visible Nulling Coronagraph Progress Report. In Coudé du Foresto, V., Gelino, D. M., and Ribas, I., editors, *Pathways Towards Habitable Planets*, volume 430 of *Astronomical Society of the Pacific Conference Series*, page 485.

Lyot, B. (1932). Étude de la couronne solaire en dehors des éclipses. Avec 16 figures dans le texte. *ZA*, 5, 73.

Lyot, B. (1939). The study of the solar corona and prominences without eclipses (George Darwin Lecture, 1939). *MNRAS*, 99, 580.

Macintosh, B., Graham, J., Palmer, D., Doyon, R., Gavel, D., Larkin, J., Oppenheimer, B., Saddlemyer, L., Wallace, J. K., Bauman, B., Evans, J., Erikson, D., Morzinski, K., Phillion, D., Poyneer, L., Sivaramakrishnan, A., Soummer, R., Thibault, S., and Veran, J.-P. (2006). The Gemini Planet Imager. In *Society of Photo-Optical Instrumentation Engineers (SPIE) Conference Series*, volume 6272 of *Proc. SPIE*, page 62720L.

Macintosh, B., Graham, J. R., Barman, T., De Rosa, R. J., Konopacky, Q., Marley, M. S., Marois, C., Nielsen, E. L., Pueyo, L., Rajan, A., Rameau, J., Saumon, D., Wang, J. J., Patience, J., Ammons, M., Arriaga, P., Artigau, E., Beckwith, S., Brewster, J., Bruzzone, S., Bulger, J., Burningham, B., Burrows, A. S., Chen, C., Chiang, E., Chilcote, J. K., Dawson, R. I., Dong, R., Doyon, R., Draper, Z. H., Duchêne, G., Esposito, T. M., Fabrycky, D., Fitzgerald, M. P., Follette, K. B., Fortney, J. J., Gerard, B., Goodsell, S., Greenbaum, A. Z., Hibon, P., Hinkley, S., Cotten, T. H., Hung, L.-W., Ingraham, P., Johnson-Groh, M., Kalas, P., Lafreniere, D., Larkin, J. E., Lee, J., Line, M., Long, D., Maire, J., Marchis, F., Matthews, B. C., Max, C. E., Metchev, S., Millar-Blanchaer, M. A., Mittal, T., Morley, C. V., Morzinski, K. M., Murray-Clay, R., Oppenheimer, R., Palmer, D. W., Patel, R., Perrin, M. D., Poyneer, L. A., Rafikov, R. R., Rantakyrö, F. T., Rice, E. L., Rojo, P., Rudy, A. R., Ruffio, J.-B., Ruiz, M. T., Sadakuni, N., Saddlemyer, L., Salama, M., Savransky, D., Schneider, A. C., Sivaramakrishnan, A., Song, I., Soummer, R., Thomas, S., Vasisht, G., Wallace, J. K., Ward-Duong, K., Wiktorowicz, S. J., Wolff, S. G., and Zuckerman, B. (2015). Discovery and spectroscopy of the young jovian planet 51 Eri b with the Gemini Planet Imager. *Science*, 350, 64.

Macintosh, B., Graham, J. R., Ingraham, P., Konopacky, Q., Marois, C., Perrin, M., Poyneer, L., Bauman, B., Barman, T., Burrows, A. S., Cardwell, A., Chilcote, J., De Rosa, R. J., Dillon, D., Doyon, R., Dunn, J., Erikson, D., Fitzgerald, M. P., Gavel, D., Goodsell, S., Hartung, M., Hibon, P., Kalas, P., Larkin, J., Maire, J., Marchis, F., Marley, M. S., McBride, J., Millar-Blanchaer, M., Morzinski, K., Norton, A., Oppenheimer, B. R., Palmer, D., Patience, J., Pueyo, L., Rantakyro, F., Sadakuni, N., Saddlemyer, L., Savransky, D., Serio, A., Soummer, R., Sivaramakrishnan, A., Song, I., Thomas, S., Wallace, J. K., Wiktorowicz, S., and Wolff, S. (2014). First light of the Gemini Planet Imager. *Proceedings of the National Academy of Science*, 111, 12661.

Malbet, F. (1996). High angular resolution coronography for adaptive optics. *A&AS*, 115, 161.

Malbet, F., Yu, J. W., and Shao, M. (1995). High-Dynamic-Range Imaging Using a Deformable Mirror for Space Coronography. *PASP*, 107, 386.

Mandell, A. M., Groff, T. D., Gong, Q., Rizzo, M. J., Lupu, R., Zimmerman, N. T., Saxena, P., and McElwain, M. W. (2017). Current science requirements and planned implementation for the WFIRST-CGI Integral Field Spectrograph (IFS). In *Society of Photo-Optical Instrumentation Engineers (SPIE) Conference Series*, volume 10400 of *Society of Photo-Optical Instrumentation Engineers (SPIE) Conference Series*, page 1040009.

Mao, Y., Andersen, T. B., Kubo, T., Virgen, M., Chan, H., Feller, G., Huff, L. W., Smith, E., Vasudevan, G., Somerstein, S., Jamieson, T., Horner, S., Krist, J., Beichman, C. A., Barone, C., Schmidt, R., Levin, D., Seymour, S., Kelly, D., and Rieke, M. J. (2011). NIRCam coronagraphic Lyot stop: design, fabrication, and testing. In *Cryogenic Optical Systems and Instruments XIII*, volume 8150 of *Proc. SPIE*, pages 81500E–81500E–12.

Martin, S., Rud, M., Scowen, P., Stern, D., Nissen, J., and Krist, J. (2017). HabEx space telescope optical system. In *Society of Photo-Optical Instrumentation Engineers (SPIE) Conference Series*, volume 10398 of *Society of Photo-Optical Instrumentation Engineers (SPIE) Conference Series*, page 1039805.

Martinez, P., Beaulieu, M., Janin-Potiron, P., Preis, O., Gouvret, C., Dejonghe, J., Abe, L., Spang, A., Fantéï-Caujolle, Y., Martinache, F., Belzanne, P., Marcotto, A., and Carbillet, M. (2016). The Segmented Pupil Experiment for Exoplanet Detection: 2. design advances and progress overview. In *Ground-based and Airborne Telescopes VI*, volume 9906 of *Proc. SPIE*, page 99062V.

Martinez, P., Dorrer, C., Kasper, M., Boccaletti, A., and Dohlen, K. (2010). Design, analysis, and testing of a microdot apodizer for the apodized pupil Lyot coronagraph. III. Application to extremely large telescopes. *A&A*, 520, A110.

Maszkiewicz, M. (2017). Near- infrared imager and slitless spectrograph (NIRISS): a new instrument on James Webb Space Telescope (JWST). In *Society of Photo-Optical Instrumentation Engineers (SPIE) Conference Series*, volume 10564 of *Society of Photo-Optical Instrumentation Engineers (SPIE) Conference Series*, page 105642Q.

Mawet, D., Pueyo, L., Moody, D., Krist, J., and Serabyn, E. (2010a). The Vector Vortex Coronagraph: sensitivity to central obscuration, low-order aberrations, chromaticism, and polarization. In *Modern Technologies in Space- and Ground-based Telescopes and Instrumentation*, volume 7739 of *Proc. SPIE*, page 773914.

Mawet, D., Serabyn, E., Liewer, K., Burruss, R., Hickey, J., and Shemo, D. (2010b). The Vector Vortex Coronagraph: Laboratory Results and First Light at Palomar Observatory. *ApJ*, 709, 53.

Mawet, D., Wizinowich, P., Dekany, R., Chun, M., Hall, D., Cetre, S., Guyon, O., Wallace, J. K., Bowler, B., Liu, M., Ruane, G., Serabyn, E., Bartos, R., Wang, J., Vasisht, G., Fitzgerald, M., Skemer, A., Ireland, M., Fucik, J., Fortney, J., Crossfield, I., Hu, R., and Benneke, B. (2016). Keck Planet Imager and Characterizer: concept and phased implementation. In *Adaptive Optics Systems V*, volume 9909 of *Proc. SPIE*, page 99090D.

Mayor, M., Pepe, F., Queloz, D., Bouchy, F., Rupprecht, G., Lo Curto, G., Avila, G., Benz, W., Bertaux, J.-L., Bonfils, X., Dall, T., Dekker, H., Delabre, B., Eckert, W., Fleury, M., Gilliotte, A., Gojak, D., Guzman, J. C., Kohler, D., Lizon, J.-L., Longinotti, A., Lovis, C., Megevand, D., Pasquini, L., Reyes, J., Sivan, J.-P., Sosnowska, D., Soto, R., Udry, S., van Kesteren, A., Weber, L., and Weilenmann, U. (2003). Setting New Standards with HARPS. *The Messenger*, 114, 20.

Mayor, M. and Queloz, D. (1995). A Jupiter-mass companion to a solar-type star. *Nature*, 378, 355.

Mazoyer, J., Baudoz, P., Galicher, R., Mas, M., and Rousset, G. (2013). Estimation and correction of wavefront aberrations using the self-coherent camera: laboratory results. *A&A*, 557, A9.

Mazoyer, J., Baudoz, P., Galicher, R., and Rousset, G. (2014). High-contrast imaging in polychromatic light with the self-coherent camera. *A&A*, 564, L1.

Mazoyer, J., Pueyo, L., N'Diaye, M., Fogarty, K., Zimmerman, N., Leboulleux, L., St. Laurent, K. E., Soummer, R., Shaklan, S., and Norman, C. (2018a). Active Correction of Aperture Discontinuities-Optimized Stroke Minimization. I. A New Adaptive Interaction Matrix Algorithm. *AJ*, 155, 7.

Mazoyer, J., Pueyo, L., N'Diaye, M., Fogarty, K., Zimmerman, N., Soummer, R., Shaklan, S., and Norman, C. (2018b). Active Correction of Aperture Discontinuities-Optimized Stroke Minimization. II. Optimization for Future Missions. *AJ*, 155, 8.

Mazoyer, J., Pueyo, L., N'Diaye, M., Mawet, D., Soummer, R., and Norman, C. (2016). Correcting for the effects of pupil discontinuities with the ACAD method. In *Space Telescopes and Instrumentation 2016: Optical, Infrared, and Millimeter Wave*, volume 9904 of *Proc. SPIE*, page 99044T.

Moriarty, C., Brooks, K., Soummer, R., Perrin, M. D., Comeau, T., Brady, G. R., Gontrum, R., and Petrone, P. (2018). High-contrast imager for complex aperture telescopes (HiCAT): 6. software control infrastructure and calibration. volume 10698 of *Proc. SPIE*.

Murakami, N., Uemura, R., Baba, N., Nishikawa, J., Tamura, M., Hashimoto, N., and Abe, L. (2008). An Eight-Octant Phase-Mask Coronagraph. *PASP*, 120, 1112.

N'Diaye, M., Choquet, E., Pueyo, L., Elliot, E., Perrin, M. D., Wallace, J. K., Groff, T., Carlotti, A., Mawet, D., Sheckells, M., Shaklan, S., Macintosh, B., Kasdin, N. J., and Soummer, R. (2013a). High-contrast imager for complex aperture telescopes (HiCAT): 1. testbed design. In *Techniques and Instrumentation for Detection of Exoplanets VI*, volume 8864 of *Proc. SPIE*, page 88641K.

N'Diaye, M., Dohlen, K., Caillat, A., Costille, A., Fusco, T., Jolivet, A., Madec, F., Mugnier, L., Paul, B., Sauvage, J.-F., Soummer, R., Vigan, A., and Wallace, J. K. (2014). Design optimization and lab demonstration of ZELDA: a Zernike sensor for near-coronagraph quasi-static measurements. In *Adaptive Optics Systems IV*, volume 9148 of *Proc. SPIE*, page 91485H.

N'Diaye, M., Dohlen, K., Fusco, T., El Hadi, K., Soummer, R., Cuevas, S., Zerrad, M., and Ferrari, M. (2012). Lab results of the circular phase mask concepts for high-contrast imaging of exoplanets. In *Modern Technologies in Space- and Ground-based Telescopes and Instrumentation II*, volume 8450 of *Proc. SPIE*, page 84500N.

N'Diaye, M., Dohlen, K., Fusco, T., and Paul, B. (2013b). Calibration of quasi-static aberrations in exoplanet direct-imaging instruments with a Zernike phase-mask sensor. *A&A*, 555, A94.

N'Diaye, M., Pueyo, L., and Soummer, R. (2015). Apodized Pupil Lyot Coronagraphs for Arbitrary Apertures. IV. Reduced Inner Working Angle and Increased Robustness to Low-order Aberrations. *ApJ*, 799, 225.

N'Diaye, M., Vigan, A., Dohlen, K., Sauvage, J.-F., Caillat, A., Costille, A., Girard, J. H. V., Beuzit, J.-L., Fusco, T., Blanchard, P., Le Merrer, J., Le Mignant, D., Madec, F., Moreaux, G., Mouillet, D., Puget, P., and Zins, G. (2016). Calibration of quasi-static aberrations in exoplanet direct-imaging instruments with a Zernike phase-mask sensor. II. Concept validation with ZELDA on VLT/SPHERE. *A&A*, 592, A79.

Norris, B., Schworer, G., Tuthill, P., Jovanovic, N., Guyon, O., Stewart, P., and Martinache, F. (2015). The VAMPIRES instrument: imaging the innermost regions of protoplanetary discs with polarimetric interferometry. *MNRAS*, 447, 2894.

Paul, B. (2014). *Post-coronagraphic wave-front sensing for high contrast imaging for ground and space based observations*. Theses, Université d'Aix-Marseille.

Paul, B., Sauvage, J.-F., and Mugnier, L. M. (2013). Coronagraphic phase diversity: performance study and laboratory demonstration. *A&A*, 552, A48.

Perrin, M. D., Pueyo, L., Van Gorkom, K., Brooks, K., Rajan, A., Girard, J., and Lajoie, C.-P. (2018). Updated optical modeling of JWST coronagraph performance contrast, stability, and strategies. In *Society of Photo-Optical Instrumentation Engineers (SPIE) Conference Series*, volume 10698 of *Proc. SPIE*.

Perruchot, S., Bouchy, F., Chazelas, B., Díaz, R. F., Hébrard, G., Arnaud, K., Arnold, L., Avila, G., Delfosse, X., Boisse, I., Moreaux, G., Pepe, F., Richaud, Y., Santerne, A., Sottile, R., and Tézier, D. (2011). Higher-precision radial velocity measurements with the SOPHIE spectrograph using octagonal-section fibers. In *Techniques and Instrumentation for Detection of Exoplanets V*, volume 8151 of *Proc. SPIE*, page 815115.

Pueyo, L., Kay, J., Kasdin, N. J., Groff, T., McElwain, M., Give'on, A., and Belikov, R. (2009). Optimal dark hole generation via two deformable mirrors with stroke minimization. *ApOpt*, 48, 6296.

Quirrenbach, A. (2005). Coronographic Methods for the Detection of Terrestrial Planets. *ArXiv Astrophysics e-prints*, .

Radovan, M. V., Cabak, G. F., Laiterman, L. H., Lockwood, C. T., and Vogt, S. S. (2010). A radial velocity spectrometer for the Automated Planet Finder Telescope at Lick Observatory. In *Ground-based and Airborne Instrumentation for Astronomy III*, volume 7735 of *Proc. SPIE*, page 77354K.

Ragazzoni, R. (1996). Pupil plane wavefront sensing with an oscillating prism. *Journal of Modern Optics*, 43, 289.

Ragazzoni, R. and Farinato, J. (1999). Sensitivity of a pyramidic Wave Front sensor in closed loop Adaptive Optics. *A&A*, 350, L23.

Ricker, G. R., Winn, J. N., Vanderspek, R., Latham, D. W., Bakos, G. Á., Bean, J. L., Berta-Thompson, Z. K., Brown, T. M., Buchhave, L., Butler, N. R., Butler, R. P., Chaplin, W. J.,

Charbonneau, D., Christensen-Dalsgaard, J., Clampin, M., Deming, D., Doty, J., De Lee, N., Dressing, C., Dunham, E. W., Endl, M., Fressin, F., Ge, J., Henning, T., Holman, M. J., Howard, A. W., Ida, S., Jenkins, J. M., Jernigan, G., Johnson, J. A., Kaltenegger, L., Kawai, N., Kjeldsen, H., Laughlin, G., Levine, A. M., Lin, D., Lissauer, J. J., MacQueen, P., Marcy, G., McCullough, P. R., Morton, T. D., Narita, N., Paegert, M., Palle, E., Pepe, F., Pepper, J., Quirrenbach, A., Rinehart, S. A., Sasselov, D., Sato, B., Seager, S., Sozzetti, A., Stassun, K. G., Sullivan, P., Szentgyorgyi, A., Torres, G., Udry, S., and Villasenor, J. (2015). Transiting Exoplanet Survey Satellite (TESS). *Journal of Astronomical Telescopes, Instruments, and Systems*, 1, 014003.

Riggs, A. J. E., Cady, E. J., Prada, C. M., Kern, B. D., Zhou, H., Kasdin, N. J., and Groff, T. D. (2016a). Low-signal, coronagraphic wavefront estimation with Kalman filtering in the high contrast imaging testbed. In *Space Telescopes and Instrumentation 2016: Optical, Infrared, and Millimeter Wave*, volume 9904 of *Proc. SPIE*, page 99043F.

Riggs, A. J. E., Kasdin, N. J., and Groff, T. D. (2016b). Recursive starlight and bias estimation for high-contrast imaging with an extended Kalman filter. *Journal of Astronomical Telescopes, Instruments, and Systems*, 2, 011017.

Roddier, F. (1988). Curvature sensing and compensation: a new concept in adaptive optics. *ApOpt*, 27, 1223.

Roddier, F. and Roddier, C. (1997). Stellar Coronograph with Phase Mask. *PASP*, 109, 815.

Rouan, D., Riaud, P., Boccaletti, A., Clénet, Y., and Labeyrie, A. (2000). The Four-Quadrant Phase-Mask Coronagraph. I. Principle. *PASP*, 112, 1479.

Rousset, G. (1999). *Wave-front sensors*.

Rousset, G., Lacombe, F., Puget, P., Hubin, N. N., Gendron, E., Fusco, T., Arsenault, R., Charton, J., Feautrier, P., Gigan, P., Kern, P. Y., Lagrange, A.-M., Madec, P.-Y., Mouillet, D., Rabaud, D., Rabou, P., Stadler, E., and Zins, G. (2003). NAOS, the first AO system of the VLT: on-sky performance. In Wizinowich, P. L. and Bonaccini, D., editors, *Adaptive Optical System Technologies II*, volume 4839 of *Proc. SPIE*, pages 140–149.

Saif, B., Chaney, D., Greenfield, P., Bluth, M., Van Gorkom, K., Smith, K., Bluth, J., Feinberg, L., Wyant, J. C., North-Morris, M., and Keski-Kuha, R. (2017). Measurement of picometer-scale mirror dynamics. *ApOpt*, 56.

Sauvage, J.-F., Fusco, T., Petit, C., Costille, A., Mouillet, D., Beuzit, J.-L., Dohlen, K., Kasper, M., Suarez, M., Soenke, C., Baruffolo, A., Salasnich, B., Rochat, S., Fedrigo, E., Baudoz, P., Hugot, E., Sevin, A., Perret, D., Wildi, F., Downing, M., Feautrier, P., Puget, P., Vigan, A., O'Neal, J., Girard, J., Mawet, D., Schmid, H. M., and Roelfsema, R. (2016). SAXO: the extreme adaptive optics system of SPHERE (I) system overview and global laboratory performance. *Journal of Astronomical Telescopes, Instruments, and Systems*, 2, 025003.

Sauvage, J.-F., Fusco, T., Petit, C., Mugnier, L., Paul, B., and Costille, A. (2012a). Focal-plane wave front sensing strategies for high contrast imaging: experimental validations on SPHERE. In *Adaptive Optics Systems III*, volume 8447 of *Proc. SPIE*, page 844715.

Sauvage, J.-F., Mugnier, L., Paul, B., and Villecroze, R. (2012b). Coronagraphic phase diversity: a simple focal plane sensor for high-contrast imaging. *Optics Letters*, 37, 4808.

Sauvage, J.-F., Mugnier, L. M., Rousset, G., and Fusco, T. (2010). Analytical expression of long-exposure adaptive-optics-corrected coronagraphic image First application to exo-planet detection. *Journal of the Optical Society of America A*, 27, A157.

Schechter, P. L., Burley, G. S., Hull, C. L., Johns, M., Martin, H. M., Schaller, S., Shectman, S. A., and West, S. C. (2003). Active optics on the Baade 6.5-m (Magellan I) Telescope. In Oschmann, J. M. and Stepp, L. M., editors, *Large Ground-based Telescopes*, volume 4837 of *Proc. SPIE*, pages 619–627.

Shack, R. V. and Platt, B. C. (1971). *Production and Use of a Lenticular Hartmann Screen*.

Sivaramakrishnan, A., Koresko, C. D., Makidon, R. B., Berkefeld, T., and Kuchner, M. J. (2001). Ground-based Coronagraphy with High-order Adaptive Optics. *ApJ*, 552, 397.

Snik, F., Otten, G., Kenworthy, M., Miskiewicz, M., Escuti, M., Packham, C., and Codona, J. (2012). The vector-APP: a broadband apodizing phase plate that yields complementary PSFs. In *Modern Technologies in Space- and Ground-based Telescopes and Instrumentation II*, volume 8450 of *Proc. SPIE*, page 84500M.

Soummer, R. (2005). Apodized Pupil Lyot Coronagraphs for Arbitrary Telescope Apertures. *ApJL*, 618, L161.

Soummer, R., Aime, C., and Falloon, P. E. (2003a). Stellar coronagraphy with prolate apodized circular apertures. *A&A*, 397, 1161.

Soummer, R., Brady, G. R., Brooks, K., Comeau, T., Choquet, E., Dillon, T. E., Egron, S., Gontrum, R., Hagopian, J. G., Laginja, I., Leboulleux, L., Perrin, M. D., Petrone, P., Pueyo, L. A., Mazoyer, J., N'Diaye, M., Riggs, A. E., Shiri, R. S., Sivaramakrishnan, A., St. Laurent, K., Valenzuela, A. M., and Zimmerman, N. T. (2018). High-contrast imager for complex aperture telescopes (HiCAT): 5. first results with segmented-aperture coronagraph and wavefront control. volume 10698 of *Proc. SPIE*.

Soummer, R., Dohlen, K., and Aime, C. (2003b). Achromatic dual-zone phase mask stellar coronagraph. *A&A*, 403, 369.

Soummer, R., Sivaramakrishnan, A., Pueyo, L., Macintosh, B., and Oppenheimer, B. R. (2011). Apodized Pupil Lyot Coronagraphs for Arbitrary Apertures. III. Quasi-achromatic Solutions. *ApJ*, 729, 144.

Spergel, D., Gehrels, N., Breckinridge, J., Donahue, M., Dressler, A., Gaudi, B. S., Greene, T., Guyon, O., Hirata, C., Kalirai, J., Kasdin, N. J., Moos, W., Perlmutter, S., Postman, M., Rauscher, B., Rhodes, J., Wang, Y., Weinberg, D., Centrella, J., Traub, W., Baltay, C., Colbert, J., Bennett, D., Kiessling, A., Macintosh, B., Merten, J., Mortonson, M., Penny, M., Rozo, E., Savransky, D., Stapelfeldt, K., Zu, Y., Baker, C., Cheng, E., Content, D., Dooley, J., Foote, M., Goullioud, R., Grady, K., Jackson, C., Kruk, J., Levine, M., Melton, M., Peddie, C., Ruffa, J., and Shaklan, S. (2013). Wide-Field InfraRed Survey Telescope-Astrophysics Focused Telescope Assets WFIRST-AFTA Final Report. *ArXiv e-prints*, .

Stapelfeldt, K. R., Dekens, F. G., Brenner, M. P., Warfield, K. R., Belikov, R., Brugarolas, P. B., Bryden, G., Cahoy, K. L., Chakrabarti, S., Dubovitsky, S., Effinger, R. T., Hirsch, B., Kissil, A., Krist, J. E., Lang, J. J., Marley, M. S., McElwain, M. W., Meadows, V. S., Nissen, J., Oseas, J. M., Pong, C., Serabyn, E., Sunada, E., Trauger, J. T., and Unwin, S. C. (2015). Exo-C: a probe-scale space observatory for direct imaging and spectroscopy of extrasolar planetary systems. In *Techniques and Instrumentation for Detection of Exoplanets VII*, volume 9605 of *Proc. SPIE*, page 96050T.

Stevenson, K. B., Lewis, N. K., Bean, J. L., Beichman, C., Fraine, J., Kilpatrick, B. M., Krick, J. E., Lothringer, J. D., Mandell, A. M., Valenti, J. A., Agol, E., Angerhausen, D., Barstow, J. K., Birkmann, S. M., Burrows, A., Charbonneau, D., Cowan, N. B., Crouzet, N., Cubillos, P. E., Curry, S. M., Dalba, P. A., de Wit, J., Deming, D., Désert, J.-M., Doyon, R., Dragomir, D., Ehrenreich, D., Fortney, J. J., García Muñoz, A., Gibson, N. P., Gizis, J. E., Greene, T. P., Harrington, J., Heng, K., Kataria, T., Kempton, E. M.-R., Knutson, H., Kreidberg, L., Lafrenière, D., Lagage, P.-O., Line, M. R., Lopez-Morales, M., Madhusudhan, N., Morley, C. V., Rocchetto, M., Schlawin, E., Shkolnik, E. L., Shporer, A., Sing, D. K., Todorov, K. O., Tucker, G. S., and Wakeford, H. R. (2016). Transiting Exoplanet Studies and Community Targets for JWST's Early Release Science Program. *PASP*, 128, 094401.

Tamura, M., Hodapp, K., Takami, H., Abe, L., Suto, H., Guyon, O., Jacobson, S., Kandori, R., Morino, J.-I., Murakami, N., Stahlberger, V., Suzuki, R., Tavrov, A., Yamada, H., Nishikawa, J., Ukita, N., Hashimoto, J., Izumiura, H., Hayashi, M., Nakajima, T., and Nishimura, T. (2006). Concept and science of HiCIAO: high contrast instrument for the Subaru next generation adaptive optics. In *Society of Photo-Optical Instrumentation Engineers (SPIE) Conference Series*, volume 6269 of *Proc. SPIE*, page 62690V.

ten Brummelaar, T. A., Gies, D. G., McAlister, H. A., Ridgway, S. T., Sturmann, J., Sturmann, L., Schaefer, G. H., Turner, N. H., Farrington, C. D., Scott, N. J., Monnier, J. D., and Ireland, M. J. (2016). An update on the CHARA array. In *Optical and Infrared Interferometry and Imaging V*, volume 9907 of *Proc. SPIE*, page 990703.

Traub, W. A. and Vanderbei, R. J. (2003). Two-Mirror Apodization for High-Contrast Imaging. *ApJ*, 599, 695.

Trauger, J. T., Burrows, C., Gordon, B., Green, J. J., Lowman, A. E., Moody, D., Niessner, A. F., Shi, F., and Wilson, D. (2004). Coronagraph contrast demonstrations with the high-

contrast imaging testbed. In Mather, J. C., editor, *Optical, Infrared, and Millimeter Space Telescopes*, volume 5487 of *Proc. SPIE*, pages 1330–1336.

Troy, M., Dekany, R. G., Brack, G., Oppenheimer, B. R., Bloemhof, E. E., Trinh, T., Dekens, F. G., Shi, F., Hayward, T. L., and Brandl, B. (2000). Palomar adaptive optics project: status and performance. In Wizinowich, P. L., editor, *Adaptive Optical Systems Technology*, volume 4007 of *Proc. SPIE*, pages 31–40.

Udalski, A., Szymanski, M., Kaluzny, J., Kubiak, M., and Mateo, M. (1992). The Optical Gravitational Lensing Experiment. *AcA*, 42, 253.

Vanderbei, R. J. and Traub, W. A. (2005). Pupil Mapping in Two Dimensions for High-Contrast Imaging. *ApJ*, 626, 1079.

Vérinaud, C., Catalano, C., Antichi, J., and Preis, O. (2011). First experimental results of the FFREE bench: investigation of Fresnel effects in high contrast imaging. In *Second International Conference on Adaptive Optics for Extremely Large Telescopes. Online at <A href="http://ao4elt2.lesia.obspm.fr">http://ao4elt2.lesia.obspm.fr</A>, id.P10*, page P10.

Vievard, S., Cassaing, F., Bonnefois, A., Mugnier, L. M., and Montri, J. (2016). Real-time alignment and co-phasing of multi-aperture systems using phase diversity. In *Ground-based and Airborne Telescopes VI*, volume 9906 of *Proc. SPIE*, page 99062Q.

Vievard, S., Cassaing, F., and Mugnier, L. M. (2017). Large amplitude tip/tilt estimation by geometric diversity for multiple-aperture telescopes. *Journal of the Optical Society of America A*, 34, 1272.

Vigan, A., Otten, G. P. P. L., Muslimov, E., Dohlen, K., Phillips, M. W., Seemann, U., Beuzit, J.-L., Dorn, R., Kasper, M., Mouillet, D., Baraffe, I., and Reiners, A. (2018). Bringing high-spectral resolution to VLT/SPHERE with a fibre coupling to VLT/CRIRES+. *ArXiv e-prints*, .

Vigan, A., Postnikova, M., Caillat, A., Sauvage, J.-F., Dohlen, K., El Hadi, K., Fusco, T., Lamb, M., and N'Diaye, M. (2016). Characterisation of a turbulent module for the MITHIC high-contrast imaging testbed. In *Adaptive Optics Systems V*, volume 9909 of *Proc. SPIE*, page 99093F.

Vohnsen, B., Castillo, S., and Rativa, D. (2011). Wavefront sensing with an axicon. *Optics Letters*, 36, 846.

Wang, J., Mawet, D., Ruane, G., Delorme, J.-R., Klimovich, N., and Hu, R. (2017). Baseline requirements for detecting biosignatures with the HabEx and LUVOIR mission concepts. In *Society of Photo-Optical Instrumentation Engineers (SPIE) Conference Series*, volume 10400 of *Society of Photo-Optical Instrumentation Engineers (SPIE) Conference Series*, page 104000Z.

Wang, Y. and Vaughan, A. H. (1988). Simplified solution of diffraction from a Lyot system. *ApOpt*, 27, 27.

Werner, M. W. (2005). The spitzer space telescope mission. *Advances in Space Research*, 36, 1048.

Wilby, M. J., Keller, C. U., Snik, F., Korkiakoski, V., and Pietrow, A. G. M. (2017). The coronagraphic Modal Wavefront Sensor: a hybrid focal-plane sensor for the high-contrast imaging of circumstellar environments. *A&A*, 597, A112.

Wolszczan, A. and Frail, D. A. (1992). A planetary system around the millisecond pulsar PSR1257 + 12. *Nature*, 355, 145.

Yaitskova, N., Dohlen, K., and Dierickx, P. (2003). Analytical study of diffraction effects in extremely large segmented telescopes. *Journal of the Optical Society of America A*, 20, 1563.

Zernike, F. (1934). Diffraction theory of the knife-edge test and its improved form, the phase-contrast method. *MNRAS*, 94, 377.

Zimmerman, N. T., Eldorado Riggs, A. J., Jeremy Kasdin, N., Carlotti, A., and Vanderbei, R. J. (2016). Shaped pupil Lyot coronagraphs: high-contrast solutions for restricted focal planes. *Journal of Astronomical Telescopes, Instruments, and Systems*, 2, 011012.